



REFERENCE ONLY

UNIVERSITY OF LONDON THESIS

Degree PhD Year 2005 Name of Author LOUSTALAN, P.W

COPYRIGHT

This is a thesis accepted for a Higher Degree of the University of London. It is an unpublished typescript and the copyright is held by the author. All persons consulting the thesis must read and abide by the Copyright Declaration below.

COPYRIGHT DECLARATION

I recognise that the copyright of the above-described thesis rests with the author and that no quotation from it or information derived from it may be published without the prior written consent of the author.

LOANS

Theses may not be lent to individuals, but the Senate House Library may lend a copy to approved libraries within the United Kingdom, for consultation solely on the premises of those libraries. Application should be made to: Inter-Library Loans, Senate House Library, Senate House, Malet Street, London WC1E 7HU.

REPRODUCTION

University of London theses may not be reproduced without explicit written permission from the Senate House Library. Enquiries should be addressed to the Theses Section of the Library. Regulations concerning reproduction vary according to the date of acceptance of the thesis and are listed below as guidelines.

- A. Before 1962. Permission granted only upon the prior written consent of the author. (The Senate House Library will provide addresses where possible).
- B. 1962 - 1974. In many cases the author has agreed to permit copying upon completion of a Copyright Declaration.
- C. 1975 - 1988. Most theses may be copied upon completion of a Copyright Declaration.
- D. 1989 onwards. Most theses may be copied.

This thesis comes within category D.

This copy has been deposited in the Library of OCL

This copy has been deposited in the Senate House Library, Senate House, Malet Street, London WC1E 7HU.



University College London

**Experimental Investigation of Near-Nozzle
Characteristics of Gasoline Sprays from
Pressure-Swirl Atomisers**

Ph.D. Thesis

Paul William Loustalan

July 2005

This thesis is submitted in partial fulfilment of the requirement for the degree
of Doctor of Philosophy

UMI Number: U592263

All rights reserved

INFORMATION TO ALL USERS

The quality of this reproduction is dependent upon the quality of the copy submitted.

In the unlikely event that the author did not send a complete manuscript and there are missing pages, these will be noted. Also, if material had to be removed, a note will indicate the deletion.



UMI U592263

Published by ProQuest LLC 2013. Copyright in the Dissertation held by the Author.
Microform Edition © ProQuest LLC.

All rights reserved. This work is protected against
unauthorized copying under Title 17, United States Code.



ProQuest LLC
789 East Eisenhower Parkway
P.O. Box 1346
Ann Arbor, MI 48106-1346

Abstract

This thesis presents an experimental investigation of the near-nozzle region of the fuel spray issuing from a pressure-swirl injector commonly found in a direct injection spark ignition engine. Specifically, the effects of the back pressure and impinging air flows were investigated. In addition to this the effect of fuel pressure was investigated.

The literature survey reveals only limited published work on the near-nozzle characteristics of fuel sprays, and the requirement for more detailed knowledge of the area to aid in the general understanding of the topic and the development of mathematical models.

Two separate experimental test rigs were designed and built to carry out the testing, firstly a static pressure chamber to identify the effects of back pressure on the fuel spray, and secondly a steady state flow rig, to investigate the effects of an impinging air flow. The steady state air flow rig was designed to simulate the air flow from the inlet valves of a direct injection spark ignition engine cylinder head.

A novel void fraction technique was utilised to quantify the fuel spray break-up process. It was found that there was a correlation between the void fraction and the fuel spray break-up length. The results from this analysis were compared to mathematical models currently available in the literature. It was found that the models do not compare well with the experimental results. A modified mathematical model was therefore proposed by the author, which can be easily integrated into existing computational codes.

It was shown that impinging air flows do not affect the primary fuel spray break-up process, however they do affect the secondary break-up of the fuel spray from ligaments into droplets. Impinging air flows also affect the general fuel spray shape, and will determine the location of the fuel spray within the cylinder far downstream of the injector.

Acknowledgements

The author wishes to thank the Engineering and Physical Sciences Research Council, EPSRC, the Ford Motor Company and Jaguar Cars for their funding of this work. Thanks are also due to Jaguar for the supply of the hardware utilised in this project.

The technical staff at the Department of Mechanical Engineering at UCL deserve thanks for their help in manufacturing the experimental test rigs and other ancillaries used in this project.

Thanks are due to Dr M H Davy for his initial support and encouragement in the early days of the PhD, without whom the project would not have existed. Above all thanks are due to Dr P A Williams for his patience and amazing depth of knowledge, without whom the project would never have finished.

Finally I would like to thank my Mum and Dad, who have always supported me in more ways than one, and Ronnie for pushing me to the end....

Table of Contents

Abstract	2
Acknowledgements	3
Table of Contents.....	4
List of Figures	8
List of Tables.....	15
Nomenclature	16
Introduction	18
Chapter 1 Direct Injection Spark Ignition Engines – A	
Literature Review.....	19
1.1 OVERVIEW – DIRECT INJECTION SPARK IGNITION ENGINES	20
1.2 FUEL SPRAYS.....	25
1.2.1 Requirements of Fuel Sprays.....	25
1.2.2 Fuel Injector Types	30
1.2.3 Structure of Fuel Sprays – The Pressure Swirl Atomiser	35
1.2.4 Break-Up Mechanisms	43
1.2.5 Fuel / Air Mixing Process.....	49
1.3 MATHEMATICAL MODELLING TECHNIQUES	50
1.3.1 Injector Models.....	51
1.3.2 Spray Models	53
1.3.3 Droplet Break-up Models	55
1.4 VISUALISATION TECHNIQUES FOR FUEL SPRAYS AND AIR FLOWS ...	58
1.4.1 Flow Seeding	58
1.4.2 Mie Scattering.....	60
1.4.3 High Speed Photography	61

1.4.4	Particle Image Velocimetry (PIV)	61
1.4.5	Laser Diffraction Techniques	62
1.4.6	Phosphorescent Particle Tracking (PPT)	64
1.4.7	Laser induced Fluorescence (LIF)	64
1.4.8	Laser / Phase Doppler Anemometry (LDA / PDA).....	69
1.5	SUMMARY	70

Chapter 2 Design of a Static Pressure Chamber and a Steady-State Flow Rig.....72

2.1	INTRODUCTION	73
2.2	OPTICALLY ACCESSED STATIC PRESSURE CHAMBER	74
2.2.1	Design Specifications	74
2.2.2	Design Process.....	75
2.3	OPTICALLY ACCESSED STEADY-STATE FLOW RIG	84
2.3.1	Design Specifications	84
2.3.2	Design Process.....	85

Chapter 3 Image Acquisition and Analysis Techniques.....92

3.1	IMAGE ACQUISITION	93
3.1.1	Imaging Requirements.....	93
3.1.2	Digital Image Capturing	97
3.2	IMAGE PROCESSING	98
3.2.1	Image Defect Correction.....	98
3.2.2	Image Enhancement.....	104
3.2.3	Segmentation and Processing Binary Images.....	112
3.2.4	Measurement of Features.....	116
3.3	SUMMARY	117

Chapter 4 Understanding the Phenomenon of Fuel Sheet

Break-Up in the Near-Nozzle Spray Region of a DISI Pressure-Swirl Atomiser118

4.1	INTRODUCTION	119
4.2	EXPERIMENTAL APPARATUS AND PROCEDURE	120
4.2.1	Global Imaging	122
4.2.2	Near Field Imaging	123
4.3	SINGLE SHOT NEAR FIELD IMAGING.....	124
4.4	ANALYSIS OF PHOTOGRAPHIC RESULTS	126
4.4.1	Analysis of Global Imaging.....	126
4.4.2	Analysis of Near Field Imaging.....	135
4.4.3	Analysis of Single Shot Imaging	147
4.5	CONCLUSION	164

Chapter 5 Effect of Impinging Air Flow on Near Nozzle

Characteristics of a Pressure-Swirl Atomiser166

5.1	INTRODUCTION	167
5.2	EXPERIMENTAL APPARATUS AND PROCEDURE	168
5.2.1	Global Imaging	170
5.2.2	Near Field Imaging	172
5.2.3	High Resolution Imaging – SLR Camera.....	173
5.2.4	Particle Image Velocimetry	174
5.2.5	Air Flow Seeding.....	179
5.2.6	Fidelity of Flow Seed to Air Flow.....	180
5.3	ANALYSIS OF FUEL VISUALISATION RESULTS	182
5.3.1	Fuel Spray Characteristics	182
5.3.2	Presence Probability Imaging	185
5.4	ANALYSIS OF AIR FLOW VISUALISATION RESULTS	190
5.4.1	Particle Image Velocimetry – Air Flow.....	191
5.5	EFFECT OF IMPINGING AIR FLOW ON THE NEAR-NOZZLE CHARACTERISTICS.....	205

5.5.1	Analysis of Near-Field Fuel Spray Images.....	206
5.5.2	Void Fraction Analysis.....	218
5.6	CONCLUSION	221

Chapter 6 Analysis of the Near Nozzle Spray Phenomenon of a Pressure-Swirl Atomiser.....223

6.1	INTRODUCTION	224
6.2	EFFECTS OF BACK PRESSURE ON THE NEAR-NOZZLE SPRAY CHARACTERISTICS.....	224
6.2.1	General Fuel Spray Characteristics	224
6.2.2	Near Nozzle Fuel Spray Characteristics – Back Pressure	225
6.3	ADAPTATION OF MATHEMATICAL MODEL	230
6.4	EFFECTS OF AN IMPINGING AIR FLOW ON THE NEAR-NOZZLE SPRAY CHARACTERISTICS.....	232
6.4.1	General Fuel Spray Characteristics	232
6.4.2	Near Nozzle Fuel Spray Characteristics – Impinging Air Flow	234
6.5	SUMMARY	236

References.....239

Appendix I – Technical Drawings.....250

Appendix II – Macro Programs – Image Pro Plus™266

Appendix III – Time Offsets for Global Imaging.....288

Appendix IV – Images – Varying Back Pressure.....290

Appendix V – Images – Impinging Air Flow301

List of Figures

Chapter 1

Figure 1.1 – Comparison of DISI and PFI engine systems (a) DISI engine (b) PFI engine.....	21
Figure 1.2 – Comparison of Wall Guided, Air Guided and Spray Guided Stratified Charge Combustion Strategies – Cathcart <i>et al.</i> [2000].....	23
Figure 1.3 – Comparison of Start of Injection Timings for (a) 240° BTDC, Homogeneous, and (b) 60° BTDC Stratified Charge Mode Combustion.....	26
Figure 1.4 – Schematic of an Inwardly Opening, Single Fluid, Pressure-Swirl Injector.....	31
Figure 1.5 – Schematic of an Outwardly Opening, Single Fluid, Pressure-Swirl Atomiser.....	33
Figure 1.6 – Schematic of a Multi-Hole Atomiser.....	35
Figure 1.7 – Schematic showing (a) Conventional Tumble, and (b) Reverse Tumble inlet air flows.....	43
Figure 1.8 – (a) Jet with rotational symmetry, Dilational Wave, (b) Jet with wave formation, Sinuous Wave.....	44
Figure 1.9 – Classification of modes of break-up, reproduced from Lefebvre [1989].....	45
Figure 1.10 – Schematic of Perforated Sheet Mode Break-Up of a Hollow Cone Spray.....	46
Figure 1.11 – Gas flow-liquid sheet interaction features, Yule <i>et al.</i> [1998].....	48
Figure 1.12 – Basic types of droplet deformation, Hinze [1955].....	49
Figure 1.13 – Two-State Energy Level Diagram, Eckbreth [1996].....	65

Chapter 2

Figure 2.1 – Simulation of Cylinder Pressure for Typical DISI motored engine.....	75
---	----

Figure 2.2 – Schematic diagram of window housing arrangement for Static Pressure Chamber.....	79
Figure 2.3 – A photograph of the main chamber showing the window locations for the Static Pressure Chamber.....	80
Figure 2.4 – Schematic diagram of fibre optic cable access blank for the Static Pressure Chamber.....	85
Figure 2.5 – Schematic of Wind Tunnel based Flow Rig.....	86
Figure 2.6 – Schematic of the side view of a reproduction DISI engine head.....	87
Figure 2.7 – Schematic of the side view of the Flow Rig final design...	88
Figure 2.8 – A photograph of the inlet port and injector arrangement for the Steady State Flow Rig.....	89
Figure 2.9 – Photograph of Flow Rig, showing air inlet, window and injector locations.....	90
Figure 2.10 – Schematic of Valve Positioning System on the Steady State Flow Rig.....	91

Chapter 3

Figure 3.1 – A plot of a 3-D Gaussian distribution superimposed onto a grid of pixels.....	101
Figure 3.2 – Observed distortion of an image typical when viewing a tilted surface, Russ [2002].....	103
Figure 3.3 – Plot of histogram prior to equalisation (a), and after equalisation (b).....	105
Figure 3.4 – Example of a FFT, original image (a), and the power spectrum (b).....	110

Chapter 4

Figure 4.1 – Schematic diagram of Experimental Apparatus utilised during the first phase of testing.....	121
Figure 4.2 – Schematic of optical arrangement for (a) Global Imaging, (b) Near Field.....	122

Figure 4.3 – ‘N’ Shot acquisition timing sequence for HSRDC operation.....	123
Figure 4.4 – Schematic diagram of Experimental Apparatus for single shot imaging.....	125
Figure 4.5 – Schematic of the Timing Sequence for the Single Shot Imaging.....	126
Figure 4.6 – Penetration measurement of a 1-bit image.....	128
Figure 4.7 – Schematic diagram defining the ‘root’ of the spray cone angle measurement and the boundary recognition process	129
Figure 4.8 – Global Imaging Results, 5 MPa fuel pressure.....	130
Figure 4.9 – Global Imaging Results, 10 MPa fuel pressure.....	131
Figure 4.10 – Axial Spray Penetration, (a) for 5 MPa fuel pressure and (b) for 10 MPa fuel pressure, for Injector A.....	132
Figure 4.11 – Spray Cone Angle (@ 10 mm from tip), (a) for 5 MPa fuel pressure, (b) for 10 MPa fuel pressure and (c) the effect of back pressure on the cone angle.....	133
Figure 4.12 – Example of Area within a near field image that is ‘in-focus’.....	136
Figure 4.13 – Example of void recognition program for 5 MPa fuel pressure.....	137
Figure 4.14 – Flow diagram of Void Recognition Program Procedure...	138
Figure 4.15 – Plot to show effect of AOI height for typical image analysis.....	139
Figure 4.16 – Consecutive positions of one perforation. Detailing the effects of the expanding sheet on the hole shape.....	140
Figure 4.17 – Box Width versus Distance from injector tip, a comparison of calculations to measurements.....	142
Figure 4.18 – Box Ratio versus Distance from injector tip, for varying back pressure and fuel pressure.....	143
Figure 4.19 – Void Fraction versus Distance from injector tip, for varying back pressure and fuel pressure for Injector A.....	144

Figure 4.20 – Plot to show Break-Up Length versus Back Pressure for the three models studied, (a) for 5 MPa fuel pressure and (b) for 10 MPa fuel pressure.....	145
Figure 4.21 – Near Field images at 5 MPa fuel pressure showing predicted break-up lengths from Han, Ren and Schmidt models.....	146
Figure 4.22 – Near field images at 10 MPa fuel pressure showing predicted break-up lengths from the Han, Ren and Schmidt models.....	147
Figure 4.23 – Single shot images at 5 MPa fuel pressure at both 50 and 100 kPa back pressure for Injector B.....	148
Figure 4.24 - Single shot images at 10 MPa fuel pressure at both 50 and 100 kPa back pressure for Injector B.....	149
Figure 4.25 – Enlargement of a section of fuel spray to demonstrate the granular texture.....	150
Figure 4.26 – Plot of light intensity variation along injector axis for single shot imaging.....	151
Figure 4.27 – Plot of light intensity variation across the edge of a hole to allow the image threshold value to be determined.....	152
Figure 4.28 – Example of hole in fuel sheet shown in side profile for Injector B.....	153
Figure 4.29 – Plot of void fraction vs distance from injector tip for Injectors A and B.....	154
Figure 4.30 – Void fraction analysis profiles shown individually to highlight error bars, for varying test conditions.....	155
Figure 4.31 – Images of the far Downstream Fuel Spray for (a) 5 MPa – 50 kPa and (b) 10 MPa – 50 kPa.....	158
Figure 4.32 – Void Fraction Analysis for entire FOV for (a) 5 MPa – 50 kPa and (b) 10 MPa – 50 kPa.....	159
Figure 4.33 – Void Fraction Analysis for entire FOV for 5 MPa – 50 kPa showing the plots of ± 1 standard deviation.....	162
Figure 4.34 – Image showing periodic surface features on fuel spray issuing from Injector B.....	163

Chapter 5

Figure 5.1 – Schematic diagram of Experimental Apparatus for Air Flow Rig.....	170
Figure 5.2 – Oscilloscope traces of the output current for Injector A; Trace 1: Injector Signal Pulse – 2 ms width Trace 2: Injector Drive Current – 100 mV / division.....	171
Figure 5.3 – Schematic diagram of Fibre Optic Light delivery Set-up...	172
Figure 5.4 – SLR Camera control timing sequence (all signals are TTL).....	173
Figure 5.5 – Schematic diagram of Light Sheet Set-up used for PIV....	174
Figure 5.6 – PIV Camera control timing sequence (all signals are TTL)	175
Figure 5.7 – The response of particles in Turbulent flow, from Melling [1997].....	180
Figure 5.8 – (a) Axial Spray Penetration and (b) Cone Angle for 5 MPa Fuel Pressure all with an Air Flow present at a pressure drop of 19.65 kPa.....	183
Figure 5.9 – Enlargement of the Initial phase of the Cone Angle Development.....	184
Figure 5.10 – PPI of (a) 2 mm Valve Lift, (b) 3 mm Valve Lift (c) 5 mm Valve Lift, all for 80.35 kPa Back Pressure, 5 MPa fuel pressure.....	187
Figure 5.11 – Pixel Intensity across PPI images averaged around 6.5 mm from injector tip.....	189
Figure 5.12 – Schematic of the Imaging Planes and the area of assumed consistency of the air flow.....	191
Figure 5.13 – The Calculated vs Measured Mean Velocity variation with Mass Flow Rate.....	192
Figure 5.14 – Scaled Vector Field of 5 mm Valve Lift – Plane A-A, Valve Centreline.....	194
Figure 5.15 – Velocity magnitude Profile of section Z-Z (Figure 5.10).	195
Figure 5.16 – Scaled Vector Field for 2 mm Valve Lift, 530 Pa Depression – Plane B-B.....	196

Figure 5.17 – Scaled Vector Field for 3 mm Valve Lift, 530 Pa Depression – Plane B-B.....	197
Figure 5.18 – Scaled Vector Field for 5 mm Valve Lift, 530 Pa Depression – Plane B-B.....	198
Figure 5.19 – Schematic representation of the Spray Profile Calculation Process.....	200
Figure 5.20 – Plot of Spray profiles – Obtained from Images and Calculation.....	202
Figure 5.21 – Plot of Spray profiles – (a) 2 mm Valve Lift, (b) 3 mm Valve Lift, (c) 5 mm Valve Lift.....	204
Figure 5.22 – Plot of all three Calculated Spray profiles.....	205
Figure 5.23 – Fuel Spray image, (a) Injector Tip and (b) Downstream, 2 mm Valve Lift, 19.65 kPa Depression, 5 MPa fuel pressure.....	207
Figure 5.24 – Fuel Spray image, (a) Injector Tip and (b) Downstream, 3 mm Valve Lift, 19.65 kPa Depression, 5 MPa fuel pressure.....	209
Figure 5.25 – Fuel Spray image, (a) Injector Tip and (b) Downstream, 5 mm Valve Lift, 19.65 kPa Depression, 5 MPa fuel pressure.....	211
Figure 5.26 – Scaled Vector Field for 5 mm Valve Lift, 530 Pa Depression – Plane A-A, overlaid with the Fuel Spray image with equivalent settings.....	214
Figure 5.27 – Overlay of Valve Plane PIV Vector Field on Fuel Spray Image – 2 mm Valve Lift (Fuel Spray Image – 19.65 kPa Depression, PIV Vector Field Scaled).....	215
Figure 5.28 – Overlay of Valve Plane PIV Vector Fields on Fuel Spray Images – (a) 3 mm and (b) 5 mm Valve Lifts (Fuel Spray Image – 19.65 kPa Depression, PIV Vector Field Scaled).....	216
Figure 5.29 – Plot of light intensity variation with distance along injector axis.....	218

Figure 5.30 – Plot of Void Fraction Analysis for 2, 3 and 5 mm Valve Lifts – 19.65 kPa Depression.....	219
--	-----

Chapter 6

Figure 6.1 – Plot to show Break-up Length versus Back Pressure for the three models studied and the Break-Up lengths obtained from the void fraction analysis, (a) for 5 MPa fuel pressure and (b) for 10 MPa fuel pressure.....	227
Figure 6.2 – Image of Fuel Spray for 5 MPa fuel pressure – 50 kPa back pressure, showing the break-up point found from the void fraction analysis.....	229
Figure 6.3 – Plot to show Break-up Length versus Back Pressure for the modified model and the Break-up lengths obtained from the void fraction analysis. (a) for 5 MPa fuel pressure and (b) for 10 MPa fuel pressure.	232

List of Tables

Chapter 4

Table 4.1 – Details of the two injectors utilised during testing.....	120
Table 4.2 – Table of Void Fraction turning points in comparison to model break-up length predictions for varying test conditions.....	157
Table 4.3 - Table of Void Fraction turning points in comparison to model break-up length predictions, with revised break-up lengths.....	161
Table 4.4 – Table of surface feature wavelengths.....	162

Chapter 5

Table 5.1 – Table of Mass flow rate through Flow Rig for varying Valve Lifts.....	169
Table 5.2 – Table of Pressure drop across Valves used for PIV Air Flow.....	176
Table 5.3 – Table of cone angle deflection due to impinging air flow...	185
Table 5.4 – Table of Void Fraction turning points for varying Valve Lifts.....	219

Chapter 6

Table 6.1 – Table of Turning Points / break-up lengths obtained using the Void Fraction Technique.....	228
---	-----

Nomenclature

AOI – Area Of Interest

ASOF – After the Start Of Fuel

ASOI – After the Start Of Injection

B – pixel Brightness level in an image

BDC – Bottom Dead Centre

BTDC – Before Top Dead Centre

CCD – Charge Coupled Device

CMOS – Complementary Metal Oxide Semiconductor

DISI – Direct Injection Spark Ignition

DOF – Depth Of Field

DOHC – Dual overhead cam

$D_v[10]$ – Diameter that 10 % of fuel droplets by volume are smaller than

$D_v[90]$ – Diameter that 90% of fuel droplets by volume are smaller than

EGR – Exhaust Gas Recirculation

FFT – Fast Fourier Transform

FOV – Field Of View

HSRDC – High Speed Rotating Drum Camera

ILIDS – Interferometric Laser Imaging Droplet Sizing

ISFC – Indicated Specific Fuel Consumption

L – Break-up Length

LDA – Laser Doppler Anemometry

LIEF – Laser Induced Exciplex Fluorescence

LIF – Laser Induced Fluorescence

NO_x – Oxides of Nitrogen

P – Pressure

PDA – Phase Doppler Anemometry

PDPA – Phase doppler particle analyser

PFI – Port Fuel Injection

PIV – Particle image velocimetry

PPAA – Pulse-Pressurised, Air-Assisted

PPI – Presence Probability Imaging

PPT – Phosphorescent particle tracking

RMS – Root Mean Square

SLR – Single Lens Reflex

SMD – Sauter mean diameter, ratio of liquid volume to surface area of the spray

SPG – Stanford Pulse Generator

TOC – Target Object Contrast

UBHC – Unburnt Hydrocarbons

V – Volume

Nomenclature - Mathematical Models

C = Constant of Proportionality – Ren and Nally [1998] model

D = Constant of Proportionality – Han *et al.* [2001] model

E = Constant of Proportionality proposed by the Author

d_0 = Injector hole diameter

h = Sheet thickness

L = Break-up length

$\ln(\eta_b/\eta_0)$ = Constant – Ratio of disturbance wavelength at the point of break-up to initial disturbance wavelength– Schmidt *et al.* [1999] model

Q = Density ratio of gas to fuel

U = Sheet velocity

V_r = Sheet/gas relative velocity

θ = Half cone angle

ρ_g = Density of Gas

ρ_l = Density of Fuel

σ = Surface tension of fuel

ν_l = kinematic viscosity of fuel

Ω = Maximum growth rate of a disturbance

ω_r = growth rate of wave with wavelength k

Introduction

The aim of this thesis is to provide a physical understanding of the near-nozzle characteristics of a pressure-swirl atomiser commonly utilised in direct injection spark ignition engines. A literature review was conducted which provides an introduction to direct injection spark ignition engines and their requirements concerning fuel injectors. A more detailed study was carried out to discover the current knowledge available on pressure-swirl atomisers and the associated techniques available to reveal the details of fuel sprays through imaging and analysis.

To undertake the experimental phase of the research two test rigs were required. A static pressure chamber to allow the ambient pressure to be controlled, allowing the effects of back pressure to be studied. A steady state flow rig was also designed, simulating a direct injection spark ignition cylinder head to allow the effects of an impinging air flow issuing from the inlet valves to be studied. They were designed by the author, the details of which may be found in this thesis.

The images obtained using the techniques described in the literature review required post-processing, therefore a review of the currently available image processing techniques was carried out. This enabled the quality of the results obtained to be optimised.

The results obtained from the static pressure chamber are then presented, detailing the effects of varying back pressure and fuel pressure on the near-nozzle characteristics of a pressure swirl atomiser. This is followed by the results obtained from the steady state flow rig detailing the effects of an impinging air flow on the near nozzle characteristics.

Both results chapters are then summarised in the final chapter, which includes the results from mathematically modelling the fuel break-up process.

Chapter 1
Direct Injection Spark Ignition Engines – A
Literature Review

Chapter 1 Direct Injection Spark Ignition Engines – A Literature Review

This chapter is an overview of the current literature relevant to the proposed programme of work. It investigated the current methods of fuel metering in spark ignition engines, with a specific focus on direct injection engines. An overview of injectors presently used is included, in conjunction with the theory of spray formation and break-up. Also included are existing modelling techniques, progressing from modelling the fuel flow within the nozzle to the fuel/air mixing process. Finally an overview of the current visualisation techniques relevant to fuel sprays and fluid flows is provided.

1.1 Overview – Direct Injection Spark Ignition Engines

Port fuel injection (PFI) is currently the most widely used form of fuel metering in the spark ignition internal combustion engine. Heywood [1988] describes that the concept of PFI engines is the fuel is injected into the intake port/manifold. Therefore, the majority of the latent heat of evaporation required to evaporate the fuel is obtained from the port and valve surfaces, Anderson *et al.* [1996]. When the intake valve is opened, the vaporised, and remaining liquid fuel are drawn into the cylinder with the charge air creating a homogeneous mixture. This is the case for closed valve injection, and although favourable sometimes during transients and high engine speeds, it is also necessary to inject when the inlet valve is open. During open valve injection not all of the fuel will impact the hot port and valve surfaces, leading to larger droplets entering the cylinder. This increases the amount of wall wetting present which in turn increases the unburnt hydrocarbon (UBHC) emissions.

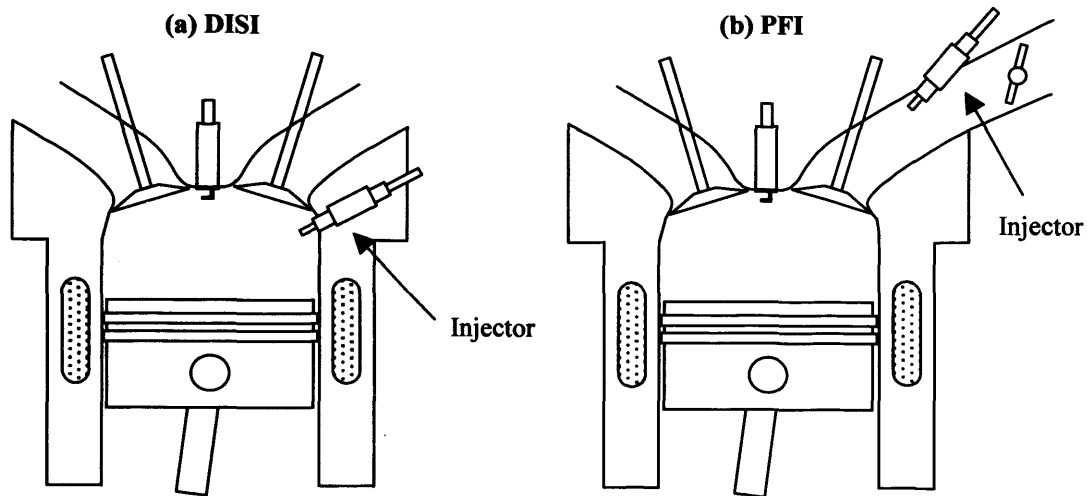


Figure. 1.1 – Comparison of DISI and PFI engine systems (a) DISI engine (b) PFI engine

Direct injection spark ignition (DISI) engines are seen as an alternative to PFI spark ignition engines due to many potential advantages. They include a thermodynamic potential to reduce specific fuel consumption, hence a reduction in CO₂ emissions, with the advantage of quicker starting, enhanced transient response and more precise control of the air/fuel ratio. There are three main forms of DISI combustion that may be utilised by the engine designer, either individually or in combination to provide suitable performance throughout the load range. They are early injection homogeneous combustion, in which the air is throttled for load control, late injection stratified charge combustion, in which the fuel is metered to provide load control, and thus benefits from the gain of reduced pumping losses. Zhao *et al.* [1997] notes that it is also possible to utilise leaner homogeneous mixtures with reduced throttling for some degree of load control.

The strategy of injecting fuel early in the cycle was adopted, prior to 1950, in some aeroplane engines before sophisticated carburettors were invented, Iwamoto *et al.* [1997]. The system was used to overcome the power deficiency inherent with carburettor systems. Early DISI technology was superseded by the invention of sophisticated port fuel injection systems. Development of DISI technologies between the 1950's and the 1980's was limited, since the technologies necessary for accurate control of the fuel injection process were not yet available. The Ford PROCO engine described by Simko *et al.* [1972], which had a close arrangement of the spark plug and injector, leading to short

mixing times, was developed in this period but there were problems associated with misfire when the engine was operated in a low NO_x configuration. It also utilised diesel derived injection components. The hydrocarbon and carbon monoxide emission could not be sufficiently controlled without the development of new technologies, such as oxidising catalysts or combustion control optimisation. Interest in DISI combustion engines declined throughout this period since the problems associated with this technology outweighed the assumed benefits, (fuel economy and emissions were not given a high priority at the time). The concept of DISI was only revisited in the 1990's due to an increasing requirement to reduce emissions. Fuel economy was the main factor since it is the main method of reducing CO₂ emissions, which are a natural product of hydrocarbon combustion, Iwamoto *et al.* [1997].

Maximum fuel economy at low loads is achieved by operating the engine in an extremely lean overall condition, metering the fuel to provide load control. In doing this the pumping losses are decreased, reducing the indicated specific fuel consumption (ISFC). Fraidl *et al.* [1996] have reported that theoretically, using this regime the overall air/fuel ratio may be as lean as 100. However in practice air/fuel ratios of between 25 and 40 are reported by Kume *et al.* [1996], Harada *et al.* [1997], which corresponds to unthrottled operation. To operate in this condition the charge must be distinctly stratified to provide an air/fuel ratio that is suitable for combustion around the spark plug. To create the stratified charge the fuel is typically injected late in the cycle, towards the end of compression. Injecting late into the cycle means that the ambient cylinder conditions are that of high pressure and temperature. Fraidl *et al.* [1996] states that to initialise combustion in this type of engine it is necessary to control the fuel charge such that the stoichiometric air/fuel mixture is located at the spark plug at the time of ignition. The three main methods by which stratification can be accomplished are typically known as, wall guided, air guided and spray guided strategies, (see Figure 1.2).

Stratified charge combustion is only suitable for low and part-loads, therefore to cope with the higher power requirements at full-load a different combustion scheme is required. Homogeneous combustion is utilised at full-load to

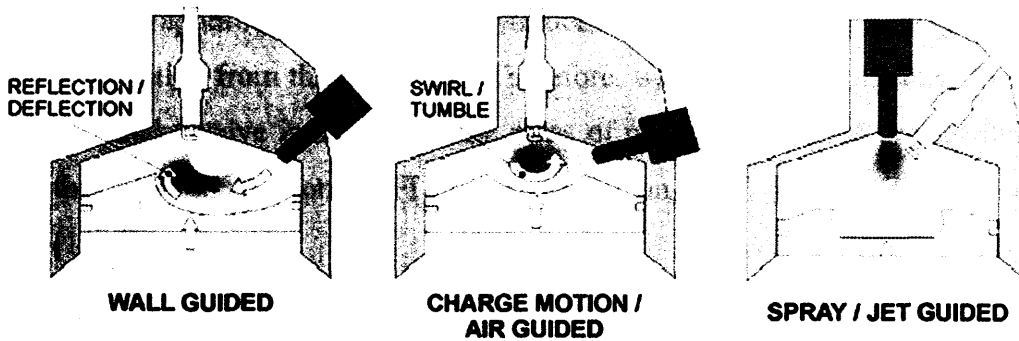


Figure 1.2 – Comparison of Wall Guided, Air Guided and Spray Guided Stratified Charge Combustion Strategies – Cathcart *et al.* [2000]

increase the power output of the engine. The homogeneous charge is obtained by injecting early in the cycle, at a time after TDC during the intake stroke. Thus, a greater amount of time is allowed for atomisation and vaporisation of the fuel and then for the mixing of fuel and air, producing a homogeneous mixture. To maximise the power output of the engine, the air/fuel ratio will be close to stoichiometric. Since the fuel is being directly injected into the cylinder when the intake valves are open, the majority of the energy required for vaporisation is obtained from the air. This is different to PFI where the fuel is injected into the intake ports/manifold, where the majority of the latent heat is obtained from the walls. Thus, the charge air is cooled, creating a more dense charge, resulting in a greater volumetric efficiency, Anderson *et al.* [1996], Zhao *et al.* [1997]. Charge cooling allows either the compression ratio to be increased to give improved efficiency, or it allows the octane requirement for any given spark timing to be decreased. In practice the octane rating of the fuel is set at the refinery, therefore the benefit obtained from charge cooling is the increase in the knock limited spark advance. This results in an increased torque output from the engine.

Advantages of DISI :

- Higher thermal efficiency because of lower pumping and heat losses. There will be lower pumping losses due to the unthrottled operation. The heat loss from the engine will be reduced due to the charge air cooling, Harada *et al.* [1997], Zhao *et al.* [1997].
- Higher volumetric efficiency and improved anti-knock characteristics because of lower temperature charge air. Charge air cooling occurs due to

fuel evaporation inside the cylinder, the fuel obtains energy for evaporation from the charge air. Therefore, when the fuel is injected when the intake valve is still open, the mass of charge air will be greater than that of a conventional PFI engine, Anderson *et al.* [1996], Zhao *et al.* [1997].

- Higher power output due to the higher compression ratio available.

Disadvantages of DISI:

- Difficulty in controlling the stratified charge under varying engine operating conditions, to keep the mixture surrounding the spark plug suitable for ignition, Zhao *et al.* [1997].
- Soot (smoke) at higher loads caused when hydrocarbons are heated without air (oxygen), causing them to be broken down into hydrogen and carbon (soot), this process is called pyrolysis. Preferably this would not be created, however sufficient excess air should be provided around the combustion zone to burn up the soot that is generated by pyrolysis, Iwamoto *et al.* [1997], Kume *et al.* [1996].
- NO_x emissions during stratified charge operation, formed through the Zeldovich reactions, when there are high temperatures and high amounts of excess air (oxygen) will lead to the formation of NO_x, Heywood [1988], Zhao *et al.* [1997]. Anderson *et al.* [1996] suggest that to combat this high amounts of exhaust gas recirculation (EGR) in the order of 40-50% should be utilised, in conjunction with lean NO_x catalysts. NO_x however does not occur solely in stratified charge operation, it will occur whenever an engine is run lean of stoichiometry. In fact when the engine is run extremely lean the NO_x levels return to there levels at the stoichiometric air/fuel ratio. However these levels of NO_x are still above the legislated values so lean NO_x catalysts are still required.

- Unburned hydrocarbon emissions at light loads, Zhao *et al.* [1997], caused by among other reasons, quenching of the flame as the flame front progresses from the rich region surrounding the spark plug to the regions significantly leaner than stoichiometry at the edge of the cylinder. Other possible reasons are the increased fuel forced into crevice volumes due to higher compression ratios, and the cyclic variation in evaporation rates, which may become significant.

1.2 Fuel Sprays

The following section will give an overview of the fuel spray requirements from a DISI engine under varying operating regimes. The different types of injector that have been developed for use in DISI applications will be highlighted. The requirements of the fuel spray in different operating regimes will be given. The characteristics of sprays from a pressure-swirl atomiser will also be discussed with their relevance to the DISI engine requirements. Finally, the spray break-up mechanisms of a pressure-swirl atomiser and the factors that affect them will be examined.

1.2.1 Requirements of Fuel Sprays

The requirements of fuel sprays in a DISI engine are very specific, since according to Fraidl *et al.* [1996] the combustion process is dependent on the mixture formation and, in the case of stratified charge operation, position of the charge relative to the point of ignition. The type of combustion strategy employed will be the main factor influencing the requirements of the fuel spray, whether that be wall, spray or air guided, see §1.1.

1.2.1.1 Homogeneous Charge Combustion

A homogeneous charge combustion strategy utilizes injection early in the cycle, Ohsuga *et al.* [1997] states that a typical injection timing would be around 240° BTDC (firing). With ignition timing typically being around 30° BTDC (firing), Shayler *et al.* [2001], this leaves 210° for atomisation,

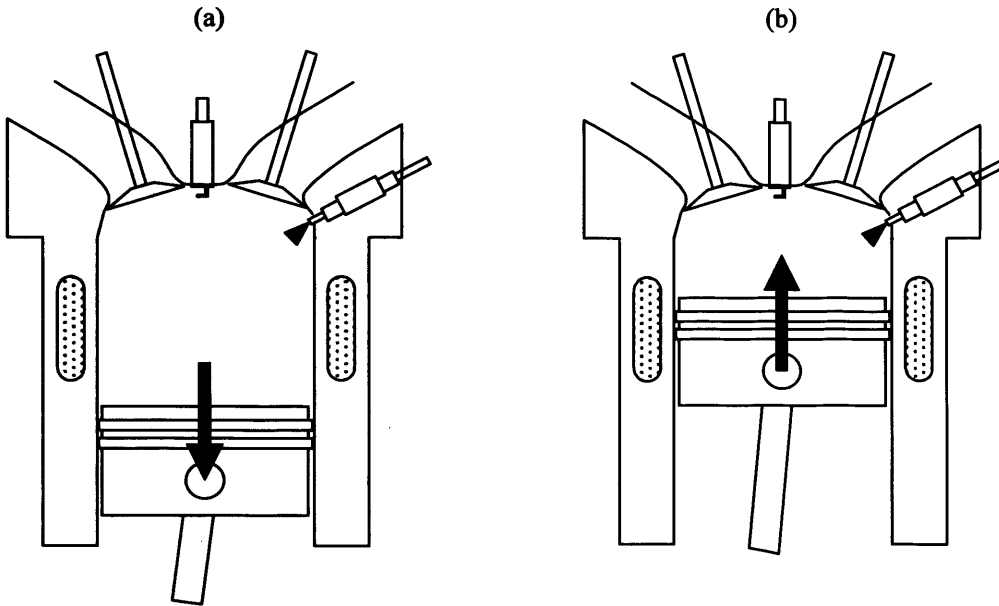


Figure 1.3 – Comparison of Start of Injection Timings for, (a) 240° BTDC, Homogeneous, and (b) 60° BTDC Stratified Charge Mode Combustion

evaporation and mixing with the charge air, which even at 3000 rpm is over 10 ms (see Figure 1.3 for schematic representation of injection timing). A typical injection pulse width proposed by Preussner *et al.* [1998], would be 2.5 ms, therefore giving a large amount of time for mixture preparation, compared to stratified charge operation, see §1.2.1.2. Even though the amount of time available is more than for stratified charge mode, it is still less than that available for conventional PFI engines.

The main requirement for a fuel spray in homogeneous mode is to provide a finely atomised, dispersed spray, while maintaining suitable penetration, to utilise the charge air to the best effect creating a homogeneous mixture throughout the cylinder. Zhao *et al.* [1999] reports that to keep unburnt hydrocarbon emissions to a minimum, impingement of the spray onto the cylinder and piston surfaces should be minimised. In homogeneous mode the engine is throttled as with a PFI engine to adjust to the load requirements. To maintain the stoichiometric air fuel ratio the fuel is metered depending on the position of the throttle.

It must be noted that a fully functional DISI fuel system need only provide for this homogeneous, stoichiometric mode of operation. However, to obtain

further fuel economy benefits of the DISI fuel system most use a minimum of two modes. The fuel system therefore must be able to adapt to the particular requirements of the vehicle at any point within its drive cycle. Due to the lack of time available and the other special requirements of the DISI fuel system, compared to the PFI fuel system, a number of different injectors have been developed solely for the DISI concept, and these will be described in § 1.2.2.

1.2.1.2 Stratified Charge

A stratified mixture combustion process utilises injection late in the cycle to enable a stoichiometric air/fuel mixture to remain locally to the spark plug, allowing combustion to take place, while maintaining an overall lean air fuel ratio. Typical injection timing for stratified charge mode would be around 60° BTDC (firing), with ignition timing around 20° BTDC (firing), depending on engine speed, Zhao et al. [1999], Nogi et al. [1998], see Figure 1.3 for schematic representation of injection timing. Calculating the time available from start of injection to start of ignition at an engine speed of 3000 rpm, gives just over 2 ms for injection and mixture formation. However, less fuel is required as the air/fuel ratio will overall be higher, it is also unlikely that the engine will be running in stratified charge mode at such high engine speeds.

Choi *et al.* [2000] reports that the main factor influencing the stratified combustion process will be the limited time for atomisation, evaporation and mixing to occur, which has now been reduced to approximately 40° crank angle. The spatial evolution of the mixture distribution and its reproducibility will also be a major factor influencing the stratified charge combustion process. The relative importance of the spatial evolution will be dependant on the type of combustion strategy employed, whether that may be, wall, spray or air guided.

Tomoda *et al.* [1997] have shown that two factors aid in the production of a stable stratified mixture, they are to decrease the time between injection and ignition and to decrease the distance from the injector tip to the spark gap. However decreasing the distance from the injector tip to the spark gap will

also reduce the amount of time available for mixture preparation, which may produce soot due to the poorly atomised fuel. This reduced distance may also lead to plug wetting and fouling. The spray is required to atomise and evaporate quickly, with control over the process coming both from the injector design, including; nominal cone angle, fuel line pressure, and swirl ratio, (i.e. ratio of tangential to axial velocity of the fuel), and also from the in-cylinder flow conditions which will affect the spray characteristics and the spatial evolution of the spray.

Wall-Guided Combustion Strategy – Zhao *et al.* [2002] states that the fundamental concept behind the wall-guided strategy is to increase the separation between the injector and the spark plug, thus allowing more time for mixture preparation. However this may lead to some combustion instability due to cycle to cycle variation. To reduce the combustion instability a shaped piston crown is used to direct the spray towards the spark plug. Utilizing a specifically contoured piston and optimised tumble and swirl it is possible to transport the fuel vapour to obtain stratified combustion. Zhao *et al.* [2002] reports that although the spray is directed onto the piston, impingement of droplets onto the piston surface is limited. Kakuhou *et al.* [1999] reports similar findings, however the results show that the amount of fuel impingement will be dependant on the injection timing. This occurs due to entrainment of the droplets and vapour by an air flow field, thus the contours of the wall direct the air which in turns affects the path of the fuel. Some liquid fuel will impinge on the piston, mainly from the pre-spray, which is formed predominantly by relatively large droplets, Kawajiri *et al.* [2002], but this must be minimised to reduce the HC, CO and soot emissions.

The effect of liquid fuel on the piston surface is that the surface temperature is not high enough to allow evaporation of the fuel, therefore when combustion occurs there will still be significant amounts of liquid fuel. Which will, according to Sandquist *et al.* [2000] generally burn as a rich diffusion flame due to limited availability of oxygen, or in a pool fire, creating increased HC, CO, and soot emissions. Conversely Huang *et al.* [2001], suggest that the lack of evaporation from the piston surface is due to the leidenfrost effect, where

the piston surface temperature is in fact so much higher than the evaporation point of the fuel that an insulating layer of vapour forms between the liquid and piston surface, thus reducing the overall evaporation rate. Both authors' present piston surface temperatures of the same order, however Huang *et al.* [2001] present this effect using single component fuels. The leidenfrost effect is apparent for the light fraction fuels with low boiling temperatures, with the effect falling with increasing mass fraction, and therefore boiling temperature, until the effect is no longer seen. However for gasoline the light fractions may initially support the heavier fractions, producing the same effect leaving the heavy fractions in the liquid phase to cause HC, CO and soot emissions.

To minimise impingement of fuel onto surfaces the location of the injector, and the general spray characteristics, cone angle and penetration etc, are an important consideration. The injector location currently used by most DISI concepts is between the inlet valves, beneath the intake port. Zhao *et al.* [2002] reports that this improves air entrainment during early injection, and aids in cooling the injector tip. To enable a compact fuel-air mixture to be developed the initial fuel spray must be compact, with small droplet sizes.

Air Guided Combustion Strategy – The air guided combustion strategy is controlled by the interaction of the spray and a strong flow field. Generally a strong tumble based flow field is established to control the spatial evolution of the spray to create the stratified charge. As with the wall guided strategy there is a large gap between the injector tip and spark gap, providing the same advantage of allowing more time for mixture preparation. The advantage associated with the air guided strategy is that notionally the stratified charge is achieved without any impingement of the spray on the wall, reducing the effects of HC emissions due to wall films. However any fluctuations in the flow field may lead to combustion instability. Low engine speeds may also lead to instability as the strength of the flow field is diminished, leading to less control over the spray path. The fuel spray must have characteristics that are similar to those of the wall guided system, namely a compact spray that is well atomised to allow fast mixture preparation and domination by the flow field.

Spray Guided Combustion Strategy – The spray guided strategy positions the injector such that the fuel spray is directed towards the spark gap, so when ignition occurs there is fuel vapour surrounding the spark gap. This approach was utilised in the initial development of DISI engines, the Ford PROCOCO system, Simko *et al.* [1972], used a spray guided strategy to achieve a stratified charge. Stratification can be realised without a dependence on charge motion or piston crown design. Takagi *et al.* [1998] reports that a bowl shape piston generally reduces maximum BMEP at higher loads and the ability to have stratified combustion with a piston crown designed for maximum BMEP is an advantage of this strategy. The proximity of the injector tip to the spark gap significantly reduces the time available for mixture preparation, increasing the problem of spark plug fouling and soot generation. To provide combustion stability an injector that has minimal cycle to cycle variation is a necessity. The injector must also provide a spray that is not affected by the in cylinder conditions, i.e. pressure and temperature, the cone angle must remain constant so that at the point of ignition there is always an ignitable fuel/air mixture.

To obtain the full fuel economy benefits of DISI as well as keeping power output at, or above the level of an equivalent modern PFI engine both modes of operation are required, unless fully variable valve control is employed. Stratified charge operation gives the benefit of increased fuel economy at low loads due to reduced levels of throttling, while homogeneous charge operation maximises the power output. For stratified charge operation, the fuel spray must be compact to avoid weakening the mixture to the extent where it is no longer combustible. In homogeneous charge operation, the fuel spray should be less compact to promote complete mixing with the air. These two conflicting requirements must be incorporated into a single combustion management system.

1.2.2 Fuel Injector Types

It has been shown that DISI engines have very specific injector requirements, which significantly differ to those of the PFI engine injector. The injector characteristics required and therefore developed, will be dependant on the

requirements of the combustion system. Therefore many different types of injector have been developed specifically for use in the DISI engine. This section will describe the basic principles behind the more commonly used injectors, and the combustion strategies that would utilise them. There are five generic types of injector, as given by Zhao *et al.* [2002]:

- **Inwardly-opening, single fluid, high pressure swirl injectors**
- **Outwardly-opening, single fluid, high pressure swirl injectors**
- **Pulse-pressurised, air-assisted injectors**
- **Hole-type nozzles**
- **Slit-type nozzles**

Inwardly-opening, single fluid, high pressure swirl injectors – This swirl type injector utilises an inwardly-opening pintle and a single exit orifice, (see Figure 1.4). Unlike an inwardly opening PFI injector, the pintle does not extend through the exit orifice. By means of tangential slots or holes upstream of the exit orifice a rotational momentum is imparted on the fuel, this combines with the axial momentum, Fraidl *et al.* [1996]. The fuel exits the orifice as an annular sheet that, due to the rotational momentum, expands radially outwards to form a hollow cone spray. Conservation of mass dictates

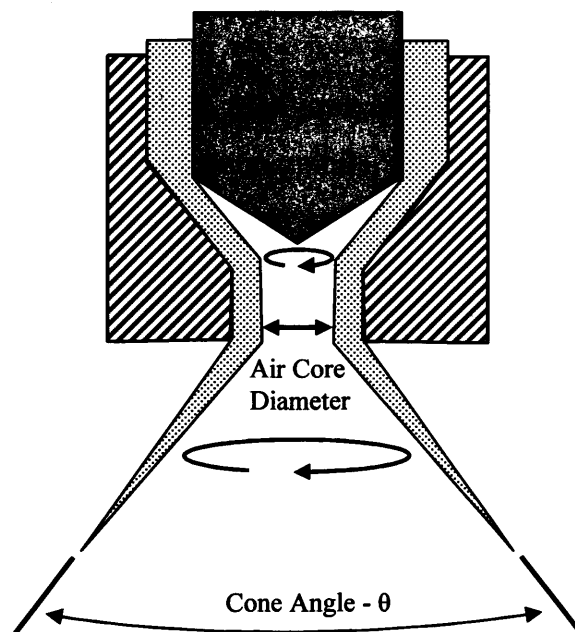


Figure 1.4 – Schematic of an Inwardly Opening, Single Fluid, Pressure-Swirl Injector

that as the hollow cone expands the fuel sheet must thin, eventually becoming unstable and breaking up into droplets. Fraidl *et al.* [1996] states that the cone angle of the spray is determined by the nozzle geometry, and to a lesser extent the fuel pressure. Typical fuel pressures range from 7 to 10 MPa. The cone angle can range from 25° to 150° depending on the requirements of the engine, Zhao *et al.* [2002]. To conform to packaging requirements the spray axis may be offset from the injector axis. Robert Bosch Gmbh and Denso are just two examples of manufacturers of inwardly-opening pressure swirl injectors.

The inwardly opening pintle injector has a pre-spray, occurring before the main fuel spray due to the sac volume. Zhao *et al.* [1997] defines the sac volume as the liquid fuel within the injector that is not at the fuel line pressure. As the sac volume has minimal radial momentum and is at low pressure, the pre-spray atomisation is relatively poor, Ipp *et al.* [1999], Karaiskos *et al.* [2002]. The relatively high velocity of the pre-spray also leads to the possibility of piston wetting, which may be a cause for hydrocarbon emissions, Williams *et al.* [1998], Davy *et al.* [1998] and Sandquist *et al.* [2000] all report similar findings. The inwardly-opening, single fluid, high pressure swirl injectors may be used in the air and wall guided combustion strategies. This type of injector is the focus of this thesis and as such its characteristics will be discussed in more detail in forthcoming sections.

Outwardly-opening, single fluid, high pressure swirl injectors – This type of injector utilises an outwardly opening pintle, and may or may not be a swirl type. The outwardly opening pintle allows the sheet thickness to be controlled via the pintle stroke rather than the angular velocity of the fuel. Xu and Markle [1998] report that this allows greater control of the sheet thickness and therefore the atomisation characteristics. The penetration and droplet sizes may be reduced with the addition of a swirling flow, along with increasing the cone angle. This type of injector has enhanced leakage resistance, compared to that of the inwardly opening injector, due to the combustion pressure acting to positively seal the pintle. This is the same concept as for engine valves. The outwardly opening pintle eliminates the sac volume and therefore the pre-spray. Thus the large droplets found within the pre-spray are not found in the

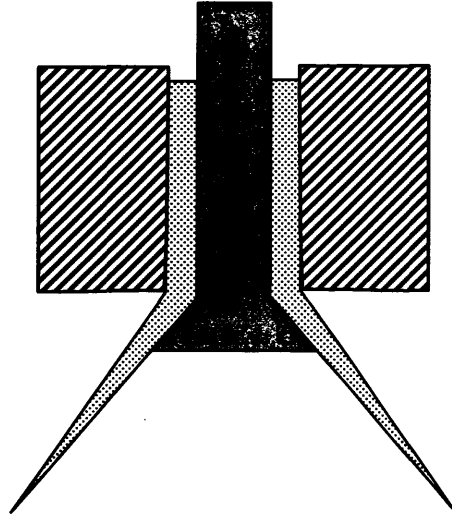


Figure 1.5 – Schematic of an Outwardly Opening, Single, Fluid Pressure-Swirl Atomiser

outwardly opening spray structure. Although the droplets found at the leading edge of the spray are likely to be larger than those which follow, similar to a PFI injector. According to Befrui *et al.* [2002] the spray structure of the injector is extremely stable compared to the inwardly opening injector, as the cone angle is set by the pintle and is not a function of the radial momentum of the spray, nor the air pressure in the spray core. It therefore presents itself as a suitable candidate for spray guided combustion systems. The injector is however sensitive to injector deposits, this may lead to non-symmetric spray geometry and atomisation according to Zhao *et al* [2002]. It is also very difficult if not impossible to provide an offset spray axis, as can be arranged for the inwardly opening pintle injector. The outwardly-opening, single fluid, high pressure swirl injectors are generally used in the spray guided combustion strategies as their cone angle remains almost constant with varying cylinder pressure.

Pulse-pressurised, air-assisted injectors – Pulse-pressurised, air-assisted (PPAA) injectors vary from those previously discussed, as they attempt to inject an already atomised air-fuel cloud. They do this utilising two solenoid injectors; A PFI injector, modified to allow operation at a lower pressure differential than it would normally operate with in a PFI engine used to meter the fuel, and an air injector to inject precise amounts of the air-fuel mixture directly into the cylinder. The fuel metering event is therefore decoupled from

the direct injection event, so the duration and timing of the direct injection event is essentially independent of the amount of fuel injected, Cathcart and Xavier [2000]. Increasing the direct injection duration therefore, does not increase the amount of fuel injected, but simply the amount of air injected. Fry *et al.* [1999] reports that this type of injection process can lead to an improvement in volumetric efficiency, by enabling the injection of air even after inlet valve closure. However, a compressed air supply is required and it is only possible to inject when the air pressure is greater than the cylinder pressure. This will increase the energy required for the injection process, though there is a trade off as high pressure fuel is not required reducing the energy required to pressurise the fuel. Typical fuel pressure utilised for this type of injector are within the range of 0.7 – 1.0 MPa, an order of magnitude smaller than for the swirl type injectors. As the injection pressures are relatively low the momentum of the spray is much lower than that of the other types of injectors, it is possible for this type of injector to do this as the atomisation process is carried out by the compressed air, Ekenberg *et al.* [2000]. The PPAA injectors are generally used in a spray guided combustion strategy, due to their ability to deliver a fuel/air mixture to the spark gap in a very short time. Orbital Engine Company are an example of a PPAA injector manufacturer.

Hole-type nozzles – The hole type nozzles for use in DISI applications, are generally multihole injectors similar to those found within diesel applications, see Figure 1.6 for a schematic diagram of a multihole injector. The major difference being the pattern angle of $30^{\circ} - 90^{\circ}$, compared to $130^{\circ} - 170^{\circ}$ of the diesel injector, Zhao *et al.* [2002]. The characteristics of the hole-type injector are determined by, the number of holes, the included angle of the spray pattern, the offset of the spray pattern from the injector axis, and the pattern itself, Zhao *et al.* [2002]. The major advantage of the hole-type injector is the flexibility of its spray pattern. However to attain satisfactory atomisation quality relatively high fuel pressures are required, within the range of 9 – 12 MPa. Magnetti-Marelli is an example of a multihole injector manufacturer.

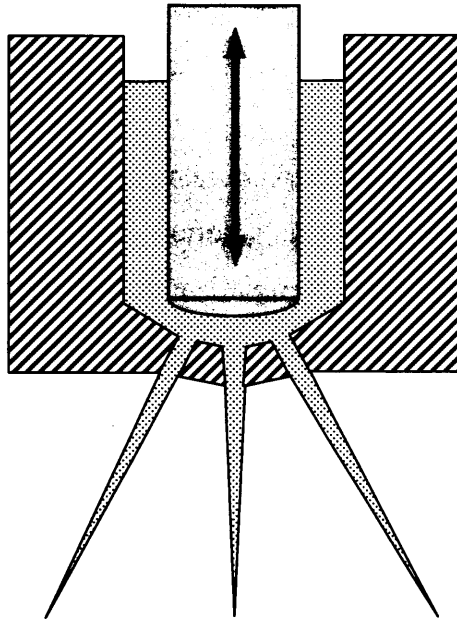


Figure 1.6 – Schematic of a Multi-Hole Atomiser

Slit-type nozzles – The slit-type injector nozzle generally has a single rectangular orifice, which may be positioned on, or off axis. It produces a fan shaped spray that reflects the shape of the orifice and expands as the sheet proceeds downstream, Zhao *et al.* [2002]. The slit-type nozzle allows an increase in spray sheet area in contact with air, Takeda *et al.* [2000] reports that this may allow an increase in the ability to control and enlarge the stratified charge combustion area. However to produce suitably small droplet SMD values high fuel rail pressures are required of at least 9 MPa, high fuel pressures are also crucial to reduce the DV[90] of the spray, (the DV[90] gives the diameter of droplet of which 90 % of the droplets are smaller than). An advantage of this type of injector is the ability to alter the nozzle specifications to suit specific requirements without changing the basic characteristics of the spray. Altering the nozzle specifications will affect the distribution of the fuel within the fan shape, although within reason the spray characteristics remain unaltered.

1.2.3 Structure of Fuel Sprays – The Pressure Swirl Atomiser

The structure of a fuel spray will be dependant on many factors. The main factor will be the type of injector being used. As discussed in the previous section many types of injector have been developed for use in DISI engines,

however, the subject of the following sections will be the inwardly opening, single fluid, pressure-swirl atomiser.

The general characteristic of a pressure-swirl atomiser is that it produces a hollow, conical fuel spray. The defining characteristics of this initial hollow cone are determined by the injector design parameters; the cone angle will be dependant on the ratio of tangential to axial velocities, and the initial sheet thickness will be dependant on this and the nozzle dimensions. The initial velocity of the spray will be determined by the fuel pressure. As given by Han *et al.* [1997b], the initial velocity rises as the square root of the injection pressure differential. These basic parameters, along with the properties of both the liquid fuel, and the gas that the fuel is injected into, will determine the structure of the fuel spray, and therefore the break-up and resulting atomisation.

The thin hollow sheet produced by the injector rapidly reduces in thickness as the fuel spreads out radially, due to conservation of mass. At a certain distance from the nozzle the sheet will be too thin to remain stable, at this point the sheet will begin to disintegrate into ligaments and then further break up into droplets. The distance at which the sheet begins to disintegrate will be dependant on the afore mentioned factors; cone angle, initial velocity, liquid and gas properties, nozzle dimensions etc. The initial sheet thickness will be dependant on the area of the air core at the nozzle exit orifice, (see Figure 1.4 for a definition of the air core). However the amount that the sheet thins as a function of distance from the nozzle will be dependant on the cone angle. Both the air core diameter and the cone angle will be related to the axial and tangential velocities of the fuel, and the diameter of the nozzle.

External factors will also influence the development of the spray cone, affecting the sheet thickness, penetration, cone angle, etc, these external factors will therefore influence the break-up length and therefore the droplet size distribution. The effects of the variables on the fuel structure and sheet break up process will be discussed later in this section.

1.2.3.1 Influence of Ambient Conditions

The ambient conditions, gas temperature and pressure, that the fuel is injected into will influence the cone angle, penetration and break-up process of the spray. The influence of both of these factors will be discussed separately, however they essentially combine to affect the gas density. Since the injection process takes place inside an engine cylinder the pressure and temperature are interdependent, thus an increase in pressure will increase the temperature. However, an increase in temperature may not lead to an increase in pressure, as a higher inlet air temperature will lead to lower cylinder pressures as the initial gas density will be less, thus the inlet air charge mass will be lower.

An effect of the injection event is to cause a pressure differential across the sheet of fuel. This is caused by the moving surface of the fuel inducing a velocity profile on the adjacent ambient gas. The velocity induced on the gas will vary from being equal to the liquid velocity at the surface of the fuel, to that of the free stream velocity at some distance away from the surface. The direction of the gas flow is the same as the liquid, therefore as the structure of the spray produces an enclosed volume a pressure drop is created as there is no source of gas to maintain the original ambient pressure. As the ambient pressure is increased the pressure differential created increases, because the gas density increases therefore the velocity profile will reach the free stream value further from the fuel sheet.

The pressure differential has the effect of collapsing the cone structure, as the force acting on the sheet due to the pressure differential is greater than the force produced by the momentum of the injected fuel. As the ambient pressure is increased the amount the spray collapses increases, until the spray hits a critical point where it can no longer collapse any further as it has filled the hollow core. Therefore the forces acting to collapse the cone due to the pressure differential can increase no further and no further contraction occurs. The increase in ambient pressure would in theory decrease the fuel droplet size as the drag forces on the droplet will increase as the density of the gas increases, however, the effect of the spray collapsing means that the

opportunity for coalescence of droplets increases. As the spray is now contracted relative to lower ambient pressure conditions, the liquid sheet will not be ‘thinned’ as rapidly, therefore allowing the fuel sheet to remain intact for longer. A consequence of this is that the spray is more compact thus inducing a more rapid acceleration of the, now smaller, volume of air in contact with the spray, thus the relative velocity is reduced. Therefore the time taken for a droplet to break-up increases, increasing the Sauter mean diameter (SMD) of the spray, the definition of SMD is described in §1.3.3. Once the spray has reached the critical amount of collapse the disintegration forces become dominant once more and the SMD begins to reduce again with any further increase in the ambient pressure. Since the drag forces acting on the spray increase with increasing ambient pressure, the penetration of the spray reduces. This compounds the affect of the collapsing spray structure, and thus increases the density of the spray. In theory the penetration rate will increase with a reduction in ambient pressure. However, Williams *et al.* [2001] have shown that although the theoretical penetration rate will increase with decreasing ambient pressure the effect of the increased cone angle in fact reduces both the penetration rate and overall penetration of the spray.

As discussed earlier the affect of increasing the ambient temperature will be to reduce the cylinder pressure. With the increase in ambient temperature and fuel temperature, the probability of flash boiling increases, which will dramatically affect the spray structure. Flash boiling occurs when a liquid is suddenly exposed to conditions where it can no longer remain as a liquid, Davy and Williams [1999] defines flash boiling as when fuel is injected into an ambient pressure which is below the saturated vapour pressure of the liquid.

The discharge coefficient of a plain orifice atomiser is governed by the pressure losses incurred in the nozzle flow passages, the extent which the liquid utilises the nozzle flow area, i.e. the size of the air core when dealing with a pressure swirl atomiser, and the pressure differential across the nozzle. The equation relating the discharge coefficient to these terms is given in equation 1.1 below;

$$Cd = \frac{\dot{m}}{A_0 \sqrt{2\rho_L \Delta P}} \quad \text{eq. 1.1.}$$

Where \dot{m} , A_0 , ρ_L , ΔP , are the mass flow rate, nozzle orifice area, liquid density and pressure differential across the nozzle respectively, Lefebvre [1989]. However, Han *et al.* [2001], Cousin and Nuglisch [2001] and Lefebvre [1989], have all shown that the discharge coefficient for a high-pressure swirl atomiser is independent of the pressure differential across the nozzle, and so is therefore independent of both fuel pressure and ambient pressure.

1.2.3.2 Influence of Fuel Properties

The fuel properties and temperature will all have an influence on the structure and break-up length of the fuel spray. The effects of the fuel properties, i.e. surface tension, volatility, etc will be discussed in conjunction with the effects of fuel temperature as they are both linked. The effect of fuel pressure will be discussed in § 1.2.3.3.

The surface tension of the fuel, when increased, will have the effect of increasing the SMD of the spray, and vice versa, however this is a minimal effect as the variation of surface tension between fuels is very small. This is the case as a droplet will reach a critical stage when the aerodynamic drag force is equal to the surface tension force, therefore for a higher surface tension the droplet can be larger with all other variables remaining constant. The effect of viscosity is similar, however the variation of viscosity varies greatly between fuels and therefore will have a greater effect.

The boiling point, or more importantly the distillation curve of multi-component fuels must be considered to have an effect on the spray structure, it will affect the evaporation of the fuel and will affect when flash boiling will occur. Davy and Williams [1999] showed that flash boiling causes the spray to contract substantially, unless it is already contracted, with the added effect of reducing the droplet size. The cone angle is reduced because the smaller droplets produced are drawn into the core of the spray, by the pressure

difference across the ‘wall’ of the spray. Hochgreb and VanDerWege [1998] demonstrate that flash boiling increases the axial penetration of the main spray as the axial momentum has increased due to the reduced cone angle, although the droplets will be smaller and thus the drag forces will be proportionately larger. This is however an indirect effect of flash boiling via the change in cone angle and will only occur if the spray is not already contracted. However the axial penetration of the pre-spray will decrease with increasing fuel volatility and temperature. This is because the droplet size will decrease within the pre-spray, increasing the drag force acting on the droplets, therefore both reducing the penetration rate and distance. Williams *et al.* [2001] did not see this effect of a reduction in the pre-spray penetration rate, in fact they saw the opposite, an increase in the penetration rate when the fuel temperature was increased. VanDerWege and Hochgreb [2000a] report that flash boiling does not have to occur to see these effects, increasing the temperature and the fuel volatility will produce similar effects to a lesser extent.

The volatility of the fuel may also cause stratification of the spray. This is the effect where a variation in the distribution between the high volatility components and low volatility components is observable. Using a PLIF imaging system Hochgreb and VanDerWege [1998] have suggested three cases for this effect that are dependant on the fuel temperature and volatility. Case one is for slow evaporation, where the fuel temperature and ambient conditions are such that the differential evaporation rates cause no observable effect on the spray structure, however small effects occur, such as the high volatility components are drawn to the centre of the spray, and are not entrained within the toroidal vortices on the outside of the spray. Case two is non-disruptive evaporation, where the fuel temperature is higher however the ambient pressure is not low enough to cause flash boiling. In this case the high volatility components are no longer present in the main structure of the spray, they are drawn to the centre core of the spray, however the low volatility components of the fuel remain as a hollow cone. Case three is disruptive evaporation, where the fuel temperature and ambient conditions are suitable for flash boiling to occur. In this case both the high and low volatility components of the fuel have noticeable differences in their structure. The

initial cone angle of the spray is seen to increase significantly due to the effects of flash boiling, the spray then rapidly contracts and as before the high volatility components are drawn to the injector axis, and are seen to have increased penetration. The low volatility components of the fuel are also seen to contract towards the injector axis, have smaller droplet sizes and higher penetration.

1.2.3.3 Influence of Fuel Pressure

The effect of the fuel pressure is to alter the penetration, cone angle and droplet size, with the consequent affects on the spray structure. With an increase in fuel pressure the penetration rate will increase, in fact it will increase as a function of the square root of the pressure differential acting across the nozzle, Han *et al* [1997b]. The overall penetration of the spray will increase with fuel pressure as a result of the increased penetration rate. However the effect of the reduction in droplet size with increasing fuel pressure will, according to Arcoumanis *et al.* [1999], lead to increased drag on the droplets. The cause for the increased penetration at higher fuel pressures despite the reduction in droplet size could be the result of a decreased cone angle.

The cone angle of the spray will decrease with increasing fuel pressure as the smaller droplets produced will be entrained into the core of the spray more easily, therefore they will have a larger ratio of axial to tangential momentum, thus increasing the penetration. The droplets will be smaller with higher fuel pressure for two reasons: the initial thickness of the spray sheet will be thinner, as the tangential velocity will be higher, this will in turn reduce the break-up length and thus produce smaller droplets at any given distance from the injector nozzle. The increased penetration rate will also increase the drag acting on the droplets, therefore they will under go faster secondary break-up producing smaller droplets.

1.2.3.4 Influence of In-Cylinder Air Flows

The effect of in-cylinder flows on the spray structure will be dependant on the type of flow structure, whether that is swirl, tumble or squish. The dominant flow structures are swirl and tumble, so these will be discussed in detail. The main characteristics that will be affected by the in-cylinder flows will be the penetration, cone angle, spray symmetry and mixture formation.

According to Kim *et al.* [2000] the spray tip penetration will be greater with a tumble flow, as compared to swirl flow. This will be dependant on injector positioning and targeting, since if the spray sees the upward flow of the tumble motion the penetration will be reduced. A tumble flow will also have the effect of increasing the homogeneity of the fuel/air mixture as compared to a swirl flow, due to an increased dispersal of the fuel droplets and vapour, depending on the direction of the tumble flow relative to the fuel flow. The effect of a swirl flow is to keep the fuel droplets and vapour close together, producing a stratified mixture. Therefore a tumble flow is more suited to homogeneous charge combustion, and swirl flow to stratified charge combustion, Kim *et al.* [2000], however this may be engine specific as Kume *et al.* [1996] report the opposite, utilising a tumble flow to maintain a compact spray to achieve stratification, therefore tumble flows may be used for either application depending on whether conventional or reverse tumble is utilised, see Figure 1.7.

To achieve these flows upright straight intake ports have been developed to produce a strong tumble flow as reported by Kume *et al.* [1996], along with swirl ports, whereby one intake port is closed to produce a strong swirl flow, as reported by Harada *et al.* [1997]. The other influence on the spray will come from direct impingement of the air jet produced by open inlet valves, this is a very high velocity, and will therefore distort the spray. Stanglmaier *et al.* [1998] reports that the spray tends to be deflected away from the inlet port, towards the exhaust port, the symmetrical conical spray pattern is also distorted and the formation of roll-up vortices are prohibited where direct impingement occurs. It must be noted that swirl and tumble flows are highly

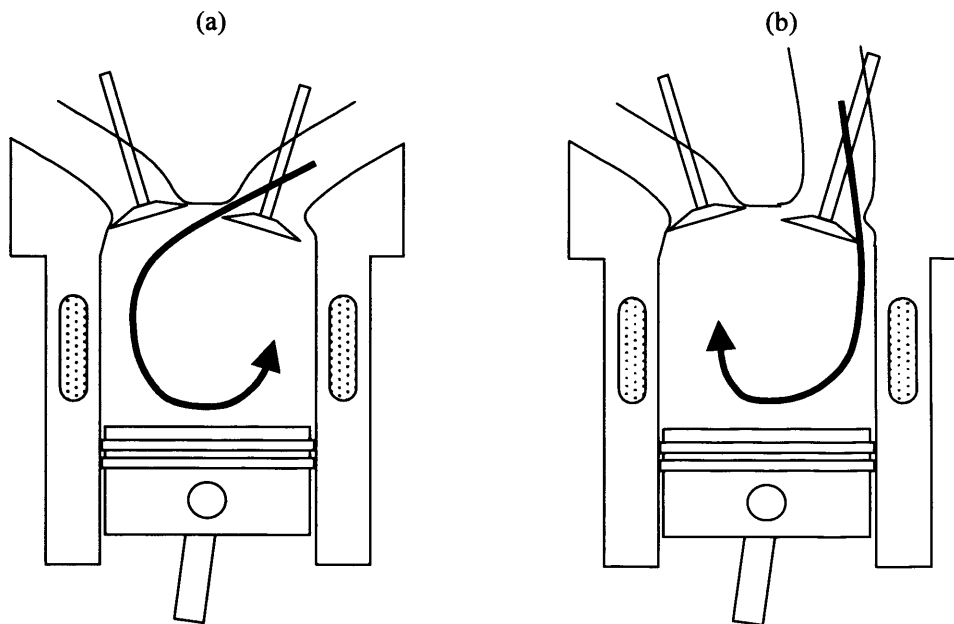


Figure 1.7 – Schematic showing (a) Conventional Tumble, and (b) Reverse Tumble inlet air flows

idealised, in practice actual flows within an engine cylinder are a chaotic mixture of both types of flow.

1.2.4 Break-Up Mechanisms

Before describing the specific break-up mechanisms associated with the hollow cone structure of pressure swirl atomisers, a more general description of liquid jet / sheet break-up will be given. A cylindrical jet of liquid issuing from a nozzle will break-up in different ways depending on the jet velocity and properties of the surrounding gas. The forces involved, surface tension, drag, etc, will lead to oscillations in the surface of the jet. For low jet velocities the influence of the gas will be minimal, and the spray will break-up via radially symmetric waves, i.e. dilational waves, see Figure 1.8, caused by surface tension forces. The relationship between break-up length and jet velocity will be linear. This is known as Rayleigh jet break-up regime. As the jet velocity increases the effect of the surrounding air is no longer negligible, the relative velocity between the air and the jet produces a static pressure distribution across the jet, its effect is to accentuate the waves formed and produce a shorter break-up length, and is known as first wind-induced break-up. For high jet velocities the break-up regime changes again, drops are

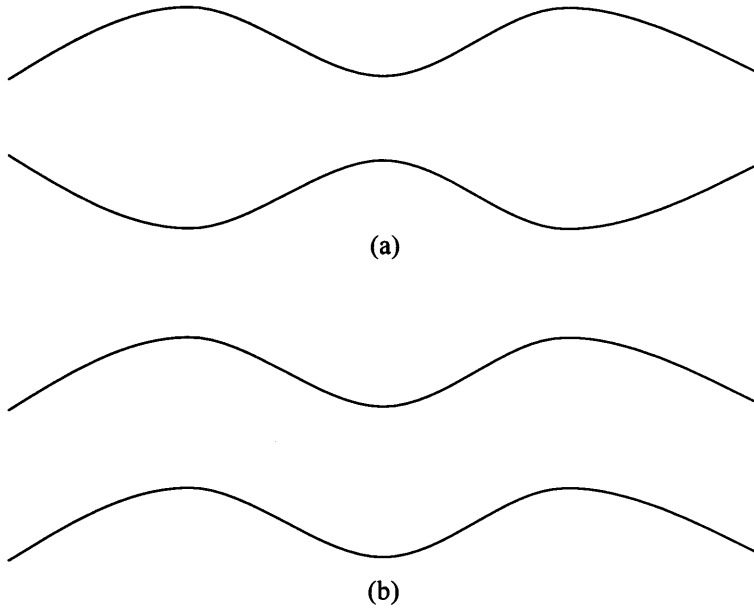


Figure 1.8 – (a) Jet with rotational symmetry, Dilational Wave, (b) Jet with wave formation, Sinuous Wave

produced by the unstable growth of short-wavelength surface waves, which are opposed by surface tension forces, this is known as second wind-induced break-up. There is a final break-up regime which is atomisation, where the jet completely atomises at the nozzle exit, producing droplet diameters much less than the nozzle diameter. Lefebvre [1989] illustrates the work of Reitz who classified all four modes in terms of their Ohnesorge number and Reynolds number, given by equations 1.2 and 1.3 respectively. See Figure 1.9 for classification.

$$Oh = \frac{\mu_L}{\sqrt{\rho_L \sigma_L d_0}} \quad \text{eq. 1.2.}$$

$$Re_L = \frac{\rho_L U_L d_0}{\mu_L} \quad \text{eq. 1.3.}$$

where μ_L is the dynamic viscosity of the liquid, ρ_L is the liquid density, σ_L is the liquid surface tension, d_o is the orifice diameter and U_L is the axial velocity of the liquid.

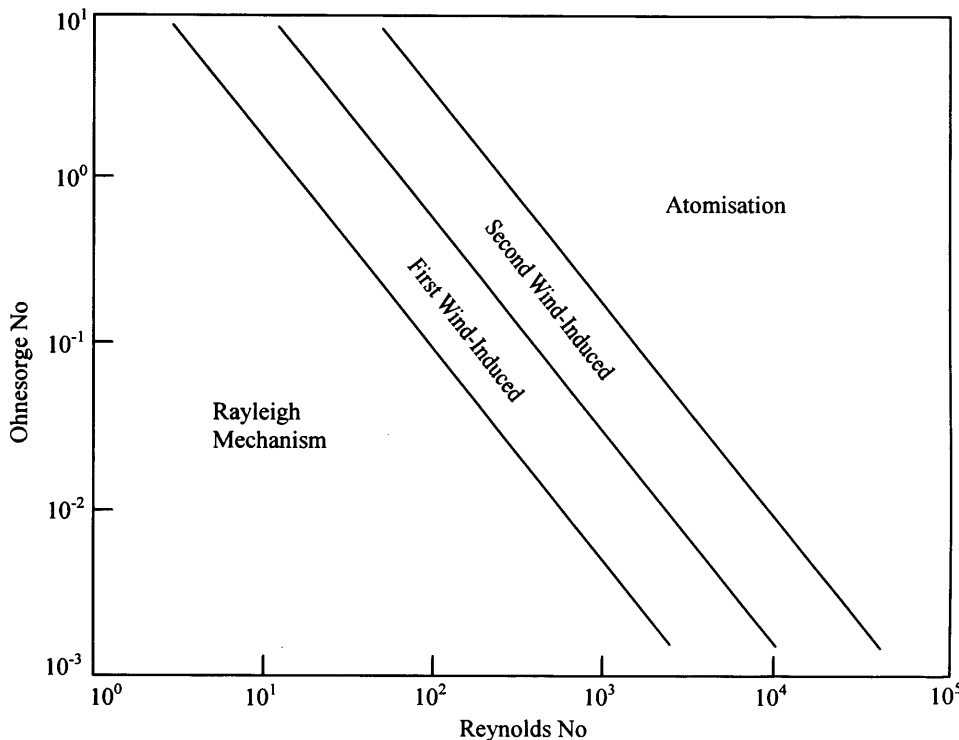


Figure 1.9 – Classification of modes of break-up, reproduced from Lefebvre [1989]

The initial hollow conical spray structure will break-up into ligaments and then further break-up into droplets. The mechanism by which the spray will break-up is of some debate. Fraser *et al.* [1953] suggested that there are three main spray break-up mechanisms that are considered to act on the hollow cone; perforated sheet, rim and wave break-up modes. These are the mechanisms by which the solid fuel sheet breaks up into ligaments and droplets. Further mechanisms produce secondary break-up of the droplets and ligaments producing smaller droplets which atomise producing a vapour.

Perforated Sheet Mode – In perforated sheet mode disintegration, holes form at places of instability in the sheet. These holes rapidly expand due to uneven surface tension forces acting on the sheet, forming toroidal rims around the holes formed from the liquid that previously filled the hole, see Figure 1.10. Perforations forming in the sheet will tend to occur at the same distance from the injector tip, and will therefore have the same history. Thus perforated sheet mode disintegration will tend to produce droplets of a fairly constant size.

This form of break-up, according to Fraser *et al.* [1962], occurs when the spray is aerodynamically stable. For a flat sheet this will occur at low air

densities or low relative velocities, however for a conical sheet, these conditions may not be necessary, although little work has been performed on conical sheets to provide any evidence. Fraser *et al.* [1962] showed that the rate of growth, e , of a perforation is independent of the hole radius, and is simply proportional to the surface tension σ , sheet thickness h and liquid density ρ_L , see equation 1.4:

$$e = \sqrt{\frac{2\sigma}{h\rho_L}} \quad \text{eq. 1.4.}$$

The validity of this equation was confirmed by measuring the growth rates of perforations from experimental data. Using typical properties of a gasoline spray, surface tension of 0.02 N/m, sheet thickness of 0.05 mm, and a liquid density of 750 kg/m³, giving a rate of growth of 1.03 m/s.

Rim Mode – Rim mode disintegration occurs when the surface tension forces cause the free edge of the liquid sheet to contract forming rims. These thick rims then break-up by a mechanism corresponding to the disintegration of a

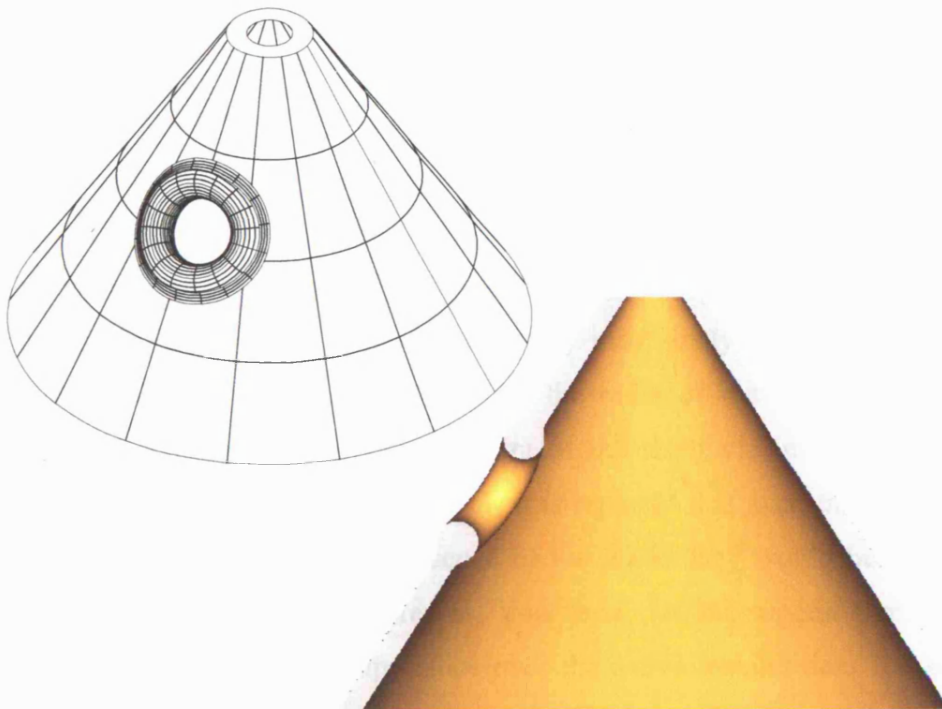


Figure 1.10 – Schematic of Perforated Sheet Mode Break-Up of a Hollow Cone Spray

free jet. This form of break-up tends to occur with liquids of high surface tension and viscosity, and produces large droplets with numerous satellite droplets. It is unlikely that this form of break-up will occur with DI gasoline sprays as the surface tension and viscosity are too low.

Wave Mode – Wave mode, or wavy sheet mode disintegration occurs in the absence of perforations, through the generation of a wave motion on the sheet. Areas on the sheet corresponding to the half or full wavelength are torn away as the sheet becomes too thin to remain stable, Lefebvre [1989]. Many authors have studied thin flat liquid sheets that break-up in this mode. Squire [1953], found that antisymmetrical waves, (sinuous waves, see Figure 1.8), had a far greater degree of instability than symmetric, (dilatational), waves. Squire [1953] investigated this break-up process, providing a criterion of stability and a description of the wave characteristics in their early stages of growth. The first order analyses used can not however show how the sheet breaks down as the sheet remains a constant thickness during wave growth. Clark and Dombrowski [1972], expanded on this work to include second order terms that enabled the sheet to have varying thickness, they also produced criterion of stability, however they went further to produce equations to predict the break-up length of a liquid sheet.

Yule *et al.* [1998] have suggested a concept of two types of sheet instability, “active” and “passive”. Active instabilities are due to “wind-driven” surface waves caused by a velocity difference between the gas and liquid, these occur relatively close to the beginning of the sheet. Yule *et al.* [1998] suggest that these instabilities are the waves predicted by most analytical investigations and they generally have a wavelength of the order of the sheet thickness. Passive instabilities are due to movement of the sheet via instabilities and eddies in the gas flows, see Figure 1.11, it is reported that even though these flows will be modified by the presence of the liquid they would be present even without the liquid being present. Yule *et al.* [1998] suggest that these instabilities are of primary importance over the active instabilities. The case shown here for gas flow on only one side of the sheet, may be relevant to conical sheet break-up as the inside of the sheet will see a smaller gas flow.

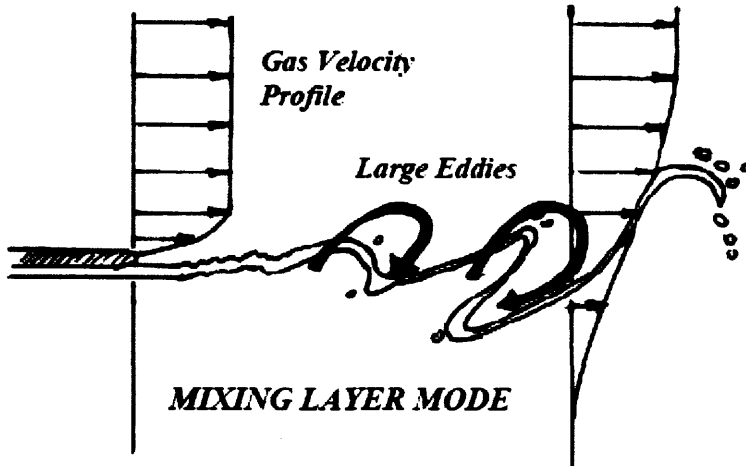


Figure 1.11 – Gas flow-liquid sheet interaction features, Yule *et al.* [1998]

However the liquid velocity illustrated in Figure 1.11 is very low, ≈ 2.5 m/s, with a gas velocity varying from 10 to 20 m/s, therefore this mode of break-up may not be applicable to DI injector sprays.

The work carried out by Clark and Dombrowski [1972] is the basis of much of the modern theoretical work carried out on the break-up of the conical sheet structure from a pressure-swirl atomiser, although their work was based on a flat sheet. Therefore no account is made for the effect of sheet curvature, the reduction in sheet thickness, fundamental effects that may affect the break-up process. The current mathematical models in the literature will be discussed further in § 1.3.

1.2.4.1 Droplet Break-Up Mechanisms

The following section will give a brief overview of the processes involved in the break-up process of a liquid drop, and is based on the review of the topic by Lefebvre [1989]. For a droplet to remain in equilibrium the internal surface pressure at any point on the drop surface is just sufficient to balance the external aerodynamic pressure and the surface tension pressure. Therefore if the aerodynamic pressure is large compared to the surface tension force then any change in the aerodynamic force can not be compensated by the surface tension and the droplet will deform. If the aerodynamic forces are large enough they will lead to a disruption in the droplet producing smaller drops. As the surface tension force for any given droplet is inversely proportional the droplet diameter, smaller droplets are less susceptible to aerodynamic break-

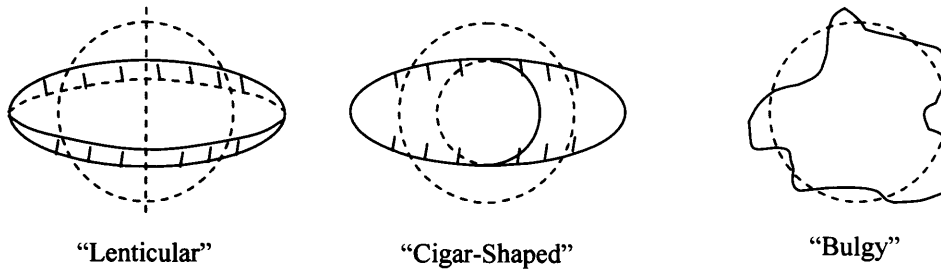


Figure 1.12 – Basic types of droplet deformation, Hinze [1955]

up than large ones, this leads to the concept of a critical drop size, above which droplet break-up will occur.

Hinze [1955] revealed that droplets can break-up a number of different ways under the action of aerodynamic forces, depending on the flow pattern around them, and identified three basic types of deformation, see Figure 1.12.

Lenticular Deformation – The drop is flattened to produce an oblate ellipsoid, with subsequent deformation being dependent on the magnitude of the internal forces causing the deformation.

Cigar-Shaped – The drop becomes elongated and breaks up directly into droplets.

Bulgy – Local deformations on the drop surface create bulges, which eventually detach themselves producing smaller drops.

The viscous forces within the droplet will also have an effect on the break-up as well as the aerodynamic and surface tension forces. The effect of viscosity is to slow down the process of break-up, such that if the aerodynamic force reduces during the break-up time, no break-up may occur even if the initial forces were great enough to cause break-up.

1.2.5 Fuel / Air Mixing Process

The fuel / air mixing process will be highly dependent on the type of combustion strategy utilised, however in all cases the complex and time

dependent spray / air and spray / wall interactions will determine the rate of fuel / air mixing and the degree of stratification, Davy *et al.* [1998], Wagner *et al.* [1999], Zhao *et al.* [2002]. This section will concentrate on the fuel / air mixing process for a wall guided combustion strategy as this generally utilises a pressure-swirl atomiser. The process can be split into three basic stages as described by Yamauchi *et al.* [1998]. The first is the free spray stage as described here in previous sections, where the in-cylinder flows at modest speeds have little effect on the spray structure, however the spray will induce air flows within the cylinder, and an important factor in the mixture preparation is air entrainment into the spray plume. However at higher engine speeds the in-cylinder flows may be more significant. The second stage begins when the spray interacts with the piston cavity, during this stage the spatial distribution of the fuel mixture will be determined by the piston shape and spray angle. In the final stage mixture convection and diffusion occurs. In this stage the number of droplets reduces significantly due to evaporation, and the rich-mixture region rapidly diminishes to form a more uniform fuel / air mixture cloud. The level of homogeneity will obviously be greatly determined by the time available for mixture preparation.

1.3 Mathematical Modelling Techniques

This section will discuss the techniques currently being used to model the injection event and subsequent break-up and atomisation. Modelling of the processes that occur within an engine are dealt with in a number of ways, for instance, it is possible to model the spray break-up process mathematically. This can then be incorporated into a computational fluid dynamics (CFD) model to carry out detailed simulation of the entire break-up process. Both mathematical modelling and CFD modelling will be discussed in this section. The following sections on injector, spray and droplet break-up models will describe methods for handling the liquid sheet, primary break-up and secondary break-up mechanisms respectively.

1.3.1 Injector Models

There are three ways to provide the spray break-up models with initial conditions; firstly, experimental data may be used to provide the initial conditions. However obtaining experimental data on sheet thickness, velocity, etc, very close to the nozzle is extremely difficult as the spray in this region is optically dense making measurements by Mie scattering difficult, and PDA is not capable of measuring irregularly shaped droplets accurately. The second method is to use an injector calibration constant that can be refined using experimental results as validation. This injector constant may then be used in zero dimensional models to calculate the required characteristics. Doumas and Laster [1953], and Cousin and Nuglisch [2001] used zero dimensional models. Finally a CFD model of the injector nozzle may be used to pass the initial parameters to the spray break-up model. A number of authors, Ren and Nally [1998], Arcoumanis *et al.* [1999], Cousin and Nuglisch [2001], have used this technique of modelling the injector. Their techniques and results will be discussed in this section, giving an overview of the modelling potential.

The initial CFD models used for simulating the internal flow of injectors were single phase (liquid) models. These models can not take into account the air core present at the centre of the nozzle. The model does however predict the existence of an air core, the air-liquid interface is located in the area where the axial velocity changes direction. Ren and Nally [1998] used this prediction for the air core to alter the mesh, treating it as a solid boundary. The calculation is then repeated with the solid boundary simulating the air core to obtain results closer to the actual injection process. It is possible to model the air core as a solid boundary as it is assumed that the air has the same axial and tangential velocities as the liquid at the air-liquid interface. Using the data obtained from this injector model the mean axial and tangential velocities of the liquid sheet are calculated, which are then passed to the liquid sheet break-up model. Gavaises *et al.* [2002] also utilised this method of predicting the air core boundary. Arcoumanis *et al.* [1999] noted that this modelling process does not however take into account any transient effects related to the initial development of the liquid film inside the nozzle.

A solution to the problems associated with the single phase model is to use a two phase model, which can account for the air core in a single calculation. The air-liquid interface is tracked using a volume of fluid (VOF) methodology, Arcoumanis *et al.* [1999]. However the computation time required to calculate accurately the position of the air-liquid interface in the work of Arcoumanis *et al.* [1999], was prohibitively long, so a 2-D approximation was used. This assumed an axisymmetric swirling motion, which was not exactly the case as the tangential slots create a 3-D motion, and so only an approximation of the swirl flow is given. The liquid flow characteristics inside the nozzle and at its exit identified in the study could be used to extend the model to calculate the liquid sheet break-up process.

Other approaches to the modelling of the flow issuing from the injector nozzle have been made. Cousin and Nuglisch [2001] used the zero dimensional model suggested by Doumas and Laster [1953], as a starting point. This method showed that the injector characteristics are a function of one parameter without dimension. However Cousin and Nuglisch [2001] found that the cone angle was overestimated, thus an empirical factor was required. This model also underestimated the coefficient of discharge. To improve upon the model developed by Doumas and Laster [1953], they took into account the fact that the inlet flow is not purely tangential, and that the viscosity and frictional effects will lead to a reduction in the angular momentum. The model remained zero dimensional which allows fast calculation, however this model remains empirical and was highly dependant on the coefficient of friction used, deduced directly from experimental data. It also took no account of the effects of the needle. They therefore decided to use a one dimensional model, to take into account the effects of the needle and the local frictional effects of the needle seat.

The one dimensional model takes the injector and slices it into horizontal layers such that calculations may be made at each layer to find the mean static pressure and mean velocities; the results are passed to the next layer and so on. The static pressure at the top of the swirl chamber is initially guessed. If the calculated static pressure at the outlet is not zero, as it should be, then a new

value for the static pressure at the top of the swirl chamber is chosen, and so on until the static pressure at the outlet is equal to zero. When convergence occurs the coefficient of discharge and cone angle are calculated. The results obtained are fairly accurate, similar to the modified zero dimensional model, however the one dimensional model takes into account the dimensions of the injector explicitly, and as such may be used in the design of DISI injectors.

1.3.2 Spray Models

Spray models use data obtained in either of the three methods described in § 1.3.1 to model the break-up of the liquid sheet emanating from the injector nozzle. These provide data to the droplet (secondary) break-up models. Similar to the modelling of the liquid within the injector, there are two possibilities to modelling the spray and sheet break-up, namely mathematically modelling the spray using empirical factors, or to use CFD to fully model the spray.

The mathematical modelling of sprays, will provide details of the break-up length, cone angle etc and may be incorporated into CFD models. The complexity of CFD models are limited by the time available for calculation and therefore by computing power, Yamauchi and Wakisaka [1996] used a Discrete Droplet Model (DDM) in KIVA code to numerically analyse the fuel spray. The KIVA code has coalescence and evaporation models which were used in this analysis. They did not include any break-up process within the model, and so therefore the liquid sheet is ignored and instead initial droplets are placed near the nozzle outlet according to the fuel injection conditions. Consequently the spray behaviour is determined by the secondary atomisation process, this reduces the computation time required. Since the initial conditions of the droplets, where they are placed, droplet size and velocity, etc, will affect the spray development, Yamauchi and Wakisaka [1996] carried out a study to see the effects of altering these parameters. They found that the initial formation of the spray was unaffected by the fuel injection flow rate, however the initial droplet size and swirl component has a significant influence on the hollow cone spray structure. Therefore it is important to

provide accurate initial conditions for this model. To reduce the effects of initial conditions, other authors have included the break-up process into the CFD models, with the initial conditions, such as nozzle diameter, swirl ratio, fuel pressure, etc, being injector dependent.

Han *et al.* [1997b] utilised a break-up model based on the work by Clark and Dombrowski [1972] who performed their analysis on a flat liquid sheet, recast to include a term for the conical sheet as equation 1.5:

$$L = B \left[\frac{\rho_L \sigma \ln\left(\frac{\eta}{\eta_0}\right) h \cos\theta}{\rho_{gas}^2 U^2} \right]^{0.5} \quad \text{eq. 1.5.}$$

Where B and $\ln(\eta/\eta_0)$ are constants set to be 3 and 12 in the study respectively. Also L is the break-up length, θ is the half cone angle, ρ_{gas} is the gas density and U is the sheet-gas relative velocity, (all other terms are as defined previously). This break-up model was implemented in KIVA-3 code, with models for drop collision and coalescence, drop and gas turbulence and also evaporation. Similarly to Yamauchi and Wakisaka [1996], the liquid sheet was modelled using discrete droplets that were not allowed to undergo secondary break-up until the break-up length is reached. They achieved good agreement between the model and experimental data, however they believed that a deeper understanding of the initial stages of sheet development was required. Other authors, including Ren and Nally [1998], Zeng and Lee [2000] and Alloca *et al.* [2002] have developed similar models, however the constants they used for the break-up length differed from Han *et al.* [1997b], suggesting that they have a high dependence on the injector used. The model proposed by Han *et al.* [1997b] was further developed in a later work, Han *et al.* [2001], to increase the accuracy of the predictions.

Models have also been developed based on a different analysis. Senecal *et al.* [1999] developed a linear stability analysis and Schmidt *et al.* [1999] went on to validate the model with experimental data from a DI injector. Gavaises and

Arcoumanis [2001] also developed a similar linear stability analysis model. The model developed by Senecal *et al.* [1999] includes the effects of the surrounding gas and liquid viscosity and is based on the analysis of the stability of cylindrical liquid jets. The model applies an infinitesimal disturbance on the liquid sheet, and once the disturbance in the form of waves reaches a critical value the sheet breaks up. This was implemented in the KIVA-3V code to calculate the behaviour of pressure swirl atomisers. The model chooses one of two break-up regimes either long or short wave based on the Weber number of the liquid. Schmidt *et al.* [1999] went on to compare the model and break-up length equation as given by equations 1.6 and 1.7 to experimental data.

$$L = \frac{U}{\Omega} \ln\left(\frac{\eta_b}{\eta_0}\right) \quad \text{eq.1.6.}$$

$$\omega_r = -2\nu_L k^2 + \sqrt{4\nu_L^2 k^4 + QU^2 k^2 - \frac{\sigma k^3}{\rho_L}} \quad \text{eq 1.7.}$$

Where Ω is found from the numerical maximisation of equation 1.7. Also ν_L is the kinematic viscosity of the liquid, k is the wavelength of a disturbance on the film, and Q is the ratio of gas to liquid density, (all other terms are as defined previously). Schmidt *et al.* [1999] noted that further refinement of the model was necessary to better represent the processes, by more accurate modelling of the coefficients. They also noted that a better understanding of the primary atomisation physics would be beneficial to the aerodynamic break-up processes.

1.3.3 Droplet Break-up Models

Droplet break-up models are the oldest of the three types of model so far considered. Mathematical relationships have been derived for the break-up of liquid droplets in many different conditions. The simplest form of droplet break-up occurs in laminar flowing air, where relationships have been found to

estimate the critical diameter of a droplet at any velocity where break-up will begin to occur. Droplet break-up processes are described in § 1.2.4.1, in this section the models that have been developed to describe these processes will be examined. It was discussed earlier in § 1.2.4.1 that there is a critical droplet size for any given conditions at which point break-up will begin to occur, Lefebvre [1989], provides equation 1.8 as a description of the critical droplet size in terms of the Weber number, however this does not account for any viscosity effects:

$$We_{crit} = \left(\frac{\rho_{gas} U_R^2 D}{\sigma_L} \right) = \frac{8}{C_D} \quad \text{eq. 1.8.}$$

Where D is the diameter of the droplet, (all other terms are as defined previously). As the value of C_D is unknown and will change depending in the level of droplet deformation, only empirical relationships may be found for the critical Weber number, these relationships will include the effects of viscosity. Lefebvre [1989], presents the work of Brodkey, who derived the empirical relationship in equation 1.9, which is claimed to be accurate to within 20%:

$$We_{crit} = \dot{W}e_{crit} + 14Oh \quad \text{eq. 1.9.}$$

Where $\dot{W}e_{crit}$ is the critical Weber number without the influence of viscosity. These equations are not directly applicable to the modelling of DI engines, however they are the basis of these models.

O'Rourke and Amsden [1987] developed the TAB model, which is based on Taylor's analogy between an oscillating and distorting drop and a spring-mass system. The external forces acting on the mass, the restoring force of the spring, and the damping force are analogous to the gas aerodynamic force, the liquid surface tension force and the liquid viscosity force respectively. The parameters and constants in the TAB model equations were determined from

theoretical and experimental results, and in the model the force balance gives equation 1.10:

$$\frac{d^2y}{dt^2} + \frac{5\mu_L}{\rho_L r^2} \frac{dy}{dt} + \frac{8\sigma}{\rho_L r^3} y - \frac{2\rho_{gas}U^2}{3\rho_L r^2} = 0 \quad \text{eq. 1.10.}$$

Where t is time and y is the normalised (by the drop radius) drop distortion parameter, and r is the droplet radius, (all other terms as defined previously). It is assumed that break-up occurs if and only if $y > 1$. When this condition is reached the droplet breaks up into smaller droplets with sizes determined by an energy balance, taken before and after break-up occurs as equation 1.11:

$$\frac{r_1}{r_2} = \frac{7}{3} + \frac{1}{8} \frac{\rho_L r_1^3}{\sigma} \left(\frac{dy_1}{dt} \right)^2 \quad \text{eq. 1.11.}$$

Where r is the drop radius and subscripts 1 and 2 are the before and after break-up conditions. The drop size distribution in the O'Rourke and Amsden [1987] model was given by the χ^2 function (chi-squared function), with r_2 taken to be the Sauter mean radius, this was based on diesel spray work. Many authors have utilised this break-up method, Han *et al.* [1997a] was one who did work with the χ^2 function and found that for pressure-swirl atomisers an over-estimated population size of large droplets was produced. Han *et al.* [1997a] decided to use the rosin-rammler distribution to better match the droplet size distribution of a pressure-swirl atomiser. Other authors such as, Schmidt *et al.* [1999] and Park *et al.* [2002] have used the TAB method.

There are other models that have been developed by other authors, such as the stochastic lagrangian model, implemented in one form in KIVA II code by Gorokhovski [2001], and in a slightly different form by Alloca *et al.* [2002]. This model treats the fuel as a coherent liquid column that has been divided into discrete lagrangian material volumes each of which represent a group of physically similar droplets. Once the criteria for break-up of the liquid sheet

has been reached the drops are then treated as individual droplets that may interact with the surrounding gas, being affected by drag and turbulence.

1.4 Visualisation Techniques for Fuel Sprays and Air Flows

In this section, the main methods for visualising and characterising fuel sprays and in-cylinder air flows will be discussed. The techniques fall into two categories, qualitative and quantitative measurements. The techniques that fall into the qualitative category are imaging techniques, such as High-speed photography or Laser induced Fluorescence (LIF). Quantitative techniques give numerical results, such as velocity or drop size. These can be used to give an understanding of the character of the spray/flow. These techniques include Laser Doppler Anemometry (LDA) and Particle Image Velocimetry (PIV). Techniques such as Mie scattering can be used to size droplets using image processing software, however the resolution of the camera system often limits the smallest measurable droplet sizes to many tens of micrometres. When sizing the droplets, other effects such as focus and density of droplets must also be considered. Image analysis techniques will be examined in chapter 3, which will include droplet sizing, spray measurement techniques, multiple scattering effects etc. The following sections will describe the general techniques utilised to obtain images and data.

1.4.1 Flow Seeding

Many of the laser diagnostic techniques require a tracer material to be introduced to the fluid flow for it to be visualised. These techniques will be discussed in later sections, however the general principles of flow seeding will be given here, they apply to all of the techniques such as Particle Image Velocimetry, Phosphorescent Particle Tracking, Laser Induced Fluorescence etc.

There are essentially two types of tracer that will either utilise Mie scattering or some form of luminescence, whether that is fluorescence or phosphorescence. However both types of tracer must have certain properties to produce reliable experimental results. Drain [1980] suggest there are two main requirements of either type of tracer; most importantly the seeding particles must be able to follow the fluid flow faithfully or the perceived flow that is measured will not be the actual flow being observed, and secondly they must scatter/fluoresce sufficient light to give an acceptable signal to noise ratio. Occasionally it is possible to use impurities within the fluid being observed as tracers, however the concentration and size distribution are hard to control. The factors influencing the choice of tracer to be used will be the type of visualisation technique used, the type of fluid being studied, the expected velocity fluctuation, etc. Depending on the environment being studied special factors such as temperature or chemical reactivity of the fluid may have to be considered. There are a number of different types of tracer available, two of which are:

- Atomisation
- Fluidisation

Atomisation – The atomisation process draws a liquid into a thin film where the action of shear force against the surface tension breaks the film into droplets. The droplet size will be determined by the gas flow velocity. A carburettor is an example of this type of atomiser.

Fluidisation – The fluidisation process is limited to producing solid particle aerosols. The process utilises a flow of fluid, usually a gas through a bed of particles, entraining some of the particles within the gas flow to produce a seeded flow. A variation of this process is to use a cyclone seeder whereby air is introduced tangentially to a cylinder that contains a layer of particles at its base. The spiralling flow then picks up the particles producing the seeded flow before exiting the cylinder through an outlet at its top.

1.4.2 Mie Scattering

Mie scattering is the elastic scattering of light from particles such that the relationship $d/\lambda \ll 1$ does not hold, d being the particle diameter and λ the wavelength of incident light. Eckbreth [1996] describes an elastic scattering process is one in which there is no energy transfer between the incident photons of light and the target particles, therefore the scattered light is unshifted from its original incident frequency. This effect underlies techniques such as LDA/PDA and PIV. The Mie theory was developed by Gustav Mie in 1908, and deals with light scattering from spherical particles of any size, Hecht [1998]. However, Mie scattering is generally associated with scattering from particles that are approximately the same size as the wavelength of light, i.e. where $d/\lambda \approx 1$. The Mie signal will be proportional to the diameter squared, i.e. the area of the scattering particles.

Mie scattering is a qualitative method generally used to give an overview of the general spray structure. Two main light sources can be used to illuminate the spray, global (flood light) illumination or laser sheet illumination. The former can be a flash lamp, stroboscope or simply ambient light, in the case of fuel spray imaging this technique will give an image mainly of the external structure of the spray, Wagner *et al.* [1999], Hentschel *et al.* [1999], Glaspie *et al.* [1999]. The laser light sheet illuminates a slice of the spray, and can be directed into the spray in a number of different orientations. These are, parallel to the injector from the side, parallel to the injector from beneath, and perpendicular to the injector from the side as described by Zhao *et al.* [1996] and also by Williams *et al.* [2001]. Depending on the repetition rate of the light source used, the development of the spray can be visualised during one injection event, or it can be compiled together from images taken from different injection events. The latter images will be taken at progressive times after start of injection. This procedure allows a virtual ‘sequence’ of images that is extremely large, however if there is cycle to cycle variation then allowances for this must be taken. This technique can be used to advantage if the variations need to be averaged out to get an overall picture of the spray, ignoring anomalies.

1.4.3 High Speed Photography

High-speed photography can be used in conjunction with Mie scattering to give a high temporal resolution of the spray. Using a rotating drum camera frame rates up to 200,000 Hz are achievable, albeit with a cost penalty. The advantages of using high speed photography are that it can be used to image highly dense sprays close to the injector nozzle, the only problem being the difficulty in providing sufficient lighting. This means that qualitative results can be obtained that will give a general understanding of the spray behaviour. High-speed photography can also be used for drop sizing after being calibrated using drops of a known size. Velocity measurements may also be made by taking consecutive images with a short time delay between exposures. The distance between droplets can be measured then divided by the known time difference to give velocity.

1.4.4 Particle Image Velocimetry (PIV)

PIV is a technique that allows the velocity of particles within the flow to be measured, these particles may be droplets, or if a fluid flow is being measured, they may be tracers, see §1.4.1. The system takes two consecutive images, correlates them, finding the distance travelled by each particle, it is then able to calculate the velocity distribution within the measurement area. As now the time of flight, distance, and direction of travel are known. This technique allows the entire flow field to be measured at one instance, unlike LDA/PDA that measures only a single point at any one time. Depending on the velocity of the spray being analysed, the time interval between images must be altered to suit. For fast flows the time interval must be short so that the droplets being observed have not travelled too far. Kubo *et al.* [2001] utilised two CCD cameras to capture the consecutive images at time intervals down to 2 μ s, thus enabling velocities up to 200 m/s to be measured. To give a representative mean of the flow field a number of PIV velocity maps will be required, according to Faure *et al.* [1998] this number will vary from flow to flow.

There are a number of problems associated with the use of PIV when applied to IC engines, such as out of plane movement, dynamic range and velocity gradients. If out of plane movement is significant then the interrogation of the images may be difficult, due to the loss of matching particle pairs within the light sheet. This may be especially significant in the highly turbulent flows of an IC engine cycle. The dynamic range, which is defined as the ratio of maximum to minimum velocity, will be limited by the size of the interrogation region and the particle diameter. However utilising cross-correlation techniques where images between neighbouring interrogation regions are correlated, it is possible to increase the dynamic range of the system. The cross-correlation technique also partly resolves the effect of large velocity gradients within a small region, however this technique reduces the spatial resolution. Directional ambiguity resulting from the symmetry of the auto-correlation function also poses a problem. Gajdeczko and Bracco [1999] utilised a two colour PIV system to overcome this problem. The technique used two sheets of pulsed light at different wavelengths to illuminate the flow, producing a double exposure picture that may be spectrally separated before the correlation function is applied, thus giving the direction of the flow. However, more modern techniques utilising CCD cameras with faster response times eliminate this problem by producing two separate images.

1.4.5 Laser Diffraction Techniques

Laser diffraction techniques use the theory of diffraction to enable drop sizes to be calculated. If we imagine parallel light, i.e. laser light, passing through a pinhole, then an interference pattern will be created. This pattern will have a characteristic energy distribution, whose intensity will be determined on the intensity of the incident laser light, the lens focal length, the radial distance in the focal plane, the wavelength of light and the radius of the pinhole. Therefore knowing all other factors the pinhole radius can be calculated. This technique may be applied to sizing droplets as a droplet will diffract the light in a similar manner to the pinhole. However, as this technique utilises an expanded laser beam of the order of 10 mm in diameter, it is not quite this simple as more than one droplet will be in the measurement volume at any one

time, therefore the signal will be a composite of all the diffracted light from many droplets, i.e. the receiver is acting as a Fourier transform. Solving this set of simultaneous equations finds the sets of intensity distributions that would make up the composite signal. Using the knowledge that small droplets will have a peak intensity at larger angles than large droplets the actual drop size distribution may be calculated from the intensity distributions. Leading to the output of data such as the Sauter mean diameter and DV[90] of the spray.

There are two main limitations to this type of technique, and are given by Robart *et al.* [2001], firstly, as caused by a highly dense spray, and secondly caused by liquid vapour, (evaporation of the spray) being present within the measurement volume, (within the laser beam). Unfortunately highly dense sprays are a characteristic of DI injectors, therefore to combat this limitation it is necessary to perform the measurement far enough from the spray to provide accurate results. This in turn increases the problem of the second limitation, evaporation, the amount of evaporation of the spray will increase with distance from the injector tip. The effect of liquid vapour within the measurement volume is to cause a change in the refractive index of the gas, thereby causing a beam steering effect. This does not produce the characteristic diffraction effect as compared to the effect from the droplets, however the result is that a false energy distribution is produced, that has more energy in the detector rings closest to the centre of the detector plate. As small droplets diffract the light to a greater degree, the effect of evaporation is to increase the large droplet size. To counteract this effect it may be possible to use a less volatile fuel, Robart *et al.* [2001], however this is not always possible or practical. Another solution as suggested by Williams [1994], is to correct for evaporation by removing it in a pre-processing application, using a linear best fit algorithm. This requires knowledge of the amount of evaporation present in the raw data signal, which is not available, however an estimate of the amount of evaporation present may be made by an experienced user.

1.4.6 Phosphorescent Particle Tracking (PPT)

PPT is a technique similar to PIV, in the sense that it allows the entire flow field to be measured at any one time, although as of yet only qualitative data is obtained. It was developed by Guerrier [1999]. However, PPT uses the property of some materials to exhibit phosphorescence. Phosphorescence is the ability of a molecule to give out light for extended periods after it is excited by an energy source, between 10^{-4} s to seconds, much longer than fluorescence which emits for periods between 10^{-10} s to 10^{-5} s. The PPT technique goes further than PIV as it allows the tracking of two flows simultaneously using two dopants that are excited by the same wavelength of light but have different emission spectrum, to track two separate flows, for instance the flows from separate inlet ports to measure the level of mixing/stratification. Currently the technique utilises a filter which produced a pair of identical images of the original object. A low pass filter is also used to eliminate the light emitted by one of the tracers on one of the images, thus producing the double image, one with both tracers, known as the composite image and one with one tracer. Image processing may then be used to eliminate the unfiltered tracer from the composite image. Thus producing two images, one for one tracer one for the other, therefore comparisons may be made of the two flows being observed.

1.4.7 Laser induced Fluorescence (LIF)

Eckbreth [1996] defines Fluorescence as the emission of light from a molecule following promotion to an excited state by an energy source. Energy is emitted when the electrons return to their original ground state. A proportion of this energy is released as light, by means of spontaneous emission (fluorescence). The molecule may be promoted to an excited state by various means, including heating, chemical reaction (chemiluminescence), or photon absorption. The process that will be considered here is photon absorption, by means of laser light (LIF). The molecule in an excited state may not necessarily emit radiation as a means of returning to its ground state. Other processes, see Figure 1.13 for a summary, can cause the molecule to return to

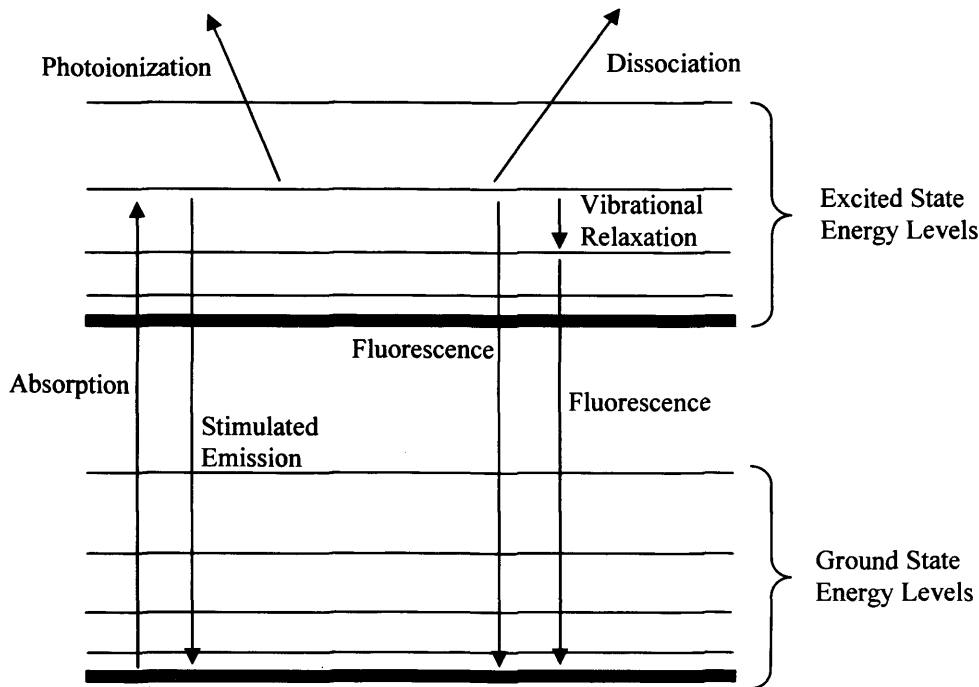


Figure 1.13 – Two-State Energy Level Diagram: Eckbreth [1996]

the ground state. In general these processes, i.e. transfer of energy to another molecule, ionisation, dissociation, etc are termed quenching. Of these processes the most important is the transfer of energy to other molecule, which is known as collisional quenching. The quantum efficiency of the fluorophor is defined as the ratio of emission energy to excitation energy, or the ratio of fluoresced photons to incident photons, which is the case when the excitation energy is light.

For any particular fluorophor the absorption spectra will be different, therefore the laser may be tuned such that only the fluorophor being observed is excited, this is the basis of species detection using LIF. Many fluorophors exhibit a stokes shift in the fluoresced light they emit, this allows for filtering of the excitation laser. Stokes shift is the termed applied when the emitted light wavelength is increased when compared to the excitation light wavelength, an anti-Stokes shift is the opposite effect. This produces an image of the fluorophor, reducing the effects of potential spurious results from Mie scattered or reflected laser light. When the incident and radiant light have different wavelengths this is called fluorescence, when the wavelengths are the same, this is called resonance fluorescence.

Generally the term Planar Laser Induced Fluorescence PLIF as utilised by Shelby *et al.* [1998] and VanDerWege *et al.* [2000] among others, is used to describe the technique when used with a laser sheet to provide spatial resolution along the camera axis. The property of fluorescence can be found in the primary fluid, i.e. the fluid flow that needs to be imaged, or the fluorophor can be added separately. Fluids such as gasoline exhibit fluorescence and can therefore be used directly in LIF. However care must be taken to ensure the fluorescence produced is uniform and not affected by evaporation, quenching, or other substances in the control volume. VanDerWege *et al.* [2000a] reports that when in the case of gasoline, the batch to batch changes may be high and therefore results can differ. When utilising gasoline LIF it must be noted that the components of gasoline that fluoresce are usually of low volatility, Davy *et al.* [2000], Hentschel *et al.* [1999]. Therefore, this may not produce an accurate picture of the fuel spray. In these cases, the fluid can be replaced by a non-fluorescing fluid with a fluorophor (dopant) added to increase the accuracy of the experiment. Care must be taken to choose a fluid and dopant that accurately describes the process, especially if evaporation may occur, since this can affect the results obtained, Han *et al.* [2002], Davy *et al.* [2000].

It is important to choose the correct fluorophor when using LIF. When using a substance other than the primary fluid according to Lee *et al.* [2002] it is necessary that the fluorophor follow the flow of the liquid faithfully, so that an understanding of the actual flow can be established. To give a broad test range with similar results consistent quantum efficiency is desirable, with varying temperature, pressure and oxygen concentration, VanDerWege *et al.* [2000a]. If evaporation is likely then the liquid and vapour phases should be distinguishable, in the case of exciplex fluorophors the liquid and vapour phases fluoresce at different wavelengths.

The absorbency and concentration of the fluorophor is a very important factor to consider since this will effect how the images are interpreted. If the fluorophor has a high absorbency, the laser light will be absorbed before it travels very far through the droplet, this is an important factor when using LIF for droplet sizing. In this case the results will be determinate on the area of the

droplet, i.e. diameter squared, however to obtain results that are easiest to interpret the image obtained should be proportional to the volume, i.e. diameter cubed, Jermy [2002]. This allows the volume fraction of the spray to be analysed, avoiding biasing towards the larger droplets, as would be the case for diameter squared proportionality, allowing an understanding of the entire range of droplets. Using a combination of LIF, and Mie scattering images, the size of the droplets within the flow can be calculated. This is accomplished by dividing the intensity of the LIF image by that of the Mie image, thus giving the Sauter mean diameter, or D_{32} , this is the case since LIF is proportional to the diameter cubed and Mie is proportional to the diameter squared. Since the Sauter mean diameter is defined as the diameter of a droplet whose ratio of volume to surface area is the same as that of the entire spray, Lefebvre [1989]:

$$\frac{\sum N_i D_i^3}{\sum N_i D_i^2} = D_{32} \quad \text{eq_ 1.12}$$

The LIF and Mie images give an overall summation of the flow so they can be used to perform this calculation. It is important to note that this technique does not give any understanding of the droplet size distribution, only the Sauter mean diameter, and it relies upon the fluorophor correctly representing the droplets.

Due to absorbency and scattering, the laser light sheet progressively weakens as it passes through the spray. Therefore, the intensity/liquid mass concentration will have a different constant of proportionality at each point in the spray. How weak the signal from the laser is at any point within the spray will depend on the spray structure, however this is what is being imaged, therefore other correction methods must be utilised. There are non-exact and exact methods of correction, the non-exact method involves producing two light sheets propagating from opposite directions into the spray. Other methods include a linear stepwise correction and a sequential bi-directional sheet correction. The linear stepwise method uses an algorithm to proceed along each row of pixels, correcting for attenuation based on the previous

pixel and an external factor. The external factor is generally the overall attenuation along the row, this can therefore correct accurately over the entire image. The sequential bi-directional sheet method corrects the attenuation by taking two consecutive images, using laser sheets entering the spray from opposite directions. It is also possible to simultaneously propagate two laser sheets into the spray from opposite directions. In both cases the images are combined in a way that cancels the attenuation, Sick and Stojkovic [2001] compares both methods and their accompanying algorithms for attenuation compensation. Sick and Stojkovic [2001] reported that although the algorithm used in the sequential method theoretically produced less accurate results than the simultaneous method, when the signal noise was high the results could not be filtered sufficiently to allow the simultaneous algorithm to be applied successfully. Calibration of vapour/gas phase fluorescence requires a known concentration, this can be accomplished by injecting a known volume of fluorophor into a known volume of gas. The mixture is then given time to homogenise, then an image is taken, and then intensity can be related to concentration. Calibration of liquid phase fluorescence is more difficult as jets and sheets behave optically different to droplets and can therefore not be used for calibration. It is best to calibrate from a known concentration of droplets, i.e. from a monodisperse droplet generator. Using quantitative LIF, i.e. finding concentrations, has to be used with care since if any evaporation occurs then it is possible to obtain misleading information about the spray.

There is another form of LIF, LIEF, or Laser Induced Exciplex Fluorescence, that can be used to areas containing liquid and areas containing vapour. The term exciplex is used to describe fluorophors that consist of two, or more, monomers that may be identical or different, that combine to create a short lived, energetic weakly bonded complex. The exciplex fluoresces and often breaks up in this process, returning to its ground state, i.e. the two separate monomers. The exciplex concentration is highest in the liquid state since its rate of formation is proportional to the product of local concentrations of monomers, which is very high in liquid, not low in a vapour. Therefore, if the monomers are also fluorophors that fluoresce at different wavelengths to the exciplex, it is possible to distinguish from the liquid and vapour state. Since

the liquid state will fluoresce at both the exciplex and monomer wavelength but the vapour state will only fluoresce at the monomer wavelength.

1.4.8 Laser / Phase Doppler Anemometry (LDA / PDA)

LDA and PDA are based on the same theory, but PDA can give both the velocity and size of the particle, instead of just the velocity, as is the case with LDA. The difference between LDA and PDA is the number and way the detectors are used, LDA utilises just one detector, while PDA utilises at least two and generally three. The basic LDA system uses a pair of laser beam that cross at their waist to form a small control volume. The two beams create a fringe pattern so that a particle crossing the fringes will create a signal with a sinusoidal oscillation frequency, Drain [1980]. Knowing the frequency and the fringe spacing the velocity of the particle can be calculated. Using a simple set up like this enables the velocity of the particle to be determined, however the direction is unknown since the frequency that the receiver sees is not determinate on direction, only speed. Therefore, to enable the direction of the particle to be determined a frequency is added to one laser beam, using a Bragg cell, to give the fringe pattern a constant velocity. The system can now measure negative velocities up to the velocity that the fringes are moving, simply by subtracting the travelling wave velocity the actual particle velocity can be obtained. The Bragg cell also has the property of diffracting the laser into two beams, one frequency shifted, therefore this can be used as a beam splitter, however the angle between the two beams is very small therefore a large distance is required to obtain suitable separation.

The principles of PDA are the same as for LDA, except that two, but generally three detectors are used. This enables the particle size to be measured as well as the velocity. The system works by measuring the phase difference between the signals collected at the two detectors, the phase, or time, between the two signals can be used to calculate the size of the particle. The two laser beams must be coherent and in phase for the system to operate correctly. Without these properties the fringe pattern will not be set up, so no pattern will be detected by the detectors.

1.5 Summary

This chapter has presented a review of the current DISI engine technologies and compared them to PFI technologies. It was shown that the advantages of DISI, in terms of the potential to improve fuel economy and high-load performance, means that it is likely to be the future fuelling strategy for gasoline engines. However to realise these potential advantages the engine is required to operate in both stratified and homogeneous charge mode. The fuelling requirements for a DISI engine were therefore considered for both stratified and homogeneous charge operation, and it was shown that the type of injector best suited to a wall-guided combustion strategy, was an inwardly opening, single fluid, high pressure swirl injector. The air-guided combustion strategy is gaining popularity, where the multihole injector is utilised, however the pressure-swirl injector still dominates, and is cheaper to produce.

The structure of fuel sprays emanating from a pressure swirl atomiser were reviewed, providing details of the effects of ambient conditions, fuel properties and in-cylinder air flows. It was shown that the initial break-up of the thin hollow sheet is dependent on these factors as well as the injector parameters such as the cone angle, and nozzle dimensions. Mathematical and computational models are currently available to describe the injection process, from inside the nozzle to droplet break-up. However a greater understanding of the specific break-up mechanisms close to the nozzle, associated with a pressure swirl injector is required if the mathematical models are to be improved.

This chapter also gives an overview of the principal visualisation techniques available for the study of fuel sprays and air flows. It was shown that techniques that can be utilised in the region close to the nozzle of a pressure swirl injector are limited. Imaging techniques that utilise Mie scattering in conjunction with digital or conventional photography will produce qualitative results that with suitable calibration can be used for quantitative analysis, even in the region close to the nozzle. PIV may also be used in this region to obtain

quantitative results on the air flow around the fuel spray by utilising a suitable tracer.

This thesis will describe the near-nozzle characteristics of the pressure-swirl atomiser, utilising the techniques described in this chapter to obtain detailed results. The results will enable a physical understanding of the break-up mechanisms and flow structure of the fuel spray to be obtained. Mathematical models available in the literature will then be adapted to include these findings.

Chapter 2
Design of a Static Pressure Chamber and a
Steady-State Flow Rig

Chapter 2 Design of a Static Pressure Chamber and a Steady-State Flow Rig

2.1 Introduction

It has been shown that there is a requirement for knowledge of the initial break-up process of the inwardly opening, single fluid pressure swirl atomiser. The initial break-up of the fuel spray has been predicted by mathematical models to be of the order of a few millimetres, Han *et al* [2001], Ren and Nally [1998] and Schmidt *et al.* [1999] therefore to study this process the test rigs must have excellent optical access of the injector nozzle. To gain knowledge of this process two test rigs were designed to see the effects of a number of factors; cylinder pressure, fuel pressure and temperature, and air flow. To enable a study to be made of all of these parameters, a static pressure chamber and a steady state flow rig were designed. This chapter will describe the design process of the test rigs used for the experimental studies carried out.

The static pressure chamber would allow for the simulation of fuel injection into the engine cylinder, at pressures equivalent to those that would be experienced when injecting early, and late in the cycle, i.e. for homogeneous and stratified charge modes. This rig would also allow the fuel temperature to be controlled to detail the effects of temperature on the break-up mechanism, including the effects of flash boiling.

The steady state flow rig allowed the effects of an air flow field on the break-up mechanisms to be characterised. This rig also allowed the injector to be recessed into a void, as is the case in many DISI engine cylinder heads, to observe the effects that this would have on the spray behaviour. To determine the effect of the depth of the void, it was possible to control the distance that the injector protruded. To simulate air flow fields found within a typical DISI engine the flow rig used valves as the air inlet, some modification of the

valve/injector geometry was necessary to allow full optical access to the tip of the injector and the first few millimetres of the spray.

2.2 Optically Accessed Static Pressure Chamber

2.2.1 Design Specifications

The main requirements for the static pressure chamber are to simulate the in-cylinder pressure conditions of a DISI engine, operating in homogeneous or stratified charge modes. For homogeneous combustion the fuel is injected early in the cycle, thus injection will be into a low pressure environment, and in some circumstances a partial vacuum may be seen. The pressure chamber must therefore be capable of operating under a partial vacuum.

To gain an understanding of the pressures involved a simulation of cylinder pressure based on the formula $PV^n = \text{constant}$, where $n = 1.3$, with engine parameters based on a DISI engine was made, see Figure 2.1. Two lines are shown, one for a fully open throttle position and one for a partially open throttle position. It was assumed that the cylinder pressure at BDC (intake) would be equal to the intake manifold pressure. With the throttle fully open there would be no pressure drop across the throttle and so cylinder pressure will be equal to atmospheric pressure, 100 kPa. With the throttle partially open, a significant drop in pressure will occur across the throttle, so it was assumed the cylinder pressure will be sub-atmospheric, approximately 50 kPa. For stratified charge operation the fuel is injected late in the cycle, therefore the cylinder pressure will have increased significantly, compared to homogeneous charge operation. Typical late injection timing for stratified charge mode was discussed in § 1.2.1.2 and a value of 60° BTDC (firing) was given. This was an average injection timing and so it may occur later or earlier than that point. It can be seen that at 60° BTDC (firing) the cylinder pressure is approximately 200 kPa. However just 20° later the pressure has increased to 400 kPa, this injection timing is feasible and so must be considered. This cylinder pressure trace is for an almost closed throttle, increasing the amount of throttle will increase the cylinder pressure, and so the pressure chamber

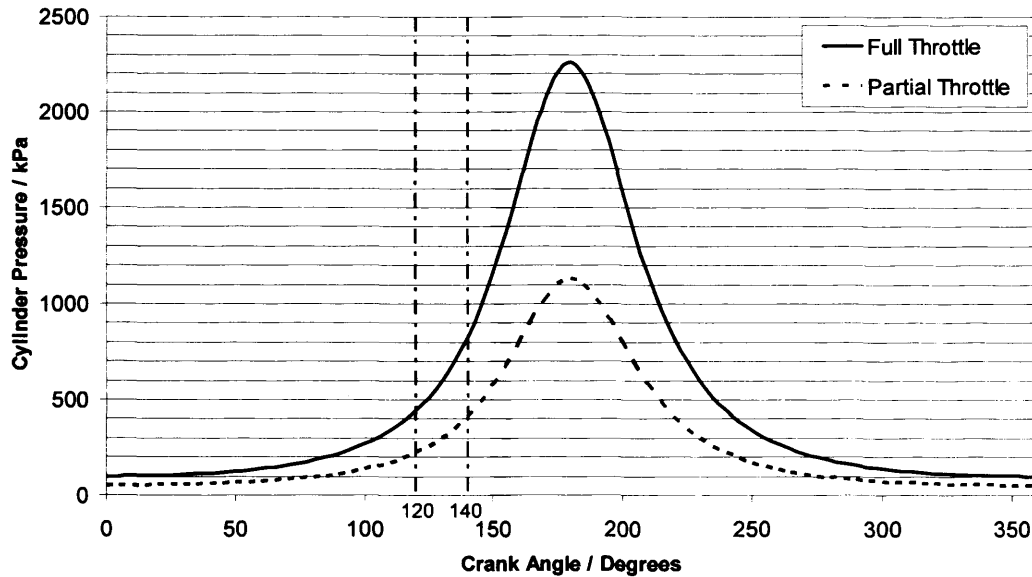


Figure 2.1 – Simulation of Cylinder Pressure for Typical DISI motored engine

must be capable of operating at pressures up to 600 kPa. However the pressure in the cylinder, unlike that in the chamber is rising during the injection event, to simulate injecting into the rising pressure the chamber is designed to an operating pressure of 1000 kPa.

A further requirement of the static pressure chamber was to allow the fuel temperature to be controlled. To observe effects such as flash boiling it must be possible to heat the fuel to a maximum of approximately 80°C, and maintain any temperature from ambient to this maximum.

2.2.2 Design Process

The initial design of the static pressure chamber was based on a design by Connif [2001], which would allow for techniques such as phase doppler anemometry to be carried out within the rig as well as Mie scattering, PIV etc. However the cost of this rig put it over budget and therefore a simpler static pressure chamber was designed, that would allow Mie scattering, PIV etc, without the ability for phase doppler anemometry, which requires windows at specific scattering angles. This would also allow larger windows to be used giving greater optical access to the fuel spray. The goal of the pressure chamber design is to allow excellent optical access to the fuel spray, while providing a high ambient pressures and the ability to heat the fuel.

2.2.2.1 Window Design

The design of the windows will be discussed first as the window dimensions are required for the design of the pressure chamber main body. The optical access requirement for the windows was to allow light from ultraviolet up to visible wavelengths to pass through without significant losses. The windows must also be able to withstand the pressure with negligible deflection to minimise any distortion this might cause. To allow the use of UV light, (for LIF), the material choice is limited to UV grade fused silica or sapphire as other materials such as BK 7 do not transmit light in the UV range adequately. Sapphire is more expensive than UV grade fused silica, however it has a higher tensile strength. A comparison was made to discover which material would prove less expensive, as the thinner sapphire would require less stainless steel. Although the minimum thickness, calculated using equations 2.1 and 2.2, of UV grade fused silica was more than double that of the sapphire, it was still less expensive than the sapphire option. Therefore the material chosen for the windows was UV grade fused silica. Using equations 2.1 and 2.2 from Young [1989], the minimum thickness required for the windows was calculated.

$$t = \sqrt{\frac{-6M}{\sigma_{UTS}}} \quad \text{eq. 2.1}$$

where t , M and σ_{UTS} are the minimum thickness required, maximum moment in the window, and ultimate tensile strength of the material respectively. For a circular clamped plate, the equation governing the maximum moment which will occur at the clamped edge is given by equation 2.2;

$$M = \frac{-\Delta P \cdot r^2}{8} \quad \text{eq. 2.2}$$

where ΔP and r are the pressure differential across the window and the window radius respectively. The required thickness to withstand 10 bar internal pressure with a safety factor of 5 was calculated to be 31.25 mm, a

thickness of 32 mm was chosen for the final design. To enable the windows to be installed easily a 45° chamfer by 0.5 mm was manufactured on both edges, this would allow the o-ring seal to pass over the window with greater ease. This feature would also help prevent any chipping of the edges as sharp corners are more likely to be damaged. Fused silica is very susceptible to chipping and scratches, these must be avoided as it weakens the structure and may lead to failure.

The optical properties of UV grade fused silica are;

Transmittance @ 355 nm:	> 93 %
Transmittance @ 532 nm:	> 93 %
Optically Polished to:	$\lambda/10$ @ 630 nm

and mechanical properties;

Tensile Strength:	48 MPa
Young's Modulus:	74 GPa
Coefficient of Thermal Expansion:	$5.5 \times 10^{-7} / ^\circ\text{C}$

2.2.2.2 Pressure Chamber Design

The individual components of the pressure chamber body will be discussed here, giving design calculations, final dimensions and the materials specified. Technical drawings may be found in Appendix I. BS 5500:2000 “Unfired Fusion Welded Pressure Vessels” was used in the design process of all of the structural components of the pressure chamber, providing formulae for the calculation of wall thickness’, flange thickness’, bolt numbers required etc. All formulae used in this section are obtained from BS 5500:2000 unless otherwise stated.

The materials chosen for the pressure chamber structural components were austenitic stainless steel, types 303 and 304L. They are standard austenitic stainless steels and so have excellent corrosion and heat resistance with good

mechanical properties over a large range of temperatures. Stainless steel was chosen as the material to be corrosion resistant, so that it would remain usable for many years. It also has excellent mechanical properties at elevated temperatures, therefore it could be used for future projects that required a heated pressure chamber. Both types of stainless steel are very similar however type 303 was not available in the large sizes required for the chamber therefore type 304L was chosen for the main chamber body.

Chamber Body – The main body of the pressure chamber is a cylinder and was designed such that it could incorporate the windows within the chamber walls without the need of external window holders. The internal diameter of the chamber was set to 180 mm, this would prevent any fuel being deposited on the windows, and will therefore reduce the requirement for cleaning them. Using this internal diameter an external diameter was calculated to be 300 mm to house the windows. This criterion determined the minimum wall thickness required, however the minimum thickness required to withstand the internal pressure must be considered as well. This minimum thickness is given by equation 2.3a and b whichever is the greater;

$$e = \frac{pD_i}{2f - p} \quad \text{eq. 2.3a.}$$

$$e = \frac{pD_o}{2f + p} \quad \text{eq. 2.3b.}$$

where p is the design pressure, D_i and D_o are the internal and external diameters of the cylinder respectively, and f is the design stress. The design pressure of 15 bar, the design stress of 109 MN/m² (this is the design stress of stainless steel at 200 °C, allowing the chamber to be utilised in the future at high temperature if necessary) were used in the calculation. The dimensions of the cylinder obtained through the design criterion of housing the windows within the walls, along with the other parameters resulted in a minimum thickness of approximately 2.0 mm. This does not include the holes required

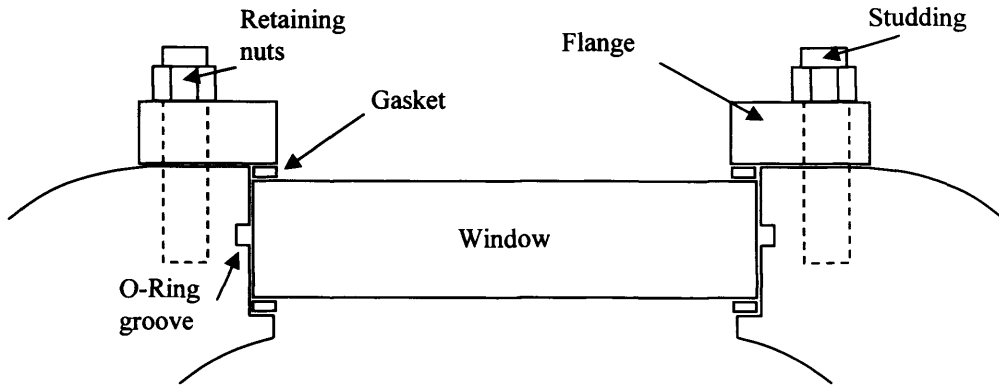


Figure 2.2 – Schematic diagram of window housing arrangement for Static Pressure Chamber

for the windows, however it is far less than the 60 mm wall thickness required to house the windows. A schematic of the window housing arrangement can be seen in Figure 2.2. To seal the windows and the end plates o-rings were utilised. The o-rings were required to be resistant to heat, gasoline and any other liquid that may be used as a seed for flow visualisation. The material chosen was a fluoroelastomer as it has an excellent resistance to degradation by a large variety of fluids and chemicals including oils, fuels and lubricants. It is also capable of operating at high temperatures, without degradation, while still providing an excellent seal. The o-rings sealing the top and bottom plates were situated inside the bolt circle. This will eliminate any loss of pressure through the bolt holes in the plates. The o-ring and bolts were placed close to the centre of the chamber wall, a bolt circle diameter of 250 mm was chosen for the bolts, and a 5.7 mm section diameter o-ring with an internal diameter 219.3 mm was selected. The dimensions for the o-ring grooves were obtained from the o-ring manufacturers guidelines.

The chamber was designed to be 300 mm long with the windows vertically offset, their centres being 125 mm from the top of the chamber. The windows were offset so that the fuel vapour and liquid droplets at the bottom of the chamber would provide minimal influence over the results. A photograph of the rig showing the window locations can be seen in Figure 2.3.

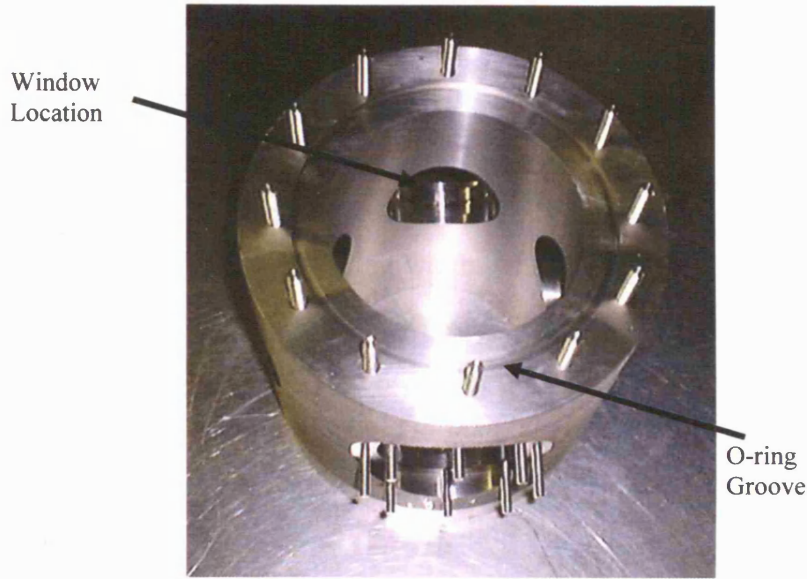


Figure 2.3 - A photograph of the main chamber showing the window locations for the Static Pressure Chamber

End Plates – The top plate was designed to incorporate a hole to accept the injector holder, this was designed to be 100 mm, so that access was available to the electrical connection on the injector. It would also allow access to the heating element surrounding the injector. Using the dimensions already given, i.e. the internal diameter of the chamber, o-ring diameter etc and equation 2.4 it is possible to obtain the thickness required of the top and bottom plates without any openings.

$$e = \sqrt{\frac{0.3G^2 p}{S_{FO}} + \frac{1.909W_{ml}h_G}{GS_{FO}}} \quad \text{eq. 2.4.}$$

where G is the mean diameter of the gasket contact face, p is the design pressure, S_{FO} is the design stress of the material used, W_{ml} is the minimum required bolt load for the operating conditions and h_G is the radial distance from the gasket load reaction to the bolt circle. To calculate W_{ml} equation 2.5 is required;

$$W_{ml} = H_G + H \quad \text{eq. 2.5a.}$$

$$H_G = 2b \cdot 3.14Gmp \quad \text{eq. 2.5b.}$$

$$H = 0.785G^2 p \quad \text{eq. 2.5c.}$$

where b is the basic gasket seating width, which = $N/2$, where N is the contact width of the gasket, and m is the gasket factor, obtained from BS 5500:2000 and is equal to 0.25 for an o-ring. Using these equations a thickness of 16.4 mm was obtained without any hole in the plate. To account for the hole in the top plate equation 2.6 is required;

$$Y = \sqrt{\frac{D}{D - d_e}} \quad \text{eq. 2.6.}$$

where Y is the multiplying factor to account for the opening, D is the opening factor equal to the bolt circle diameter and d_e is the effective diameter of the opening. This gives Y as 1.3 for the 100 mm hole in the top plate, increasing the required thickness to 22.1 mm, this was rounded up to 23 mm for an added factor of safety, and to allow for the extra hole for the pressure relief valve. The bottom plate also required a small hole to accommodate the connection for the vacuum pump, this produced a Y factor of 1.06, increasing the minimum thickness to 17.4 mm, however a small gradient was required on the bottom plate to funnel any liquid fuel out of the chamber, therefore the nominal plate thickness was 23 mm, with a gradient to 18 mm at the centre. Finally the size and number of bolts required is given by equation 2.7;

$$A_{m1} = W_{m1} / S_b \quad \text{eq. 2.7.}$$

where A_{m1} is the total cross sectional area of bolts required for operating conditions, and S_b is the design stress of the bolt material. This gives a total area required of 470 mm², the root area of M10 bolts is 52.3 mm², therefore 9 bolts are required, however due to the large bolt circle diameter 12 bolts were chosen.

Window Flange – The window flange was designed to give a viewing window 95 mm in diameter. The design pressure was increased from 15 bar to 25 bar, effectively increasing the factor of safety from 1.5 to 2.5, the design pressure was increased to minimise the deflections in the flange. Any deflections may cause increased pressure on the fused silica windows, this in turn could lead to failure of the windows. The flanges were designed using the same formulae as the end plates, equations 2.4 – 2.6. This produced a minimum thickness of 11 mm, with a Y factor of 1.93, increasing the minimum thickness to 21.23 mm. A 2.5 mm 45° chamfer was machined on the outer face of the flange, this reduced the local thickness, therefore the total thickness of the flange was increased to 23 mm. The number of bolts required for the flange was calculated using equation 2.7, giving a total bolt area of 189 mm², the root area of M8 bolts is 32.84 mm², therefore 6 bolts are required, however to reduce any deformation of the flange 8 bolts were utilised.

Injector Holder – This section will discuss the design of both the injector holder that the injector is seated in, and the crucible that the injector holder is held in. The crucible is the component that seals the pressure chamber, with the injector holder simply allowing the injector to be positioned accurately. The dimensions of the injector holder are identical to the DISI engine head the injector is designed for, however the walls surrounding the injector are as thin as possible so that under heating the injector and fuel are heated quickly and to a uniform temperature. This holder is held in place in the crucible using a screwed ring, this allows the injector to be rotated 360° into any orientation relative to the windows.

The crucible was designed using BS 5500:2000, for vessels under external pressure. The design process for vessels under external pressure is more iterative than for vessels under internal pressure, therefore an initial thickness of the crucible wall was required. This thickness is then used in equations 2.8 and 2.9 along with tables of data to calculate the maximum operating pressure.

$$p_y = \frac{sfe}{R} \quad \text{eq. 2.8.}$$

where p_y is the pressure at which the mean circumferential stress reaches the yield point of the material, s is the factor relating the design stress to the effective yield point of the material and is 1.1 for austenitic steels, f is the design stress, e is the thickness of the vessel wall and R is the mean radius of the cylinder.

$$P_m = \frac{Ee\varepsilon}{R} \quad \text{eq. 2.9.}$$

where p_m is the elastic instability pressure for collapse of a cylindrical shell, E is the Young's modulus of the material and ε is the mean elastic circumferential strain at collapse (obtained from tables). The design process is to calculate p_y and p_m then use these values to determine p/p_y (obtained from tables), where p is the allowable pressure. If the value of p is insufficient then the initial value for e must be increased until the allowable pressure exceeds the design pressure.

An initial value of 10 mm was chosen for the wall thickness of the crucible, this is large however the top flange of this component must have tapped holes machined to allow for the studding, 20 mm is required to provide enough room for the studding. Also the bottom of the crucible must provide enough material for the injector seal to be fully in the crucible to prevent any pressure loss, the minimum distance required for the injector seal is approximately 10 mm. Therefore the top of the crucible must be 20 mm and the bottom 10 mm, the wall of the crucible must also be tapped to retain the injector holder, thus reducing the local thickness. Using this initial thickness and the other parameters such as the internal diameter of 100 mm, (discussed in the end plate section) an allowable pressure of 69 bar, much higher than the 15 bar design pressure. Another advantage to having thick walls are a large mass, such that during temperature controlled experiments a stable temperature may be obtained.

2.2.2.3 Design of Ancillaries

A brief description will be given here on the ancillary components required to run the static pressure chamber. This will include the pressurisation system, fuel heating system and fibre optic cable access.

Pressurisation System – A description of the pressurisation system used to both obtain positive and negative gauge pressure within the rig will be given here. To positively pressurise the system a nitrogen bottle was utilised with a 10 bar regulator to set the required pressure. A vacuum pump was used to produce a negative pressure in the chamber, but was also connected to the pressure chamber in conjunction with the nitrogen bottle to allow the chamber to be purged of fuel liquid / vapour when testing with positive pressure. To measure the sub atmospheric pressure in the chamber a water filled manometer was utilised. A pressure relief valve was used to vent off excess pressure in the event of over pressurisation due to a fault in the pressure regulator. It could be set to a relief pressure between 6 and 14 bar, and was set to 12 bar in this case so that no pressure relief would occur during normal operation up to 10 bar.

Fibre Optic Cable Access – An aluminium blank was utilised to allow access for the fibre optic cable used to illuminate the fuel spray with laser light from within the chamber. The blank replaced one of the fused silica windows and had a hole for the fibre optic cable to pass through. A holder and sealing tape was utilised to provide a seal around the cable. A schematic diagram of this arrangement may be seen in Figure 2.4.

2.3 Optically Accessed Steady-State Flow Rig

2.3.1 Design Specifications

The main requirements for the steady-state flow rig are to simulate the in-cylinder flow conditions that the spray may see due to valve opening, i.e. high velocity air flows, and to allow the effects injector positioning within the

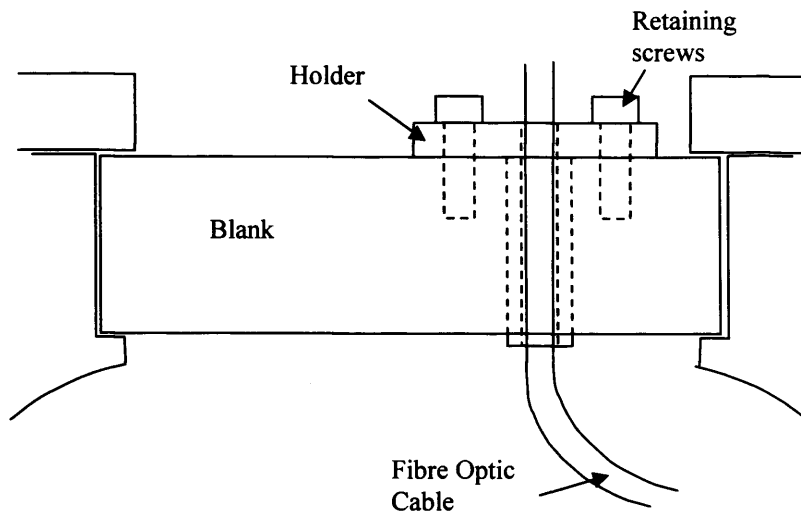


Figure 2.4 – Schematic diagram of fibre optic cable access blank for the Static Pressure Chamber

engine head to be investigated. The geometry of the valves and injector must be similar to that of a typical DISI engine head, while allowing for optical access of the injector tip. The valve lift available should be equivalent to the DISI engine head, which is typically 8-10 mm. The air inlet to the rig is required to have an entry for the particle seeder used to visualise the flow for particle image velocimetry (PIV). The rig should be capable of measuring the air flow rate through the valves, so that an approximation of the flow velocities may be made and compared to the results from the PIV, thus giving some validation of the results.

2.3.2 Design Process

2.3.2.1 Flow Rig Design

The initial design for the flow rig was to adapt a conventional wind tunnel design to allow an injector to be mounted and optically accessed at the throat. This would allow air flow velocities of around 15 m/s to be created, with a uniform flow, in comparison to the highly turbulent in-cylinder air flows experienced in a DISI engine. Although this initial design based on research carried out by Choi *et al.* [2000] would allow simulation of the in cylinder air flow during late injection, after inlet valve closure, it would not allow simulation of the very high air velocities impinging on the fuel spray created by the opening of the inlet valves during early injection. The initial design

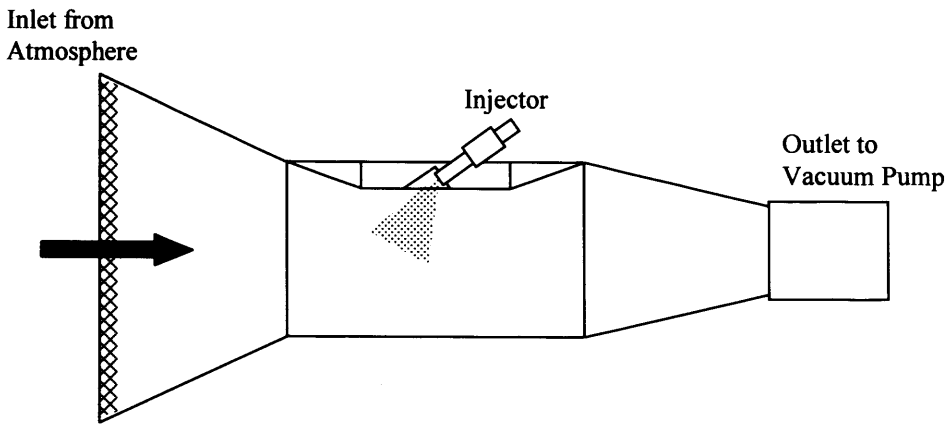


Figure 2.5 – Schematic of Wind Tunnel based Flow Rig

may be seen in Figure 2.5 and would allow low velocity air flows to be created, as well as allowing the injector to be mounted in a manner that would allow its depth and possibly orientation to be altered relative to the flow rig wall.

It was decided that the inclusion of inlet valves would allow the high velocity air flows that impinge on the fuel spray to be imaged. These high velocity flows would produce larger deformations on the spray, and will allow the conditions needed for stratified charge to be observed. There are essentially three possibilities for this type of design; to adapt a DISI engine head to allow optical access, attempt to reproduce the DISI engine head geometry to allow better optical access, or to recreate only the essentials of the engine geometry. Modifying a DISI engine head to allow optical access to the injector tip is extremely difficult. It would lead to a confined field of view that would not produce good results. Therefore the design moved to reproducing the engine head geometry while allowing excellent optical access. This included reproducing the inlet port geometry and injector positioning as closely as possible. Also the injector would be within a recess as in the DISI engine head, making it difficult to provide good optical access to the injector tip, see Figure 2.6. However the main problem with this design was manufacturing the inlet ports to a higher enough standard to produce smooth flows. The design could not be made without sharp edges close to the valve seats. Therefore a simpler design was conceived to eliminate this problem, however to do so the

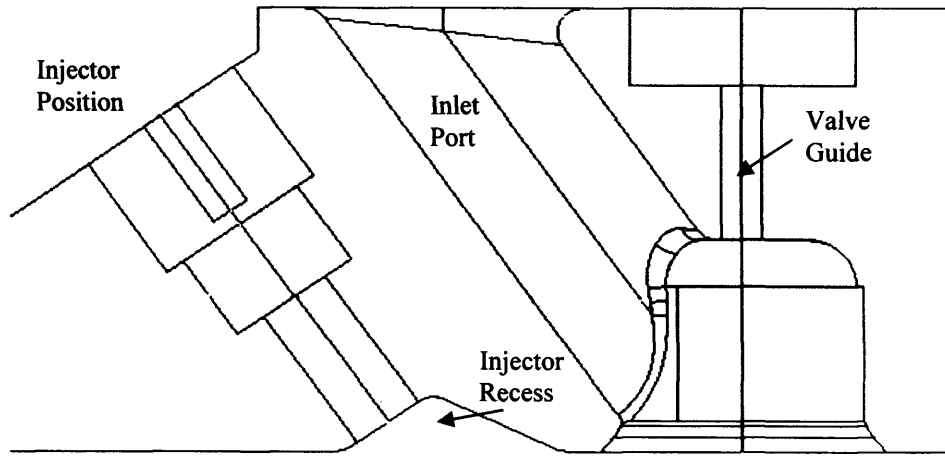


Figure 2.6 – Schematic of the side view of a reproduction DISI engine head

injector was no longer housed within a recess. The advantage of smooth flow was deemed to be greater than the disadvantage of no longer having a recessed injector tip.

The final design for the flow rig was therefore based on a specific DISI engine head geometry, however to produce a rig capable of observing the injector tip, with flows comparable to that of a DISI engine it was necessary to alter the geometry somewhat. Observing Figure 2.7, a schematic of the final flow rig design it can be seen that the inlet port has been simplified, and now has the valve guide supported by a web, this may also be seen in Figure 2.8, a photograph of the inlet ports. The distance between the web and the valve seat is large enough to eliminate most of the disturbances it may cause. The web is also on the opposite side of the inlet port to the injector, which will be the main area of interest. The other major alteration is that the injector is no longer in a recess, however the distance from the injector to the valves remains similar to that of a DISI engine head, and is closer than the recessed design. This is because to allow optical access to the injector tip when it is in the recess it was necessary to move the injector further from the valves. The orientation of the injector to the valves has been altered in order to simplify the design. The main injector utilised in these studies has a 15° offset, it has been orientated such that the spray axis is parallel to the valve axis. This will limit the amount of fuel directed at the windows of the flow rig, therefore reducing the amount of cleaning the windows require. To produce high quality

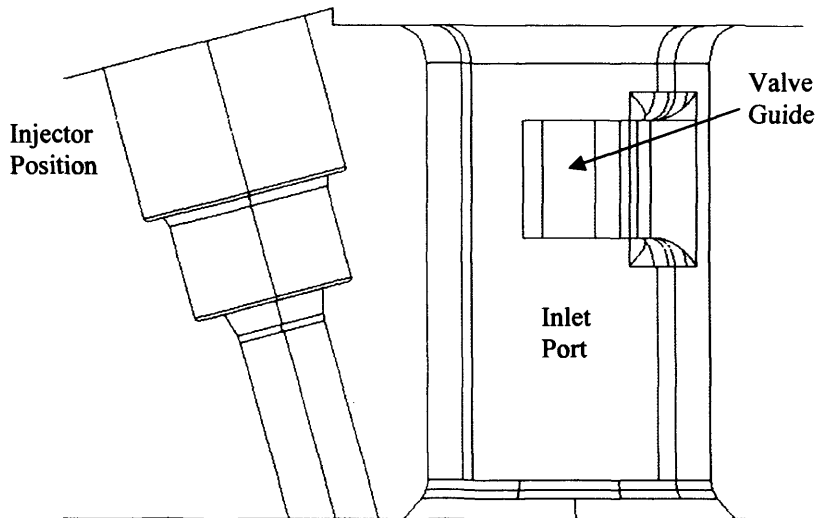


Figure 2.7 – Schematic of the side view of the Flow Rig final design

results it is important that the windows remain clean. Access to the windows for cleaning is limited, therefore reducing the amount of fuel impacting the windows is important.

Similarly to the pressure chamber the four windows were arranged orthogonally to provide a number of different lighting options. This would allow for side lighting, with either a sheet of laser light or global illumination, (using either laser light or a spark flash), and also back lighting of the fuel spray.

The material chosen for the flow rig was type 6082 aluminium, with the main walls of the rig consisting of 10 mm thick plates for a very rigid structure to avoid any leakage due to warping or misalignment. Any small leaks in the optical chamber of the rig may result in extremely high velocity air flows impinging on the flow structure, producing undesirable effects. Engineering drawings of the flow rig components may be found in Appendix I, also Figure 2.9 shows a photograph of the flow rig with the injector in place.

2.3.2.2 Window Design

The window requirements for this rig were less rigorous than for the pressure chamber as it was not expected that light in the ultraviolet wavelength region would be utilised. Also this rig will not be pressurised so the only forces



Figure 2.8 - A photograph of the inlet port and injector arrangement for the Steady State Flow Rig

exerted on the windows will be due to the depression caused by the flow restriction at the valves. Therefore the material chosen is a less expensive borosilicate optical glass, with the following optical properties;

Transmittance @ 532 nm:	> 90%
Flatness:	≤ 5 Fringes
Parallelism:	≤ 3 Arc min.

and mechanical properties;

Tensile Strength:	90 MPa
Young's Modulus:	63.7 GPa

The size of the windows is dependent on the flow rig dimensions, and these were chosen to match the bore of a DISI engine. A diameter of 50 mm was chosen as a suitable dimension that would allow good optical access. The standard window thickness for a 50 mm diameter window is 6 mm, providing for a safety factor of over 11, based on equation 2.1, using a pressure of 50 kPa. The thickness of the window will allow it to be fixed in place easily and will provide a large area for the epoxy resin to hold the windows in position, this will also seal the windows, preventing any air ingress into the test section.

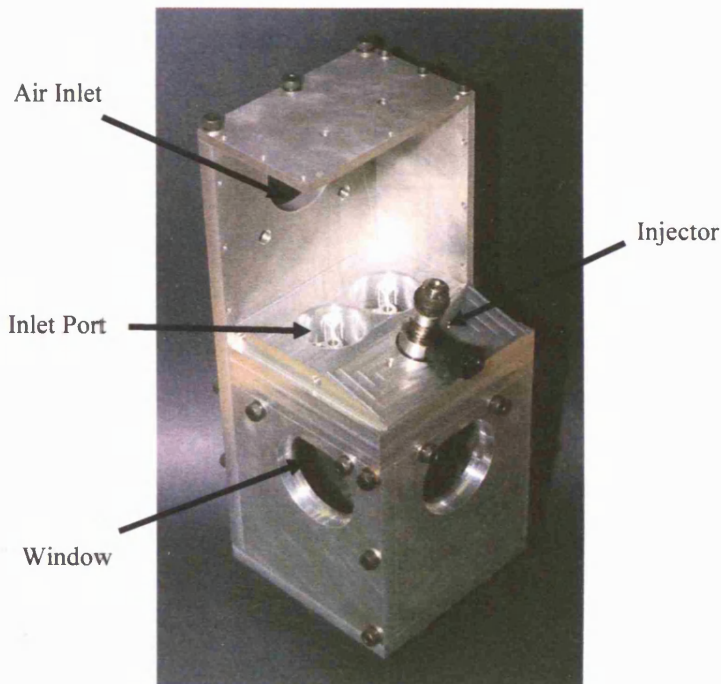


Figure 2.9 – Photograph of Flow Rig, showing air inlet, window and injector locations

2.3.2.3 Design of Ancillaries

A brief description will be given here on the ancillary components required to run the steady state flow rig. This will include the valve positioning system, air flow meter and vacuum pump.

Valve Positioning System – This is a steady state flow rig and therefore the valves are stationary throughout the experiment. However to observe the effects of different valve lifts it must be possible to alter the valve position. The solution used is to position the valves using studding, this will allow the valves to be moved into position by screwing the studding down or up as necessary, then using lock nuts, maintain its position. A pointer is attached to the studding to provide a method of measuring the valve lift, see Figure 2.10. This system will also allow independent valve lift, allowing for simulation of swirl control in an engine where one inlet port is closed to induce swirl in the cylinder.

Air Flow Meter – The air flow meter used in this rig was obtained from a Ford Zetec engine and is comprised of a hot wire anemometer. This gave an output in volts that is relative to the volumetric air flow rate. The hot wire

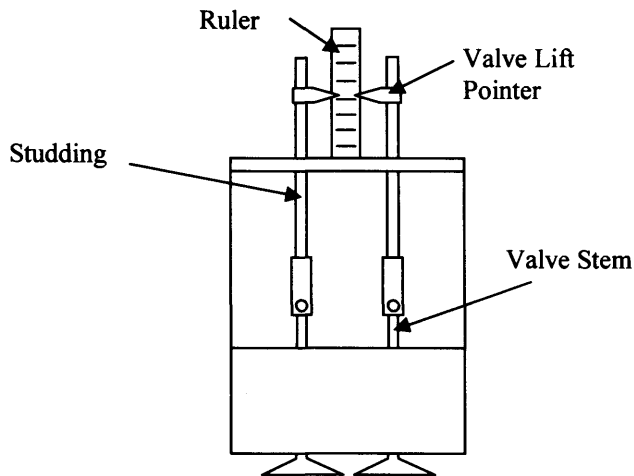


Figure 2.10 – Schematic of Valve Positioning System on the Steady State Flow Rig.

anemometer was calibrated using a laminar flow element air flow meter calibrated to NIST standards with an accuracy of $\pm 1.0\%$ of the reading.

Vacuum Pump – The vacuum pump used to draw the air through the flow rig and has a maximum volumetric flow rate of approximately 180 Litres / s. This was connected to the flow rig via flexible pipe and a flange attached to the base of the rig. The volumetric flow rate through the rig was determined by throttling the connection between the rig and the vacuum pump, as well as throttling the amount of air bypassing the rig being drawn directly from atmosphere. To control the pressure within the flow rig a throttle placed upstream was used.

Chapter 3

Image Acquisition and Analysis Techniques

Chapter 3 Image Acquisition and Analysis Techniques

An important requirement in order to complete the proposed study, was to be able to adequately illuminate the spray issuing from the injectors and to be able to capture and process the resulting images. This chapter will cover the problems associated with imaging, including camera resolution, multiple scattering, lighting effects, focusing etc. These will be defined as pre-processing difficulties that can in some way be accounted for in the image acquisition phase. These problems may also be dealt with by image processing techniques used to filter noise, size features, account for background irregularities etc. The text by Russ [2002] contains more detailed explanations of image processing techniques and should be referred to for further information.

3.1 Image Acquisition

Two forms of image acquisition will be considered, wet film, (conventional 35 mm film) and CCD (Charge Coupled Device) cameras. The advantages and disadvantages, as well as the specific problems associated with each will be discussed. However, there are some problems associated with image acquisition in general and these will be considered first along with the imaging requirements.

3.1.1 Imaging Requirements

Although there is a diverse range of imaging techniques, several general criteria may be established for images intended for computer processing and analysis. All of the imaging techniques discussed previously in Chapter 1 will require some form of analysis to obtain qualitative or quantitative information, some of these criteria will also apply to the other laser based techniques such as LIF and LDA / PDA. The first criterion is the need for global uniformity in

both illumination and the surface being imaged. This means that the same type of feature will look the same wherever it appears in the image, for this to be possible the illumination must be even both spatially and temporally, i.e. it must be repeatable between images so that comparisons may be made. If the surface being imaged is not planar, such as the earth being imaged from space, then distortion of the image will occur, this may be corrected with a prior knowledge of the surface shape and the source of illumination. When the surfaces are non-planar, factors such as overlapping features may cause disruptive shadows on the image. Overlapping features are a problem when imaging fuel sprays and tracers within air flows, it is known as multiple scattering, and this will be discussed in § 3.1.1.3. In addition to these criteria, local sensitivity to variations is required. This means that edges and boundaries must be well defined and accurately located, Russ [2002] states that in general anything that degrades high frequencies in the signal chain will disturb the subsequent ability to identify feature boundaries or locate edges for measurement. This is a very important factor when dealing with fuel injection sprays as the ability to detect the boundaries of sheets, holes and droplets is vital. The camera resolution will affect the ability to detect edges and boundaries and will be discussed in § 3.1.1.1.

3.1.1.1 Camera Resolution

The camera resolution as discussed earlier will determine the size of feature that can be distinguished from the background and surrounding features. Important considerations are the type of lens being used and its cleanliness, the target object contrast (TOC), which will have a large effect on the resolving power of the camera, and the signal to noise ratio which will also have an effect on the final resolution of the image.

The type of camera used will affect the resolution; there are many types of camera available however there are two main types, digital and wet film. Digital cameras may be further subdivided into CCD and CMOS (Complementary Metal Oxide Semiconductor), however the limitations in terms of resolution and noise levels means that currently CMOS cameras can

not compete with CCD cameras for applications in scientific imaging. Wet film resolution will depend not only on the camera being used, but also on the type of film being used and the developing process. In general the faster a film, (the speed of wet film is determined by the total amount of light required for a correctly exposed image), the lower the resolution. The reason for this is the minimum size of grain required increases with the speed of the film, therefore the density of the grains decreases lowering the resolution. In comparison wet film will give a higher resolution than CCD cameras, however results may be obtained immediately with CCD cameras, as compared with wet film which requires developing and digitising before any analysis may be carried out. A typical resolution of a 'fast', ISO 3200 film, would be approximately 125 lp / mm (line pairs per mm), and for a 'slow', ISO 100 film, would be approximately 200 lp / mm. A typical CCD camera has a resolving power of approximately 50 lp / mm, depending on the camera. Therefore a choice must be made of speed of results versus image quality. Although in its base format wet film has a higher resolution than CCD cameras, careful selection of the digitisation process must be carried out to ensure that this resolution is maintained.

3.1.1.2 Focusing

To obtain reliable results from image processing, drop size measurements etc, it is important that the image is in focus. Out of focus images may lead to incorrect measurements as the distortion produced will affect calibration and the ability to define the edges of features. Determining 'in-focus' criteria is extremely difficult, however a number of methods have been described to attempt to quantify the level of focus. An important feature of in-focus criteria is the depth of field of the imaging system. The depth of field is defined as the distance range along the optical axis within which the focal plane is considered to exist. When imaging a droplet distribution some of the droplets will fall outside the depth of field, either closer to or further away from the optics, Koh *et al.* [2001] provides a criteria to determine which droplets are in focus so that out of focus droplets may be eliminated from the measurement process. The criterion is based on the contrast of the droplet to the local

background. This is based on a general criterion that the binary image of the objects within the focal plane may be found using equation 3.1 to a reasonable accuracy. Where G_{LT} , G_{LB} and G_{OM} represent the threshold level, the local background and object minimum grey levels respectively.

$$G_{LT} = G_{LB} - 0.5(G_{LB} - G_{OM}) \quad \text{eq. 3.1.}$$

Koh *et al.* [2001] have proposed a criterion for small droplets, the normalised value of contrast (VC), as given in equation 3.2.

$$VC = \frac{G_{LB} - G_{OM}}{G_{LB}} \quad \text{eq. 3.2.}$$

The value of VC approaches unity when the droplet is in the focal plane, however for small droplets it will be smaller than for larger droplets, therefore the focal plane will be approximately where the maxima occurs. This is a difficult technique to utilise as the maxima will vary in magnitude depending on the droplet size. Therefore some calibration is required to obtain the location of the maxima for varying droplet sizes.

The depth of field will vary with the optical characteristics of the system, for instance reducing the aperture of the camera lens will generally increase the depth of field. Generally the smaller the field of view, i.e. the area that the camera system is focused on, the smaller the depth of field.

3.1.1.3 Multiple Scattering

Another effect that has to be considered is multiple scattering, usually it is assumed that each photon emitted from the light source interacts with only one droplet and then goes directly to the camera without further interaction with another droplet. In dense sprays, such as DISI sprays, this may not be true, therefore multiple scattering must be considered. When droplets are close together the mean free path of the photons decreases and hence the probability of multiple scattering increases. As the mean free path approaches the size of

the droplets in the experiment, the effect of multiple scattering becomes important. A photon that has been multiply scattered carries information about more than one droplet so therefore the information becomes ambiguous. This can lead to the image becoming blurred, the laser sheet broadening (if using sheet illumination) and signal attenuation that varies with the out of plane spray structure. This problem can therefore add structure to the image that should not be there and remove other details that should be there. To obtain images that give a better understanding of the processes involved it is sometimes necessary to take an average of a large number of images. This enables any cycle to cycle variations to be reduced helping to alleviate the problem of multiple scattering. However, this technique masks details, which vary spatially from image to image, (e.g. break-up features). Multiple scattering can also be reduced by carefully selecting the method of illumination and imaging in less dense regions of the spray. Obviously the less fuel that the light travels through the less multiple scattering occurs.

3.1.2 Digital Image Capturing

If post processing of the images is required, such as feature enhancement before measurement, then it is necessary to acquire the image in a digital format. This is a trivial matter when dealing with a CCD camera as the image will be directly stored as a digital image when captured by the camera and stored in a computer. However care must be taken to store the images in a suitable format, so that no information is lost. For instance a JPEG format (or officially JFIF, JPEG File Interchange Format), will dramatically reduce the file size, however information will be lost leading to a reduction image quality. However formats such as TIFF (Tagged Image File Format), will allow for storage of the image with no loss of quality, as such this is a popular method for storing high resolution images. However when dealing with wet film, negatives are produced. Therefore it is necessary to digitise these images using a suitable process that will minimise any losses in quality. There are a number of methods available for the digitisation of negatives as discussed by Fry [1994], including:

- Projecting the images onto an opaque screen and viewing the image with a CCD camera.
- Projecting the film images onto one side of a semi-transparent screen and recording the image from the other with a CCD camera.
- Slide mounting the negatives and commercially transferring them to Photo CD.

Arguably the best method for the digitisation of negatives is to commercially transfer them onto Photo CD, however a loss in resolution will occur and it must be considered when choosing whether or not wet film is an advantage over CCD imaging systems. The Photo CD has a typical resolution of 3072 x 2048 pixels, while a typical CCD camera used in this application will have a resolution of 1280 x 1024 pixels.

3.2 Image Processing

Generally it is necessary to carry out image processing of the results obtained prior to measurements being taken. This may take the form of simple image cropping and zooming into an area of interest, or may involve more detailed processing, involving thresholding, filtering within the spatial and or frequency domain etc, prior to measuring features. This section will describe some of the more commonly used operations when dealing with fuel spray images.

3.2.1 Image Defect Correction

This section will deal with image processing that corrects for some of the image defects that occur during image acquisition. The optimum process for eliminating image defects is to attempt to capture the perfect image initially. However this often proves extremely difficult if not impossible. Noise, non-planar surfaces, non-uniform lighting or limited availability of light are just a few factors that will cause defects in the captured image.

The simplest form of defect correction is contrast expansion, Russ [2002], this can be used to enhance the contrast of an image when the full dynamic range of the camera system is not utilised. The image histogram which is a plot of the number of pixels with each possible brightness level may be expanded such as to utilise the full range of brightness levels. This is a linear process that sets the brightest pixel level recorded to white and the darkest to black. The remaining pixels are linearly spaced between these two extremes depending on their original brightness level. This leads to an increased visual contrast in the image but has not increased the ability to distinguish between subtle variations in grey scale that were not recorded in the original image.

The effect of this contrast expansion is to increase the visibility of the noise present in the image. Noise in imaging is extremely difficult to eliminate in the process of capturing the image. Noise in this case will be defined as any effect that will alter the grey level value of a pixel that is not part of the original image. In CCD cameras this may be due to noise introduced through outputting the photons to be read as a voltage, or any noise introduced through the wires or even through the ac voltages within the computer itself. Noise may also be introduced due to instability in the light source, such as uneven light intensity during image capture. In all cases however, pixels affected by noise are assumed to be surrounded by neighbours that correctly represent the captured image. Therefore a simple method of noise reduction is to average a number of images to eliminate the random influence of noise. This may not always be possible, especially for time dependent images.

3.2.1.1 Neighbourhood Operations

There are more efficient methods of eliminating noise from an image, namely methods that use the surrounding pixels to alter the grey level value of the centre pixel. These are generally known as neighbourhood averaging methods, the more common of which utilise kernels in a convolution process. A 'kernel' is a matrix of numbers by which the pixel values are multiplied. The basic neighbourhood averaging technique simply averages the grey level values of the surrounding pixels and replaces the centre pixel value with this average,

Russ [2002]. This however dramatically reduces the resolution of the image and small structures tend to be eliminated. The more common form replaces the pixel with the average of itself and its neighbours. This is described as a kernel operation since its implementation can be generalised as the sum of the pixel values in the region multiplied by a set of weights. This process is called a convolution, and can be described by equation 3.3, where P^* is the new pixel value, P is the original pixel value and W is an array of weights:

$$P_{x,y}^* = \frac{\sum_{i,j=-m}^{+m} W_{i,j} P_{x+i,y+i}}{\sum_{i,j=-m}^{+m} W_{i,j}} \quad \text{eq. 3.3.}$$

This operation is performed over a square of dimension $2m + 1$, which is odd, therefore the neighbourhood sizes range from 3×3 upwards, 5×5 , 7×7 etc. The array of weights may simply contain only 1s, however it has been shown that a kernel based on a 3-D Gaussian distribution, see Figure 3.1, produces the most effective reduction in noise while producing the least amount of blurring of the image. For this type of operation the weighting values will all be positive. This type of noise reduction assumes that the surrounding pixels are part of the same structure, therefore when the operation is performed near feature edges some amount of blurring will occur, the Gaussian distribution helps to minimise this by weighting centre pixel significantly higher than the pixels at the edge of the kernel. However some amount of blurring will still occur, so more complex kernels have been developed, some with negative values surrounding the centre pixel to attempt to emphasise edge details, these will be discussed later.

Another form of neighbourhood noise reduction is generally called neighbourhood ranking, Russ [2002], in this process the neighbouring pixels are ranked according to their brightness. There are many ways of selecting the pixel value to replace the original pixel, however so called median filtering, where the original pixel is replaced by the median value of the surrounding

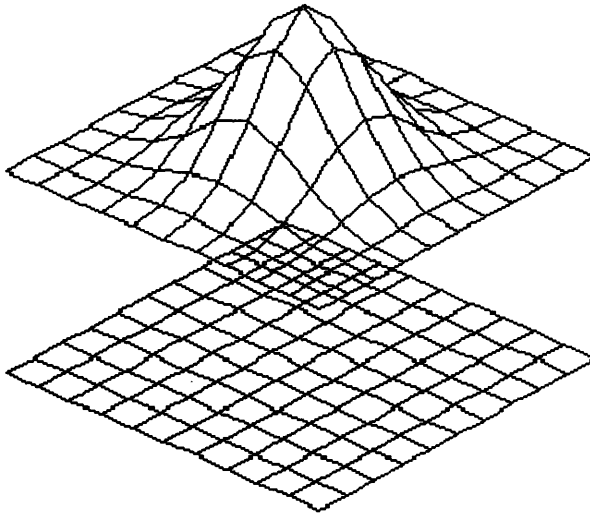


Figure 3.1 – A plot of a 3-D Gaussian distribution superimposed onto a grid of pixels.

pixels is an efficient way of reducing certain types of noise without blurring edges. It is also possible to use different shaped filters with less computation time than for neighbourhood averaging, such as crosses, or filters that simulate circles etc.

Neighbourhood ranking filters may be used to sharpen edges while reducing the amount of noise present in the image, by utilising a mode filter where the original pixel is replaced by the mode, or most common pixel value of the surrounding pixels. However the mode is poorly defined for small neighbourhoods, so a truncated median filter may be used. This is accomplished by discarding some of the pixel values, generally the ones that lie furthest from the mean and using the median value of the remaining pixels. This will have the effect of moving the median closer to the mode of the original set of neighbourhood values. All of the neighbourhood operations will reduce the image resolution to some extent, and therefore must be used with care. The size of the filter must be chosen such that the smallest features that are to be retained are not eliminated during the process.

3.2.1.2 Non-Uniform Illumination

Another defect that can occur in images is non-uniform illumination, this is extremely difficult to eliminate while capturing the image, especially for non-planar surfaces. A simple method for correcting this defect is to obtain a

background image without the object being imaged present. This background image is then subtracted from the image thus correcting for any non-uniform illumination. Although this method is generally called background subtraction, Russ [2002], the actual operation performed will be dependent on the type of camera being used, if logarithmic then subtraction is the correct operation, however if the camera has a linear response then division by the background image is the correct operation. A CCD camera for instance, has a linear response between light intensity and grey scale output. This process will reduce the dynamic range of the original data, i.e. the number of different grey levels a pixel may be, and will also increase the levels of noise present in the image. This is therefore not always an appropriate process to use.

When using a background subtraction technique care must be taken to ensure that the removal of the object does not affect the overall lighting in the image. This may be a problem in imaging fuel sprays, especially within an optical engine as the reflected light from the spray interacts with the surroundings producing a different background with and without the fuel being present. If it is not possible or practical to obtain a background image separately, then it is sometimes possible to fit a background function. This can be accomplished by the user selecting points within the image that should all have the same brightness. These points are then used to perform a least-squares fitting of a function, $B(x,y)$ that approximates the background, this may then be subtracted (or divided) just as with a physically acquired background. A second order polynomial would have the form of equation 3.4:

$$B(x, y) = a_1 + a_2x + a_3y + a_4x^2 + a_5y^2 + a_6xy \quad \text{eq 3.4.}$$

To obtain a good background function it is important to select points that are well distributed throughout the image as locating all of the points close to one location will require extrapolation of the polynomial and may lead to significant errors.

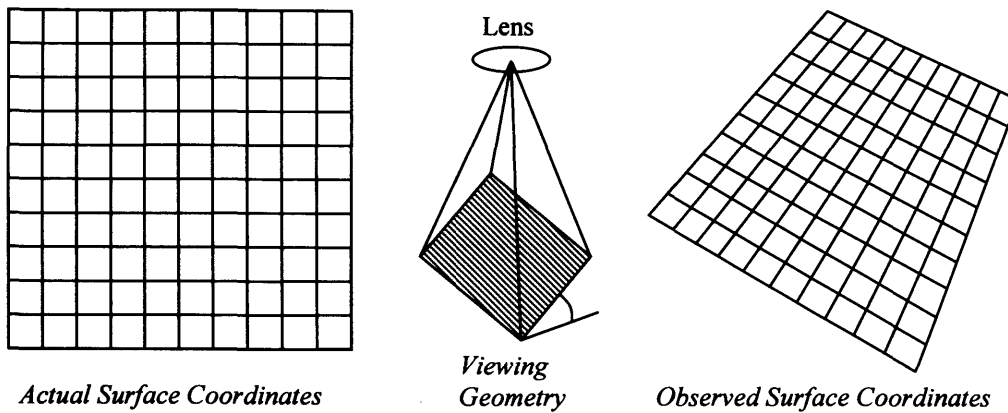


Figure 3.2 – Observed distortion of an image typical when viewing a tilted surface, Russ [2002]

Rank levelling is a further method of eliminating non-uniform illumination. This process is similar to the neighbourhood operations discussed earlier, however in this operation the darkest (in the case where the background is darker than the features) pixel replaces the original centre pixel. This has the result of reducing the size of the features and replacing them with the local background pixel grey level. If this procedure is performed a number of times eventually the features will be entirely eliminated leaving only a background image which again may be subtracted (or divided).

3.2.1.3 Non-Planar Images

Non-planar views will lead to distortions of the object, and in this case this will be considered to be a defect of the image. This may be corrected if a prior knowledge of the object geometry is known. If the distortion of the image is large then this may lead to errors when measurements are taken. An example of the image seen when looking at a planar surface at an angle can be seen in Figure 3.2. Using the prior knowledge of the object it is possible to create formulae that transform the distorted image back into its correct proportions. These will take the form of equation 3.5, Russ [2002]:

$$X' = a_1 + a_2X + a_3Y + a_4XY + a_5X^2 + a_6Y^2 + \dots \quad \text{eq 3.5.}$$

A similar relationship will exist for Y' . The more complex the shape of the object, the more higher order terms are required to transform the image.

However a second order polynomial will produce a good approximation for complex shapes including that of looking at curved surfaces. It is necessary to know the coordinates of a number of points on the object, and their corresponding coordinates in the image. Using these known points a set of simultaneous equations may be solved to find the constants and transform the image back to its correct proportions.

3.2.2 Image Enhancement

This section will discuss the image enhancement operations that may be performed on digital images. The distinction made here between image enhancement and image correction is that image correction attempts to return the image to an optimal state that would have occurred anyway if the image was perfectly captured. Image enhancement will deal with operations that increase the contrast between features, highlight edges etc, which will allow measurements to be taken more easily. This section will cover enhancements that can be carried out in the spatial and frequency domain.

3.2.2.1 Spatial Domain

This section will specifically discuss the enhancement operations available within the spatial domain. The ability to expand the contrast by manipulating the pixel brightness histogram was discussed in terms of correcting defects within the image and was a linear process. It is not possible to implement this operation if there are a small number of either very dark or very light pixels as there is no room for the histogram to be expanded, unless these pixels are removed. If these need to be retained but some of the grey scale values are under-utilised then it may be better to spread out the displayed grey levels in the peak areas, while compressing them in the troughs, this is called histogram equalisation, Russ [2002]. The transfer function may be simple. Considering Figure 3.3, if the cumulative histogram of the grey levels is plotted then it can be seen that there is an uneven spread of the grey level values. If the histogram is equalised to produce a linear cumulative plot then this will better utilise the available grey level values. This has the effect of showing detail in regions that have a high brightness gradient, and also makes it possible to see minor

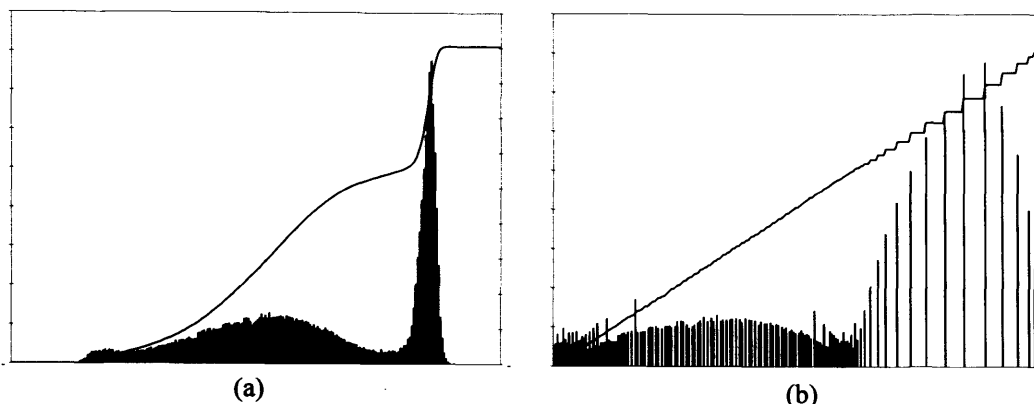


Figure 3.3. – Plot of histogram prior to equalisation (a), and after linear equalisation (b)

variations within regions that appeared nearly uniform originally. The process to produce the linear cumulative plot is quite simple, for each brightness level j in the original image, the new assigned brightness value k is calculated as;

$$k = \sum_{i=0}^j N_i / T \quad \text{eq 3.6.}$$

Where N_i is the number of pixels in the image with brightness equal to or less than j , and T is the total number of pixels in the image. This procedure may be performed in order to produce a cumulative histogram in forms other than a straight line. A logarithmic distribution concentrates the histogram at the low brightness level values, and as such is useful for stretching the contrast of very light images. The opposite of this is the exponential distribution which concentrates the histogram at the high end of the scale, thus is useful for increasing the contrast of dark images. A further histogram equalisation is the best fit algorithm, this assigns the bottom and top 3 % of the pixels to black and white respectively and then linearly spaces the remaining pixels between these two values, *Image-Pro Plus reference guide*.

Other operations that will attempt to increase the contrast between features are similar to the operations discussed in § 3.2.1.1, more specifically referring to equation 3.3, the neighbourhood averaging procedure. However adjusting the kernel such that it no longer contains only positive values but negative ones as well can lead to interesting results. For example the Laplacian operator, Russ

[2002], is a common kernel used to enhance edges. It takes the form shown below, and is W , the array of weights, (or kernel) used in equation 3.3 to modify the pixel values;

$$\begin{array}{ccc} -1 & -1 & -1 \\ -1 & +8 & -1 \\ -1 & -1 & -1 \end{array}$$

This subtracts the brightness values of each of the surrounding pixels from the centre pixel. Therefore in regions that are uniform in brightness or where there is a uniform brightness gradient the sum will be zero. However, when there is a discontinuity, i.e. a feature boundary, then the results will be non zero. Obviously there is a possibility of negative results which can not be shown so it is common to add a medium grey level value, 128 for an 8 bit grey level image ranging from 0 to 255. As the name implies this is an approximation to the linear second derivative of brightness B in directions x and y , as given in equation 3.7 below;

$$\nabla^2 B \equiv \frac{\partial^2 B}{\partial x^2} + \frac{\partial^2 B}{\partial y^2} \quad \text{eq. 3.7.}$$

This is invariant to rotation, and therefore to the direction that the discontinuity runs. The Laplacian image by itself is difficult to interpret so addition of the Laplacian operator enhanced image to the original image will allow for easier interpretation by the human viewer. Although the Laplacian operator is computationally efficient and will define edges in some circumstances, if the image does not contain edges that have sharp variations in brightness then it does not work very well. Also, if the image contains a large amount of noise, then because the operator will enhance local changes in pixel brightness, especially points, then it will enhance the noise as well as the edges.

A more effective, if not more efficient method for detecting edges is to use the first derivative of the pixel values, Russ [2002], which will highlight gradients in brightness, and therefore feature edges. Obviously in a digitised image a continuous derivative may not be performed, instead the difference value between adjacent pixels can be calculated as a finite difference. This difference produces noise within the image, however averaging in the direction perpendicular to the derivative, (as this is essentially a one dimensional process), can smooth the result. The kernels shown below apply both the finite difference and the averaging in one operation therefore reducing computation time, there are eight possible orientations, with only three shown;

$$\begin{array}{ccc}
 1 & 0 & -1 \\
 2 & 0 & -2 \\
 1 & 0 & -1
 \end{array}
 \qquad
 \begin{array}{ccc}
 2 & 1 & 0 \\
 1 & 0 & -1 \\
 0 & -1 & 2
 \end{array}
 \qquad
 \begin{array}{ccc}
 1 & 2 & 1 \\
 0 & 0 & 0 \\
 -1 & -2 & -1
 \end{array}$$

However this only extracts one dimensional data from two dimensional images. It is therefore necessary to extend this method into two dimensions, the Sobel operator, Russ [2002], is a method of accomplishing this that uses the derivatives in both directions, see equation 3.8, and combines them to obtain results independent of orientation;

$$\text{Magnitude} = \sqrt{\left(\frac{\partial B}{\partial x}\right)^2 + \left(\frac{\partial B}{\partial y}\right)^2} \qquad \text{eq. 3.8.}$$

This is computationally intensive as it will produce non-integer results, to overcome this, the Kirsch operator, Russ [2002], was developed. This method applies each of the eight orientations of the derivative kernel shown earlier keeping the maximum value obtained and will produce results similar to the Sobel operator.

3.2.2.2 Frequency Domain

This section will specifically discuss the enhancement operations available within the frequency domain. To perform any operations within frequency space it is first necessary to transform the spatial image into frequency space. This is accomplished using the Fourier transform, James [1999], and although a rigorous mathematical analysis will not be performed here, a brief explanation of the process will be given.

The Fourier Transform – The Fourier transform begins with a function $f(x)$, where x is a real variable representing distance in one dimension across an image. Fourier's theorem states that it is possible to form any one dimensional function $f(x)$ as a summation of a series of sine and cosine terms of increasing frequency, this Fourier transform function is written $F(u)$, and is written as equation 3.9;

$$F(u) = \int_{-\infty}^{+\infty} f(x)e^{-2\pi iux} dx \quad \text{eq. 3.9.}$$

where using Euler's formula;

$$e^{-2\pi iux} = \cos(2\pi ux) - i \sin(2\pi ux) \quad \text{eq. 3.10.}$$

This generally produces a complex result and can therefore be expressed in polar form so that an image may be produced that is generally the magnitude, (of the complex result) or the square of the magnitude which is called the power spectrum;

$$F(u) = |F(u)| \cdot e^{i\Phi(u)} \quad \text{eq 3.11.}$$

where $|F(u)|$ is the magnitude and Φ is the phase. Obviously this operation can not be performed between minus and plus infinity, therefore it is performed on

a finite number of summations given by the size of the image. This is called the discrete, or fast Fourier transform and is given by equation 3.12;

$$F(u) = \frac{1}{N} \sum_{x=0}^{N-1} f(x) \cdot e^{-i2\pi ux / N} \quad \text{eq. 3.12.}$$

this process may also be performed in reverse to convert from the frequency domain to the spatial domain, and is given by equation 3.13;

$$f(x) = \sum_{u=0}^{N-1} F(u) \cdot e^{i2\pi ux / N} \quad \text{eq. 3.13.}$$

This summation is usually performed over terms up to one-half the dimension of the image (in pixels), this will lead to the Fourier transform having the same number of pixels as the original image as it requires both the magnitude and phase to describe the Fourier transform. This process can also be performed on two dimensional images, as the directions x and y are orthogonal, the operation may be performed in one direction to create an intermediate transform, then in the other direction to create the final transform.

When performed in two dimensions the power spectrum of the Fourier transform can be shown as an image. The image is plotted such that the low frequencies are points close to the origin, (which is the centre of the image), and the high frequencies are points further away, their directions will indicate the orientation of the lines (features). Superposition of any two images in the spatial domain will equate to their Fourier transforms simply being summed together. Therefore, in reverse, if a periodic noise is apparent then this may be eliminated from the power spectrum, though not from the phase information as this gives information on the location of the feature, thus eliminating the periodic noise from the image in the spatial domain. An example of an image and its corresponding FFT can be seen in Figure 3.4.

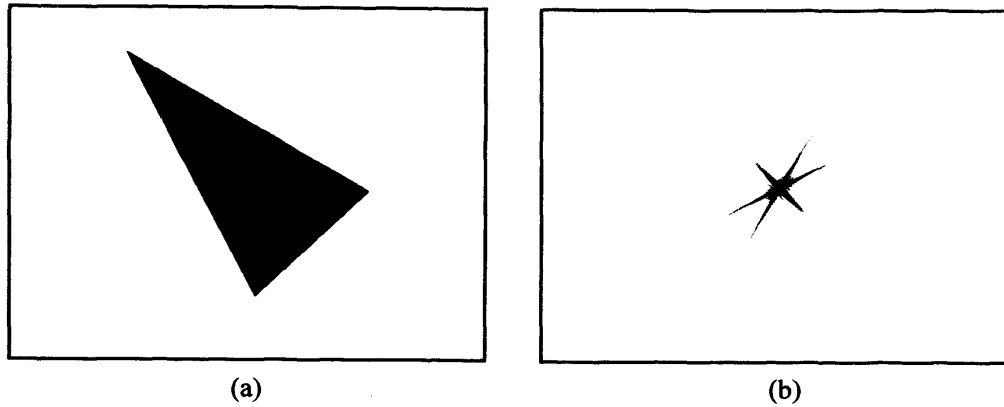


Figure 3.4 – Example of a FFT, original image (a), and the power spectrum (b)

Filtering Images – Filtering in the frequency domain is similar to that discussed earlier in the spatial domain. Once the Fourier transform has been performed then the periodic noise, for instance, will be shown as spikes in the power spectrum. These may be isolated by putting a small circle around the spike and then removing it by a suitable method. As long as a smoothing function is used to modify the edges of the circle, (generally a Gaussian smoothing operation is acceptable), then no problems should occur.

It is a common occurrence to utilise high and low pass filters, depending on the application, on the Fourier transform. A high pass filter will remove any frequency below a certain threshold, this may be used for instance to eliminate the low frequency noise and produce an image with a higher contrast. The opposite is true for the low pass filter, it removes any high frequency above a certain threshold. Care must be taken when using these types of filters as simply eliminating all frequencies above or below a certain value will produce ringing around the image when the inverse transform is applied. This can be avoided by smoothing the edge of the filter, this can either be linear, parabolic, Gaussian or some other form of smoothing function.

Convolution – Convolution was discussed in § 3.2.1.1 and is a common operation in the spatial domain, where a kernel of numbers is multiplied by each pixel and its neighbours in a small region, the results of which are used to replace the original pixel. This operation may also be performed in the frequency domain, and is in fact a much more efficient process. Therefore at

there is a point at which for large kernel sizes it becomes more efficient to perform the Fourier transform, then the convolution and the reverse Fourier transform back into the spatial domain. This is because the equivalent operation is a single multiplication of each pixel in the magnitude image by the corresponding pixel in a transform of the kernel. The transform of the kernel may be performed and stored earlier, and if the kernel is smaller than the image it must be padded with zeros to the same size as the image. This process may only be carried out for linear processes within the spatial domain, therefore ranking techniques, histogram modification etc cannot be performed in the frequency domain.

A process known as deconvolution is perhaps the most useful of the operations that can be performed in the frequency domain as it allows for the removal of image blur. Image blur may be caused by out of focus optics, or more importantly perhaps for the imaging of high speed fuel sprays, motion blur. However to understand motion blur correction it is first necessary to look at the general process of deconvolution. If the amount of blur is known, either by measuring what is known as the point spread function (PSF), Russ [2002], or by knowing the amount of movement over the exposure time, then a Fourier transform of this may be performed. The PSF is the amount of spread of the information introduced by the optics on a single point being imaged. The transform of the blurred image is then divided by the transform of the PSF, then reverse Fourier transformed to give a dramatic improvement in image quality. This is a complex division therefore the magnitudes are divided and the phases are subtracted. Care must be taken not to divide by zero or to cause numeric overflow problems due to division by small numbers. This process is also influenced greatly by noise, and this must therefore be minimised before applying this technique, especially in the PSF.

If there is a significant amount of noise then the Wiener deconvolution process may be used, Russ [2002]. The basic deconvolution process may be described by equation 3.14;

$$F(u, v) \approx \left[\frac{1}{H(u, v)} \right] G(u, v) \quad \text{eq. 3.14.}$$

Where $F(u, v)$ is the theoretical image without any blur, $G(u, v)$ is the blurred image and $H(u, v)$ is the blur function, i.e. the function which describes the blur in the image. The wiener deconvolution essentially adds a constant to the denominator in an attempt to reduce the noise. Equation 3.14 then becomes;

$$F(u, v) \approx \left[\frac{1}{H(u, v)} \right] \cdot \left[\frac{|H(u, v)|^2}{|H(u, v)|^2 + K} \right] \cdot G(u, v) \quad \text{eq. 3.15}$$

The constant K is theoretically dependent on the statistical properties of the images, however in practice it is normally an adjustable parameter.

If the image blur is caused by motion and the amount of motion is known then a motion vector may be used to eliminate the blur, Russ [2002]. As the vector includes information of both the magnitude and direction of the motion then significant improvements may be made. Again the Wiener deconvolution process may also help in increasing the image quality if there is a significant amount of noise. When performing this technique it is important to use images with at least 8-bit grey scale depth, 12-bit is preferable to limit the amount of losses due to numeric overflow etc.

3.2.3 Segmentation and Processing Binary Images

After any image defect correction and image enhancement is carried out it is generally necessary to perform segmentation and further processing before detailed measurements can take place. Segmentation is the process of dividing the image into regions of interest, generally to highlight features. Thresholding is the main process by which segmentation is accomplished, with further processing after this operation.

3.2.3.1 Thresholding

Thresholding is the process of defining a range of pixel brightness levels such that the pixels within the range are considered to be the foreground, or the feature, and the rest of the image is set to be the background. Often the foreground is set to white and the background black making it into a binary image, Russ [2002]. This threshold level or region is generally set by a user interface in which the operator alters the settings until the desired affect is found. This process uses the histogram of brightness levels to select the range of brightness values to threshold. Obviously it is important that over the region thresholding is taking place that the brightness levels are uniform, i.e. two identical features will have the same brightness value independent of their location in the image.

When a user sets the threshold range separately for each individual image, accuracy and reproducibility are low. Therefore it is necessary to automate the process somewhat. There are options that still include user interaction, where the user will set a value such as N number of standard deviations from the mean brightness value, however this will be consistent over all of the images thresholded. There can be many interpretations of this thresholding technique, and therefore an iterative process is required to obtain the best threshold range for each particular set of images.

Another method of selecting the threshold level, outlined by Fry [1994], is to attempt to minimise the sum of the entropy in both regions, i.e. the background and foreground. Entropy is a measure of disorder, and will be equal to a maximum if the image is equally distributed in all grey levels, and a minimum, equal to zero when it is a uniform grey value. The algorithm requires the selection of a high and low value between which the threshold will be computed. This may cover the entire brightness range, however this is a computationally intensive operation and therefore the smaller the range the better. The following equations are utilised in the process of calculating the threshold level k ;

$$P_i = \frac{N_i}{N} \quad \text{eq. 3.16.}$$

where P_i is the probability of a pixel to have intensity i , N_i is the number of pixels at level i , and N is the total number of pixels.

$$w_0 = \sum_{low}^k P_i \quad \text{eq. 3.17.}$$

where w_0 is the probability of a pixel to have an intensity less than k but higher than the low value. Similarly;

$$w_1 = \sum_k^{high} P_i \quad \text{eq. 3.18.}$$

The entropy for each region is defined as;

$$F_0(k) = \left[- \sum_{low}^k \left(\frac{P_i}{w_0} \right) \cdot \log \left(\frac{P_i}{w_0} \right) \right] \quad \text{eq. 3.19.}$$

$$F_1(k) = \left[- \sum_k^{high} \left(\frac{P_i}{w_1} \right) \cdot \log \left(\frac{P_i}{w_1} \right) \right] \quad \text{eq. 3.20.}$$

The threshold value k is the grey level that minimises the sum of the entropy of the two regions;

$$F(k) = F_0(k) + F_1(k) \quad \text{eq. 3.21.}$$

This is a brief introduction to thresholding, and although there are other techniques that are utilised in the segmentation of images they are extremely computationally intensive and so will not be introduced here.

3.2.3.2 Processing Binary Images

The processing of binary images is performed after the thresholding operation, the goal of which was to separate features from the background to allow, measurement, counting etc. The goal of further processing these binary images is to eliminate any noise etc that has survived the thresholding process, or for instance to compare two images using Boolean math. Boolean math may be used to compare two images to obtain features that are, or are not present in both. More complex Boolean math may be used in conjunction with masks to eliminate some features while keeping others that are only partially eliminated by the mask.

Erosion and Dilation – Although erosion and dilation are part of the larger category of morphological operations they are an important feature and so will be discussed independently. Erosion removes pixels from features in an image, the purpose of which is to remove pixels that should not be there. The simplest kind of erosion removes, (i.e. converts to background), any pixel that is touching a pixel that is already the background. Therefore the features are reduced in size until eventually they disappear, however it is generally not taken this far and only the noise pixels are eliminated, being the smallest and most isolated features. Obviously if the image is left like this then any measurements taken will have an error associated with the erosion process. Therefore there is a complementary function called dilation, which adds pixels, (i.e. converts to foreground), which are touching a foreground pixel, thus increasing the size of features. Combining erosion and dilation of equal magnitude, is called an opening process, and removes small features, noise, but returns the large features to their original size. It also has the effect of separating just touching features. Using dilation then an erosion is called a closing process, and has the effect of closing small gaps between features.

It is possible to apply a coefficient to these operations such that when counting how many pixels are background surrounding a pixel, a certain number must be reached before any change will occur. The shape that is utilised for making this judgement can be changed from the eight surrounding pixels, to a cross or

circle of pixels etc. These changes may be important depending on the image to avoid anisotropy. A circle for instance will not shrink uniformly with a standard operation, as the pixel distances are greater at a 45° angle, it will therefore tend towards a diamond shape. Using different shapes and coefficients can aid in keeping the circle circular.

3.2.4 Measurement of Features

There are two main methods of measuring features within digital images, they are manual, whereby features are picked out by eye, and then measured, and automatic whereby an algorithm within the image analysis software will define and measure features. There are advantages and disadvantages to both. Measuring features manually may decrease the time required to evaluate each image, however this is only the case for low numbers of images and simple features, such as the penetration of a fuel spray. The disadvantage of this method is that the variability and accuracy of the measurements will be dependent on the experience and ability of the user. Grimaldi *et al* [2000] gives an example of an automated procedure for determining the fuel spray characteristics. This involves thresholding and filtering the original image before analysing each row of pixels to determine where the boundary of the fuel spray is. A criterion is defined that informs the procedure when the fuel boundary is present, this may be adjusted by the user to discriminate between small droplets detached from the main spray body and the main spray body itself. Adjusting this criterion will allow for larger or smaller droplets, or even ligaments to be included or excluded from the measurement depending on the requirements of the user. Therefore although this is an automated procedure, some user input and knowledge of the spray being measured is required before the automated procedure may take place. The results obtained will also be highly dependent on the thresholding and filtering carried out on the image before the measurement procedure. Therefore care must be taken to choose threshold and filtering levels such that true measurements are taken.

For both types of measurements it is necessary to perform a calibration of the image to obtain the measurements in standard units, millimetres or metres etc.

To accomplish this, an object of known size within the image must be measured to determine the calibration. Care must be taken that the object is parallel to the focal plane so that there are no errors introduced. A common form of calibration is to image a ruler either during the actual experiment or afterwards taking care not to change any settings. An alternative is to introduce an object of known dimensions in all images.

3.3 Summary

This chapter has reviewed the techniques available to obtain and then process images utilising the techniques examined in chapter 1. Difficulties with camera resolution, focusing and multiple scattering were discussed and methods of reducing their affect on the captured image were examined. Procedures for the correction of image defects that cannot be eliminated in the capturing stage were discussed. Such as noise elimination, background correction to account for non-uniform illumination and transformations to account for non-planar images. The next stage of image processing is to attempt to enhance the captured image to enhance the appearance of edges and features. Finally to allow quantitative results to be obtained it is often necessary to apply thresholding to produce a binary image.

Chapter 4

Understanding the Phenomenon of Fuel Sheet Break-Up in the Near-Nozzle Spray Region of a DISI Pressure-Swirl Injector

Chapter 4 Understanding the Phenomenon of Fuel Sheet Break-Up in the Near-Nozzle Spray Region of a DISI Pressure-Swirl Atomiser

This chapter presents the results obtained from an experimental study carried out to investigate the fuel sheet break-up in the near-nozzle region of an inwardly opening, high pressure-swirl atomiser. Mie scattering was utilised to visualise the fuel spray in conjunction with a high speed camera and a long distance microscope lens to provide both high temporal and spatial resolution. The results shown in this chapter may be found in Loustalan *et al.* [2003(a)] and Loustalan and Davy [2003(b)].

4.1 Introduction

The review of current methodologies for modelling the fuel spray close to the injector nozzle in Chapter 1 has shown that there is a requirement for experimental data in this region. The difficulties associated with obtaining experimental data are such that detailed imaging in this area is often limited to that of the sheet edge. Kubo *et al.* [2001], Alloca *et al.* [2002], and Kawahara *et al.* [2004] all show images with limited detail except for the spray edge.

This work is intended to extend the present level of knowledge regarding the near nozzle flow structure and liquid sheet break-up, and to provide experimental data for future theoretical modelling. To obtain this information a novel ‘void fraction’ analysis technique was developed and applied to multiple images from the steady-state period of a single injection event in order to characterise and quantify details of the sheet break-up process.

The sheet break-up length was calculated for this injector using three commonly employed models from the literature. The sheet break-up lengths obtained by the author were compared to these predictions, in order that future modelling work may improve upon the currently available models.

4.2 Experimental Apparatus and Procedure

The experiments were undertaken in a static pressure chamber with four orthogonal fused-silica parallel-face windows, see §2.2 for the design of this experimental rig. The operating pressure range of this chamber was 50 – 1000 kPa. To control the pressure in the chamber, both a vacuum pump, (for sub-atmospheric pressures), and a high pressure nitrogen bottle, (for higher than atmospheric pressures) were used. Two pressure-swirl atomisers were tested, Injector A had a spray axis inclined at 15° to the (vertical) injector axis, while Injector B had a spray axis that was parallel to the injector axis. However the majority of the testing was carried out using Injector A. Details of the two injectors may be found in table 4.1.

Injector	Spray Axis Offset	Nozzle Diameter / μm	Manufacturer	Prototype Part No.
A	15°	600	Denso	JCD-003
B	0°	600	Denso	JCF-005

Table 4.1 – Details of the two injectors utilised during testing

The fuel was supplied to the injectors at a constant pressure from a pneumatic ram coupled to a hydraulic ram, as first described by Salters *et al.* [1996]. The Fuel Systems Test Facility located at University College London (UCL), UK, allowed for the safe use of commercial grade unleaded gasoline, thereby showing the behaviour of real fuel. Two fuel pressures were tested for both the global and near-field imaging, 5 MPa and 10 MPa. These pressures were used as they are comparable to those used in DISI engines.

An Oxford Lasers copper-vapour laser, which provided ~ 20 ns duration pulses of light was utilised as the light source for these experiments. The copper-vapour laser was capable of operating up to a maximum repetition frequency of 40,000 Hz. A High Speed Rotating Drum Camera (HSRDC), capable of operating up to 300 revolutions per second, (rps), was used to capture the

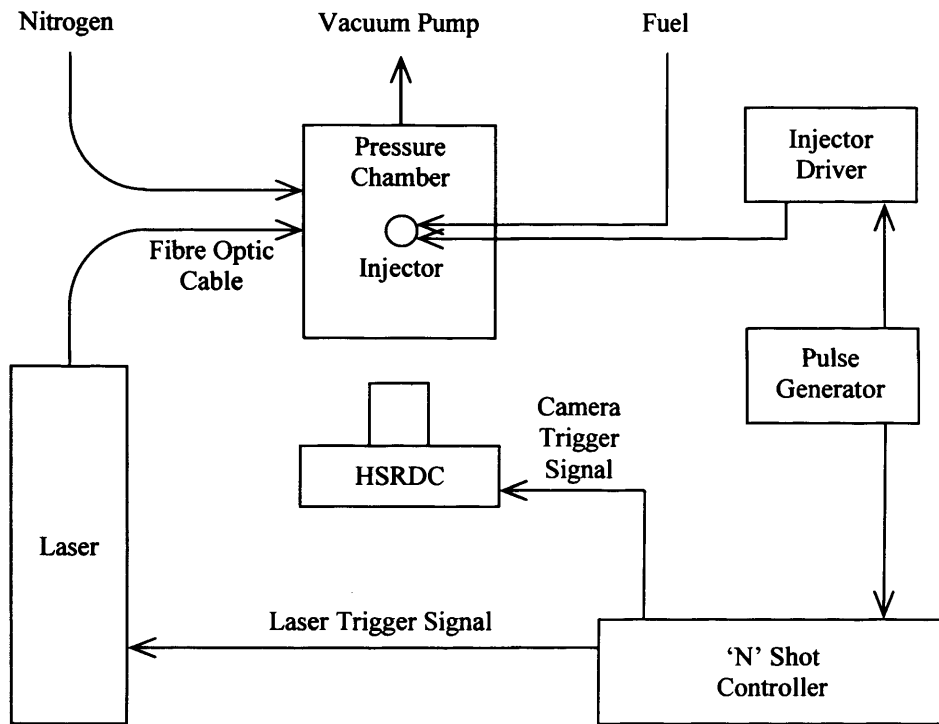


Figure 4.1 - Schematic diagram of Experimental Apparatus utilised during the first phase of testing

images on a one metre length of photographic film, as described by Davy *et al.* [1998]. The standard frame size for the HSRDC was 15 mm. To avoid overlapping of images the camera speed must be set according to the laser frequency. For example for a laser frequency of 10 kHz the camera speed must be 180 rps, to allow 1.5 mm either side of the imaging. The laser and camera were synchronised with the injection event using an Oxford lasers ‘N’ shot controller. Figure 4.1 shows a schematic diagram of the experimental apparatus.

The film used for all tests was Kodak TMAX ASA 3200 black and white film, this is a very fast film, required for the low light levels. The exposed films were developed using Kodak TMAX developer and Kodak TMAX fixer, taking great care to avoid any exposure to light. The developing times were dependent on the ambient temperature, however it is possible to perform an operation called ‘push-processing’ of the films to account for underexposure. After development of the film the images were digitised prior to post-processing using the software package *Image-Pro Plus*™ V4.5. This process is described in § 3.1.2. The digitisation process produces images that have a

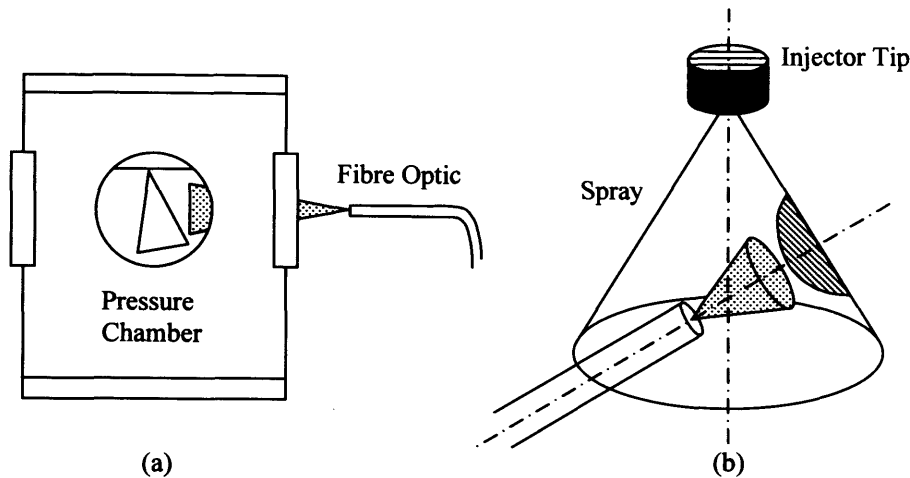


Figure 4.2 – Schematic of optical arrangement for: (a) Global Imaging (b) Near Field

resolution of approximately 110 lp / mm, this is a minimal loss of resolution as the film used has a resolution of approximately 125 lp / mm. Despite this loss in resolution it remains approximately twice that of a CCD camera.

4.2.1 Global Imaging

For this part of the study the laser light was directed through a fibre optic cable and arranged to illuminate the entire spray from one side, see Figure 4.2(a). The pulse repetition rate of the laser was set to be 10 kHz, giving a frame separation time of 0.1 ms. Injector A was used with a pulse width of 2.0 ms, this enabled the entire spray event to be captured and is a comparable pulse width to that used within a DISI engine under many operating conditions. To provide an understanding of the effects of back pressure on the characteristics of the spray, chamber pressures of 50, 100, 200, 400, 600, 800, 1000 kPa were used. All tests were carried out at ambient room temperature of 20 – 25°C.

A Nikkor 60 mm macro lens gave a field of view (FOV) of approximately 60 x 70 mm, this enabled the global characteristics of the spray to be measured, such as the cone angle and penetration, for the entire spray event. The variations in spray density can also be observed, providing an understanding of the difficulties that may arise in the near field work, due to the very dense spray at higher back pressures.

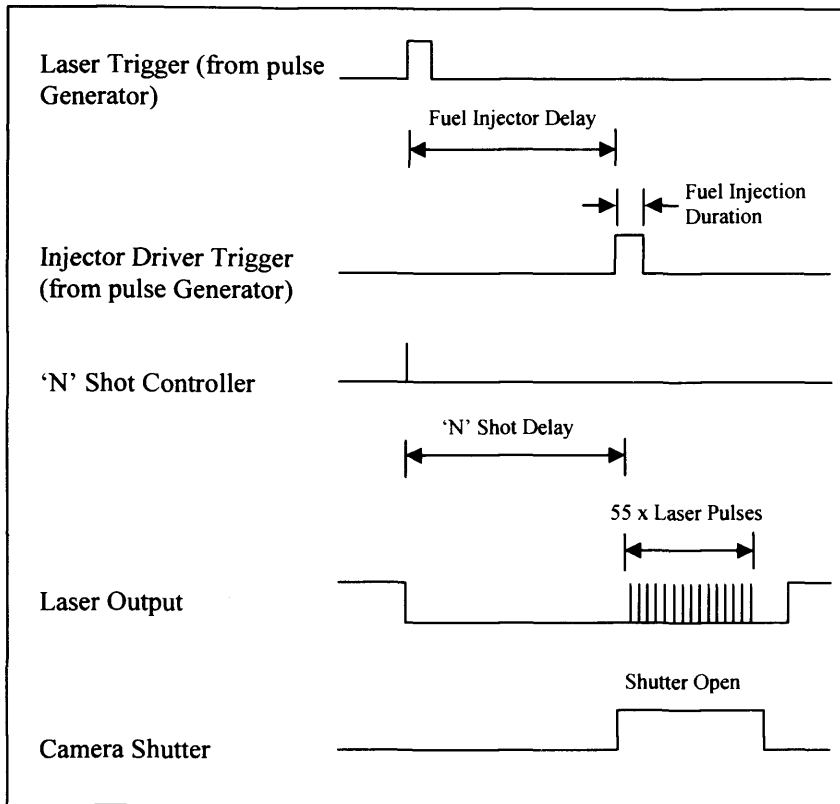


Figure 4.3 – ‘N’ Shot acquisition timing sequence for HSRDC operation

The experimental procedure for both the global and near-field imaging was the same. The pressure in the chamber was set to the test condition, and the camera was loaded with film and motored up to speed. The ‘N’ shot acquisition sequence was triggered by the pulse generator which also triggered the injector drive unit, this sequence may be seen in Figure 4.3. The ‘N’ shot controller temporarily extinguished the laser before opening the camera shutter. Following a pre-set delay period, the film was exposed by a burst of 55 laser pulses at the programmed frequency. On completion of the laser pulse burst, the laser is once more extinguished and the shutter is allowed to close.

4.2.2 Near Field Imaging

For this study the laser light was again directed through a fibre optic cable, initially the cable was situated outside the hollow cone of the fuel spray, in a conventional back lighting technique. This produced images that suffered severely from multiple scattering of the light, leading to difficulties producing an ‘in-focus’ image. Therefore the cable was moved inside the hollow cone of the spray, see Figure 4.2(b). This allowed the laser light to be concentrated on

the area of the spray that was being imaged, thus increasing the light levels, while reducing the amount of error due to multiple scattering of the light. The cable was considered to be situated far enough downstream to cause no effect on the characteristics of the spray in the region that was being imaged. For this section of work an Infinity K2 long-distance microscope with a CF-2 objective lens was used, giving a FOV of approximately 2.7 x 4.2 mm. After digitization the images had a scale of approximately 1 pixel = 2.2 μm .

The original test matrix included the same pressures as for the global imaging, however, as it can be seen from the global images, see Figures 4.8 & 4.9; the spray becomes denser with increasing back pressure. It was found that the available light levels decreased due to the dense spray, restricting the useable range of gas pressure, to 50, 100 and 200 kPa. The only means available to increase the light levels was to open the aperture of the camera. Unfortunately this reduces the depth of field (DOF), making focusing on the sheet extremely difficult. Therefore to ensure high quality images the back pressure was further limited to a maximum of 100 kPa for the higher fuel pressure of 100 MPa. The DOF was approximately 1.3 mm with a back pressure of 50 kPa, this reduced to approximately 1.0 mm with a back pressure of 100 kPa.

4.3 Single Shot Near Field Imaging

A second series of tests were performed on Injector B to confirm that the findings were not injector specific. A similar pressure swirl injector was used, however there was no offset, i.e. the spray axis was parallel to the injector axis. A different system was utilised to acquire these results as the copper vapour laser and HSRDC were not available. A high power Nd:YAG laser with a pulse width of 3-5 ns was utilised as the light source, and illuminated the spray in a similar manner to that shown in Figure 4.2(b). The camera used was a 12 bit CCD camera with a 1280 x 1024 pixel array in conjunction with the Infinity K2 long-distance microscope. This produced images with a resolution of approximately 58 lp / mm. A CF-1 objective lens was required for this series of testing to obtain the same magnification as with the HSRDC

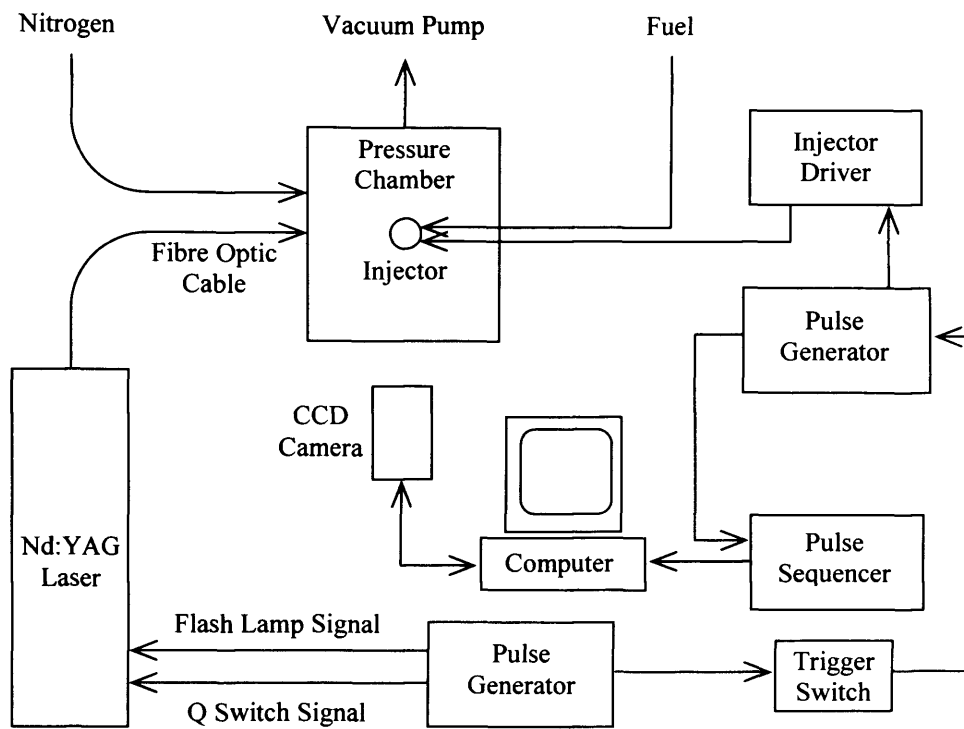


Figure 4.4 - Schematic diagram of Experimental Apparatus for Single Shot Imaging

and the CF-2 objective lens, due to the differing optical properties of the two camera systems. To control the laser, injector and camera timings two high precision digital delay/pulse generators were connected together via a triggering switch. One pulse generator operated the laser with a flash lamp and Q switch signal at 12.5 Hz, (the free run frequency of the laser), the second connected via a trigger switch was set to external trigger. The second delay/pulse generator operated the injector and camera at the required timings for the test and used the previous Q Switch pulse such that the injector may be triggered prior to the laser pulse, Figure 4.4 shows a schematic diagram of the set-up while Figure 4.5 shows the timing sequence.

The single shot testing was carried out at the same two fuel pressures as for the initial high speed imaging, 5 and 10 MPa. The problem of the dense fuel spray at higher back pressures again restricted the testing to 50 and 100 kPa back pressure. To provide a suitable average image during the steady state period of the injection event, ten images were obtained at 1.5 ms ASOF for all of the test conditions.

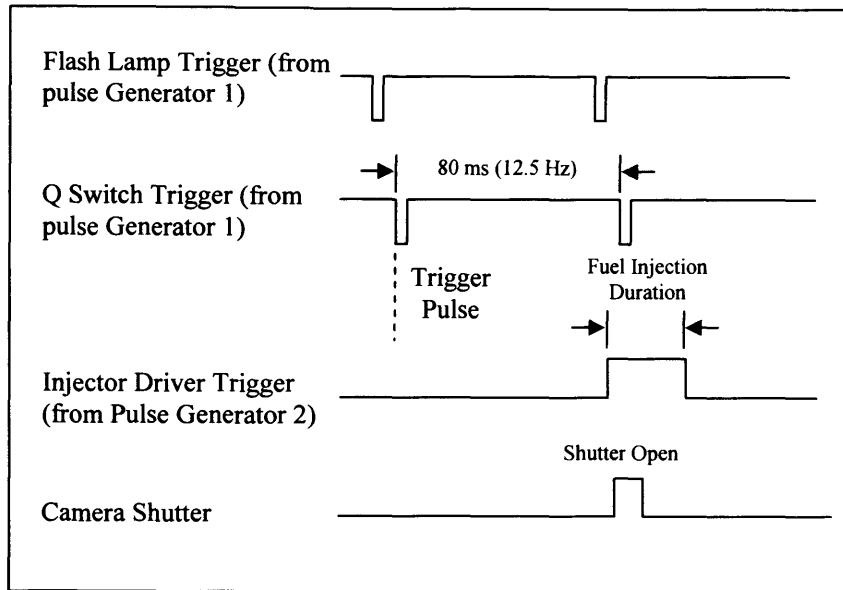


Figure 4.5 – Schematic of the Timing Sequence for the Single Shot Imaging

4.4 Analysis of Photographic Results

4.4.1 Analysis of Global Imaging

The sequences of images obtained from the global photographic tests were analysed to give an overall understanding of the spray characteristics. It was first necessary to process the images so that consistent measurements could be made under all conditions.

4.4.1.1 Image Analysis

A number of measurements were taken using the injector tip as a scale. The maximum penetration of the spray was measured using an automated process. The process is a macro that was developed by the author within the image processing package, Image Pro Plus, see Appendix II for the macro program code. Not only does this save time in analysing the large number of images produced, it also removes any subjective error that may arise with human measurements. Obviously this allows for reproducible measurements, which are therefore consistent throughout the test matrix.

The first step of the procedure was to threshold the image to obtain a 1 bit image from the 8 bit original image. This procedure set the pixels below the

threshold value to black and the remaining pixels to white, see Chapter 3 for a more detailed explanation of the thresholding process. The decision on the threshold value was determined by the amount of background noise, from reflections off of the chamber wall etc. In general the initial images, a short period after the start of fuel (ASOF), and at higher back pressures, had a far greater amount of noise due to less fuel being present to scatter the light. In this condition the threshold value was set to be an arbitrary value of the mean grey level plus one standard deviation. This value was chosen subjectively, however it was not a constant parameter, but varied with each image depending on the light levels, the amount of fuel present, etc. For the less noisy images the threshold value was set to be simply the mean grey level value.

Grimaldi *et al.* [2000], Araneo *et al.* [2000], Schmitz *et al.* [2002] and Kim *et al.* [2001], among others, have all reported methods for determining spray boundaries. Two differing methods are reported by these authors, Araneo *et al.* [2000], set the threshold value to be 10 (out of the 256 grey levels of an 8-bit image). Pixels below this value were considered to be background. Thresholding the images in this manner may lead to errors as the lighting will change depending on the amount of fuel in the image. Therefore if the lighting changes the grey level of the background will change, such that too much or too little of the image is set to be background. However, the majority utilise a technique similar to that presented here, whereby the threshold level is set subjectively to be a percentage of the dynamic range. The threshold level will therefore change depending on the image.

Once the thresholded image was obtained, the penetration was found by row-by-row analysis of the image starting from the bottom up. For each row the number of white pixels was obtained, this is based on an algorithm described by Grimaldi *et al.* [2000]. The criterion for furthest penetration was defined as follows; if, for ten consecutive rows the row contains nine or more pixels of fuel, then the tenth row is deemed to be the tip of the spray penetration. Again

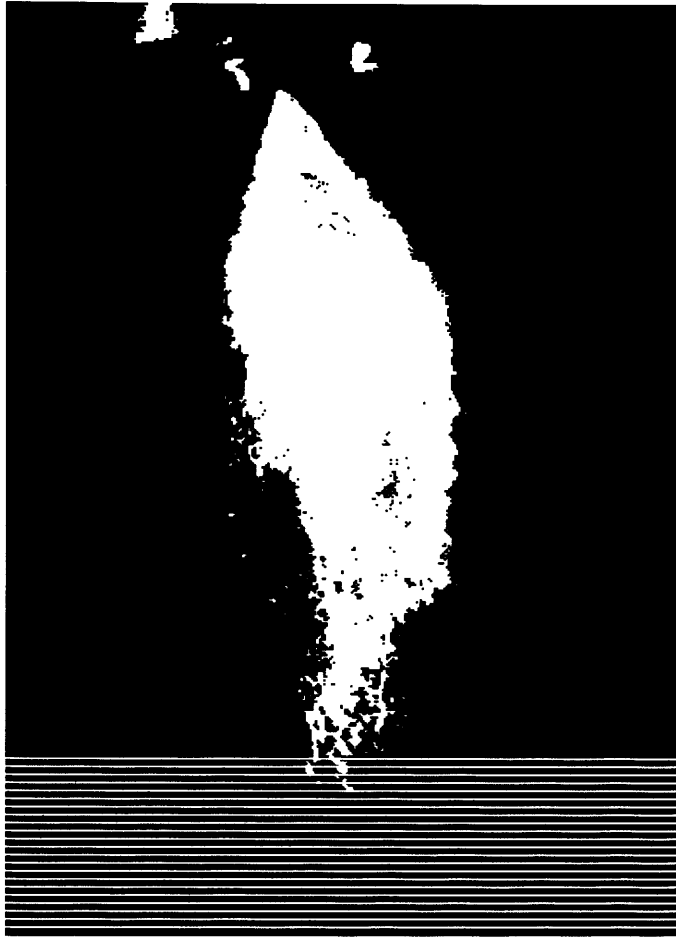


Figure 4.6 – Automated penetration measurement on a 1-bit image

these values, (ten rows, nine pixels) were found subjectively, the values were chosen such that if made any smaller they would produce false and inconsistent results. However, if they were larger then the penetration would not be accurately described, as the analysis would proceed too far into the spray. This technique may be seen in Figure 4.6. Araneo *et al.* describes a different technique for obtaining the penetration of the fuel spray. An image intensity profile along the spray axis, averaged over the spray width was measured. The spray tip penetration was assumed to be where the intensity profile fell below 10% of its maximum. This was not used because it may provide false results when analysing noisy images.

A similar method for obtaining the cone angle was utilised. The cone angle was calculated at both 5 and 10 mm axial distance from the injector tip along the axis of the spray, to obtain both the emerging and fully developed cone angles. The spray edge was found through column-by-column analysis,

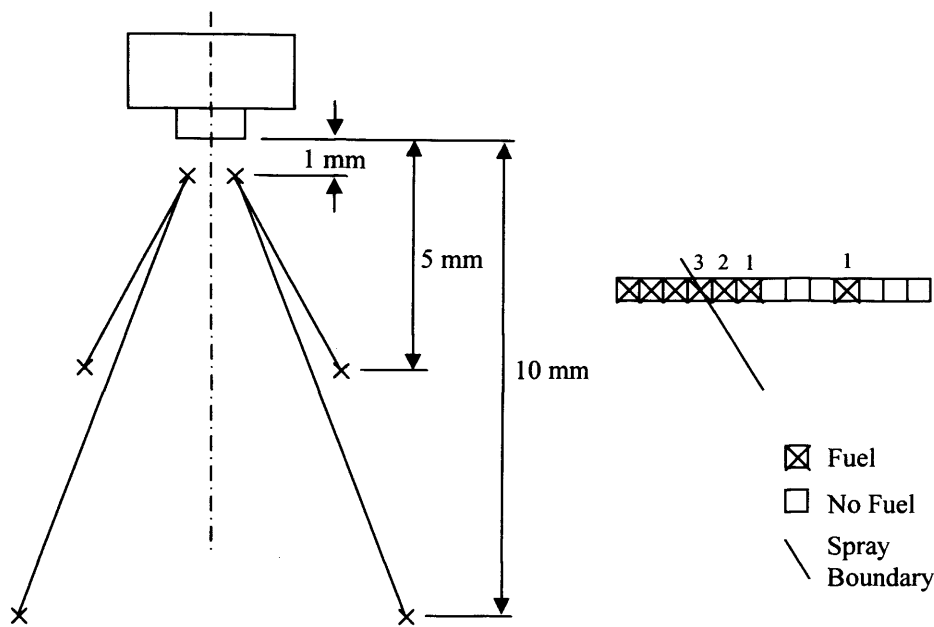
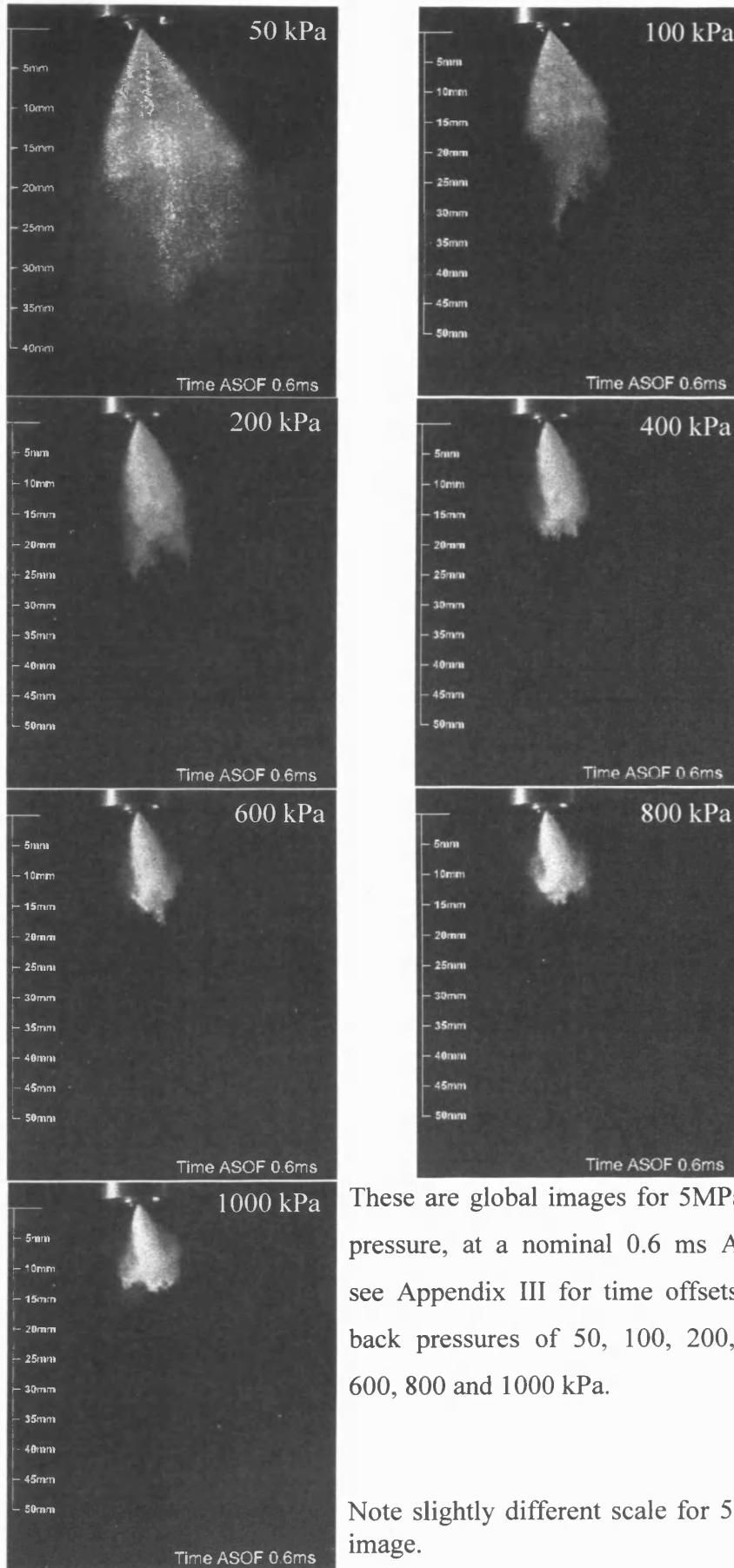


Figure 4.7 – Schematic diagram defining the ‘root’ of the spray cone angle measurement and the boundary recognition process

starting from both the left and right hand sides of the image. The number of consecutive pixels required to define the edge was altered depending on the distance from the injector tip. At 1 mm from the tip, (to find the cone angle at 5 and 10 mm a starting point is required for both edges of the spray), when three consecutive pixels are counted this is deemed to be the edge of the spray, this may be seen in Figure 4.7. However as the distance from the injector tip increases, the amount of small droplets on the periphery of the spray increases. These are not actually part of the main body and therefore should not be used in the calculation of the cone angle. Therefore at 5 and 10 mm the number of consecutive pixels required is five and eight respectively.

4.4.1.2 Global Imaging Results

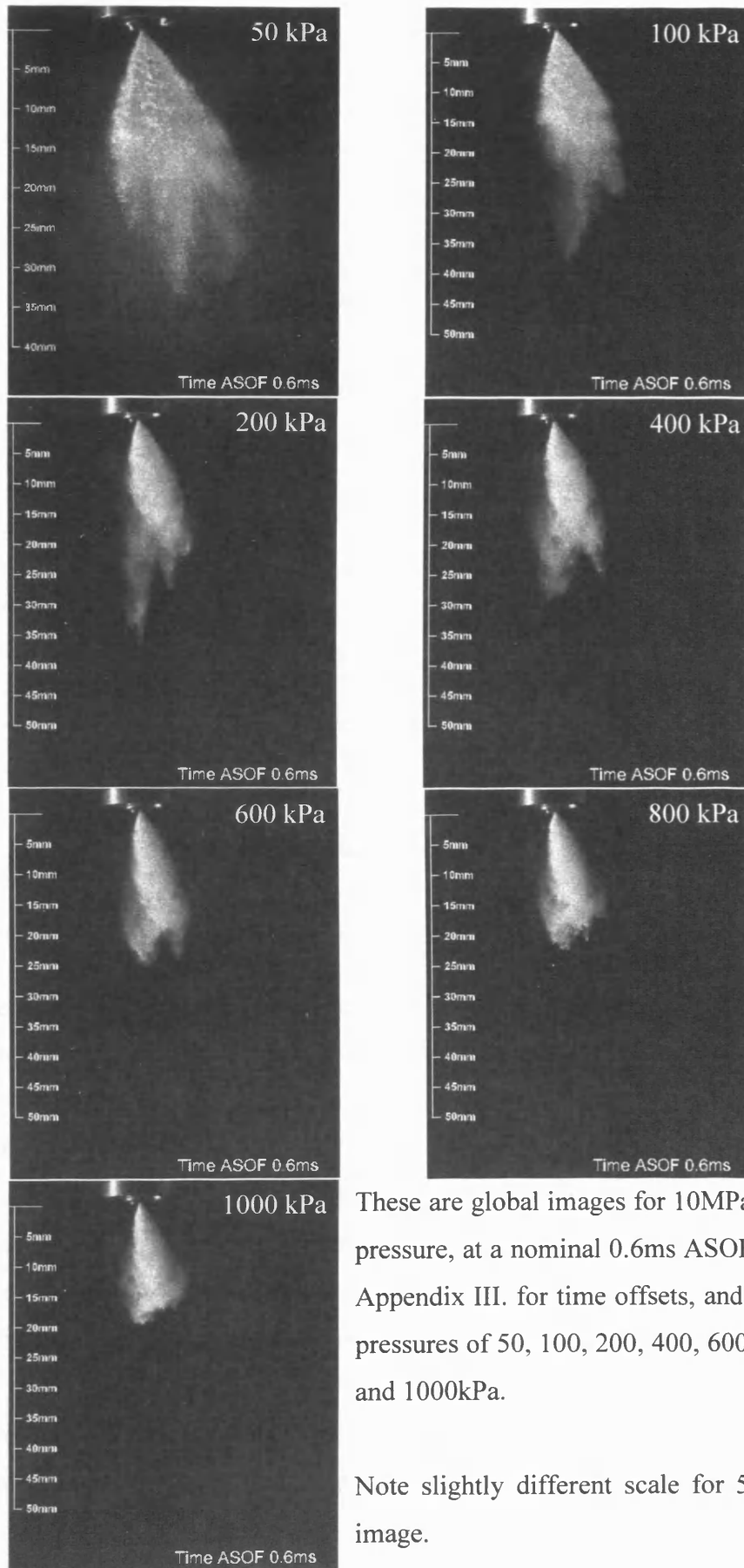
The fixed interval imaging process dictates that there is no knowledge of the precise time, after the start of injection (ASOI), when fuel appears. The only knowledge of timing is when fuel is first seen, so $t \leq 0$ ms at the last image with no visible fuel. Since the time difference between images is 0.1 ms, the fuel may appear at any time between the last image with no visible fuel and the first image with visible fuel. To correct for this the initial velocity of the



These are global images for 5MPa fuel pressure, at a nominal 0.6 ms ASOF, see Appendix III for time offsets, and back pressures of 50, 100, 200, 400, 600, 800 and 1000 kPa.

Note slightly different scale for 50 kPa image.

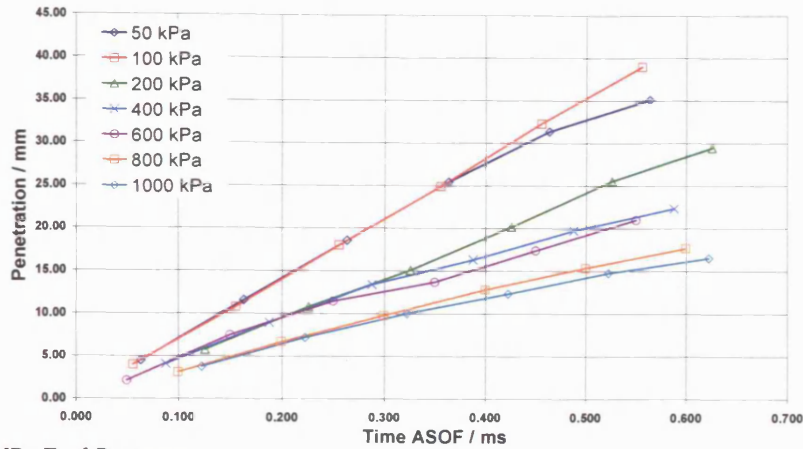
Figure 4.8 – Global Imaging Results, 5 MPa fuel pressure



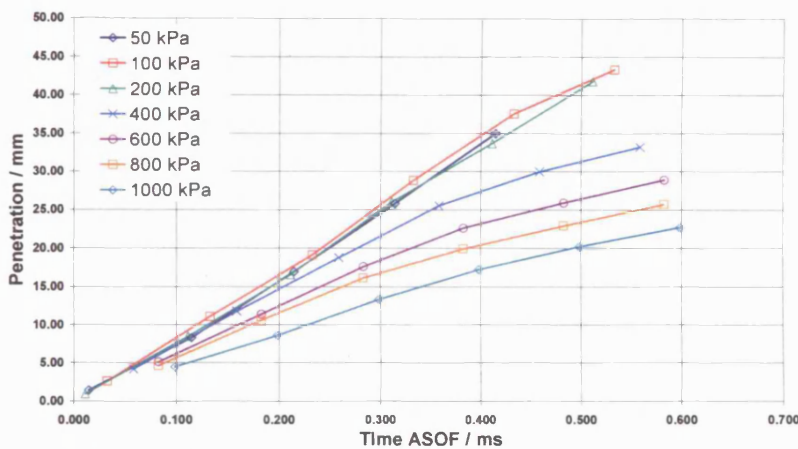
These are global images for 10MPa fuel pressure, at a nominal 0.6ms ASOF, see Appendix III. for time offsets, and back pressures of 50, 100, 200, 400, 600, 800 and 1000kPa.

Note slightly different scale for 50kPa image.

Figure 4.9 – Global Imaging Results, 10 MPa fuel pressure



(a) 5 MPa Fuel Pressure

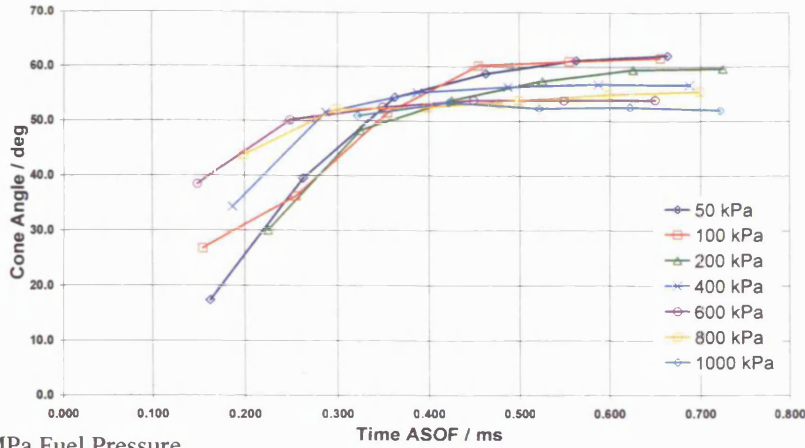


(b) 10 MPa Fuel Pressure

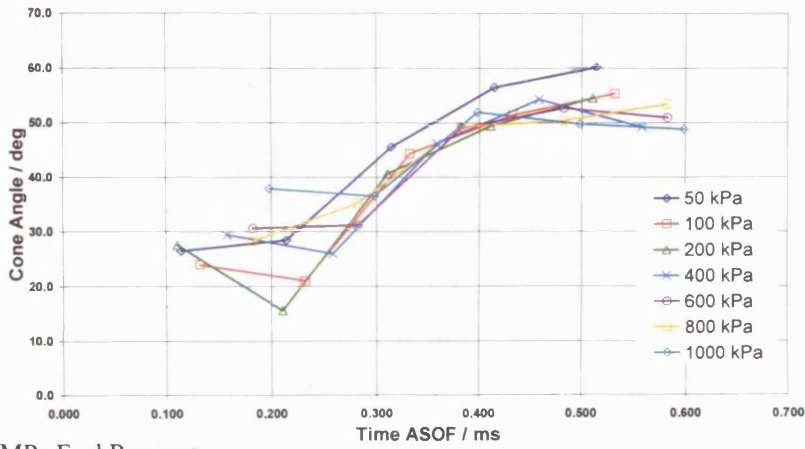
Figure 4.10 – Axial Spray Penetration; (a) for 5 MPa fuel pressure and (b) for 10 MPa fuel pressure, for Injector A

spray is calculated using a linear best fit line, calculated using the least squares method, for the first three data points. This line can then be used to find the time offset required to force the line through the origin, i.e. at $t = 0$ ms, penetration = 0 mm, and for any time $t > 0$ ms, penetration > 0 mm. This ensures that the data from different injection events is comparable; see Appendix III for time offsets for images in Figures 4.8 & 4.9 respectively.

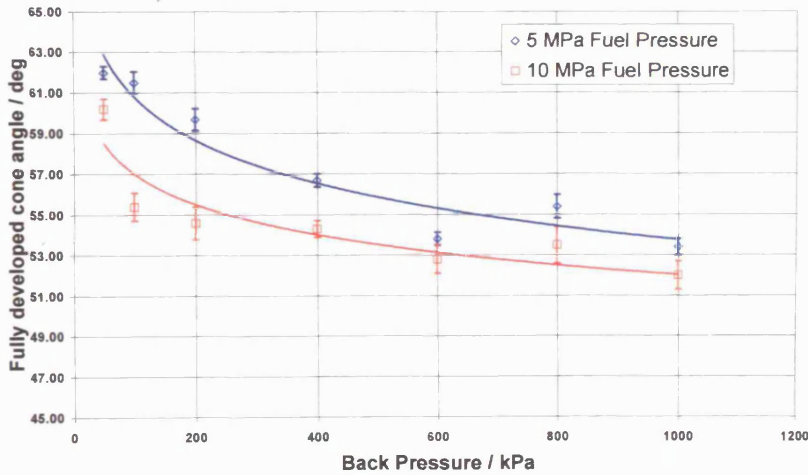
Observing Figure 4.10 it can be seen that the penetration rate with 10 MPa fuel pressure is higher than that for 5 MPa, the penetration rates found here were 70 m/s and 84 m/s respectively at atmospheric back pressures. Comparing these results to other published data, shows that these penetration rates are normal, Ledoyen *et al.* [1999], found that for 5 MPa fuel pressure the penetration rate was in the region of 65 m/s depending on the injector used, for



(a) 5 MPa Fuel Pressure



(b) 10 MPa Fuel Pressure



(c) Effect of back pressure on fully developed cone angle

Figure 4.11 – Spray Cone Angle (@ 10 mm from tip); (a) for 5 MPa fuel pressure, (b) for 10 MPa fuel pressure and (c) the effect of back pressure on the cone angle. Bars show ± 1 S.D. indicating fluctuations in results.

similar conditions Nouri *et al.* [2001] found the penetration rate to be 50 m/s, while Lee *et al.* [2001], found the penetration rate to be approximately 45 m/s. For the larger fuel pressure of 10 MPa, the published results are also similar to those found here, Williams *et al.* found the penetration rate to be 92 m/s for a comparable injector. The larger penetration rate caused by the higher fuel injection pressure, induces a greater pressure difference across the sheet. Therefore the higher fuel pressure causes the spray to collapse more, this is especially evident at 100 kPa back pressure. Figure 4.11 shows that the spray collapses to a critical point, as shown by Williams *et al.* [2001] at which the spray collapses no further. For 5 MPa fuel pressure this occurs at a back pressure between 400 kPa and 600 kPa. The corresponding point with 10 MPa fuel pressure occurs at a back pressure between 200 kPa and 400 kPa. These points also correspond to the back pressures that cause the spray to become too dense to obtain near field images successfully. It can be seen that the higher fuel pressure causes the pre-spray penetration to increase, Williams *et al.* [2001]. The pre-spray is the fuel from the sac-volume of the injector that exits the nozzle with no tangential velocity. With no tangential velocity the axial velocity is increased, therefore the sac-volume can be seen to travel at a greater velocity than the main spray. The spray penetration for the images presented in Figures 4.8 & 4.9 is defined as that of the pre-spray. The pre-spray may be seen in these images as being the area of fuel that is separated from the main body of the spray. It can also be seen that the amount of pre-spray present decreases with increasing back pressure.

Note that whilst the images provide useful information on the global behaviour of the spray, images at a much higher magnification are required in order to understand the initial break-up mechanism in the region close to the injector tip. However the information concerning the penetration rate and cone angle of the spray with varying back pressure will be utilised in the spray models. The data for the initial spray development can be seen in Figures 4.10 and 4.11.

4.4.2 Analysis of Near Field Imaging

The spray could now be viewed in sufficient detail to be able to see holes forming in the otherwise continuous conical sheet. Magnification of these images (see Figure 4.12) suggests that the holes in the sheet are initially ‘empty’ and do not contain droplets. As the distance from the injector tip increases, the holes are observed to fill with droplets as the remaining liquid sheet disintegrates. This break-up process will be discussed in more detail later in this chapter.

The sequences of images obtained from the near field photographic tests were analysed using a novel ‘void fraction’ technique. This technique processed the images to find the proportion of spray that was holes, i.e. the ‘void fraction’, in an attempt to identify a break-up length.

4.4.2.1 Void Recognition Program

The void fraction technique commenced with the identification of an area of interest (AOI) in the near field image. Care was taken to ensure the AOI is completely in focus. As the fuel spray being imaged was curved surface a proportion of the spray would be out of focus unless the DOF is large enough to incorporate the entire spray width. As can be seen in Figure 4.12 for this study the optics were focussed on the centre of the spray. This enabled the spray break-up process to be studied. However, the DOF was not large enough to incorporate the entire spray width, therefore the edges were out of focus. Although the edges were out of focus, obtaining the edge profile was possible, with the caveat that no quantitative measurements could be taken outside the area in focus.

The Custom written macros within the image processing software, Image Pro Plus, were used to perform the analysis, see Appendix II for the macro program code. Once the AOI was selected it was copied as a new image so that it could be processed as its own entity. This processing involved thresholding, erosion and dilation. Then a counting process was used to count

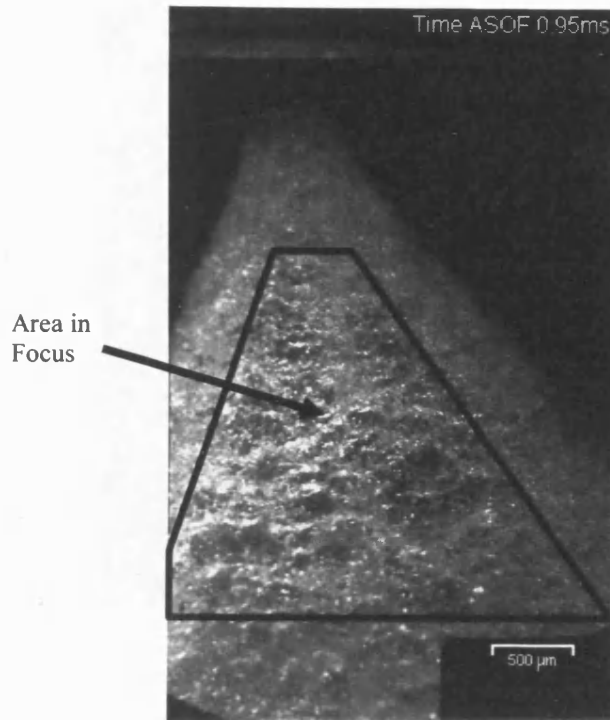


Figure 4.12 – Example of Area within a near field image that is ‘in-focus’

the number of holes, this was an in built function within the image processing software.

The thresholding process was similar to that of the global imaging analysis. Firstly a best fit algorithm was applied to the AOI. The results were achieved by stretching the histogram to achieve the best possible contrast distribution of pixel values in AOI, the bottom 3% of the values were assigned to the shadow point, (0) and the top 3% of the values to the highlight point (255), for an 8 bit image. The rest of the values were distributed evenly across the scale. The AOI was then thresholded to give a 1 bit image, the threshold point was set to be the mean pixel value minus 12% of the mean, this value was obtained subjectively to achieve the best results for these images.

After thresholding, the erosion algorithm operated by removing any white pixels that were not surrounded entirely by white pixels, thus the edges of holes and any drops were eroded, this had the effect of removing noise from within the AOI, allowing for a more accurate hole count. The erosion process on its own would cause errors in the area calculation, therefore following the erosion, a dilation algorithm was used. This had the opposite effect, so added

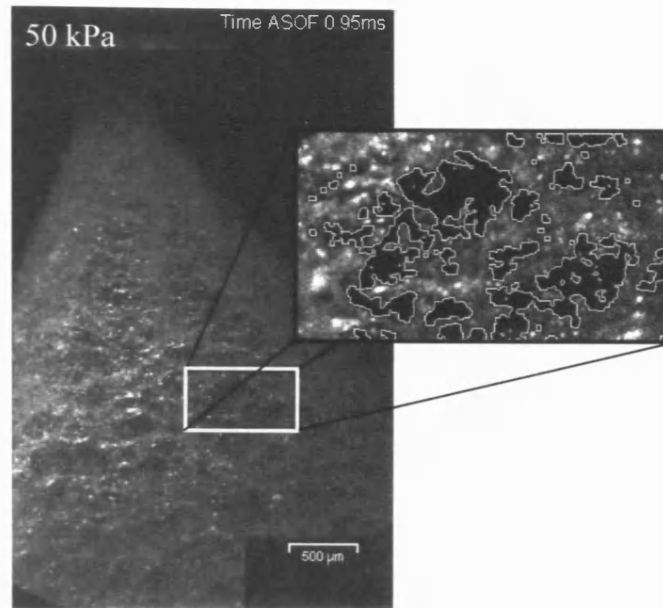


Figure 4.13 – Example of void recognition program for 5 MPa fuel pressure.

white pixels where black pixels were not entirely surrounded by black pixels. Thus the net outcome of these two algorithms, as long as they were both performed in the same manner, was that any small droplets etc would have been removed. This was due to the erosion process completely removing them, and so as the dilation process had no knowledge of them they would remain removed, while the hole edges would be dilated back to their original size. The final process was to count and size both the hole area and the AOI area, so that a void fraction could be calculated, see Figure 4.13 for an example of the void recognition process. The data obtained from the void recognition process was averaged over the steady state spray condition for each condition. The steady state period of the spray was determined to be from the point just after the cone angle had fully developed to when it began to break down again.

The macro written within the image processing software, required the user to identify the centre of the injector tip, this was then used as the datum for all future measurements. A flow diagram outlining the main procedures within the void recognition program may be seen in Figure 4.14. The first AOI was chosen to be 0.9 mm from the injector tip to the centre of the AOI, as this was approximately where the images came completely into focus. The height of

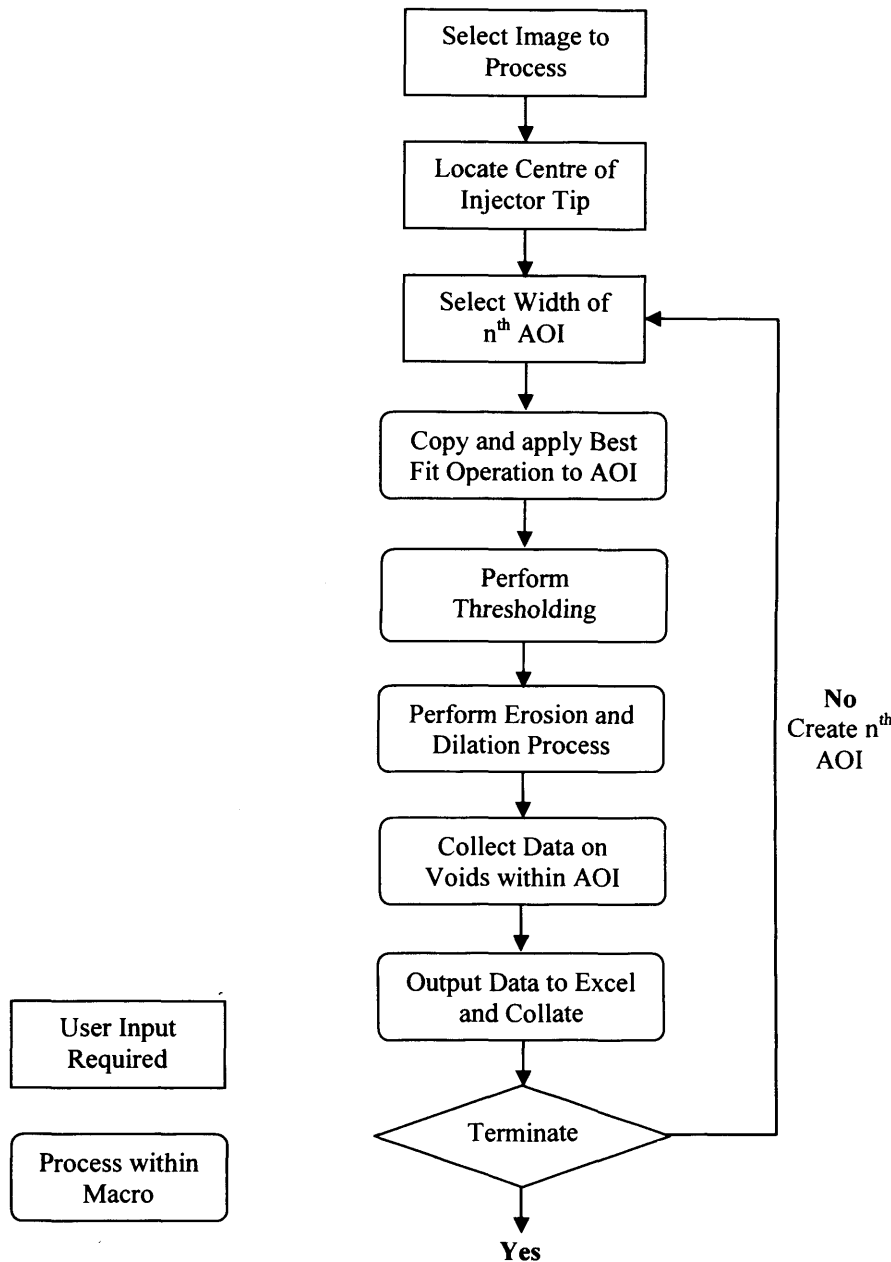


Figure 4.14 – Flow diagram of Void Recognition Program Procedure

the AOI was user definable so a selection of heights was tested to obtain the best results. It was found that for 0.5, 0.25 and 0.1 mm the results were very similar, see Figure 4.15. Observing the plot for an AOI height of 0.1 mm it can be seen that the trend line oscillates about the other lines, this is because the holes are non-uniformly distributed, see Figure 4.13. Therefore some of the AOI's will fall on sections that have a smaller void fraction than the surrounding areas. To reduce the effect of falling in between holes, and to reduce processing time an AOI height of 0.5 mm was chosen, as there was little difference to the overall trend between 0.5 and 0.25 mm. The first AOI

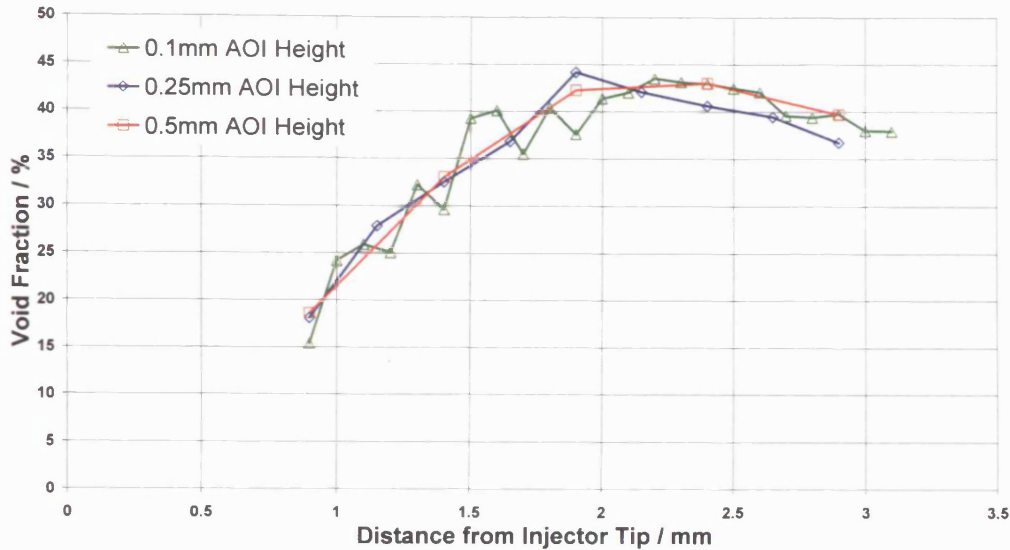


Figure 4.15 – Plot to show effect of AOI height for typical image analysis.

immediately precedes the next, therefore the second AOI had a centre at 1.4 mm for an AOI height of 0.5 mm, and so on. This gave five AOI's covering the entire spray, and therefore five points on the plot.

4.4.2.2 Sheet Break-Up Theory

Using the data obtained from this process the void fraction could be plotted against distance from the injector tip. This showed the profile of how the spray breaks up, see Figure 4.15, firstly by forming holes then the holes are filled with liquid droplets. This break-up process is known as perforated sheet disintegration, Fraser *et al.* [1953], whereby point disturbances on the sheet produce holes. These holes grow, producing ligaments, as they coalesce these ligaments then break-up into droplets.

The hollow cone produced by the pressure-swirl atomiser due to conservation of mass has a sheet thickness that thins as the sheet progresses along the injector axis. Waves that form on the sheet propagate along its length; two forms of wave are possible, sinuous waves, where the two waves on the inner and outer surface oscillate in phase, and dilation waves, where the two waves are out of phase, Lefebvre [1989]. The dilation waves may be neglected since their degree of instability is always less than that of sinuous waves, Fraser *et al.* [1962]. Due to non-uniformities in the sheet thickness, some points will

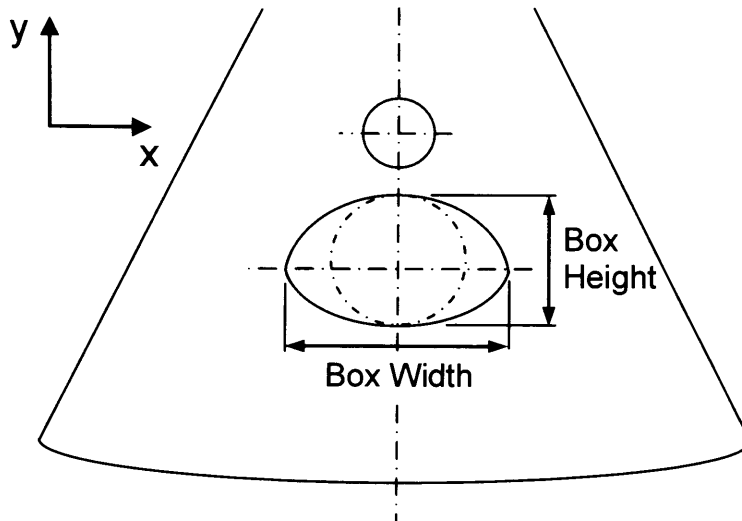


Figure 4.16 – Consecutive positions of one perforation. Detailing the effects of the expanding sheet on the hole shape.

perforate causing holes. These holes will expand due to unbalanced surface tension forces if their diameter is greater than the sheet thickness. Schmidt *et al.* [1999], present results of a mathematical analysis of the sheet profile. These results show the initial thickness of the fuel sheet to be approximately 0.2 mm, reducing to 0.05 mm 2.5 mm from the injector tip. Therefore any disturbance greater in diameter than these values will lead to a growth in the hole diameter. If the hole were on a flat sheet that was not itself expanding then these holes would be circular and expand uniformly. However the spray surface itself is expanding along one axis, therefore the holes will expand at a greater rate along the x axis, see Figure 4.16.

4.4.2.3 Shape of Perforation

The analysis performed on the captured images was twofold. Firstly the void fraction was assessed, and secondly the shape of the perforations was examined. The macro used to perform the ‘void fraction’ analysis also gave data on the dimensions of the holes as well as their area. The characteristic dimensions were measured, i.e. the major and minor dimensions of the hole, defined here as the box width and box height respectively. This gave a method of verifying the expansion of the measured holes due to the sheet surface area growth, which also confirmed the applicability of the perforated sheet theory. Equation 4.1 gives the ‘width’ of a hole solely through being stretched due to the sheet area growth.

$$w = \frac{(H + r_{inj} \tan \theta)w_0}{H + r_{inj0} \tan \theta} \quad \text{eq. 4.1.}$$

Where w is the width of the hole in the sheet, r_{inj} is the injector hole radius, and H is the distance of the hole in the sheet from the injector tip. This is a simplified model that assumes a linear progression of the external surface from the spray tip. In reality the initial expansion of the spray will be non-linear and dependant on nozzle geometry. The expansion caused simply by the sheet growth will not cause any holes to coalesce and form ligaments. This is because although the holes will expand due to the increasing surface area of the sheet, they are also moving further apart due to the increasing diameter of the spray cone. Therefore this expansion must be taken away to obtain the growth rate of the hole due to surface tension forces alone. This is accomplished by simply calculating the growth rate due to the expansion of the fuel sheet and subtracting it from the measured growth rate. The hole sizes will also be affected by aerodynamic forces, non-uniformities in the fuel, atomisation and evaporation etc.

Observing Figure 4.17 it can be seen that initially the simple prediction of growth taking into account the increasing diameter of the spray cone underestimated the measured hole width. The first point is equal as data upstream is required to predict the width. This is due to alternative growth caused by the uneven surface tension forces. However the amount that it under predicted the hole width reduced with distance from the injector tip.

The box ratio given by box width / box height is plotted in Figure 4.18 for varying back pressure and fuel pressure. The plot only shows the data from the first three AOI's as these are the points that corresponded to an increasing void fraction, and therefore the holes were still expanding and the spray had not as yet undergone any significant atomisation.

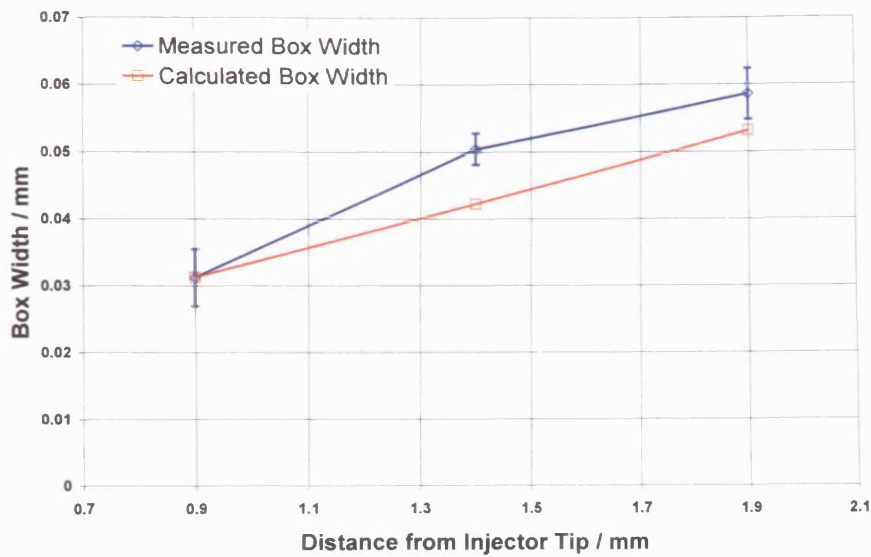


Figure 4.17 – Box Width versus Distance from injector tip, a comparison of calculations to measurements. Bars show ± 1 S.D. indicating fluctuations in results.

It can be seen that all of the conditions produced an almost linear relationship between box ratio and distance from the injector tip. However the gradient of the lines and therefore the growth rate of the holes did vary with back pressure and fuel pressure. The steeper the gradient of the line the more skewed the hole that it represents will be, thus relatively the expansion due to the sheet area growth becomes more prominent. Therefore the cone angle of the spray should affect the box ratio, which can be seen, since the difference in gradient between the lines for 50 kPa and 100 kPa back pressure were negligible, as were their respective cone angles, see Figure 4.11. However increasing the back pressure to 200 kPa had a significant effect on the cone angle and therefore reduced the gradient of the box ratio. Increasing the back pressure from 50 kPa to 100 kPa, i.e. sub-atmospheric to atmospheric, for both fuel pressures tested, increased the box ratio without affecting the gradient significantly. This may have been due to increased aerodynamic effects, acting to reduce the amount of rotational swirl on the spray sheet as the spray progressed. Therefore not only will the holes be skewed by the increasing spray sheet area, they will also be twisted by the reduction in swirl with increasing distance from the injector tip.

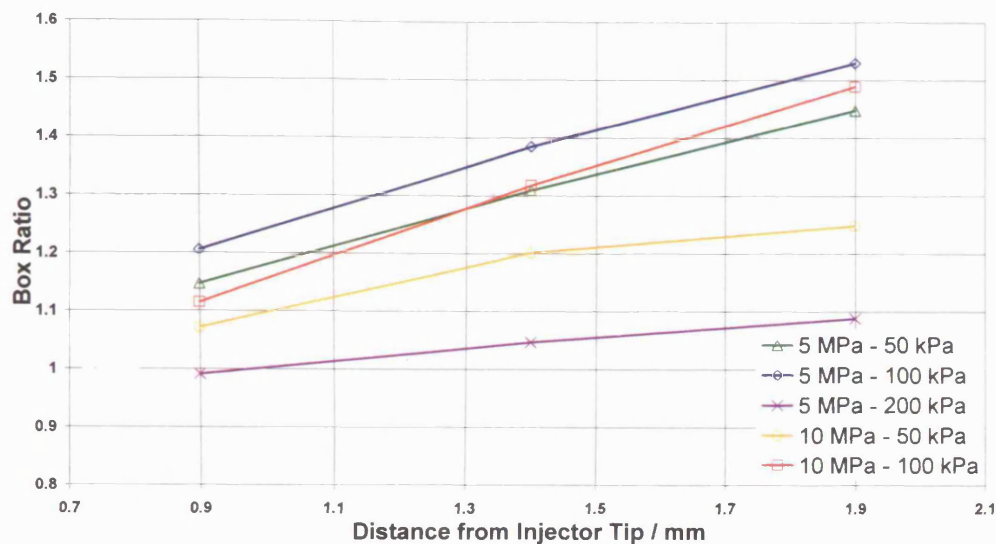


Figure 4.18 – Box Ratio versus Distance from injector tip, for varying back pressure and fuel pressure.

4.4.2.4 Void Fraction Analysis

The void fraction analysis removed small singular droplets from within each void. Consequently as the distance from the injector tip increased the void fraction was seen to increase. However, once the number of droplets contained within a void became so large that they began to overlap, the void fraction analysis no longer removed them and treated them as part of the liquid sheet. Consequently as the sheet breaks up the void fraction will increase, to a point, at this point the ligament break up into droplets will begin to dominate the break up process. Thus, the holes will begin to fill with droplets, decreasing the void fraction until the spray has completely broken-up (where the entire spray will be droplets and there will be no holes). This can be seen in Figure 4.19.

A break-up length can be defined as the distance from the injector tip at which the gradient of the lines in Figure 4.19 changes from positive to negative. This figure shows that for increasing back pressure the break up length decreases, and for increasing fuel pressure the break-up length decreases. This agrees with the break-up theories proposed by, Han *et al.* [2001], Ren and Nally [1998] and Schmidt *et al.* [1999], see equations 4.2 – 4.4, respectively, though the actual distances differ.

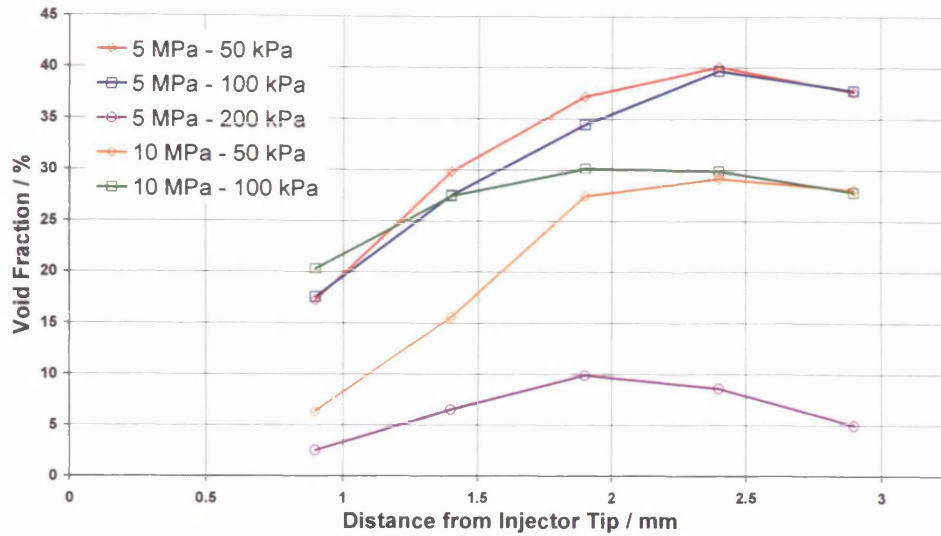


Figure 4.19 – Void Fraction versus Distance from injector tip, for varying back pressure and fuel pressure for Injector A.

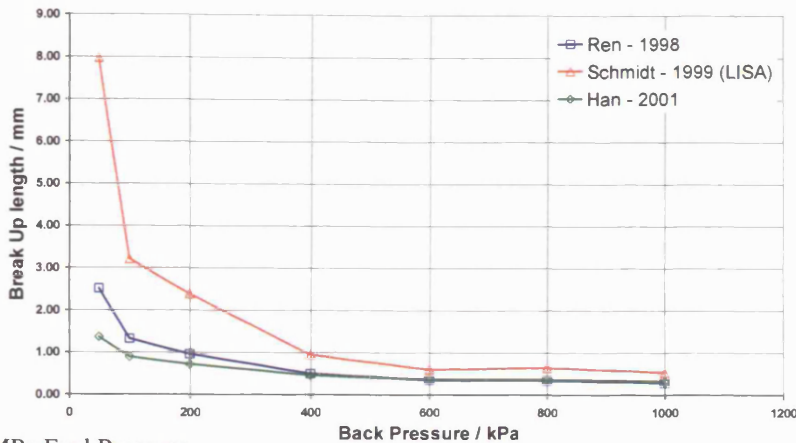
$$L = D \left[\frac{\rho_l \sigma h d_0}{\rho_g^2 U^2 \tan \theta} \right]^{1/3} \quad \text{eq. 4.2.}$$

$$L = C \left[\frac{\rho_l \sigma h \cos \theta}{\rho_g^2 V_r^2} \right]^{1/2} \quad \text{eq. 4.3.}$$

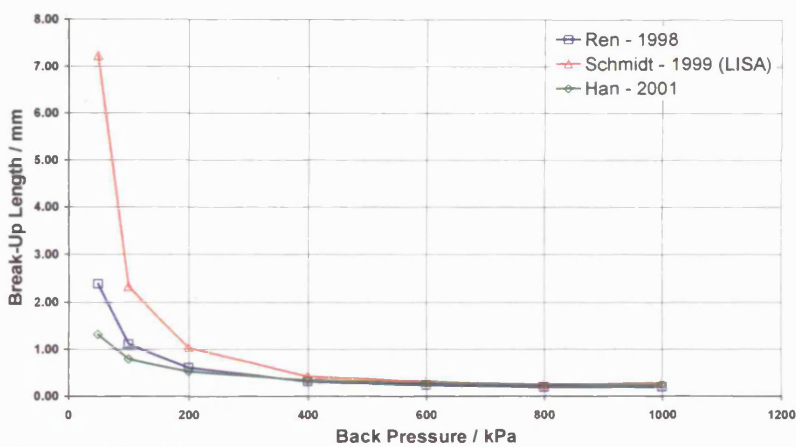
$$L = \frac{U}{\Omega} \ln \left(\frac{\eta_b}{\eta_o} \right) \quad \text{eq. 4.4(a)}$$

$$\omega_r = -2v_l k^2 + \sqrt{4v_l^2 k^4 + QU^2 k^2 - \frac{\sigma k^3}{\rho_l}} \quad \text{eq. 4.4(b)}$$

The break-up models of Han, Ren and Schmidt were used to calculate the break-up lengths for the injector used in this work, using input data from the global imaging. The plot of the break-up length with varying back pressure can be seen in Figure 4.20. This shows that the Han and Ren models give very similar results throughout, however the initial stages of the Schmidt model show a much longer break-up length, but then converges towards the other two models. Observing Figures 4.21 and 4.22, it can be seen that at the point



(a) 5 MPa Fuel Pressure



(b) 10 MPa Fuel Pressure

Figure 4.20 – Plot to show Break-Up Length versus Back Pressure for the three models studied. (a) for 5 MPa fuel pressure and (b) for 10 MPa fuel pressure.

that these models predict that break-up would have occurred, a perforated fuel sheet was still visible. It was shown that the models consistently under predicted the break-up length. Further examples of the images shown in Figures 4.21 and 4.22 may be found in Appendix IV.

Observing the 200 kPa case in Figure 4.8 it can be seen that even at this relatively low back pressure the spray was already very dense. This restricted the amount of light available and therefore the aperture of the camera had to be opened fully, as mentioned earlier this reduced the DOF, this can be seen in Figure 4.12 where the area of fuel in focus is very limited, even for the low back pressure case. The higher fuel pressure of 10 MPa produced a denser spray as the spray breaks up earlier producing finer droplets than at the lower

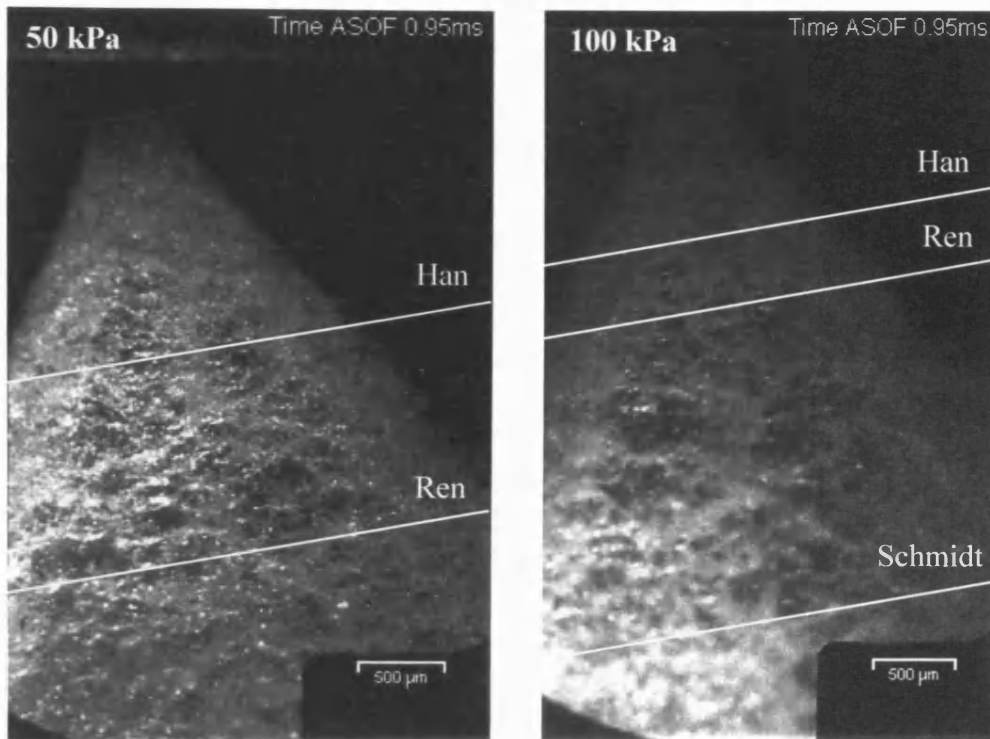


Figure 4.21 – Near field images at 5 MPa fuel pressure showing predicted break-up lengths from the Han, Ren and Schmidt models.

fuel pressure for at any given distance from the injector tip. Therefore the 200 kPa back pressure, could not be imaged successfully.

It is suggested that the reason for the discrepancy between the break-up length predicted by the models and that observed in the experiments is the extra fuel available due to the creation of the perforations in the liquid sheet. Conservation of mass dictates that the volume of fuel must remain constant. The experimental evidence suggested that the fuel was retained in the liquid sheet, rather than breaking up into droplets. This retained fuel will be available for the continuation of the liquid sheet, taking a toroidal form around the edges of the voids. As the voids are in close proximity to each other the toroids will link together producing a thicker sheet than that suggested by the models. However due to the irregular nature of the size and spacing of the holes, the toroidal structures will be irregular, with irregular ligaments, thus sections of the fuel sheet will have increased thickness. This thickening of the sheet will mean that more time is required for the sheet to thin and become unstable, than that predicted by the models.

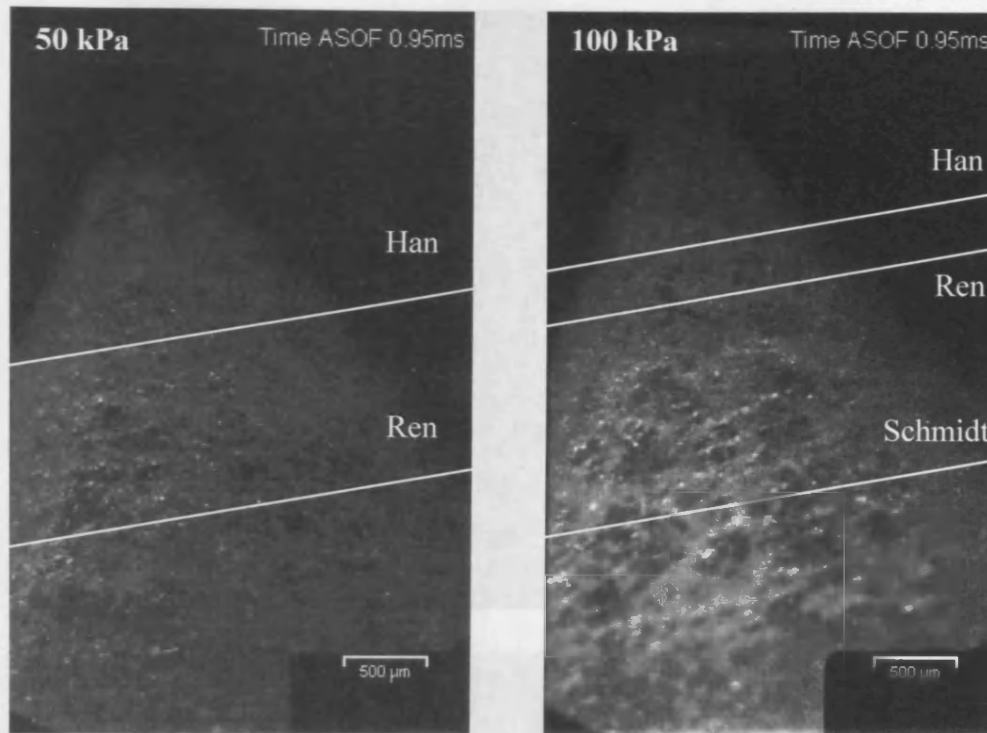


Figure 4.22 – Near field images at 10 MPa fuel pressure showing predicted break-up lengths from the Han, Ren and Schmidt models.

4.4.3 Analysis of Single Shot Imaging

The images taken in this series of testing had a similar FOV to the previous near field testing. In this case the FOV was positioned axially such that the top of the image was 1.05 mm from the injector tip. The FOV was set at this position to provide data further from the injector tip than in the previous tests, however positioning the FOV further from the tip would locate the FOV entirely within the spray, therefore removing any reference point from within the image. This made it difficult to provide directly comparable results to the first tests. The overall field of view was approximately 5.5 x 4.4 mm with a resolution of 4.3 μm / pixel. This is approximately half the resolution of that obtained using the HSRDC in the previous series of near field imaging. Therefore the images are of a lower quality, further limiting the maximum back pressure where useable images may be obtained. Despite these limitations, these images were quicker to obtain than those captured with the HSRDC and provided an opportunity to extend the void fraction analysis.

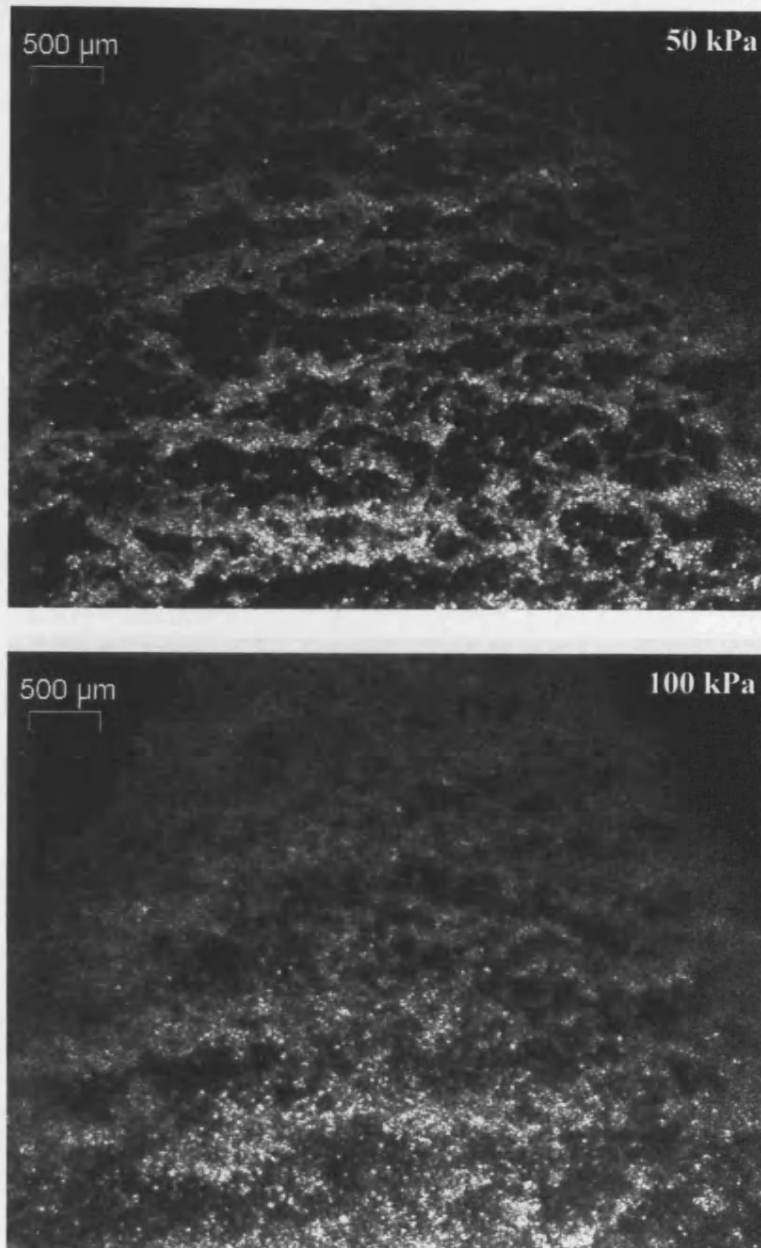


Figure 4.23 – Single shot images at 5 MPa fuel pressure at both 50 and 100 kPa back pressure for Injector B.

Observing Figures 4.23 and 4.24 it can be seen that the fuel spray emanating from Injector B breaks up in a similar manner to the previous pressure swirl injector, Injector A. It can be seen in Figure 4.24 that for the atmospheric back pressure case the spray is already too dense to allow the use of the void fraction analysis due to the limitations of the camera system. Therefore no quantitative information will be obtained from that test case. The void fraction analysis was carried out for the other three test cases shown in Figures 4.23 and 4.24, and these results were compared to those from the original series of



Figure 4.24 – Single shot images at 10 MPa fuel pressure at both 50 and 100 kPa back pressure for Injector B.

near field imaging. Further examples of the images shown in Figures 4.23 and 4.24 may be seen in Appendix IV.

The same void recognition program was used to analyse the images however it was adapted to account for the different optical system used. The threshold values used and the amount of erosion and dilation were altered as described in the following section.

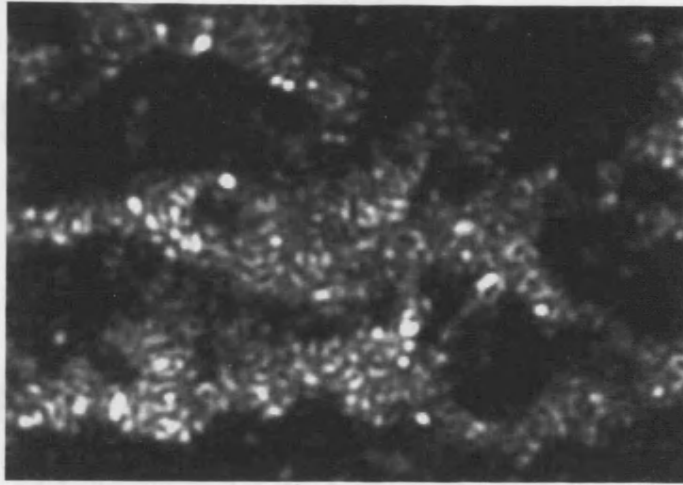


Figure 4.25 – Enlargement of a section of fuel spray to demonstrate the granular texture.

4.4.3.1 Thresholding and Erosion and Dilation Levels

The threshold level utilised for this series of testing was found to be more influential than for the first series of near field imaging. This may be due to a number of factors including the reduced resolution of the optical system reducing the ability to define the edges of holes. The lighting for this series of testing was also less uniform as the light source – a Nd:Yag laser @ 532 nm wavelength – has a greater light pulse energy, producing a larger gradient across the image. Observing Figure 4.25, an enlargement of a section of the fuel spray, it can be seen that it appears to be granular in texture. This leads to the threshold level being harder to define, especially at low light levels as the inter-granular light intensity can be similar to the hole light intensity. The granular texture is due to a combination of refraction and reflection from the liquid fuel sheet / droplets. This phenomena is utilised in a technique called Interferometric laser Imaging Droplet Sizing (ILIDS), as described by Golombok *et al.* [1998] and Kobayashi *et al.* [2000]. However in this technique the image is collected from a non-focal plane where fringes occur that may be measured to determine the droplet diameter. However when the image is obtained from the focal plane glare points occur, similar to those seen in Figure 4.25. The angle between the laser light and the fuel sheet was minimised to reduce this effect however it could not be completely eliminated.

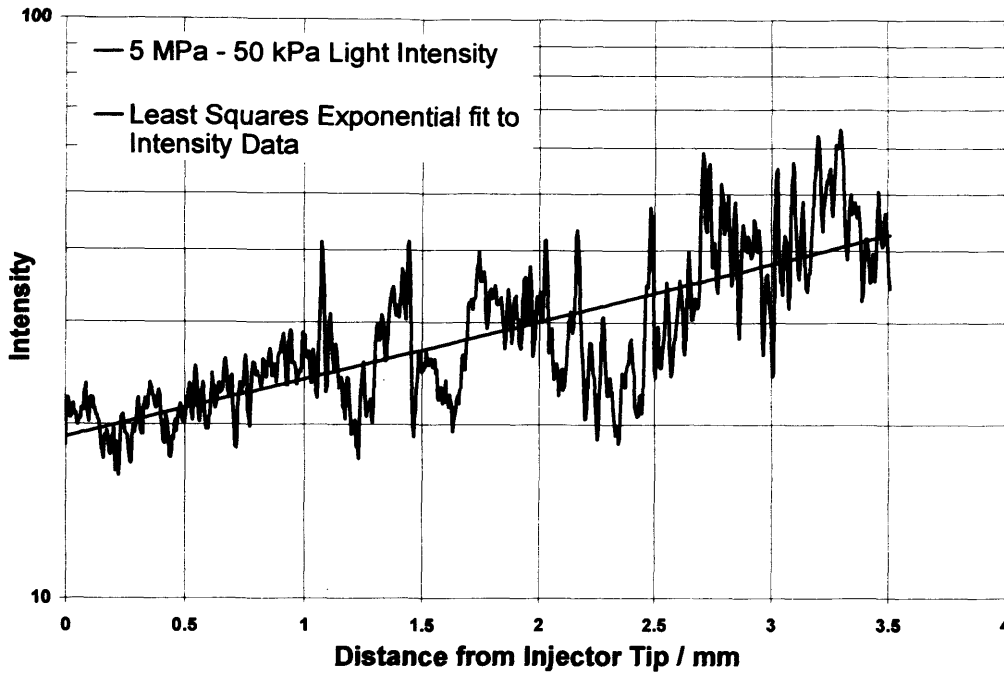
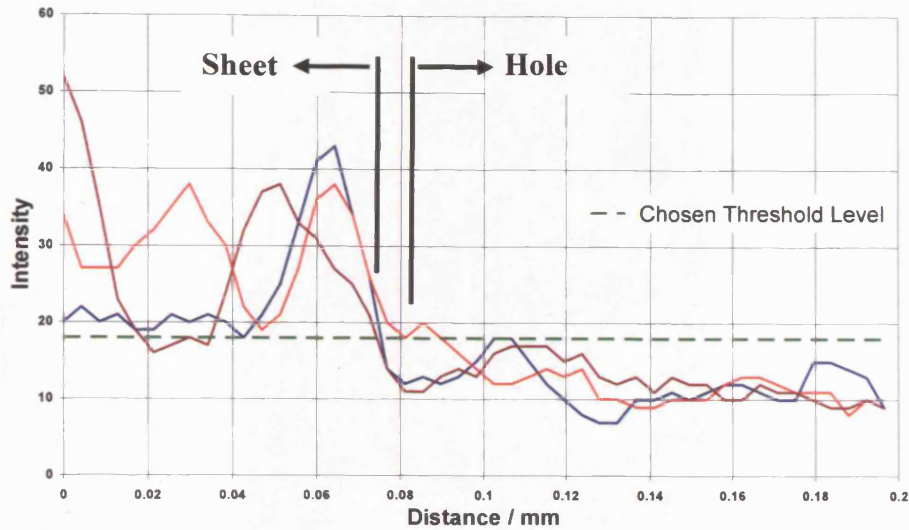
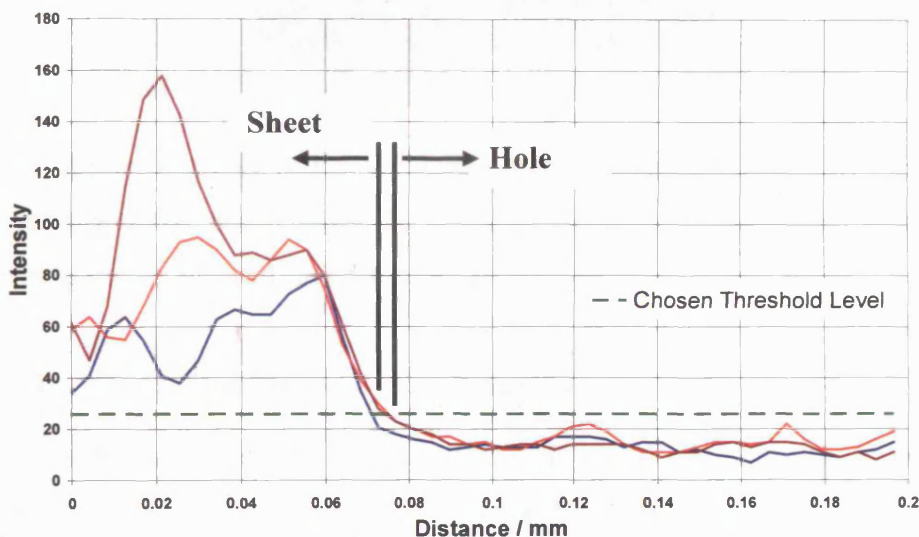


Figure 4.26 – Plot of light intensity variation along injector axis for single shot imaging.

The system used for defining the threshold level for each series of images at each AOI looked at the overall gradient in intensity across the entire image, and also at the gradient of intensity across individual holes at the first and last AOI's. Observing Figure 4.26 which is a plot of the light intensity variation with distance from injector tip, averaged over ten images and plotted on a logarithmic scale, (the origin being the top of the first AOI), it can be seen that there is an exponential relationship between light intensity and distance. An average is taken to minimise the effect of increasing void fraction with distance. This average was based on an intensity profile along a vertical line, using the average of several images means that the intensity is an average level of light and dark areas at a given distance. The profile remains spiky as a sample size of ten images is probably not large enough to eliminate all possibility of coincident holes at any given pixel location. Therefore, correspondingly the threshold level was varied exponentially along the injector axis. To obtain appropriate threshold levels it was necessary to look at the variation of light intensity across the edge of a hole, this variation may be seen in Figure 4.27 (a) and (b).



(a) First AOI



(b) Last AOI

Figure 4.27 – Plot of light intensity variation across the edge of a hole to allow the image threshold value to be determined. Different coloured lines represent hole edges from separate images.

The threshold level was chosen by observing the variation of light intensity close to the edge and assuming that the hole occurs at the point where the intensity rises sharply. A number of holes from separate images were observed at positions equivalent to both the first and last AOI's with an average value taken. The remaining threshold values for the AOI's in between the first and last were calculated using the assumption that they should vary exponentially between the two end points. The same process was used for all of the test cases. It was found that for all of the test cases there was an exponential distribution of the light intensity. However the first and last threshold levels

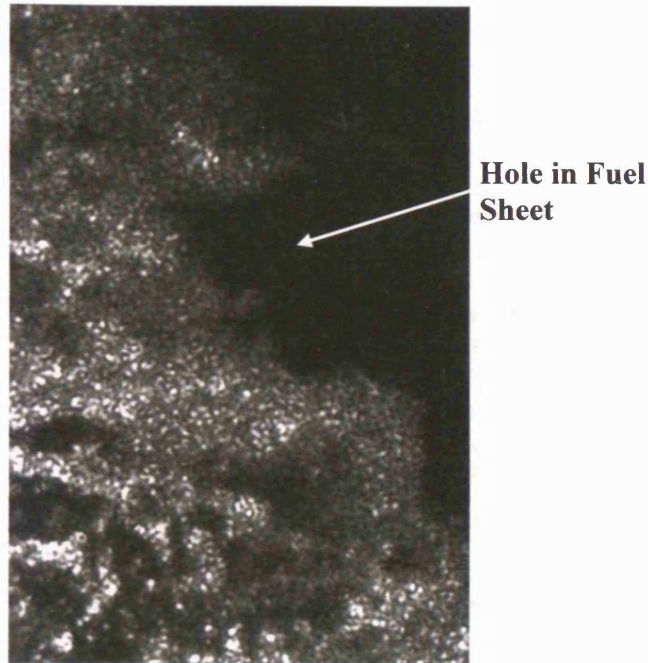


Figure 4.28 – Example of hole in fuel sheet shown in side profile for Injector B.

varied slightly between test cases due to differences in lighting, void fraction etc. The adapted macro may be seen in Appendix II together with the threshold values utilised for each separate test case.

4.4.3.2 Void Fraction Analysis – Single Shot Testing

The hypothesis that the void fraction can give an insight into the break-up process may be further tested by observing the variation of the void fraction for the second pressure swirl injector used, Injector B. It has already been shown for this injector that visually the spray appears to break up in a similar manner, via the ‘perforated sheet’ mode of break-up discussed earlier. Further evidence of the spray breaking up in this manner may be seen in Figure 4.28. This shows the ‘edge’ of the spray with a large hole in the fuel sheet shown in side profile. This evidence implies that the ‘dark’ sections of fuel spray are, as postulated, holes within the fuel sheet and not simply areas of the fuel sheet that have received less light due to the ‘wavy’ nature of the fuel spray.

It is expected that the shape of the void fraction plot will be similar to that obtained for injector A during the original series of testing, however the area of interest is further from the injector tip and it is a geometrically different

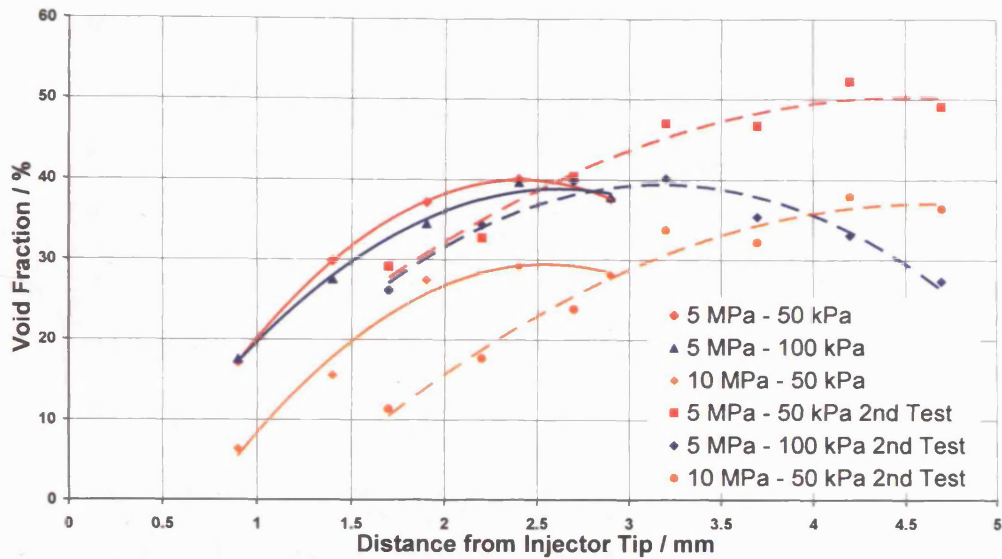
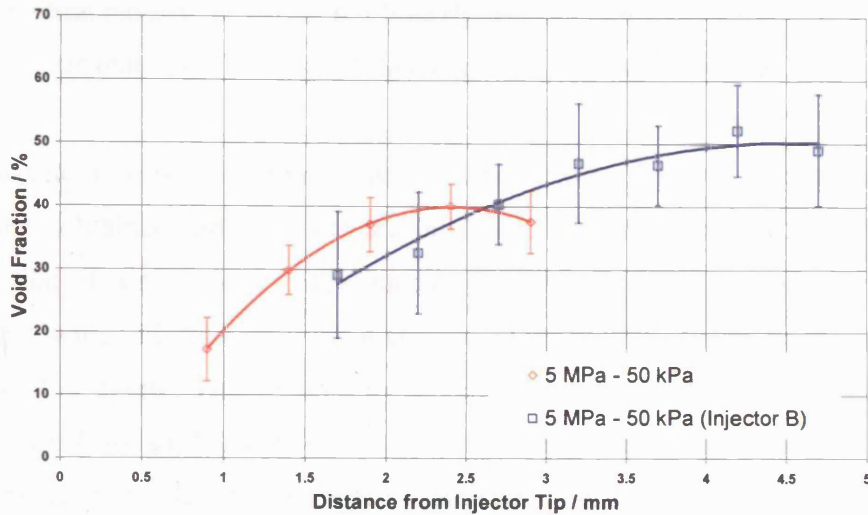


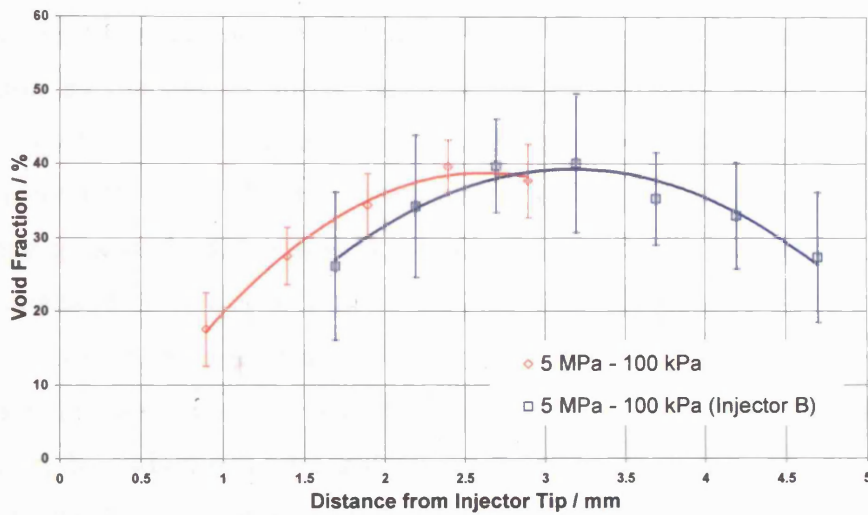
Figure 4.29 – Plot of void fraction vs distance from injector tip for Injectors A and B.

injector, albeit from the same manufacturer. Therefore the break-up length is likely to be different. It could be argued that the spray from the offset injector would be expected to break-up before that from the straight injector as the offset nozzle will produce disturbances within the fuel sheet. Figure 4.29 shows the comparison between the data from the offset injector and the straight injector for the test cases used in both sets of tests, (dashed lines represent the data for the straight injector, Injector B). It can be seen that the corresponding test cases between the two sets of data are different. There are two possibilities for this discrepancy between the two sets of data for the different injectors; either the data for the second injector is a continuation of the original data within experimental error, or the break-up length is significantly different.

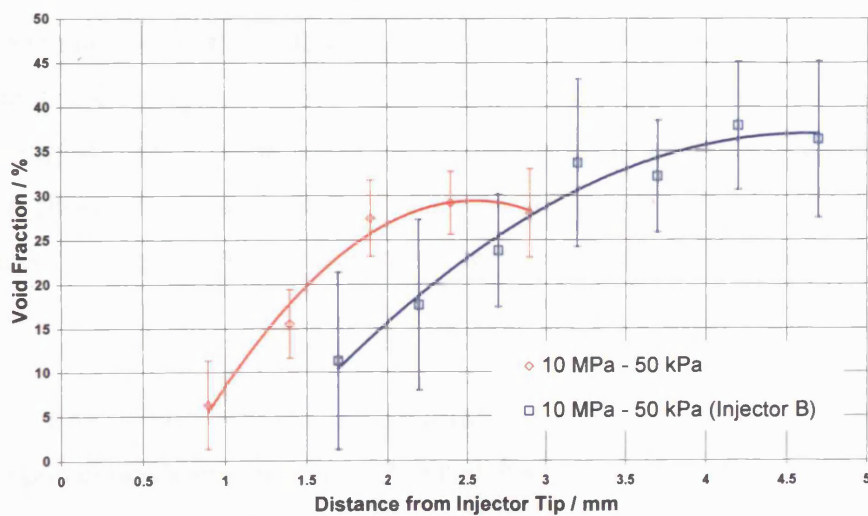
The difference in the break-up length required between the two injectors to satisfy the difference in the void fraction is very large, of the order of 100% difference. The only significant difference between the two injectors is the offset spray axis of the original injector tested. The angled nozzle utilised in producing the offset spray axis will cause one side of the hollow cone fuel spray to thin. This will therefore reduce the break-up length, causing the void fraction to rise more rapidly than for the straight injector, and peak at a shorter distance from the injector tip. The trend shown in Figure 4.30 follows this



(a) 5 MPa Fuel Pressure – 50 kPa back pressure



(b) 5 MPa Fuel Pressure – 100 kPa back pressure



(c) 10 MPa Fuel Pressure – 50 kPa back pressure

Figure 4.30 – Void fraction analysis profiles shown individually to highlight cycle to cycle variations, for varying test conditions. Bars show ± 1 S.D.

explanation closely, however not linearly, the data for the 5 MPa – 50 kPa has a far closer match to the original data than the other two test cases.

There may also be variation in the test data between the two injectors because the data obtained furthest from the injector tip for injector A is less accurate than that obtained close to the injector tip. This is due to the bottom of the image being slightly out of focus, making reliable measurements more difficult to obtain. This effect may be seen by observing the error bars shown in Figure 4.30 (a), (b) and (c), the amount of error seen in the results is larger for the first and last measurement obtained, due to the focusing issue. The error bars shown are +/- one standard deviation. The effect of using the void recognition program on a slightly out of focus image is to decrease the void fraction as the out of focus, small droplets, will seem larger, therefore reducing the size of hole seen by the program. However the opposite occurs for injector B, where the data is more accurate further from the injector tip, leading to possible differences in the void fraction due to inaccuracies in the measurement. Figure 4.30 also shows that although the data for the offset injector was an average obtained from images at different times ASOF during the steady state period compared to the single timing used for the straight injector, the variation in void fraction is greater for the straight injector, due in part to the lower resolution of the images. The most probable explanation however for the difference in void fraction trends between the two injectors, is a combination of both a different break-up length and the effect of the bottom of the image being out of focus. Confirmation that the differences were due to focusing issues was made with further imaging far downstream of the injector. It was shown that to accurately measure the void fraction the separation of the ligaments due to geometric factors was required, this will be discussed later in this section.

Figure 4.30 (b) confirms that the void fraction reaches a peak and then falls off as hypothesised using the data obtained from the offset injector. There are three data points after the peak, demonstrating that this effect is not solely due to the void fraction falling due to the image being out of focus at the bottom of the image. The other two plots showing data for both fuel pressures at 50 kPa

back pressure have again only just reached the peak; this could therefore be a product of the focus of the image. The turning points of the trend lines are shown in Table 4.2 and are compared to the break-up lengths predicted by the models. These must be treated with caution as the turning points for the 5 MPa – 50 kPa and the 10 MPa – 50 kPa cases are based on incomplete information.

Test Parameters	Turning point / mm	Break-Up length / mm		
	Void Fraction	Ren <i>et al.</i> [1998]	Schmidt <i>et al.</i> [1999]	Han <i>et al.</i> [2001]
5 MPa – 50 kPa	4.55	2.52	7.97	1.37
5 MPa – 100 kPa	3.18	1.32	3.21	0.90
10 MPa – 50 kPa	4.65	2.39	7.23	1.33

Table 4.2 – Table of Void Fraction turning points in comparison to model break-up length predictions for varying test conditions.

Observing the turning point for the 5 MPa – 100 kPa case it can be seen that it compares favourably to the break-up length as predicted by the model of Schmidt *et al.* [1999]. However, due to the lack of data after the turning point for both the 5 MPa – 50 kPa, and the 10 MPa – 50 kPa cases, the results remain ambiguous, further imaging was therefore required downstream to provide confirmation of the turning points and therefore the break-up lengths. As discussed previously moving further downstream of the injector tip with the same field of view eliminates any reference points within the image, (i.e. the spray boundary), therefore the FOV was increased to 10.75×8.125 mm, this allowed the fuel spray to be imaged more effectively. There were two main consequences of this, firstly many more data points were available due to the larger FOV, however, secondly the resolution of the images was decreased, leading to a higher degree of error associated with the measurements.

The turning point of the void fraction analysis has been defined as the break-up point of the fuel spray. After the break-up has occurred the fuel sheet is no longer continuous, and therefore the individual ligaments and droplets will



(a)



(b)

Figure 4.31 – Images of the far Downstream Fuel Spray for (a) 5 MPa – 50 kPa and (b) 10 MPa – 50 kPa

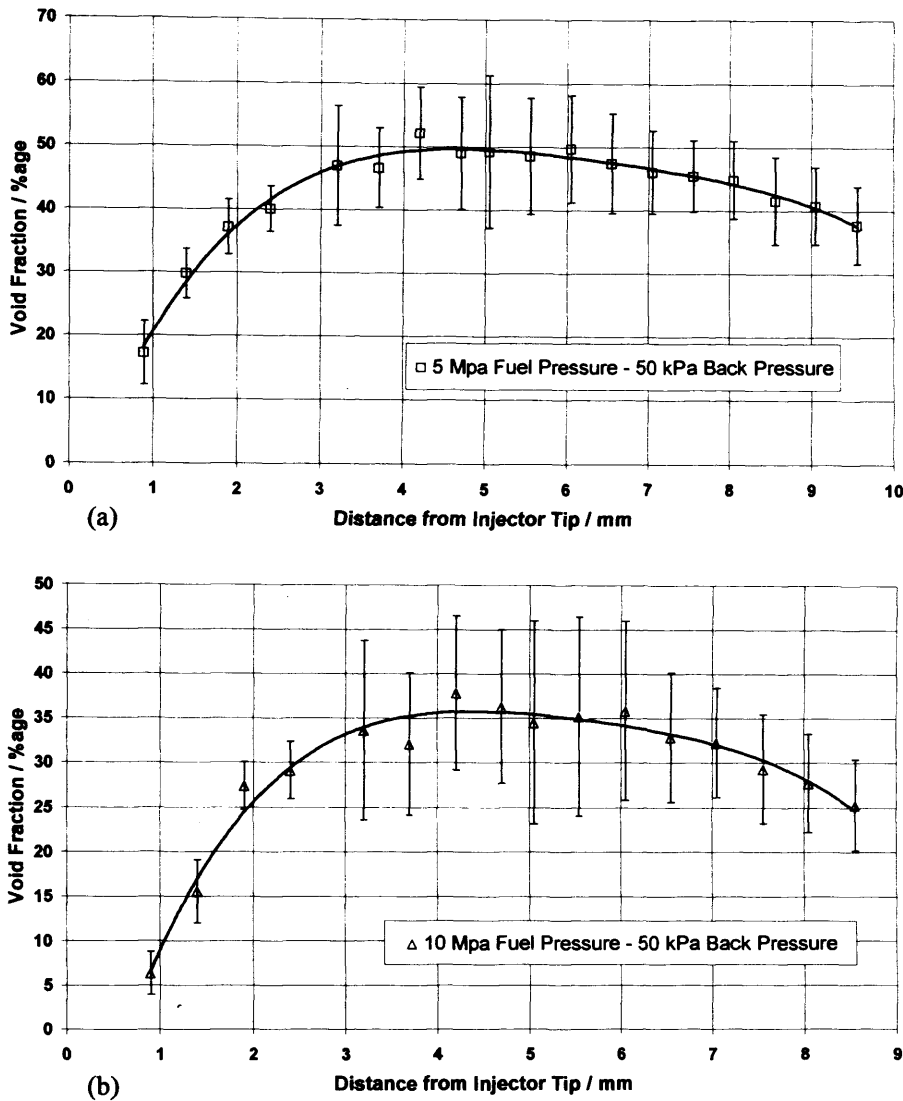


Figure 4.32 – Void Fraction Analysis for entire FOV for (a) 5 MPa – 50 kPa and (b) 10 MPa – 50 kPa

follow their previous trajectory. This causes the void fraction to increase not only due to break-up of the fuel ligaments, but also through the action of the ligaments separating as they proceed away from the injector tip. Therefore the void fraction analysis was adapted to account for geometric separation once the turning point was reached. Examples of the images obtained of the far downstream fuel spray may be seen in Figure 4.31 for both the 5 MPa – 50 kPa and the 10 MPa – 50 kPa cases that required imaging further downstream. This separation factor was not included in the original void fraction analysis. Further examples of the images shown in Figure 4.31 may be found in Appendix IV.

It is evident in Figure 4.31(a), the 5 MPa – 50 kPa case, that the fuel spray has broken up into individual ligaments and droplets and is no longer a continuous sheet. There are large dark areas where there is limited fuel present, which would dramatically increase the calculated void fraction if no account was taken for the geometric expansion of the ligaments. The same broken structure may be seen in Figure 4.31(b) also shows the same fragmented structure of the fuel spray as seen in Figure 4.31(a), however, the higher fuel pressure causes the ligaments to break-up into droplets closer to the injector tip, therefore producing a fuel spray that has large numbers of small droplets, increasing the difficulty in distinguishing fuel ligaments from clusters of droplets.

Figure 4.32 shows the void fraction analysis for the entire field of view imaged, from close to the injector tip where the fuel spray begins to break-up, to the far downstream images shown in Figure 4.31. It can be seen that the turning point has been found definitively, with a large number of data points after the turning point. The results found from this analysis, in terms of variation with back pressure, are consistent with the distribution found by the published models by Ren and Nally [1998], Schmidt *et al.* [1999], and Han *et al.* [2001]. The break-up lengths found using the void fraction analysis are similar for both fuel pressures at 50 kPa back pressure, however, the models of Ren and Han significantly under predict this break-up length, while Schmidt over predicts. Again the models by Ren and Han under predict the break-up length for the 5 MPa – 100 kPa case, however as shown previously the Schmidt model agrees very well with the value found here. Table 4.3 is the equivalent to Table 4.2 with the revised break-up lengths. The constant utilised in the Schmidt model is based on the ratio of the critical surface disturbance wavelength at break-up and the initial disturbance wavelength, perhaps this variation in the break-up mechanism discussed here, i.e. the build up of fuel around the voids, alters this critical ratio at low back pressures. Low back pressures produce a longer break-up length, therefore allowing more time for the critical ratio to be altered by the break-up regime.

In comparison to the data shown in Table 4.2 there are only minimal differences, however, previously the break-up length found for the 10 MPa –

50 kPa case was larger than that of the equivalent 5 MPa fuel pressure case. This would not be the situation in practice, where the higher fuel pressure would cause the fuel spray to break-up into ligaments earlier than that of the low fuel pressure case. This agrees with the images shown in Figure 4.31, where the 5 MPa fuel pressure appears to have a larger proportion of void within the fuel spray and therefore a greater proportion of fuel within larger ligaments, (this is apparent in the void fraction analysis where the maximum void fraction is higher for the 5 MPa fuel pressure), where the 10 MPa fuel pressure case has a greater proportion of droplets present, and therefore must have broken up prior to the 5 MPa fuel pressure case.

Test Parameters	Turning point / mm	Break-Up length / mm		
	Void Fraction	Ren <i>et al.</i> [1998]	Schmidt <i>et al.</i> [1999]	Han <i>et al.</i> [2001]
5 MPa – 50 kPa	4.63	2.52	7.97	1.37
10 MPa – 50 kPa	4.39	2.39	7.23	1.33
5 MPa – 100 kPa	3.18	1.32	3.21	0.90

Table 4.3 – Table of Void Fraction turning points in comparison to model break-up length predictions, with revised break-up lengths

The error bars in Figure 4.31 show ± 1 standard deviation, as it can be seen they increase with distance from the injector tip until reaching the turning point, where they begin to decrease. This shows that the break-up process has a high level of cyclic variability, (up to 20 samples were utilised to calculate the void fraction). The initiation of the break-up process is caused by small disturbances on the sheet surface as it leaves the injector orifice, therefore any change in that initiation process will cause large effects on the overall break-up length. Many factors could influence the small disturbances on the fuel sheet including deposits in the nozzle orifice, varying amounts of fuel in the sac volume, pintle opening time, slight variations in the fuel pressure etc. To enable the effects of the errors to be analysed the void fraction profile was plotted with values equal to ± 1 standard deviation, an example of this may be seen in Figure 4.33, for the 5 MPa – 50 kPa case. The average turning point

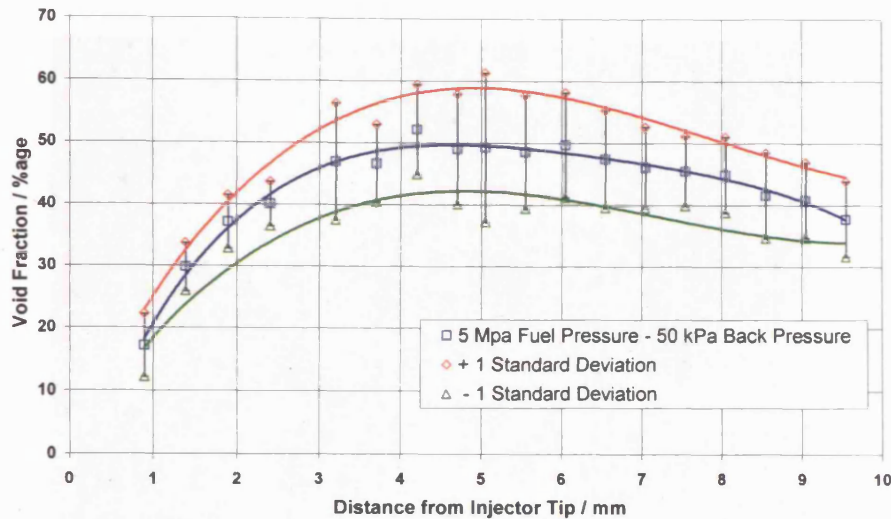


Figure 4.33 – Void Fraction Analysis for entire FOV for 5 MPa – 50 kPa showing the plots of ± 1 standard deviation

for the three plots was 4.79 mm from the injector tip, compared to the original value of 4.63, a difference of 3.5 %. The equivalent average for ± 1 standard deviation for the 10 MPa – 50 kPa case was 4.46 mm, an even smaller difference of 1.6 %, even though the level of deviation in terms of magnitude of void fraction was larger.

4.4.3.3 Periodic Surface Features

Periodic features were found on the surface of the fuel spray in some of the images taken. The periodic features are in addition to the hole features and are represented by bands of fuel running diagonally across the fuel spray. They are large scale, (relative to the perforations in the sheet), waves on the sheet surface. These features are demonstrated in Figure 4.34, for the test case of 5 MPa – 50 kPa, fuel and gas back pressures. They are similar to the Kelvin-Helmholtz waves shown by Kawahara *et al.* [2004] that are caused by the large slip velocity present between the fuel sheet and the surrounding gas. This slip velocity causes aerodynamic instabilities on the sheet surface, producing the waves seen in Figure 4.34. The results shown here are for large scale waves on the sheet surface that are independent of the small scale waves and disturbances influential in the forming of holes in the sheet.

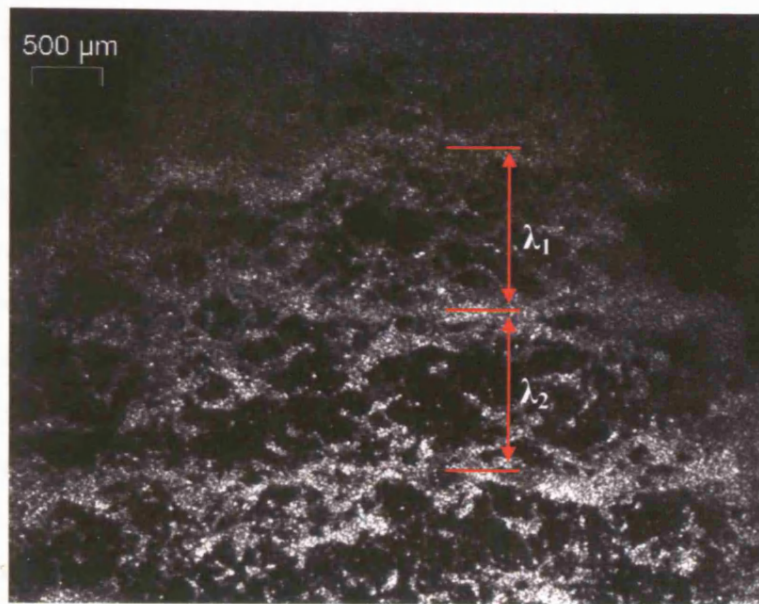


Figure 4.34 – Image showing periodic surface features on fuel spray issuing from Injector B.

	Fuel and Gas Back Pressures / wavelength given in mm			
Wave No.	5 MPa – 50 kPa	5 MPa – 100 kPa	10 MPa – 50 kPa	10 MPa – 100 kPa
1	1.22	0.86	0.78	0.79
2	1.18	0.78	0.72	0.68
3	-	-	0.68	0.52

Table 4.4 – Table of surface feature wavelengths

Table 4.4 shows the results obtained from the testing of Injector B, between two and three waves were seen per image depending on the position of the first wave seen. The waves are seen closer to the injector tip with increasing fuel pressure and back pressure, therefore at lower fuel pressure the initial wave is too far from the tip to see more than two waves. As Table 4.4 shows the wavelength of the surface features decreases with increasing distance from the injector tip. This is expected as the fuel spray will decelerate due to drag, it can also be seen that the amount that the wavelength decreases increases with fuel pressure and back pressure.

The results presented by Kawahara *et al.* [2004] were simply measured by observing the intensity variation along the injector axis. These authors assumed that the intensity of the image would increase where the fuel sheet is thicker, therefore the intensity profile provides a method of analysing the sheet thickness and therefore waves on the sheet. This author believes that Kawahara's method of measuring the waves on the surface of the sheet does not measure the waves but simply the width of the ligaments surrounding the holes. It is also not clear from their results how they determined which peaks in the intensity plots represented the wavelength. To attempt to establish whether the waves seen by Kawahara *et al.* were waves and not holes in the sheet, a comparison should have been made of the variation in the circumferential intensity profile. The results of Kawahara *et al.* were also averaged over the entire image which will provide less accurate results as the effect of the fuel spray decelerating due to drag will cause the waves to compress together as they get further from the injector tip. It would be expected that the wavelength of the Kelvin-Helmholtz waves would reduce with increasing fuel pressure, and back pressure, however Kawahara *et al.* [2004] reports wavelengths that increase with fuel pressure.

4.5 Conclusion

A study has been carried out to characterise the break-up mechanisms of a pressure swirl injector that is commonly used in DISI engines. The characteristics of the liquid sheet disintegration were investigated at two fuel pressures: 5 and 10 MPa, and three ambient back pressures: 50, 100 (atmospheric) and 200 kPa for a pre-production DISI injector. Microscopic images of the near-nozzle spray region were obtained with a high-speed rotating drum camera and copper vapour laser. An analysis has shown that the spray breaks up via a perforated sheet mechanism, producing ligaments that undergo further break-up into droplets. A novel 'void fraction' technique was developed to analyse the near field (microscopic) images obtained using a copper vapour laser and a high speed rotating drum camera. This technique uses the perforations, or voids, to show the trends in the break-up. In

conjunction with further images downstream this permitted the break-up length to be found. This break-up length was defined as the turning point where the void fraction begins to reduce after the initial rise.

The break-up lengths predicted by three known models, Han, Ren and Schmidt, were compared to the near field spray images. It was shown that they consistently under predict the break-up length. The author suggests that the reason for the under prediction of the break-up length is the extra fuel available to maintain the thickness of the unbroken sheet due to the creation of perforations. This means that the sheet can remain stable for longer, producing a longer break-up length. The formation of the holes was analysed and an attempt was made to characterise their size and shape. It was found that their shape and size was significantly affected by the back pressure.

A further study was carried out on a second injector to determine whether the results obtained from the first offset injector were injector specific. It was found that the break-up mechanism for the second injector was also via a perforated sheet. It was shown that the void fraction had the same distinctive trend, initially rising, reaching a peak and then falling down again due to increasing droplets within the voids. The trend for the second injector was similar but not a continuation of the initial results from the first injector, this was due to different break-up lengths associated with injectors A and B. Nevertheless a continuous plot of all of the void fraction data allowed the break-up lengths for this type of injector to be found.

Furthermore, periodic structures were observed on the fuel sheet, in addition to the structure produced by the perforated mode break-up. These were measured and compared to results presented by Kawahara *et al.* [2004], it was shown that the wavelength of these structures vary with both fuel pressure and back pressure. The results presented by Kawahara *et al.* [2004] were shown to represent not the surface waves on the fuel spray, but the width of the ligaments between voids.

Chapter 5
Effect of Impinging Air Flow on Near
Nozzle Characteristics of a Pressure-Swirl
Atomiser

Chapter 5 Effect of Impinging Air Flow on Near Nozzle Characteristics of a Pressure- Swirl Atomiser

This chapter presents the results obtained from an experimental study carried out to investigate the effect of impinging air flows emanating from the inlet valves of a typical direct injection cylinder head on the near nozzle characteristics of an inwardly opening, high pressure-swirl atomiser. Mie scattering was utilised to visualise the fuel spray and air flow in conjunction with a CCD camera and a long distance microscope lens to provide high spatial resolution. PIV was carried out to visualise the air flow structure and its probable effects on the fuel spray. Further Mie scattering was utilised to visualise the break-up phenomena of the fuel spray in conjunction with a single lens reflex SLR camera to provide high resolution images. This study will further improve the knowledge of the near-nozzle characteristics obtained in Chapter 4.

5.1 Introduction

The review of the current knowledge concerning the effects of in-cylinder air flows in Chapter 1 shows that the results are limited to the far field fuel spray due to restrictions in placing optical windows within an engine. Although some results have been presented, e.g. Wagner *et al.* [1999], Georjon *et al.* [2000] and Karaiskos *et al.* [2002], using a window in the pent roof of engines, they do not allow for high levels of detail to be shown in the near nozzle region of the fuel spray due to obscuration by inlet valves etc. Therefore due to the difficulties of obtaining results in this region within a firing engine often steady state results are obtained using flow rigs to allow greater optical access to the fuel spray and greater control over the air flow conditions.

Yule *et al.* [1998] studied the effects of a high velocity air stream adjacent to a thin flat sheet, this is a highly simplified model and does not attempt to observe the effects of impinging air flows. Kawajiri *et al.* [2002] performed experiments in a swirl flow rig to attempt to simulate the effects of in-cylinder flows on the fuel spray during late injection timings, i.e. for stratified charge operation. Choi *et al.* [2000] utilised a steady state flow capable of producing a maximum air flow speed of 17 m/s. Although this experiment looked at the effect of impinging flows, only far field results were produced as the air flow had negligible effect on the near field characteristics of the fuel spray due to the low momentum of the air.

5.2 Experimental Apparatus and Procedure

The steady state air flow rig utilised in this experiment was as described in §2.3. A milling machine base was utilised to mount the flow rig both rigidly and accurately. The bed of the machine allowed the illumination light optics to be mounted rigidly and then positioned effortlessly and accurately to the desired location. Further more a drill machine base was utilised to mount the camera allowing the height to be positioned precisely.

An Nd:YAG laser was used for illumination during all of the experimental studies discussed in this chapter. The light emitted had a pulse width of approximately 3 – 5 ns, and a wavelength of 532 nm. To pressurise the fuel the same system was used as described in Chapter 4, however only one fuel pressure, 5 MPa, was tested due to the limitations found in imaging the fuel spray at 10 MPa in Chapter 4. The lower fuel pressure produces a lower momentum spray, therefore the effect of the impinging air flow was accentuated allowing the effects to be studied in greater detail. The injector used was injector A and the injection pulse width was 2 ms for all of the tests carried out.

As the flow rig may only be operated in a steady state, fixed valve lift condition, the valve lifts to be studied must be chosen prior to running the

experiment. Three test points were chosen to give an understanding of the varying effects of the impinging air flow throughout the inlet valve opening process. They were 2, 3 and 5 mm, these valve lifts were chosen to provide information of varying flow velocities and momentum to observe their varying effects on the fuel spray. To provide a direct comparison images were also taken with no air flow present, whilst retaining the same back pressure in the measurement section. The pressure difference across the valve must also be set prior to running the experiment. This value was set by observing the maximum possible pressure difference across the valve at a lift of 5 mm, (the maximum flow rate of the vacuum pump). The value found was a pressure drop of 148 mm Hg, equivalent to 19.65 kPa. For the other two valve lifts the flow through the valves was set such that the pressure drop across the valve was equal to 148 mm Hg. Therefore the only effect seen on the spray is that of the impinging air flow, with no additional effect of varying back pressure. This pressure drop equated to 58.6, 80.5 and 128.0 g/s for 2, 3 and 5 mm valve lifts respectively, these values are outlined in Table 5.1. It must be noted that it was not intended to replicate specific engine conditions, but instead provide a range of useful results. The mass flow rate was measured using a hot-wire anemometer from a production engine, this unit was calibrated using a laminar flow element air flow measuring device, calibrated to international standards.

Valve Lift / mm	Pressure drop across Valve / kPa	Mass Flow Rate / g/s
2	19.35	128
3	19.35	80.5
5	19.35	58.6

Table 5.1 – Table of Mass flow rate through Flow Rig for varying Valve Lifts

The camera used for all of the digital imaging was an *Imager Intense* CCD camera from *La Vision*. The pixel resolution of this camera was 1376 × 1040, with a maximum frame rate of 10 Hz. This camera is capable of operating in double frame mode and the minimum time interval between frames was 500

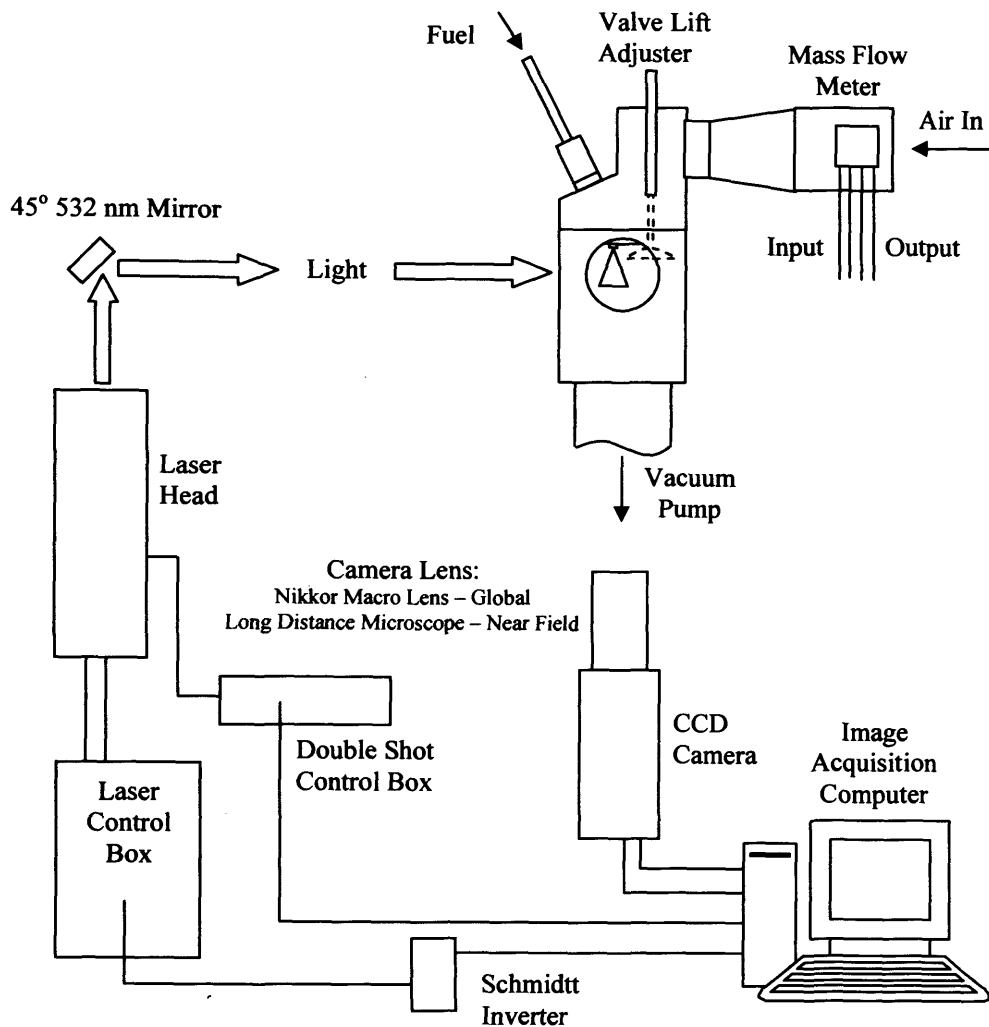


Figure 5.1 - Schematic diagram of Experimental Apparatus for Air Flow Rig

ns. However due to the limitations with using a single head laser the minimum time between the two images was determined by the minimum laser pulse separation time which was 20 μ s.

5.2.1 Global Imaging

For the global imaging study the flow rig was set up as in Figure 5.1. A simple convex lens was used to focus the laser light, with the effect of creating a cone shape of light past the focal point. This was then directed at the spray to illuminate it globally. To obtain the maximum amount of light possible the 45° mirror utilised was specified to reflect 99.5% of the light at 532 nm. The final light intensity required may then be set using the laser Q-switch timing, with a maximum light intensity occurring with a Q-switch timing of 228 μ s after the

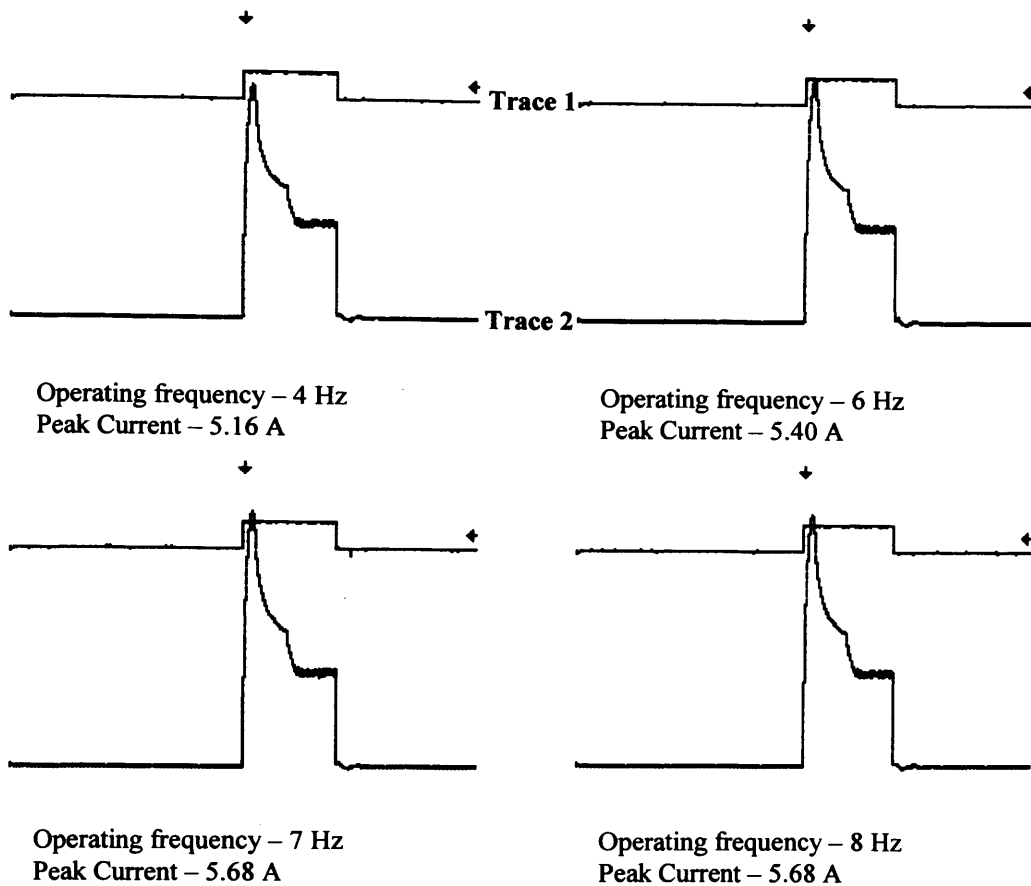


Figure 5.2 – Oscilloscope traces of the output current for Injector A;
 Trace 1: Injector Signal Pulse – 2 ms width
 Trace 2: Injector Drive Current – 100 mV / division

flash lamp signal. For the purposes of these experiments a Q-switch timing of 187 μ s was used.

A Nikkor 60 mm macro lens gave a field of view (FOV) of approximately 45 x 35 mm, this enabled the global characteristics of the spray to be measured, such as the cone angle and penetration, for the entire spray event, for varying valve lifts. The global imaging also gave an indication of the effect of the impinging air on the fuel spray.

It was found that the fuel injector driver was required to be operated at a minimum of 6.5 Hz to achieve the maximum opening current to the injector. The injector driver used a peak-and-hold circuit, where the opening current rises rapidly to a value much larger than the holding current, to enable the injector to open quickly, then after the pintle is fully open, the current is

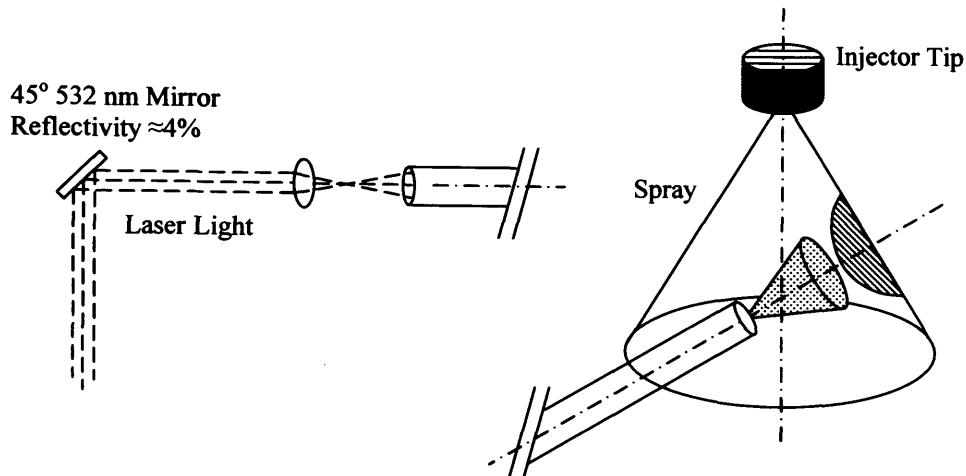


Figure 5.3 - Schematic diagram of Fibre Optic Light delivery Set-up

reduced to hold the injector open, whilst facilitating rapid closing at the end of injection. The output current of the injector driver was measured using a current clamp probe attached around one of the injector drive leads. The effects of varying the operating frequency may be seen in Figure 5.2. Therefore, to achieve the optimum opening characteristics of the injector, all of the tests must drive the injector at a minimum of 6.5 Hz.

5.2.2 Near Field Imaging

The same set-up was utilised for the near field imaging as for the global imaging, except that the Nikkor 60 mm macro lens was replaced by the Infinity k2 long distance microscope lens, producing a field of view of approximately 11×8 mm. Global illumination was utilised initially to provide a more detailed understanding of the effect of the impinging air flow on the general spray shape. However, to provide detailed images of the spray break-up phenomena, the method of placing a fibre optic cable inside the fuel spray as described in Chapter 4 was used.

The same lens as used in the global illumination was used to focus the light into the fibre optic cable. However, the amount of light required and the limitations of the fibre optic cable require that only a small proportion of the laser light be used. Therefore instead of using the previous mirror which reflected $> 99.5\%$ of the light, a mirror which only reflected approximately

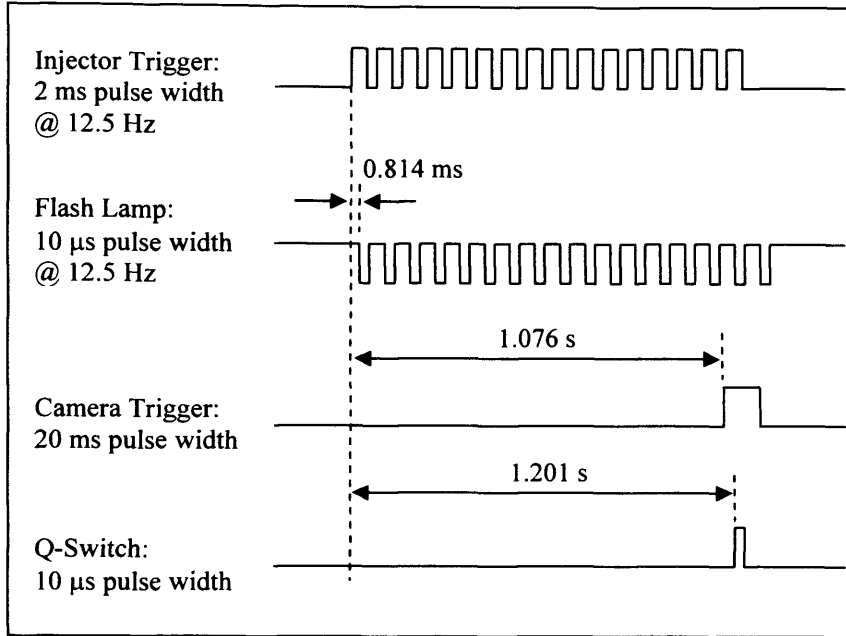


Figure 5.4 – SLR Camera control timing sequence (all signals are TTL)

4% of the light at 532 nm was used. The conditions within the flow rig, i.e. high velocity air, require that the fibre optic be held firmly in position. To accomplish this, a section of copper tubing, malleable enough to provide the required positioning resolution was utilised, this set up may be seen in Figure 5.3.

5.2.3 High Resolution Imaging – SLR Camera

To produce high resolution images, similar to those found in Chapter 4, a single lens reflex (SLR) camera was used with Kodak TMAX 3200 film. The SLR camera used was a Nikon F801s, capable of remote operation and automatic wind-on. This enabled the camera to be triggered by a Stanford Research Systems pulse generator, via a relay, and then automatically wind on to the next frame, ready for the subsequent shot.

The timing of the Nd:YAG laser, fuel injector and camera was carried out using two Stanford Research Systems pulse generators, (these will be referred to as SPG from now on). The first was set-up such that it produced a pulse to fire the flash lamp of the laser and a pulse to trigger the injector, both at 12.5 Hz, the required operational frequency of the laser. The injector was driven at

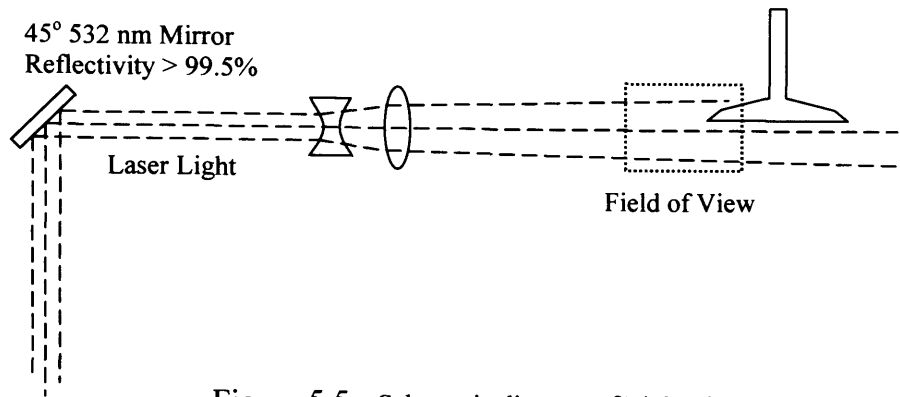


Figure 5.5 - Schematic diagram of Light Sheet Set-up used for PIV

12.5 Hz to enable the output current to build up to its maximum prior to taking an image, as discussed in §5.2.1. A second SPG was triggered by the injector pulse from the first, a suitably large delay time after the trigger pulse, equivalent to 15 injection events, firstly the camera and then the Q-switch are triggered. Therefore an image is taken every 15 injection events, allowing the camera the required time to wind on to the next frame. The timing sequence may be seen in Figure 5.4. The camera shutter time was set on the camera to be $\frac{1}{4}$ s, or 250 ms, this gave ample time for jitter in the shutter operation, and due to the test cell being completely dark produced no detrimental effects on the film, (the exposure being determined by the illumination).

Subsequently the film required developing which was carried out in-house using Kodak TMAX developer and a generic fixing solution. The developing and fixing times used were dependent on the ambient temperature, however the film was always washed for at least 20 minutes to remove any chemicals, prior to drying. It was then required that the film be digitised, to provide images of the resolution to those found in Chapter 4 they were scanned at 3072×2048 pixels and saved in the same Kodak PhotoCD format as previously described in Chapter 4.

5.2.4 Particle Image Velocimetry

The same general set-up was used for the PIV imaging, however the optics, a series of symmetric concave and spherical convex lenses, were arranged to produce a light sheet perpendicular to the focal plane of the camera, see Figure

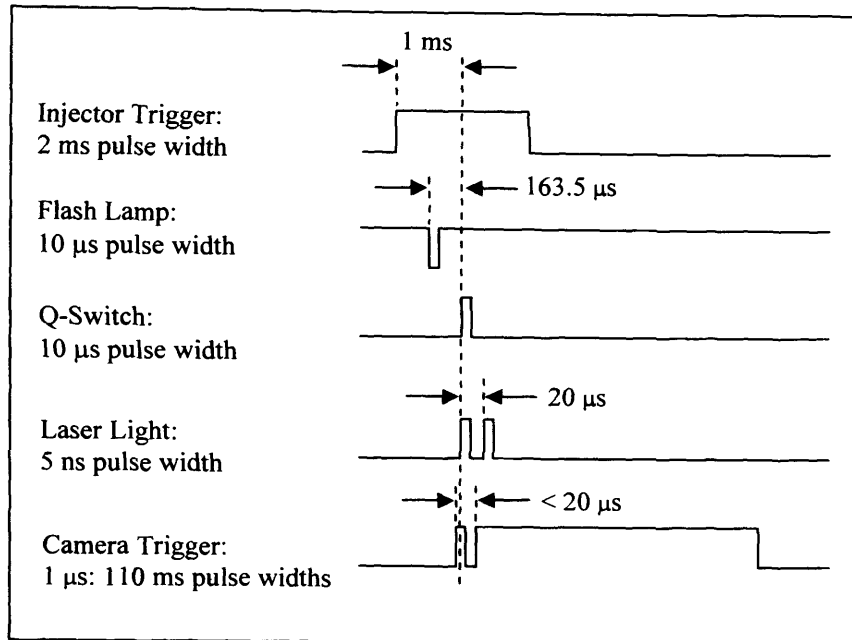


Figure 5.6 – PIV Camera control timing sequence (all signals are TTL)

5.5. The light sheet was focused such that, at the area of interest the sheet was approximately 1 mm thick, and extended over the entire field of view, which was approximately 15×11.5 mm, the same area of interest as that used for the near field imaging with global illumination.

Finally to prepare the system for double imaging the double pulse option on the Nd:YAG laser was selected. This enabled the single head Nd:YAG laser to produce a double pulse of light, controlled by a potentiometer, with a minimum separation time of 20 μs and a maximum separation time of 200 μs. As the flow velocities being visualised were high the minimum separation time of 20 μs was utilised. Therefore at 50 m/s a droplet would travel 1 mm in this time.

In double pulse mode the camera may only be shuttered for the first image and is set to 1 μs, for the second image the exposure time is 110 ms due to limitation in downloading the image from the camera. Therefore to obtain images with equal intensity levels the testing was carried out in a dark room. The timing diagram for the PIV set-up may be seen in Figure 5.6. Due to the shot to shot variability of the seed particle density and location, 50 double frame images were taken per test point. They were then cross-correlated and

then the 50 vector fields obtained were averaged to produce a single velocity flow field. The parameters used in the cross-correlation of the double frame images will be discussed later in §5.2.4.1.

Due to limitations in the seeding system and the length of the flow path from the inlet to the area of interest the density of droplets was fairly low. Therefore to obtain suitable images for the cross-correlation technique, low flow rates, lower than those used during the fuel visualisation experiments were utilised. Furthermore the flow rates were limited by the minimum separation time of the laser light pulses, therefore, values for the flow rates were selected that both provided adequate seed density, and also produced low enough air flow velocities to allow cross correlation of the double image. Unfortunately it was not possible to obtain alternative equipment with a better specification for these tests. The flow rates utilised may be seen in Table 5.2 below;

Valve Lift / mm	Depression / kPa
2	270, 400, 530
3	270, 400, 530
5	270, 530, 800

Table 5.2 – Table of Pressure drop across Valves used for PIV Air Flow

5.2.4.1 Cross-Correlation Parameters

The software used to calculate the vector field was DaVis 6.2.2 with the Pro-Package to allow PIV calculations. This software allows the input of parameters to control the calculation method of the vectors. Before a detailed explanation of the calculations involved it must be noted that a general overview of the PIV technique may be found in §1.4.4, the specific details of the technique described here may be found in the *DaVis FlowMaster Manual* [2002].

The general method utilised was the cross-correlation of a double frame image. The algorithm computes the cross-correlation of all of the

corresponding interrogation windows from both frames. The size of the interrogation window is an important factor and is dependent on the displacement of the seed particles, essentially the velocity of the air flow. The maximum displacement of the particle between the two frames must not be larger than $\frac{1}{4}$ of the interrogation window size. This is to reduce the number of particles leaving the interrogation window between frames. This effect may be greatly reduced by using adaptive multi-pass algorithms, where the initial interrogation window size is relatively large, therefore ensuring large velocity vectors are located. However this alone would produce a very sparse velocity field. Therefore the interrogation window size is reduced on further passes thereby increasing the spatial resolution of the vector field. This is accomplished by using the data supplied from the first pass to provide information on the likely vector field to the second pass, and so on.

The range of velocities within the area of interest in this case is fairly large, ranging from the high velocity flow issuing directly from the valve opening to the low velocities away from the valve near the injector tip. Therefore to adapt and cope with this a large 128×128 pixel interrogation window is utilised for the initial two passes of a ‘normalised’ $I_1 * I_2 / RMS$ correlation function. This function uses the following equation:

$$C(x, y) = \frac{\sum_{x=0, y=0}^{x < n, y < n} I_1(x, y) \cdot I_2(x + dx, y + dy)}{RMS(I_1(x, y)) \cdot RMS(I_2(x + dx, y + dy))} \quad \text{Eq. 5.3.}$$

Where I_1 and I_2 are interrogation windows one and two respectively, and C is the correlation of the two. Note that the standard deviation in the first interrogation window is a constant, while $RMS(I_2)$ normalises the correlation relative to the standard deviation of the second interrogation window. This effectively compensates for varying background intensities and particle densities, which is the reason for its use in this application as the particle density is non-uniform.

The final two passes used in the calculation of the PIV vector fields shown here have an interrogation window size of 64×64 pixels, however an overlap of 75% was chosen to ensure that a complete description of the vector field be seen, this effectively provides a vector every 16 pixels, the process of using the overlap will be discussed later in this section. The correlation function utilised in these passes was the ‘standard’ $I_1 * I_2$ (via FFT, no zero padding), this function uses the equation below to calculate the correlation:

$$C(x, y) = \sum_{x=0, y=0}^{x < n, y < n} I_1(x, y) \cdot I_2(x + dx, y + dy), -\frac{n}{2} < dx, dy < \frac{n}{2} \text{ Eq. 5.4.}$$

In fact this mathematical relationship is not computed directly, rather it is a standard cyclic FFT-based algorithm that is used to calculate a cyclic correlation of the interrogation window which is similar but not exactly the same as the mathematical true correlation given in equation 5.4. Using the cyclic correlation function provides a much faster, of the order $50\times$ faster than computing the correlation function directly. The disadvantage of this method is that it introduces a weighting of the correlation coefficients with an emphasis on the displacement (0,0), with decreasing weighting toward larger displacement. For example with an interrogation window of 32×32 pixels, displacement of (0,0) has a weighting of 1 while a displacement of (16,16) has a weighting factor of $\frac{1}{2}$ and a displacement of (32,32) a weighting of 0. This is because for a displacement of 16 pixels only the particles in the left hand half of the interrogation window add to the correlation strength, therefore when using this correlation function the maximum displacement must be no more than approximately $\frac{1}{3}$ of the interrogation window.

Limits must be set on the allowable vectors ranges to ensure that only legitimate vectors are passed onto the next pass of the correlation algorithm. The limits of the vectors sizes are imposed through both relative and absolute terms, during this analysis the relative vector sizes within each interrogation window was set to the (reference vector size + the cell size / 3), with the absolute vector size set to the (reference vector size + 12 pixels). These are

large ranges however due to the flow structure observed this was required to ensure the large velocity gradient close to the impinging air jet issuing from the valve opening was resolved.

Due to information being required about the entire vector field for further passes, after each pass a median filter is utilised to remove and replace extraneous vectors that are greater than $2 \times \text{rms}$ of its neighbours. Then an interpolation algorithm is performed to fill up the empty spaces. The final operations to be performed are to average the 50 vector fields obtained to produce a single vector field for each test point and then apply a mask to eliminate any vectors that fall outside of the field of view, i.e. within the valve area.

5.2.5 Air Flow Seeding

A flow seeder with ten Laskin nozzles was utilised to seed the air flow, with each Laskin nozzle producing approximately 1×10^8 particles / s. A Laskin nozzle is a small hole in a plate through which air is passed, the seeding liquid is situated above the hole, as the air passes through the hole a fine mist is produced. The design of the particle seeder allowed between one and all ten of the nozzles to be used at any one time. To obtain the required particle density for visualisation all ten Laskin nozzles were utilised. A section of pipe leading from the seeder to the flow rig allowed the seed particles to be focussed at the inlet port being imaged. The seed material utilised was corn oil, a common liquid to be used for flow seeding applications. When using the seeder with corn oil it produces a very regular distribution of droplet sizes. The droplet size distribution was measured at approximately 20 mm downstream of the pipe outlet with a Malvern particle analyser. The droplet size distribution was as follows;

- SMD (D_{32}) – 10.31 μm
- $D_v[10]$ – 9.56 μm
- $D_v[90]$ – 11.01 μm

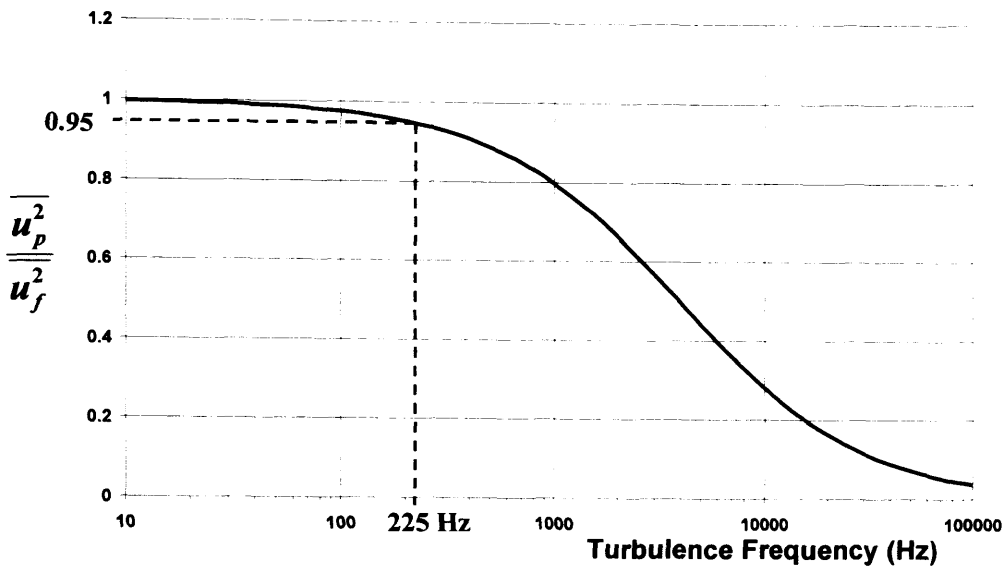


Figure 5.7 – The response of particles in Turbulent flow, from Melling [1997]

5.2.6 Fidelity of Flow Seed to Air Flow

It is important when seeding a fluid flow to ensure that the seed used to visualise the flow is small enough to follow the flow faithfully. If the seed particles are too large and/or too dense then they will not follow the fluid flow faithfully. The ability of a tracer particle to follow the flow is dependent on the particle size, the ratio of the density of the particle to that of the fluid and the kinematic viscosity of the fluid. Melling [1997], provides information on the response of a particle in turbulent flow, allowing the relative particle and fluid flow kinetic energy velocity fluctuations to be calculated. The formulae used when there is a high density ratio between the particle and the fluid from Melling are shown below;

$$\frac{\overline{u_p^2}}{u_f^2} = \left(1 + \frac{\omega_c}{C}\right)^{-1} \quad \text{eq. 5.1.}$$

$$\text{where, } C = \frac{18\mu}{\rho_p d_p^2} \quad \text{eq. 5.2.}$$

ω_c is the highest turbulence frequency of interest, μ is the gas dynamic viscosity, ρ_p and d_p are the density and diameter of the particle respectively. The curve of the characteristic frequency C plotted against varying turbulence frequency shows the relative fluctuation intensities of the particle and fluid motions in a turbulent flow summed over all turbulent frequencies below ω_c . This plot may be seen in Figure 5.7. However a criterion is required when accepting a seeding particle size. For a high density ratio situation, as is the case of an oil droplet in air, Melling showed that a suitable criterion was to select the droplet size such that $\overline{u_p^2} / \overline{u_f^2} = 0.95$. Where $\overline{u_p^2}$ is the kinetic energy fluctuation of the particle velocity and $\overline{u_f^2}$ is the equivalent for the fluid.

However due to the fixed droplet sizes produced by the seeder available, a turbulence frequency was calculated that produced this result. Figure 5.7 shows that for this application a maximum turbulence frequency of 225 Hz may be visualised. Due to the fairly uniform nature of the flows being investigated, especially in the jet of air issuing directly from the inlet valve, which is the main area of interest, this is an acceptable value.

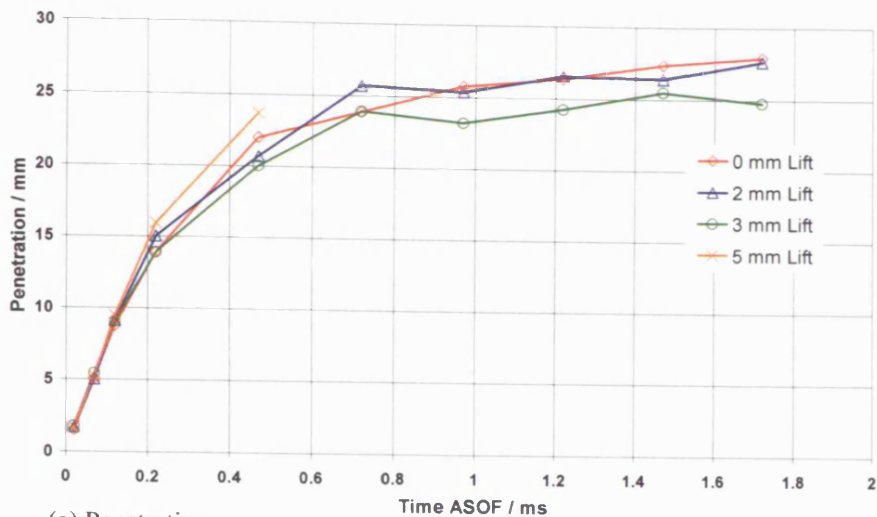
An attempt was made to produce smaller droplets by using water instead of oil as the seed material, the lower viscosity of water produces smaller droplets from the seeder. These droplets were also doped with Rhodamine-B, which is excited by 532 nm wavelength light, and fluoresces at ≈ 600 nm in an attempt to use a filter to eliminate the Mie scattered light, thereby allowing the air to be visualised while injecting fuel without observing the fuel. However the smaller scattering area of the droplets combined with the added effect of evaporation of the water droplet provided a very small laser induced fluorescent light signal, too small to produce reliable PIV results.

5.3 Analysis of Fuel Visualisation Results

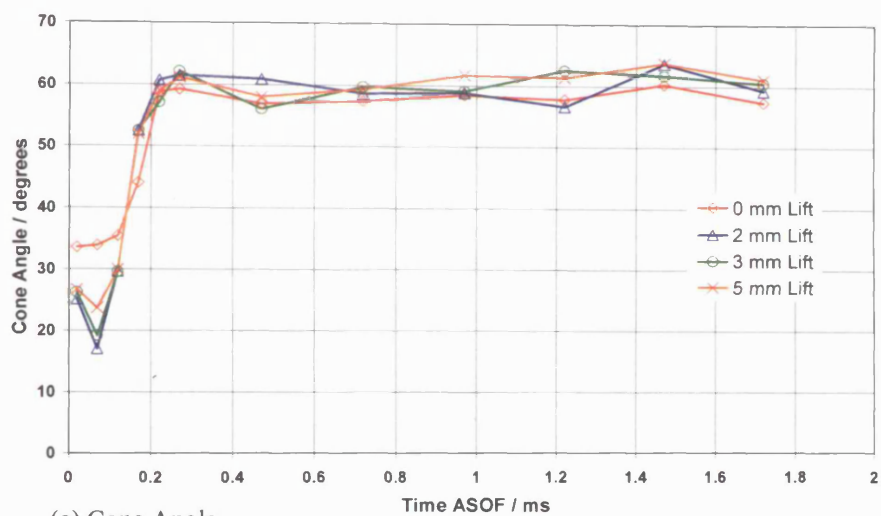
The fuel visualisation results were inspected with two different criteria, firstly a comparison with the images described in Chapter 4 was made, providing a baseline to compare the results ensuring that the general characteristics of the fuel injector remain constant. Secondly the results were inspected, with reference to the PIV vector fields to determine the effect of an impinging air flow. The results obtained from the global imaging were utilised to provide a baseline link to the previous results while the near field imaging was utilised to determine the effects of the air flow. Due to a level of overlap between the two, i.e. some global images were utilised in the analysis of the effect of the air flow, and some near field images were used in the determination of the fuel spray characteristics, the results will be discussed as a whole and not as separate series of tests.

5.3.1 Fuel Spray Characteristics

The fuel spray penetration and cone angle were measured using a similar method to that described in §4.4.1.1, and will therefore not be described again here. The results shown in Figure 5.8 show the results for 2, 3 and 5 mm valve lifts, and also results obtained at 0 mm valve lift, i.e. no flow, however the back pressure remained 80.35 kPa as it was throughout this series of tests. As no data was previously obtained at this back pressure it was assumed that the difference between the penetration and cone angle from the data obtained at 100 kPa is negligible. This was a suitable assumption as the difference between the 50 kPa and 100 kPa data obtained previously was also negligible, (this data was presented in §4.4.1.2, Figures 4.10 & 4.11). The data shown here appears different to that in Chapter 4 although the same injector, Injector A was tested. This is because the entire data set is shown here, as opposed to simply showing the data up to the steady state period. The extra data was provided here to show the negligible effect of the air flow on the fully developed cone angle.



(a) Penetration



(a) Cone Angle

Figure 5.8 – (a) Axial Spray Penetration and (b) Cone Angle for 5 MPa Fuel Pressure all with an Air Flow present at a pressure drop of 19.65 kPa.

In a similar manner to the results shown in §4.4.1.2 the origin for the time is that at the start of fuel emerging from the injector tip. This was calculated by using the first three penetration data points from the near field images, and assumed that over this time period the penetration was linear, this may be seen in Figure 5.8(a). The initial velocity was calculated from these data points and was determined to be 72.34 m/s, this compared favourably to the velocity obtained previously for the 100 kPa test point of 70.68 m/s. In fact, if an inverse square relationship is assumed between the penetration rate and the back pressure, an estimate of the penetration rate at 80.35 kPa may be made from the previous results obtained at 50 and 100 kPa, this is an appropriate

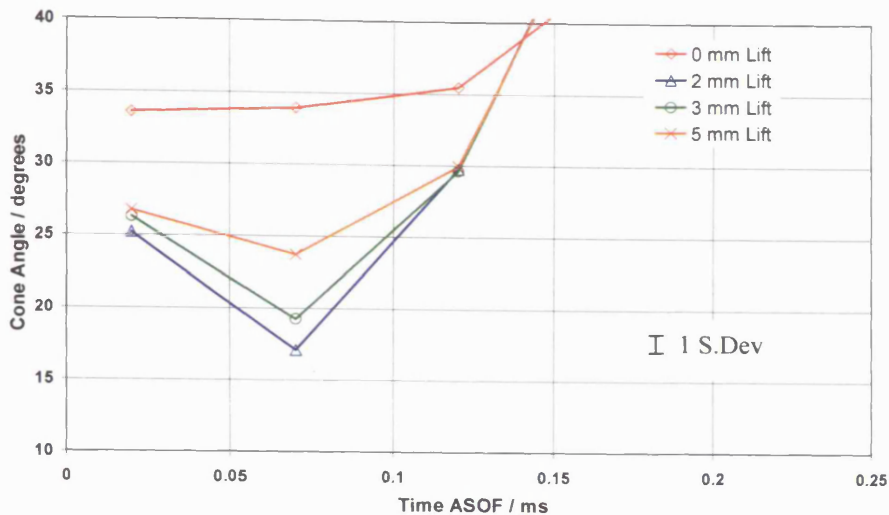


Figure 5.9 – Enlargement of the Initial Phase of the Cone Angle Development

assumption as the drag on the fuel will be dependent on the density of the air and therefore the back pressure, and the drag is proportional to the velocity squared. The calculation provides a velocity of 72.69 m/s a difference of 0.48 % from the value measured directly. At low pressures the initial penetration rate of the fuel spray may therefore be calculated from two known values. This is effectively calculating the coefficient of drag for the entire fuel spray as a whole.

Observing Figure 5.8(a) it may be seen that the penetration of the fuel spray is not affected by the impinging air flow, except to deflect it away from the injector axis. This is why the data for 5 mm valve lift stops before the other sets of data, because the penetration rate becomes ambiguous due to the air flow disrupting the fuel spray. However the data for the cone angle continues as it is measured close to the injector tip and has as yet been unaffected by the impinging air flow.

Observing Figure 5.9, an enlargement of the initial cone angle development, it may be seen that the cone angle is initially affected by the air flow. It may be seen that for no flow, i.e. 0 mm valve lift that the cone angle develops to its steady state value steadily at first, then rapidly, as the tangential component of the fuel velocity builds up as the pintle is opened. For the cases with an impinging air flow the fuel spray is deflected immediately, and therefore the

cone angle is affected. It can be seen that even the initial exiting fuel spray has its cone angle reduced by the air flow, and that the subsequent development of the fuel spray cone is dependent on the valve lift. For the smallest valve lift of 2 mm, the effect on the cone angle is the greatest, this is because the air flow jet is directed at the fuel spray closer to the injector tip. The distance at which the main impinging air flow encounters the fuel spray increases with the valve lift, therefore the effect on the cone angle is reduced with increasing valve lift. After the initial disturbance of the fuel spray, it goes on to produce a fuel spray cone similar in angle to the no flow condition, this is because the momentum of the fuel spray very close to the injector tip is very high in comparison to the air flow. The entire fuel spray is also deflected away from the injector axis by the impinging air flow. The level of deflection is dependent on the valve lift as a higher valve lift will produce an air flow with a larger momentum. The amount that the spray is deflected away from the no flow condition may be seen in Table 5.3 below, these values were averaged over the steady state period of the injection event;

Valve Lift / mm	Deflection / degrees	Standard Deviation
2	0.48	0.107
3	0.81	0.185
5	2.90	0.263

Table 5.3 – Table of cone angle deflection due to impinging air flow

5.3.2 Presence Probability Imaging

Presence probability imaging or PPI, as described initially by Münch and Leipertz [1992], and further developed by Grimaldi *et al.* [2000] and Hung *et al.* [2003], is a method of showing the probability the presence of fuel at any one point in space, averaged over a number of images. Generally this is used as an effective tool to show the effects of cyclic variations in the fuel spray. However, here the main incentive for its use is to show the effects of the impinging air flow. The intensity level of each pixel is proportional to the probability of presence of fuel, therefore an intensity level of 0 equates to a 0

% probability of fuel being present, while an intensity level of 255 equates to a 100 % chance of fuel, (8-bit greyscale images were utilised therefore 255 is the maximum intensity level possible).

This image is built up by first binarising all the images in a set, using a threshold value similar to that described in §4.4.1.1, with more detailed explanations in Chapter 3. The actual threshold value utilised for this set of images was the mean grey intensity level minus 20, which was based upon experience and selected subjectively to select the spray boundary. To eliminate any unwanted pixels within the fuel spray, an erosion filter was utilised, this is based on a 2×2 square filter, and three passes were made. This was followed by a dilation algorithm, of the same size, again, three passes were made using this filter to ensure that the overall spray shape was not altered. The images within the set were then simply arithmetically added together, finally the resulting image was multiplied by a coefficient that was equal to the ratio of the saturation level 255, and the number of images in the set. The result of this process was an 8-bit grey scale image, however to enhance visualisation of the images a pseudo-colour scheme was utilised. The scheme here uses black for 100% fuel and white for 0% fuel to further distinguish between the presence probability of fuel, with a graduation from red, 99%, to blue, 1%, in between. Before the images are discussed it must be noted that in all of the subsequent images the valves are on the right hand side of the fuel spray as it is seen here, however they are outside of the field of view.

The results of this analysis may be seen in Figure 5.10, it shows the results for all three valve lifts, 2, 3 and 5 mm, all at 80.35 kPa back pressure and 5 MPa fuel pressure. It can be clearly seen that as expected a valve lift of 5mm produces the maximum effect on the fuel spray, with a decreasing effect as the valve lift decreases. This is because the jet of air issuing from the valves will increase in size with increasing valve lift. As the air jet increases in size it will affect a larger area of the fuel spray, therefore producing a greater displacement. The PPI images also show that the smaller droplets on the right

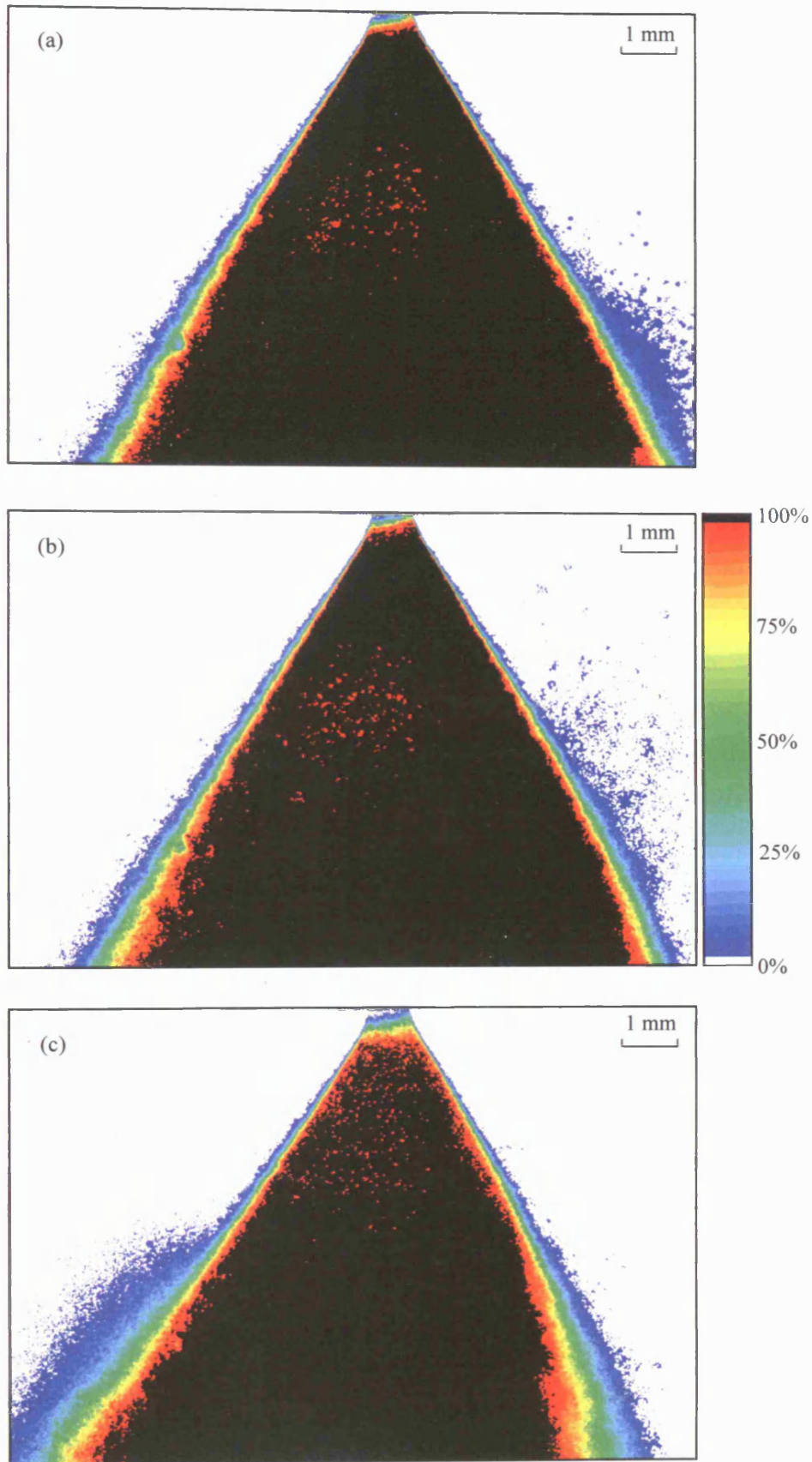


Figure 5.10 – PPI of (a) 2 mm Valve Lift, (b) 3 mm Valve Lift (c) 5 mm Valve Lift, all for 80.35 kPa Back Pressure, 5 MPa fuel pressure

hand periphery of the spray are displaced at a valve lift of 5 mm. These small droplets will be carried with the air jet back into the main spray plume, this would affect the air/fuel mixing process by essentially increasing the concentration of fuel around the fuel spray axis. However, the right hand edge of the spray as shown here was not the only portion of the spray to be affected. The effect of the air flow on the rest of the spray will be discussed later.

It may also be seen that the variability in the spray increases with valve lift, with the most significant variation occurring at 5 mm valve lift. The possible explanations for this are that the air flow becomes unsteady at higher valve lifts, although as this was a steady state flow rig this would be unlikely. The air flow was given ample time to settle to a steady state condition before the images were taken of the fuel spray and should therefore be a similar flow structure at any given time. Therefore the only explanation for the variability is differences within the fuel spray itself, however each PPI image shown here is the average of 40 separate injection events, therefore any major variability in the spray shape would show up in all cases. The variability must therefore be a consequence of the break-up regime of the fuel spray and the position at which the jet of air impinges onto the fuel spray.

The effect the impinging air jet will have on the fuel spray will be dependent on the relative momentums of the two flows. For the case of 2 and 3 mm valve lifts the air jet impinges onto the fuel spray at a point where the fuel spray has a large momentum. At this point the fuel spray is still breaking up into ligaments and will provide greater resistance to the air flow, therefore less deflection will take place. Another consequence of this is that the outcome will be more consistent as the fuel is always in the ligament break-up stage. However for the case of 5 mm valve lift, the fuel has mainly broken up into droplets where the majority of the air impinges, and will therefore be more susceptible to deflection. Differences in the break-up of each fuel injection event however will produce slightly different break-up lengths. Therefore the presence of ligaments, if any, will vary from injection event to injection event at the point of impingement of the air jet and the air jet will therefore have a

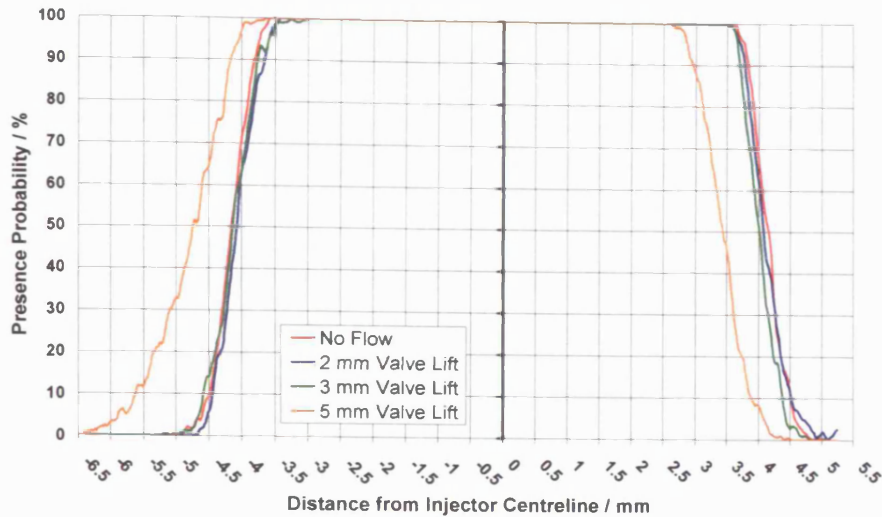


Figure 5.11 – Pixel Intensity across PPI images averaged around 6.5 mm from injector tip

varying effect on the fuel spray. This leads to cycle to cycle variations in the displacement of the fuel.

Although the major effect of the impinging air flow that may be seen was on the right hand edge of the fuel spray as seen here, the left hand edge is also affected by the air flow. This is because the air flow is far from 2-dimensional and will in fact encompass the entire fuel spray, observing Figure 5.12 which provides a schematic representation of the valve/injector layout it may be seen that the fuel spray will be affected from all sides to a varying degree. Figure 5.11 shows the presence probability across the entire PPI image for varying valve lifts, averaged at three distances from the injector tip centred on the y-axis. Further to this a moving average algorithm has been used, in which each successive 10 data points are averaged to provide the point shown. This smoothes the profile allowing the overall trends to be seen without difficulty. This figure shows the increasing affect of the impinging air flow on both sides of the fuel spray. It may be seen that for both 2 and 3 mm valve lifts that the left hand edge of the spray is very similar, the only difference being the variation approximately -3.5 mm from the injector centreline, where the 3 mm case deviates, taking more time to reach 100 % probability of fuel. However on the right hand edge of the spray, the spray boundary for the 3 mm case is shifted approximately 0.1 mm, while the profile remains approximately the same. This indicates that the increasing valve lift firstly affects the right hand

side which is adjacent to the valves, by pushing the spray boundary away from its original, no air flow position. However, there is only a very small difference between the no flow case and the 2 mm valve lift case, indicating that at very small lifts the effect on the spray is negligible.

There is a transition between the 3 and 5 mm valve lift cases, whereby the left hand edge of the spray begins to be affected. It can be seen that the right hand edge of the spray is deflected more than the left hand edge as expected. However, although the bulk of the fuel spray is deflected further on the right hand edge, by approximately 0.8 mm, the small droplets around the left hand edge are displaced away from the bulk flow, while the bulk flow is moved considerably less, approximately 0.4 mm. This may be seen in Figure 5.11 by observing the portion of the 5 mm valve lift plot around -6.5 and then -4.5 mm from the injector centreline, at -6.5 mm there is fuel further from the 2 and 3 mm valve lift cases than there is at -4.5 mm. Conversely on the right hand edge of the spray the bulk of the fuel is moved to a greater degree, this may be seen as the apparent curve of the fuel spray towards the bottom of the image.

Even though the PPI images shown here in Figure 5.10 are thresholded to obtain the spray boundary, holes, in the form of red dots, may still be seen in all cases. This shows that the same sheet break-up mechanisms, as discussed previously in Chapter 4, are in place even with an impinging air flow. The effects on the break-up regime of the fuel spray will be discussed later in this chapter. However it is interesting to note that the holes seen here are in the same location as previously seen in §4.4.2, and that qualitatively the holes seem to increase in size with distance from the injector tip.

5.4 Analysis of Air Flow Visualisation Results

This section will discuss the air flow visualisation results obtained with no fuel injection event. The purpose of this series of tests was to obtain an understanding of the air flow within the flow rig, so that the effects of impinging air flows may be understood. This series of testing was carried out

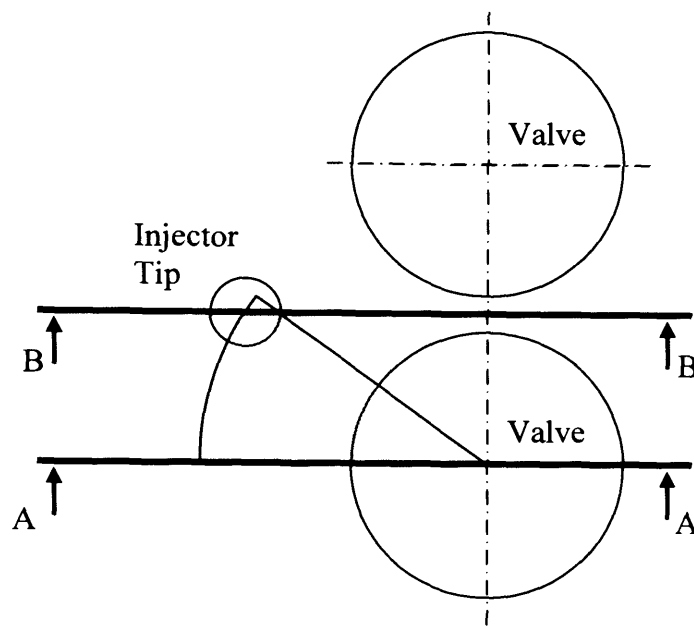


Figure 5.12 – Schematic of the Imaging Planes and the area of assumed consistency of the air flow

with no fuel present, as to produce a significant effect on the fuel spray the air flow rates required are very high, therefore the air flow velocities would be very high, eliminating the possibility of using PIV. Visualisation of the air flow at low flow rates with a fuel spray present was deemed inappropriate as the fuel spray would have affected the air flow to such an extent that the results would not be relevant. Therefore it was assumed that the general air flow topography remained constant with varying flow rates, with only the magnitude of the flow changing. This enabled an analysis of the probable effects on the fuel spray to be carried out, this will be compared to the actual effects in a later section.

5.4.1 Particle Image Velocimetry – Air Flow

Two planes of interest were investigated using the PIV technique, they were the valve centreline and the injector centreline. The flow issuing from the valves will be assumed to be uniform across the area that would have a possible direct effect on the fuel spray, therefore from the axis of the valve throughout this area the flow field may be assumed to be that found using PIV on the single valve plane. It must be noted that unlike a real port, (e.g. within a pent roof cylinder head), where there will be significant circumferential

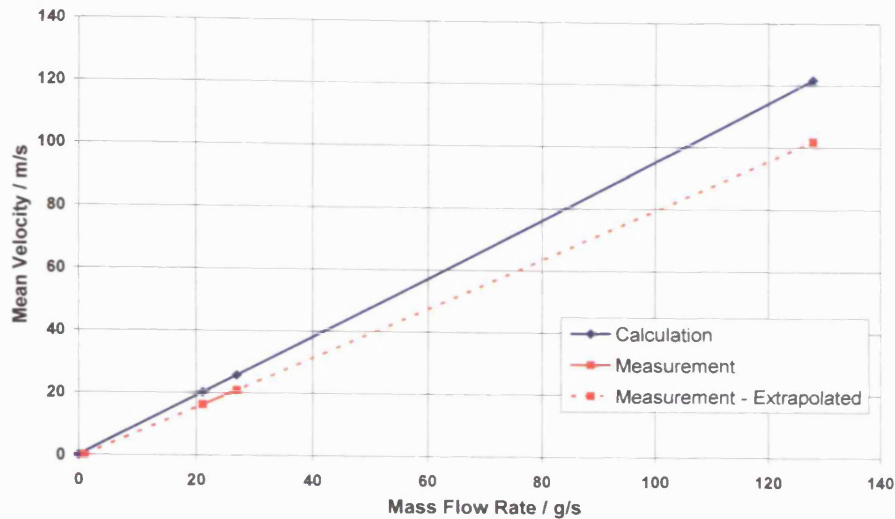


Figure 5.13 – The Calculated vs Measured Mean Velocity variation with Mass Flow Rate

variations in the flow velocity, this rig design, with vertical ports, should produce a fairly even velocity distribution around the valves. Figure 5.13, shows the area where the air flow directed at the fuel spray is assumed to be consistent with that imaged using PIV. The two imaging planes may also be seen in this figure, plane A-A being on the valve centreline and plane B-B on the injector centreline.

As detailed in §5.2.4 the flow rates utilised while visualising the air flows were significantly lower than those used during the imaging of the fuel spray. Therefore it was necessary to scale the PIV vector fields appropriately to allow calculations of the expected fuel spray deflection to provide a comparison to the actual deflection observed. To scale the flow the mass flow rate known from the measurements taken is utilised to calculate the mean velocity through each valve, equation 5.3 shows this relationship;

$$MeanVelocity(m/s) = \frac{\dot{m}(kg/s)}{A_c(m^2) \times \rho_a(kg/m^3)} \quad \text{eq. 5.3.}$$

Where \dot{m} is the mass flow rate through both valves measured by the air flow meter, A_c is the total valve curtain area for both valves and ρ_a is the density of the air inside the flow rig. This allows the mean velocity to be calculated for the flow rates utilised during both PIV and fuel visualisation. Figure 5.13

shows the calculated mean velocities with varying mass flow rates for a 5 mm valve lift. Also plotted are the mean velocities obtained from the PIV imaging, these are obtained by averaging the flow velocity at the exit from the valve. It was assumed that the relationship between the mean velocity and the mass flow rate will remain linear across the range of flows investigated. It was also assumed that the flow topography will remain constant, and that it will be similar for all three valve lifts examined, merely more and more compressed with reducing valve lift. The PIV results were unable to provide results at 2 and 3 mm valve lift as the seed density became too low, therefore the results from the 5 mm valve lift case were utilised and extrapolated to provide information regarding all test cases.

To scale the PIV vectors for the 5 mm valve lift case the measured mean velocities from the low flow conditions were simply extrapolated to provide a mean velocity for the high flow test condition. This was then used to scale the vector image to produce a vector field for the high flow test condition. However as measured velocities were not available in the valve plane for the 2 and 3 mm valve lift cases, the calculated mean velocity was utilised, modified by a factor $R_{m/c}$, to account for the differences in measured and calculated mean velocities;

$$R_{m/c} = \frac{\text{Mean Velocity}_{\text{measured}}}{\text{Mean Velocity}_{\text{calculated}}} \quad \text{eq. 5.4.}$$

The vector field shown in Figure 5.14 was scaled using the mean velocity found by extrapolation shown in Figure 5.13. It is assumed that there are no major differences between the flow fields other than the overall magnitude of the velocities. The profile for section Z-Z in Figure 5.14 is shown in Figure 5.15, and is the velocity profile of the air jet at the trailing edge of the valve. The profile was constructed by averaging the three lines of vectors on and either side of section Z-Z, the origin is at the valve. For ease of data handling the section A-A is at 45° to the valve axis, however the actual flow direction is at approximately 43°.

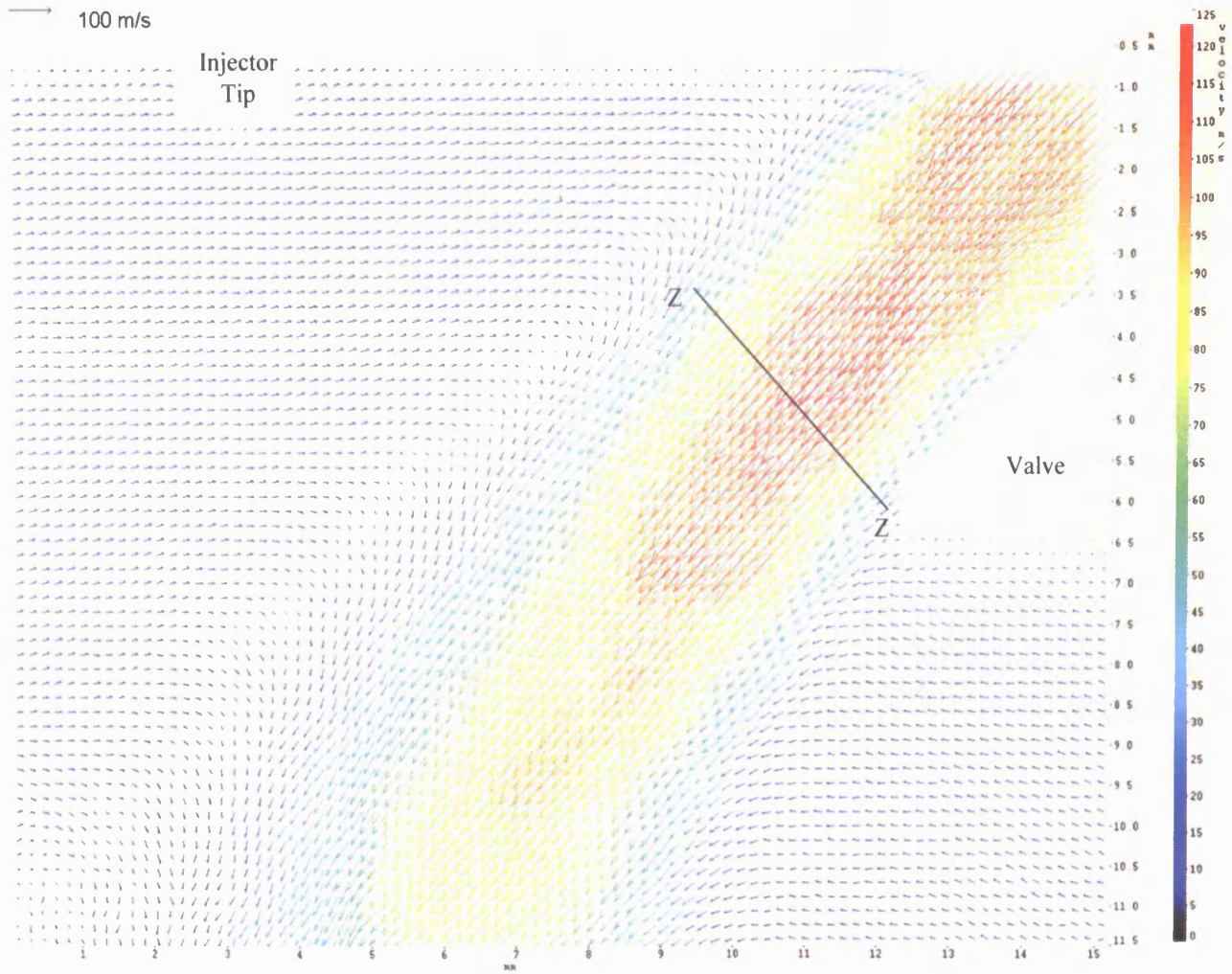


Figure 5.14 – Scaled Vector Field for 5 mm Valve Lift – Plane A-A, Valve Centreline

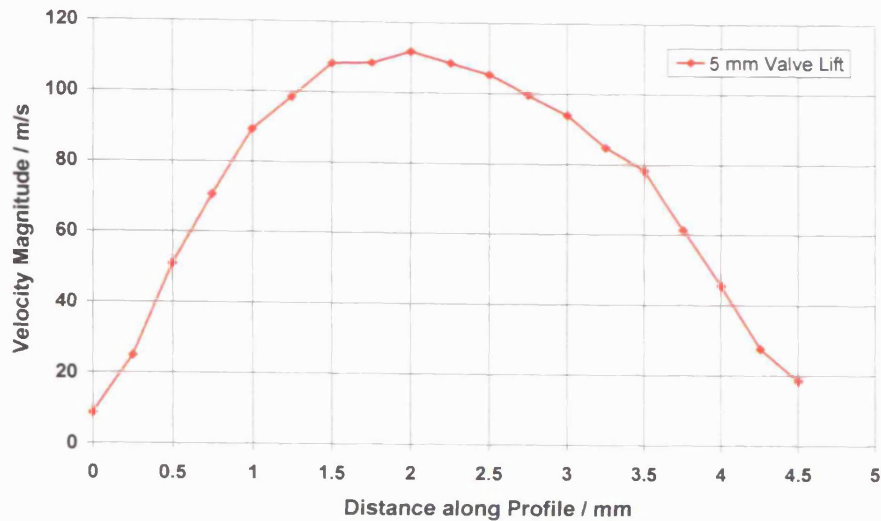


Figure 5.15 – Velocity magnitude Profile of section Z-Z (Figure 5.10)

Observing Figure 5.15 it may be seen that the velocity increases very quickly with distance away from the valve surface up to the free stream velocity of 111 m/s. As the profile proceeds away from the free stream velocity it can be seen that it falls at a lower rate. This is because this side of the air jet is open to the bulk of the air within the flow rig, therefore air may be drawn into the jet, increasing its width to some extent, while increasing the velocity at the fringes. This may be seen in Figure 5.14 at the left hand edge of the air jet, where the bulk air is drawn into the flow, with a consequent sudden change in direction.

PIV was also carried out on plane B-B, the injector centreline, this gave an indication of the flow pattern that would directly affect the spray profile as seen in the fuel spray images. It also shows how the two flows from the individual valves converged to produce a combined air flow. The vector fields for plane B-B may be seen in Figures 5.16, 5.17 and 5.18, for all three valve lifts studied at a single pressure drop across the valves of 4 mmHg, 530 Pa. The velocity vector fields are shown here at half density, i.e. only every other vector is shown, this is to give clarity to the vector field allowing the general features to be seen with ease.

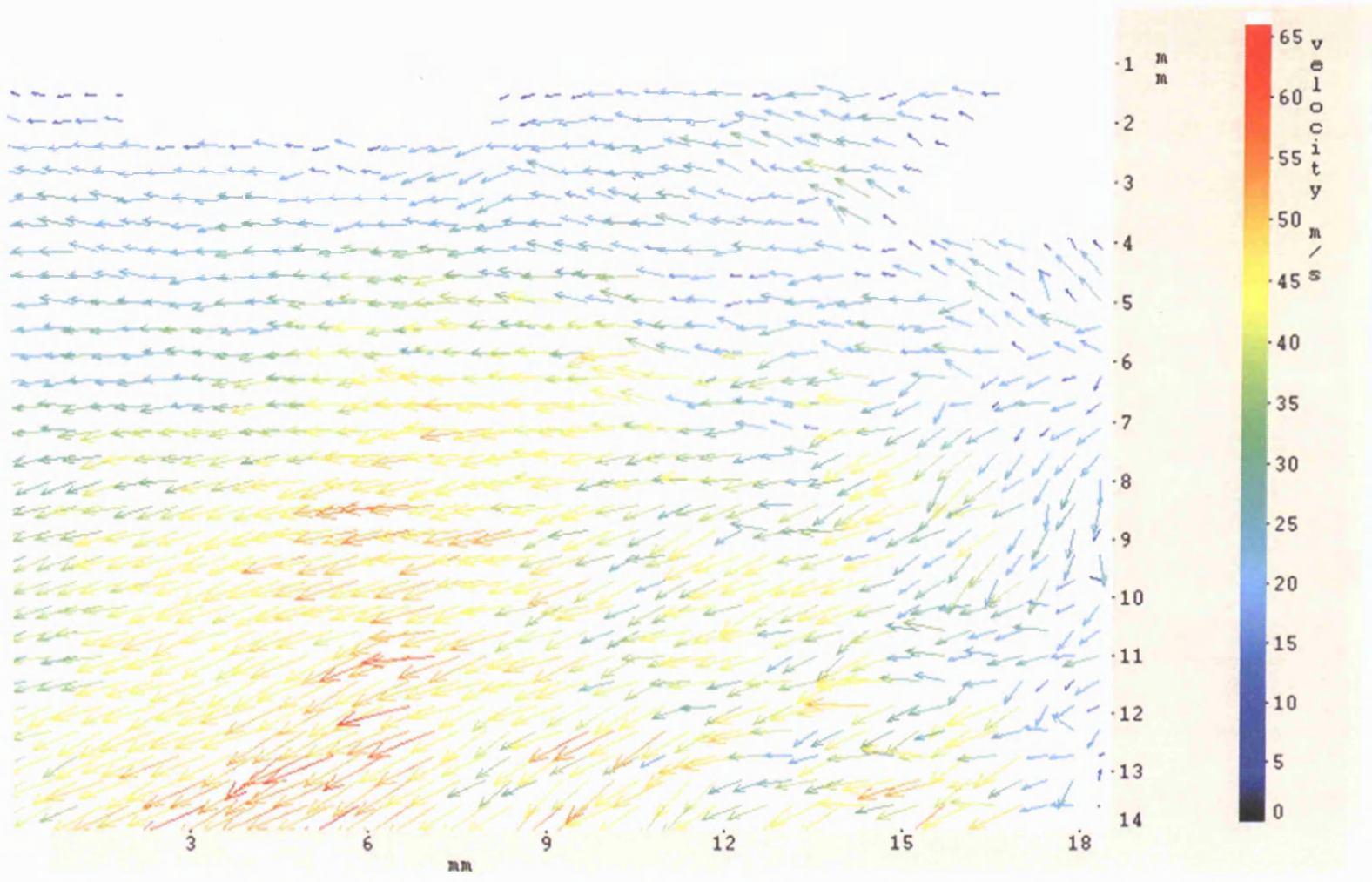


Figure 5.16 – Scaled Vector Field for 2 mm Valve Lift, 530 Pa Depression – Plane B-B

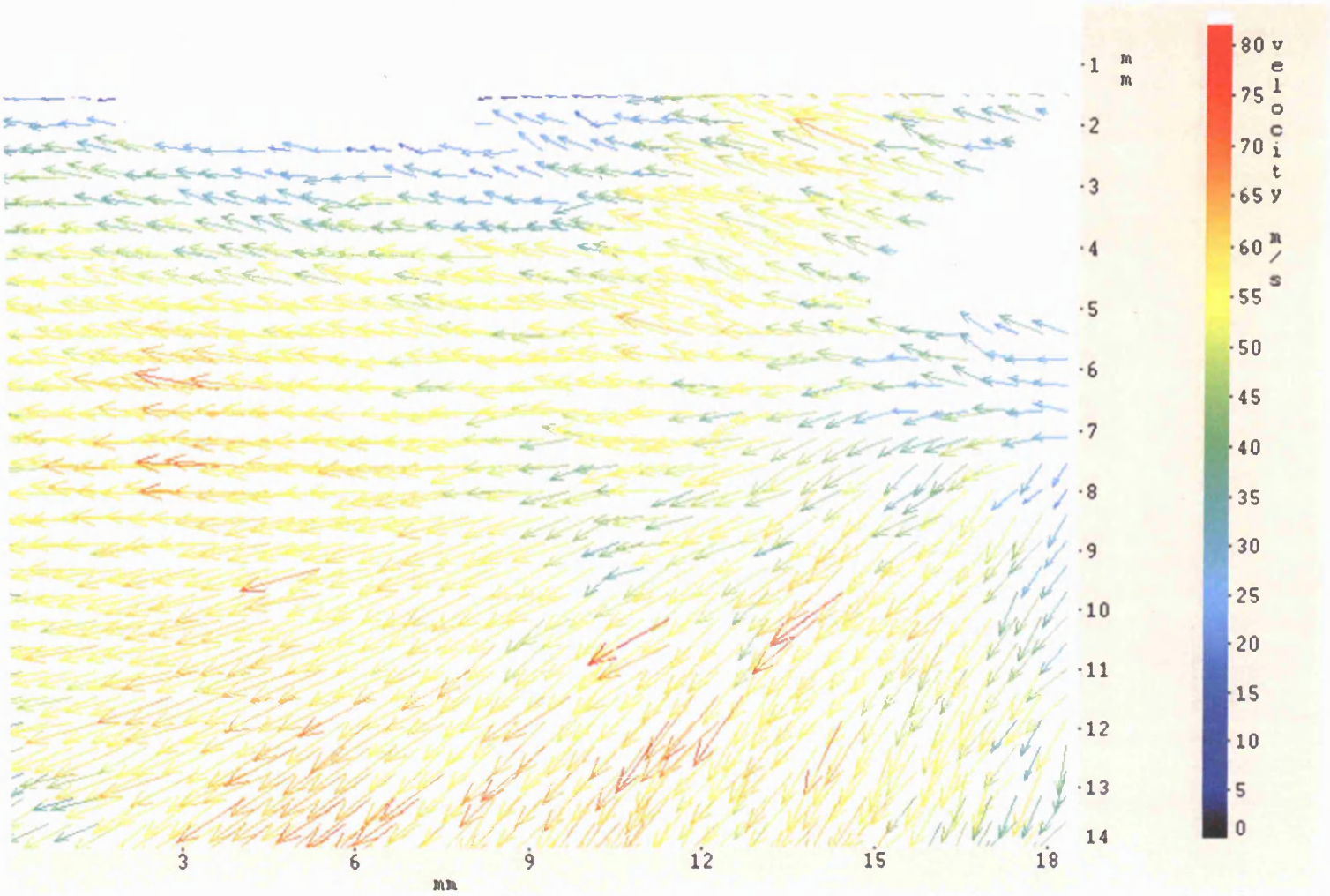


Figure 5.17 – Scaled Vector Field for 3 mm Valve Lift, 530 Pa Depression – Plane B-B

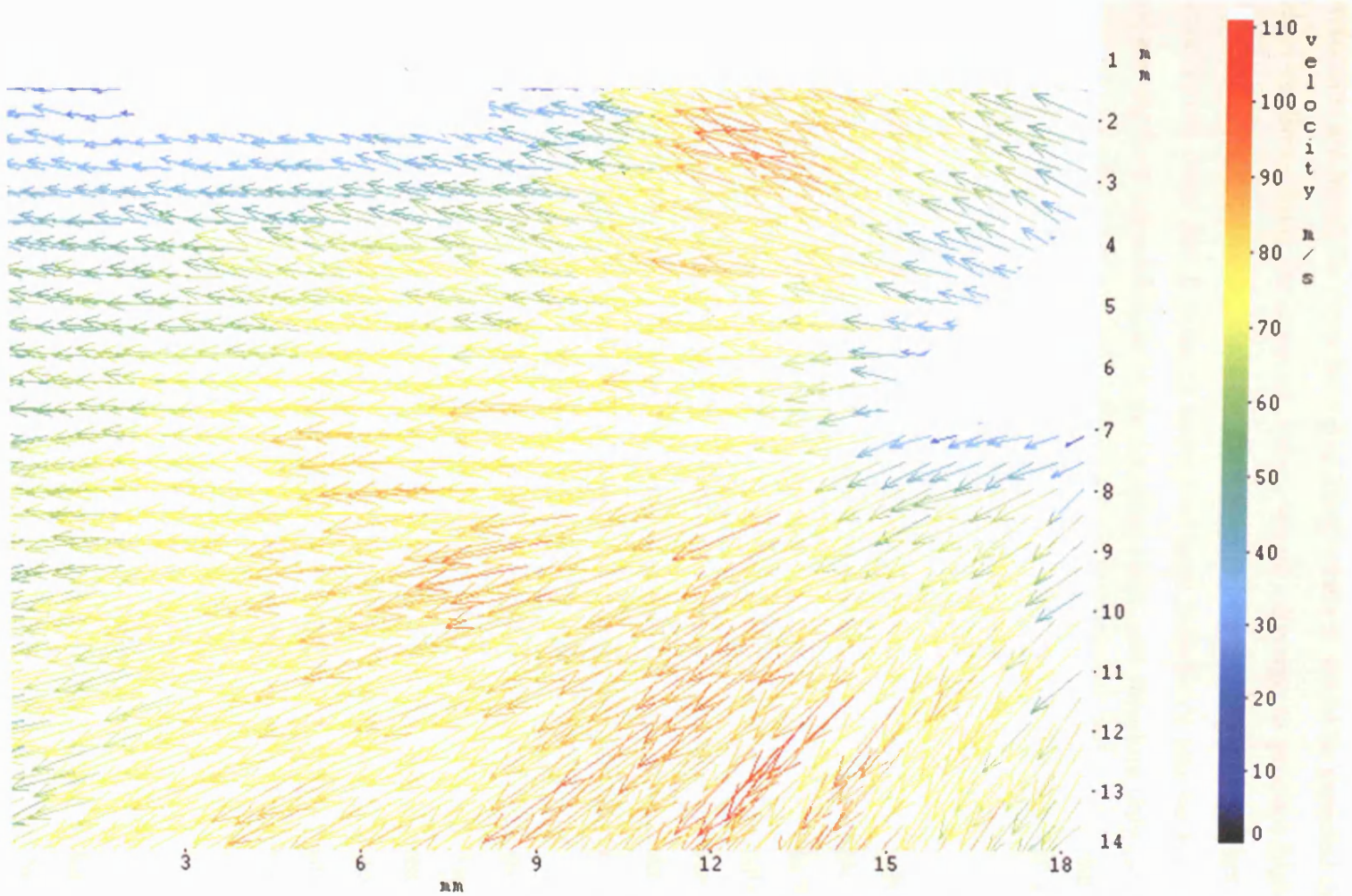


Figure 5.18 – Scaled Vector Field for 5 mm Valve Lift, 530 Pa Depression – Plane B-B

Observing Figure 5.16 to 5.18 it may be seen that the magnitude of the velocity flow field increases with increasing valve lift. Figure 5.16, shows the flow field for 2 mm valve lift, it may be seen that the maximum flow velocities are found far from the valve itself, where it would be expected that the two flows from the separate valves would converge to produce higher velocities, as opposed to close to the valves where the flows would act to cancel each other out. It must be noted that these flow fields take no account of any air flow perpendicular to the imaging plane, and therefore only give a limited insight in to the air flow within the test rig. However they are useful to allow comparisons of the imaged fuel and the apparent effects of the impinging air flow and the air flow itself.

All three valve lifts produce very low flow velocities around the valves themselves, as stated earlier this is due to the effect of not being able to visualise the flow perpendicular to the imaging plane. The flow close to the valves will mainly be out of the imaging plane, and therefore not visible. However moving further from the valve location the flow velocities increase, indeed they appear to radiate away from the valve opening. This would be expected as the two flows will merge, as they move away from the valves.

The flow for the 5 mm valve lift case appears to be the most uniform, with the highest velocities at the point of intersection between the individual valve flows, decreasing from that point on. The uniformity of the flow decreases with decreasing valve lift, and therefore mass flow rate, with the flow for 2 mm valve lift being the most disordered. Therefore the lower valve lift cases, with this fact and the concerns with scaling of the flows, must be treated with caution.

5.4.1.1 Theoretical Effect of Impinging Air Flow on Fuel Spray

The results obtained from the PIV, (after scaling by the appropriate factor to account for the increased pressure drop across the valve), of the air flow were utilised to calculate the theoretical effect on the overall characteristics of the fuel spray. To accomplish this the cone profile for the *no flow* case was extracted from the PPI images using a similar method as used in §4.4.1.1. This

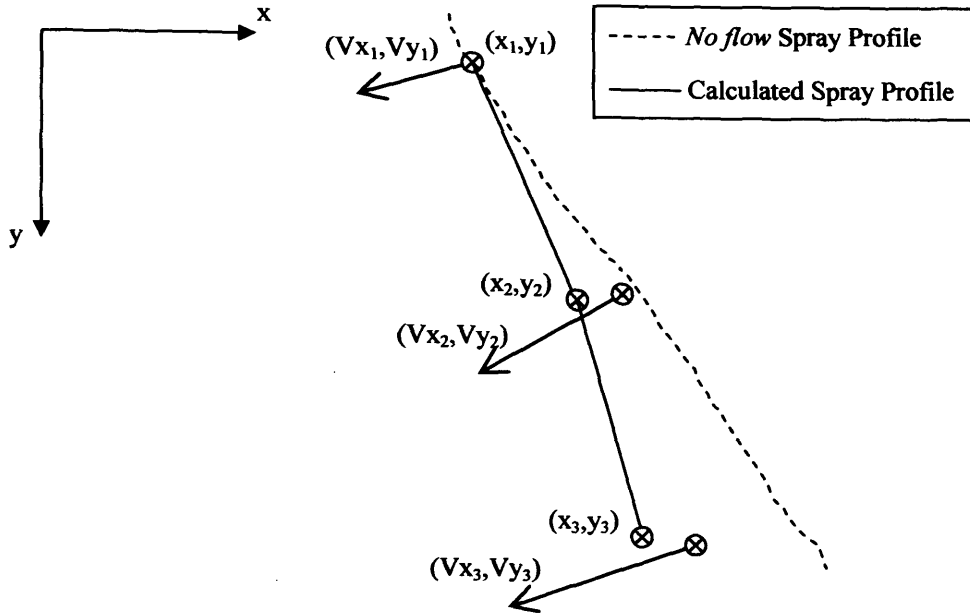


Figure 5.19 – Schematic representation of the Spray profile Calculation Process

profile was utilised as a base spray profile, to which the air flow was applied to obtain the estimated spray boundary with an impinging air flow. The PPI images were thresholded at a value equivalent to 50% fuel presence probability.

To calculate the effect of the impinging air flow, the pressure exerted on the fuel spray by the air was calculated at a series of locations along the fuel spray boundary. The number of locations utilised was determined by the density of the velocity vectors in the PIV vector fields. The velocity vectors used, as can be seen in Figure 5.19, were chosen to be as close as possible to the spray boundary. To provide an accurate result the velocity vector used for each step was based on the result of the previous calculation to find the fuel spray displacement, i.e the vector (V_{x2}, V_{y2}) , was the closest available vector to the calculated spray boundary at position (x_2, y_2) . The initial velocity vector used was that at the top of the spray boundary of the *no flow* case. This was then used to calculate the displacement it would produce on the fuel spray. Due to the vector density in the vector field the closest available velocity vector was used, this was not necessarily exactly at the spray boundary. However the maximum distance between the vector used and the spray boundary was less than 0.1 mm. It was assumed that the change in the velocity vector field over this distance would be negligible.

The algorithm utilised to calculate the fuel spray displacement may be seen below;

1. Obtain velocity vector by looking up vector in Vector Field at location of first *no flow* spray boundary coordinates.
2. Calculate Force on fuel spray utilising velocity magnitude and air properties, see equation 5.5.
3. Look up fuel spray thickness at appropriate distance from injector tip. (From Schmidt [1999] analysis)
4. Calculate Spray angle to use in calculation of Displacement.
5. Calculate Displacement of fuel spray using calculated Force and mass of fuel calculated from known area and thickness of fuel spray, see equation 5.6.
6. Repeat steps 1 – 6, substituting *no flow* spray boundary for calculated spray boundary.

The algorithm utilised the following equations to calculate the spray profile;

$$F_a = \frac{1}{2} \rho_a U_a^2 \times A_f \quad \text{eq. 5.5.}$$

Where F_a is the force applied to the fuel spray by the impinging air flow, ρ_a is the density of the air, U_a is the velocity magnitude at that spray boundary and A_f is the area of fuel. The area of fuel is based on the sample density when obtaining the spray boundary, and is a square of height and width equivalent to 10 pixels.

$$D_f = V_{f,x} \times \text{Time} \quad \text{eq. 5.6.}$$

$$V_{f,x} = \sqrt{2(F_a / m_f) d_f} \quad \text{eq. 5.6a.}$$

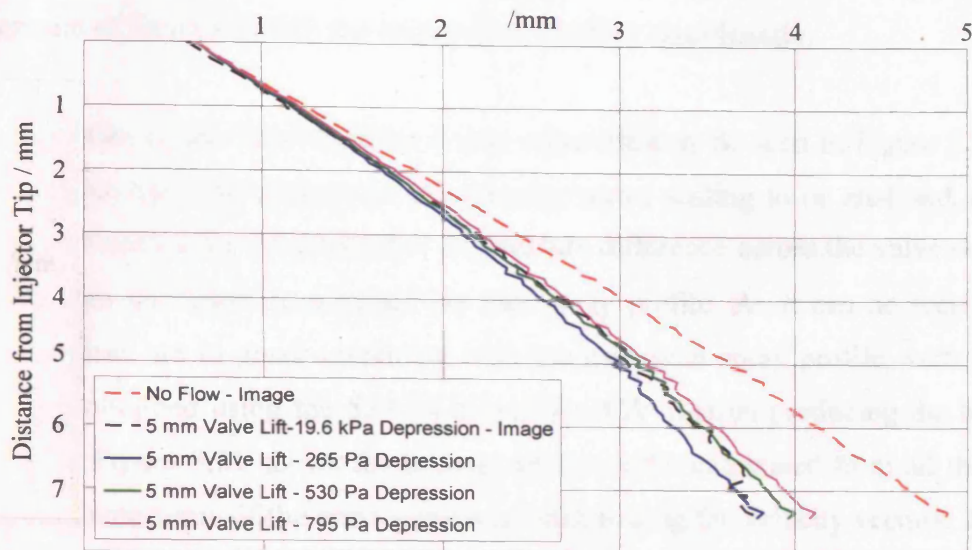


Figure 5.20 – Plot of Spray profiles – Obtained from Images and Calculation

Where D_f is the distance the fuel spray was displaced by the impinging air flow over a single time step, V_f is the velocity, in the x direction, of the fuel spray induced by the impinging air flow, m_f is the mass of the fuel spray element and d_f is the step increment, equivalent to 10 pixels.

Using the scaled velocity vector fields on the injector plane, (plane B-B, figure 5.12), and the algorithm laid out above, the expected spray boundary may be calculated. This will provide only an approximation due to the number of assumptions made. Firstly it was assumed that the velocity vector field may be scaled from the low flow conditions used during the PIV imaging to the high flow conditions used during the imaging of the fuel spray. Also the thickness of the spray used to calculate the elemental mass of fuel was assumed to be that as calculated using the Schmidt [1999] analysis, with the appropriate boundary conditions for Injector A. No account was made for the break-up of the fuel spray, it was assumed that the air flow acted upon a continuous sheet of fuel. It was also supposed that the effects due to the viscosity of the fuel were negligible, in that, the algorithm looks at only a small element of the fuel spray, the effects of the neighbouring elements were not considered. As no data was available for the air flow with fuel present, it was assumed that the air flow did not change in the presence of the fuel, this would not be the case,

however, the injection duration is very short, 2 ms, which is a very small amount of time to disturb the steady state air flow significantly.

The results of this algorithm for 5 mm valve lift may be seen in Figure 5.20. To enable the effectiveness of the velocity vector scaling to be analysed, the results obtained for 270, 530, 800 Pa pressure difference across the valve were all scaled and used to calculate the fuel spray profile. As it can be seen all three cases are in good agreement with the measured spray profile, with the results obtained using the 530 Pa depression PIV vectors producing the best results. Figure 5.21 shows the average spray profile calculated from all three to eliminate some of the error associated with scaling the velocity vectors. The average calculated spray profile shown is in excellent agreement with the measured case obtained from imaging the fuel spray directly. Therefore scaling the velocity vectors using the method described previously, may be considered an appropriate manner to obtain otherwise unobtainable results. The only major deviation occurring far from the injector tip where the fuel spray will have broken up sufficiently to allow individual droplets and ligaments to act independently, therefore the air flow has a greater effect on them.

Figure 5.21 shows three further plots of the calculated spray profile, for 2 and 3 mm, and 5 mm valve lifts, averaged over the three depressions utilised in the PIV imaging. To provide a direct comparison Figure 5.22 shows an overlay of all three profiles for varying valve lifts in comparison to the *no flow* condition. The results achieved by the algorithm get progressively better from the 2 mm to the 5 mm valve lift case. It was shown previously that the PIV images obtained on plane A-A, were inappropriate to be used in the scaling process. However the PIV images obtained on plane B-B, the injector plane, were superior to those on plane A-A, the valve plane, therefore they were utilised for these calculations. However, as no data was available for the mean velocity through the valve for the 2 and 3 mm valve lift cases, the scaling factor obtained with the 5 mm valve lift case was used. This increased the error associated with the scaling process with decreasing valve lift. Hence the improving accuracy as the valve lift approaches 5 mm.

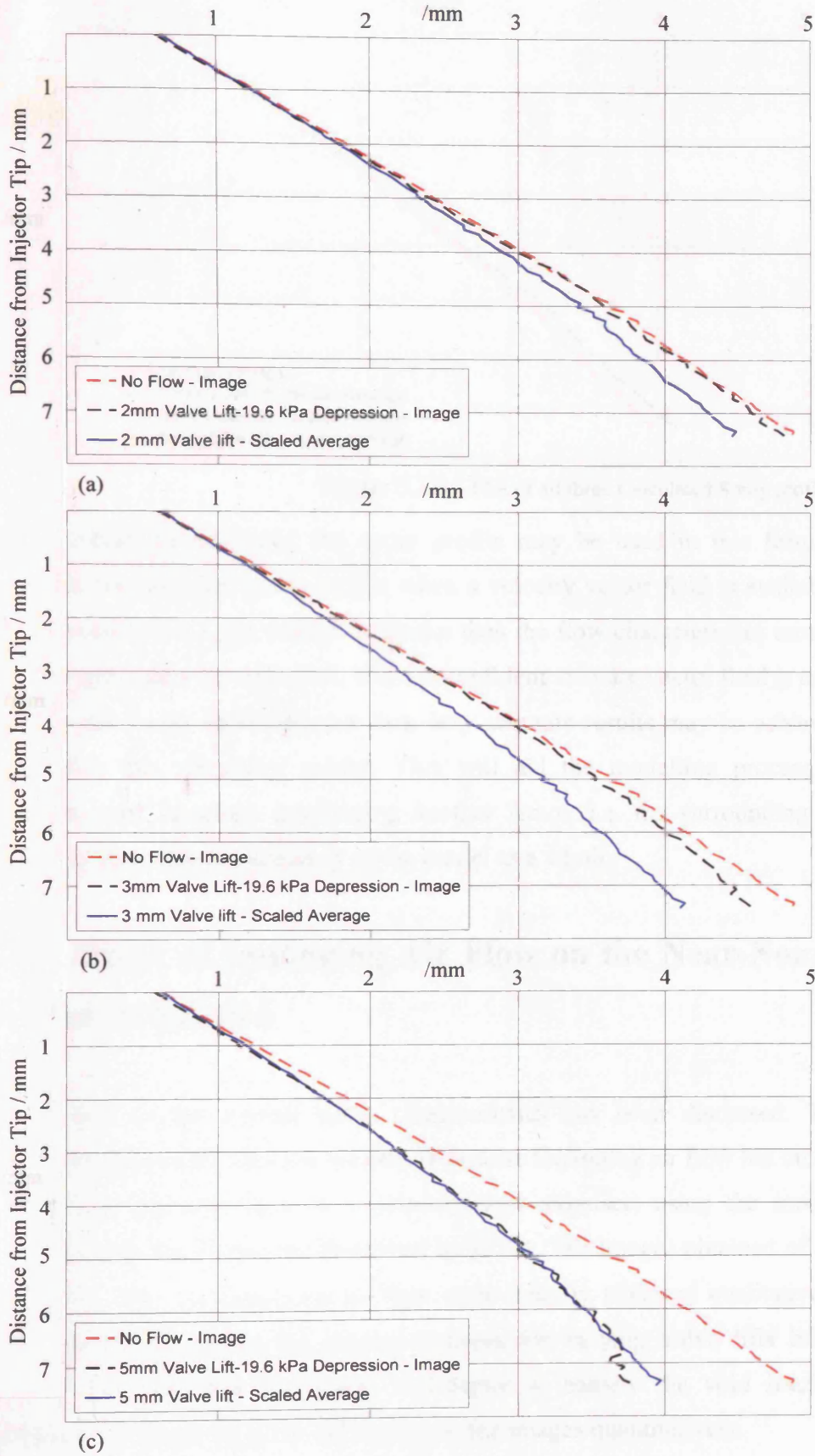


Figure 5.21 – Plot of Spray profiles – (a) 2 mm Valve Lift, (b) 3 mm Valve Lift, (c) 5 mm Valve Lift

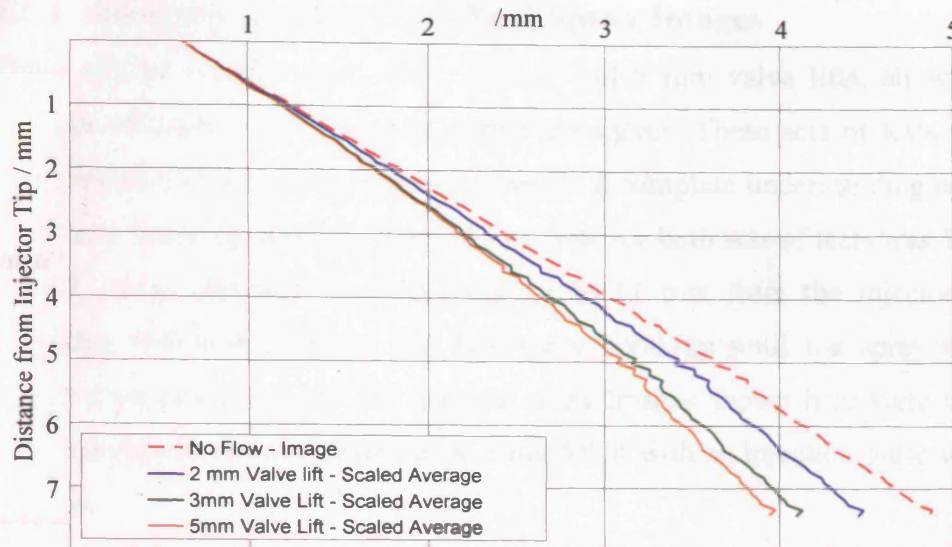


Figure 5.22 – Plot of all three Calculated Spray profiles

This method for analysing the spray profile may be used in this form to calculate the expected spray profile when a velocity vector field is available, or, conversely if a spray profile is known then the flow characteristics around the fuel spray may be estimated. When a confident velocity vector field is used as with the 5 mm valve lift case then very accurate results may be achieved even with this simplified model. This will aid the modelling process of pressure-swirl injectors, introducing another factor, i.e. the surrounding air flow, and therefore the accuracy of the model as a whole.

5.5 Effect of Impinging Air Flow on the Near-Nozzle Characteristics

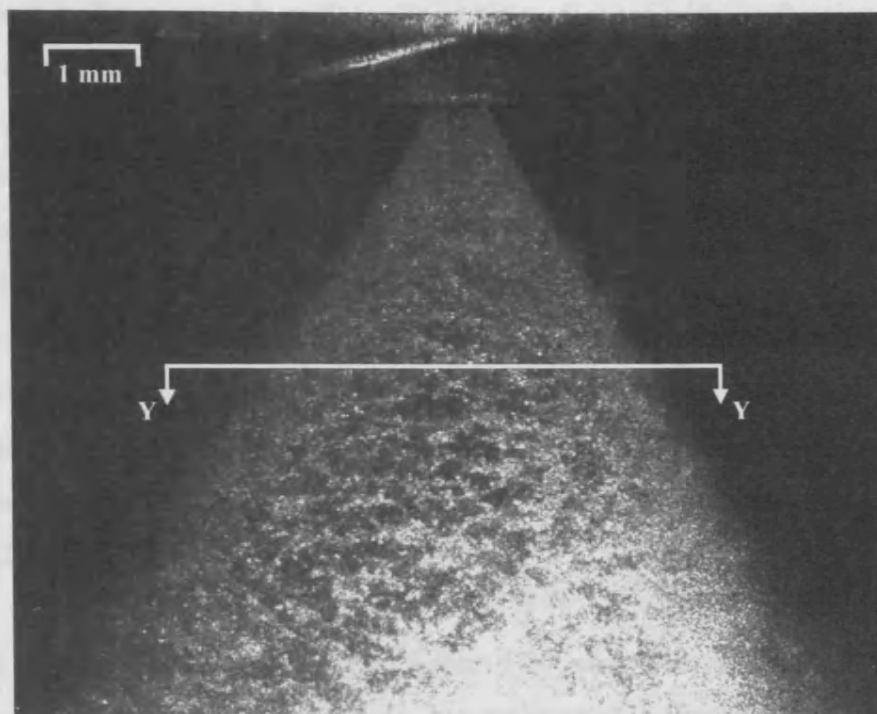
The effect on the overall spray characteristics has been discussed. The following section will discuss the effects that the impinging air flow has on the near-nozzle characteristics of a pressure-swirl atomiser, using the images obtained with the techniques described in §5.2.2. The images obtained of the fuel spray with an impinging air flow were initially analysed qualitatively, with the differences in the general features for varying valve lifts being determined. The tools developed in Chapter 4, namely the void fraction technique etc, were then utilised to analyse the images quantitatively.

5.5.1 Analysis of Near-Field Fuel Spray Images

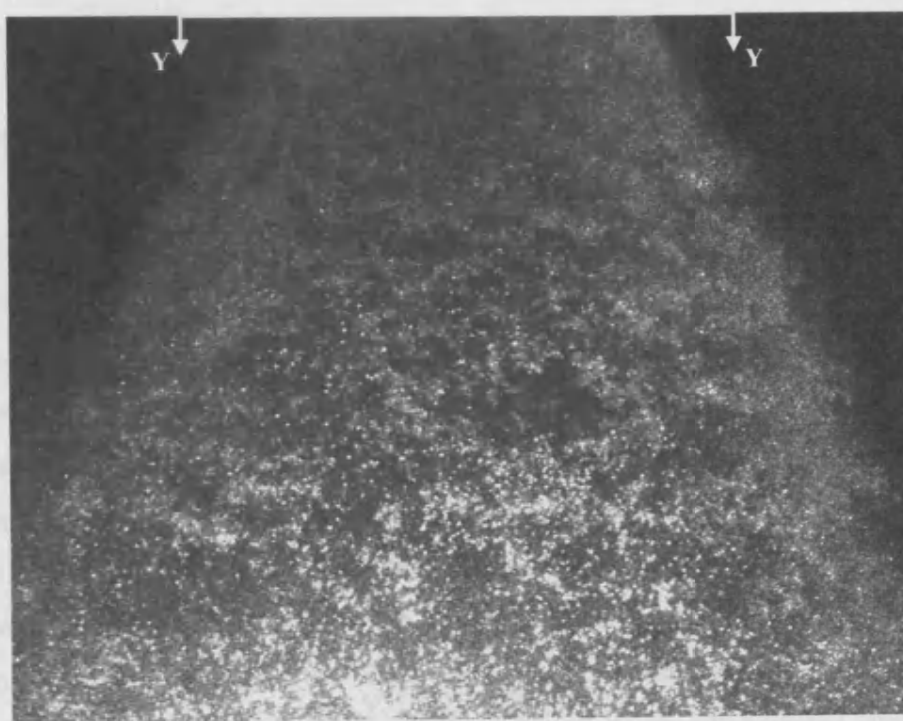
Three sets of images were taken, at 2, 3 and 5 mm valve lifts, all with a pressure difference of 19.65 kPa across the valves. These sets of tests were then repeated further downstream to provide a complete understanding of the fuel spray break-up process. The field of view for both sets of tests was 10.75×8.125 mm, imaging the fuel spray up to 11 mm from the injector tip, providing information about the fuel spray break-up until the spray is no longer a continuous sheet. All the fuel spray images shown here were taken with a fuel pressure of 5 Mpa and at 1 ms ASOI with an injection pulse width of 2 ms.

Observing Figure 5.23(a), an image of a fuel spray with an impinging air flow from a valve lift of 2 mm, it may be seen that in general the break-up mechanism is similar to that observed with no impinging air flow. The fuel sheet forms holes, these holes then increase in size until the sheet can no longer remain stable. Due to the large gradient in light intensity it is not possible to show the entire image in the best possible way, therefore the bottom of the field of view, (closest to the fibre optic light guide), is shown here with apparently no detail. However when the image display is adjusted to suit this area, more detail may be seen. Figure 5.23(b) shows the fuel spray further along the injector axis, and will be known as the downstream field of view from now on. It can be seen that the fuel sheet has fully broken up into droplets and ligaments towards the bottom of the field of view. The transition from continuous spray to ligaments and droplets can be clearly seen and gives further credence to the break-up mechanism proposed in Chapter 4.

The effect of the impinging air flow for this 2 mm case is limited, the right hand edge of the spray is marginally deflected, as shown in §5.3.2 with the PPI analysis. Observing the right hand edge of the fuel spray in Figure 5.23(b), the surface appears to be rougher than the left hand edge. The impinging air flow will disturb the sheet surface, forcing the small droplets already separated from the main sheet into the core of the spray. Therefore, where there



(a)



(b)

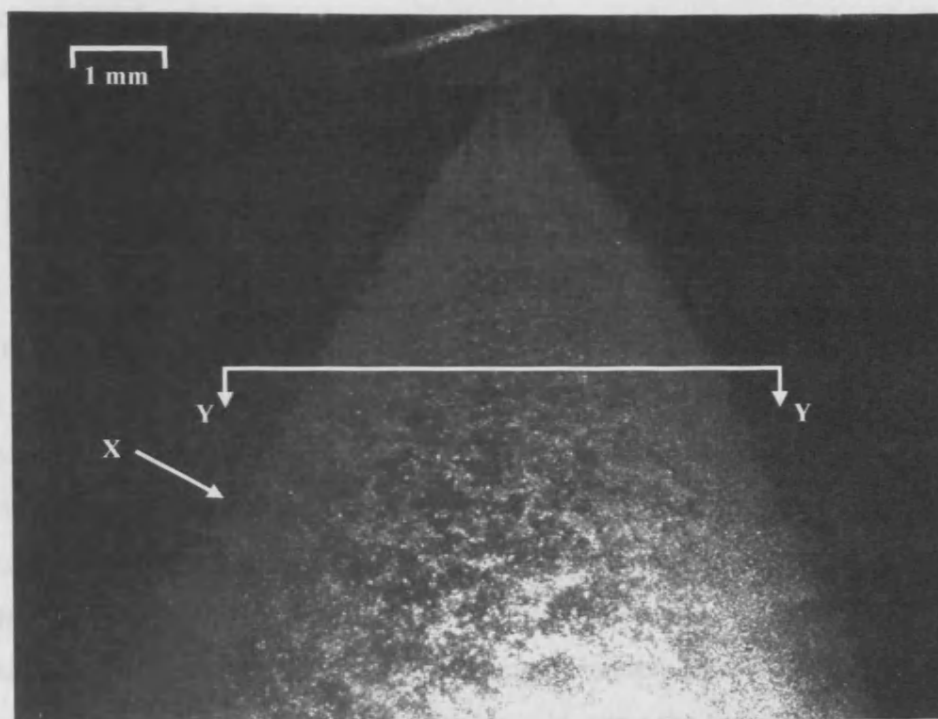
Figure 5.23 – Fuel Spray image, (a) Injector Tip and (b) Downstream, 2 mm Valve Lift, 19.65 kPa Depression, 5 MPa Fuel Pressure

appeared to be a smooth surface, consisting of sheet with perforations and small droplets, there is now only sheet, creating an apparently rough surface.

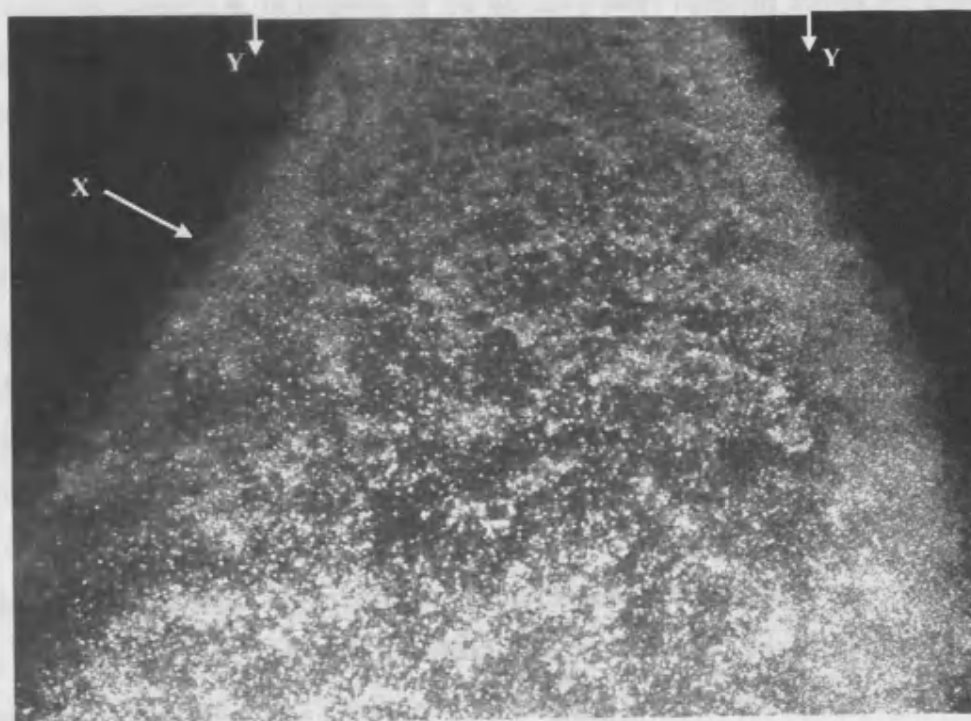
This is a very small effect on the near field characteristics of the fuel spray, and, at least qualitatively it can be said that the effect of an impinging air flow at low valve lifts will be negligible, even at relatively high mass flow rates. However, attention must be drawn to the fact that this is a steady state flow rig, with this particular valve lift being just a fifth of the maximum found in a typical direct injection spark ignition engine. Therefore care must be taken in comparing the effects seen here and the possible effects that may occur within a DISI engine cylinder.

The 3 mm valve lift case shown in Figure 5.24, shows the same field of view as for the 2 mm case in Figure 5.23. It may be seen in Figure 5.24(a) that the effect of the impinging air flow is much greater in this case, despite the difference in valve lifts being only 1 mm. The deflection of the main body of fuel spray is far more significant in this case, being visible in both the injector tip and downstream FOVs.

In addition to the deflection of the main body, the right hand edge of the spray appears to have small droplets, (although slightly out of focus), being separated from the main body of the fuel sheet. Referring back to Figure 5.12, the schematic of the valve / injector layout it can be seen that the two air flows from the individual valves will be interacting in this area. Furthermore observing the PIV vector field on the injector plane in Figure 5.17, it can be seen that around the area where droplets may be seen the air flow has a slight negative vertical component which would act to strip the small droplets away from the periphery of the fuel sheet, and to reduce their velocity. However the air flow in close proximity to the fuel spray will be greatly affected, and will not resemble the air flow visualised using PIV. Although the air flow will be disturbed, it would provide more resistance to the fuel spray than that from a quiescent air chamber, therefore any small droplets on the periphery of the fuel spray will act to mushroom, slowing in the axial direction while being pushed away from the main fuel spray by the following fuel. The air flow



(a)



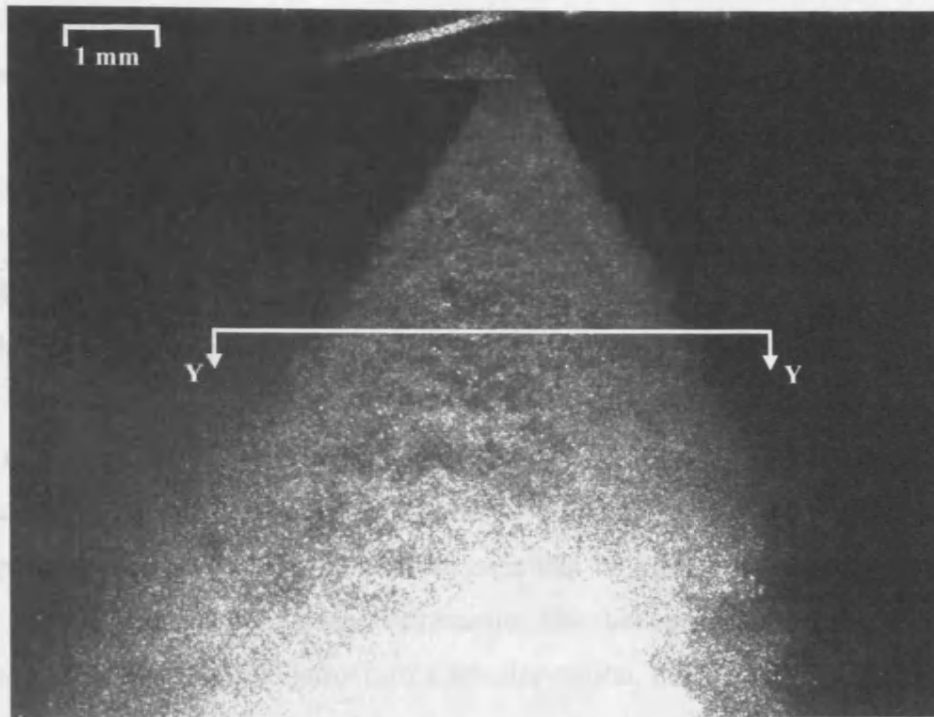
(b)

Figure 5.24 – Fuel Spray image, (a) Injector Tip and (b) Downstream, 3 mm Valve Lift, 19.65 kPa Depression, 5 MPa Fuel Pressure

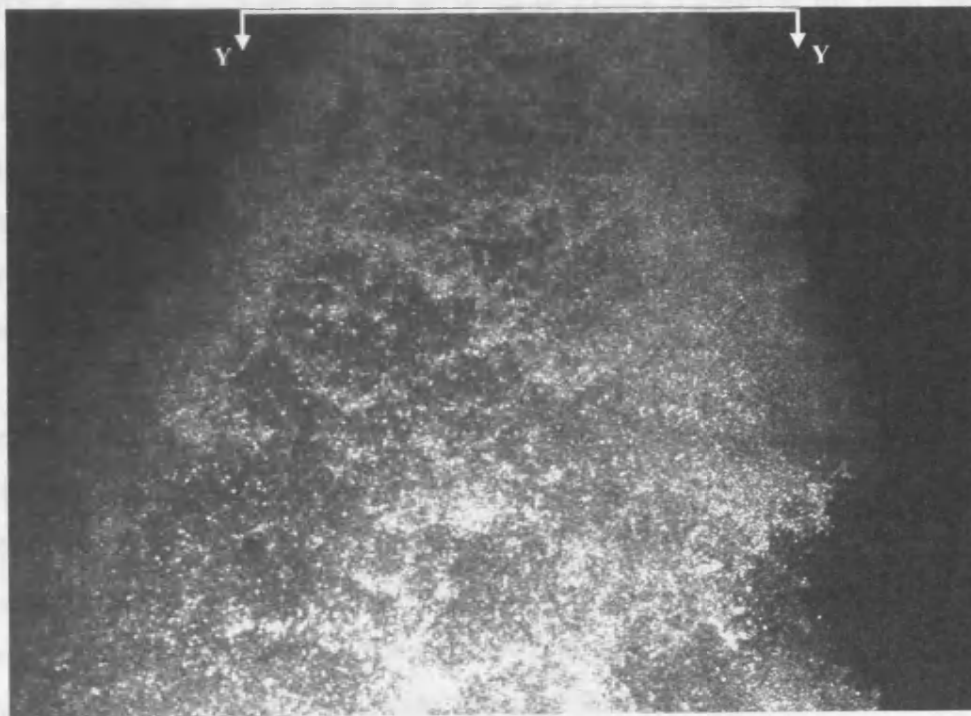
from either side of the fuel sheet will also act to envelop the spray drawing the small droplets away from the main body. The combination of both phenomena will act to produce the type of spray distribution seen here.

The point 'X' reproduced on both Figure 5.24(a) and (b) indicates where the fuel spray appears to deflect away from the injector axis. For this to take place there must be an external force acting on the fuel spray at this point. There are two possibilities, either there is an area of low pressure acting to produce a force on the sheet, or the air flow is affecting the fuel sheet from the inside. If the fuel spray were acting as a solid body, then the deflection at point B would be caused by the drag force on the body, creating a pressure drop at the back of the spray relative to the flow direction. With a continuous sheet the pressure inside of the fuel spray would remain approximately constant, therefore the pressure difference across the fuel sheet would cause the deflection. This is the same effect that causes the fuel spray to collapse with increasing back pressure as seen in Chapter 4, in reverse. If the air flow were uniform across the entire fuel spray then the deflection caused by the pressure drag would increase linearly with distance from the injector tip, as the pressure drag is dependent on a representative dimension of the fuel cone, which increases linearly with distance from the injector tip. Therefore the measured half cone angle would increase, with no sudden changes in the angle. However if the air flow was uneven, as may be expected, due to the conical shaped air flow from the valves, see Figure 5.14, then the drag force on the spray will be much greater where the jet impinges on the fuel spray, therefore producing a sudden change in the spray shape.

Although no data is available concerning the flow pattern for 3 mm valve lift on the valve plane, it may be assumed that the flow will be similar to that of the 5 mm valve lift case. The angle of the air jet to vertical will be larger for 3 mm valve lift, and would therefore impinge on the fuel spray further up, creating the flow pattern described here. The other possibility is that the air flow 'punches' a hole in the fuel spray, continues through the relatively empty core, creating an increase in pressure on the inside of the spray instead of, as previously described, a decrease of pressure on the outside of the spray. This



(a)



(b)

Figure 5.25 – Fuel Spray image, (a) Injector Tip and (b) Downstream, 5 mm Valve Lift, 19.65 kPa Depression, 5 MPa Fuel Pressure

effect may simply provide the means for air to be entrained into an otherwise impermeable spray core, therefore reducing the effect of the collapsing spray cone due to the pressure difference across the fuel sheet, this is created by the air in the core being partially evacuated by the drag at the fuel surface. As the right hand edge of the spray appears to be relatively intact it may be assumed that the affect on the left hand edge of the fuel spray due to this phenomenon would be negligible in this case.

The effect of the air flow on the fuel spray for the 5 mm valve lift case is far more significant than either of the other two cases. Figure 5.25 shows the images obtained at this test condition, as it can be seen the disruption to the right hand side of the fuel spray is dramatic. The fuel spray is deflected a large amount, compressing the spray into a smaller region, hence the increased light levels in the middle portion of the fuel spray, due to an increased continuous area of fuel, and therefore an increased level of Mie scattered light. This increase in light intensity is less apparent in Figure 5.25(b) as the light was more evenly distributed originally, for the reason that the light guide was further from the fuel sheet due to an increase in distance from the ‘back’ sheet to the ‘front’ sheet, therefore a larger and more even light distribution was possible. However the level of deflection is still large, the air flow appears to break the fuel spray up into smaller droplets than the previous two valve lift cases, with the small droplets being forced into the core of the spray.

The air flow, with velocities of the order of 100 m/s around the region of the fuel spray, will obviously dramatically decrease the life time of a droplet compared to injecting into a quiescent air regime. It will also aid in the break up of ligament structures, thereby producing a smaller drop size distribution. However the consequence of the air flow is to also produce a more compact region of fuel, increasing the time required for the fuel to mix with air to produce a combustible mixture. In an actual DISI engine, the occurrence of this situation whereby the fuel is injected during intake valve opening, will be for homogeneous charge operation, i.e. early in the cycle. The compact fuel spray is therefore a disadvantage, with the effect of resisting air/fuel mixing within the engine cylinder.

5.5.1.1 Fuel Spray Imaging in conjunction with Air Flow Visualisation

To better understand the effect of the impinging air flow the results from the PIV investigation, the velocity vector fields, were superimposed onto the images of the fuel spray. This allowed a direct comparison to be made of the flow structure and its effects on the fuel spray characteristics. Figure 5.26 has been created by overlaying Figure 5.14, the velocity vector field for the 5 mm valve lift case on the valve plane, onto Figure 5.25(a) and (b), where the two fuel spray images were merged to produce a single image. The white box signifies the FOV of the combined fuel spray images. The velocity vector field obtained on the valve plane is in fact approximately 18 mm in front of the injector plane, however as shown in Figure 5.12, it was assumed that the flow from the valves was circumferentially uniform, therefore, although at an out of plane angle to the fuel spray, this remains a valid interpretation of the situation within the flow rig.

Figure 5.26 clearly shows the high velocity jet of air, issuing from the valve, impinging on the fuel spray at the point where the greatest amount of disturbance occurs. The initial point of impact of the air jet, at point ‘W’ shows an initially small, but immediate deflection of the fuel spray as the low velocity air on the upper edge of the air jet impinges on the fuel spray. It can be seen that as the flow velocity increases, the effect on the fuel spray also increases, with the greatest affect on the fuel spray occurring at the point of maximum velocity, (refer to Figure 5.15 for the general shape of the velocity profile across the air jet). The reason for the apparent lack of disturbance to the fuel spray in the first few millimetres from the injector tip, is now clear, the air flow velocities are negligibly low in comparison to the fuel velocity. Therefore even at 5 mm valve lift, the fuel spray remains undisturbed in this region. Due to the lack of air flow data for the 2 and 3 mm valve lift cases, the equivalent overlaid image is not available, however Figures 5.27 and 5.28, show the overlay of the injector plane, B-B, velocity vector fields, onto the equivalent fuel spray images.

Observing Figure 5.27, the overlay of the 2 mm valve lift air flow on the fuel spray image, it can be seen that the reason for negligible affects on the fuel

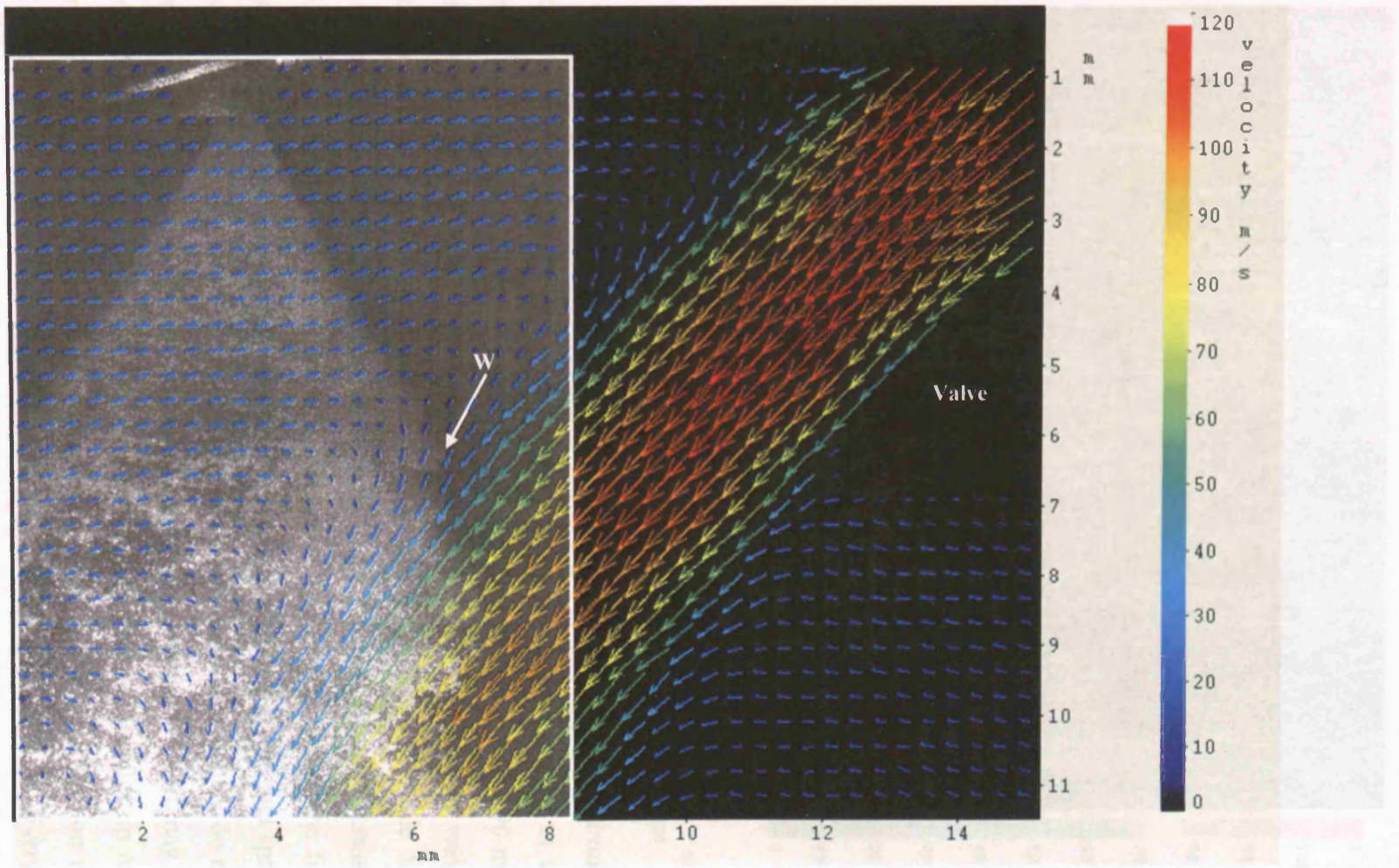


Figure 5.26 – Scaled Vector Field for 5 mm Valve Lift, 530 Pa Depression – Plane A-A, overlaid with the Fuel Spray Image with equivalent settings

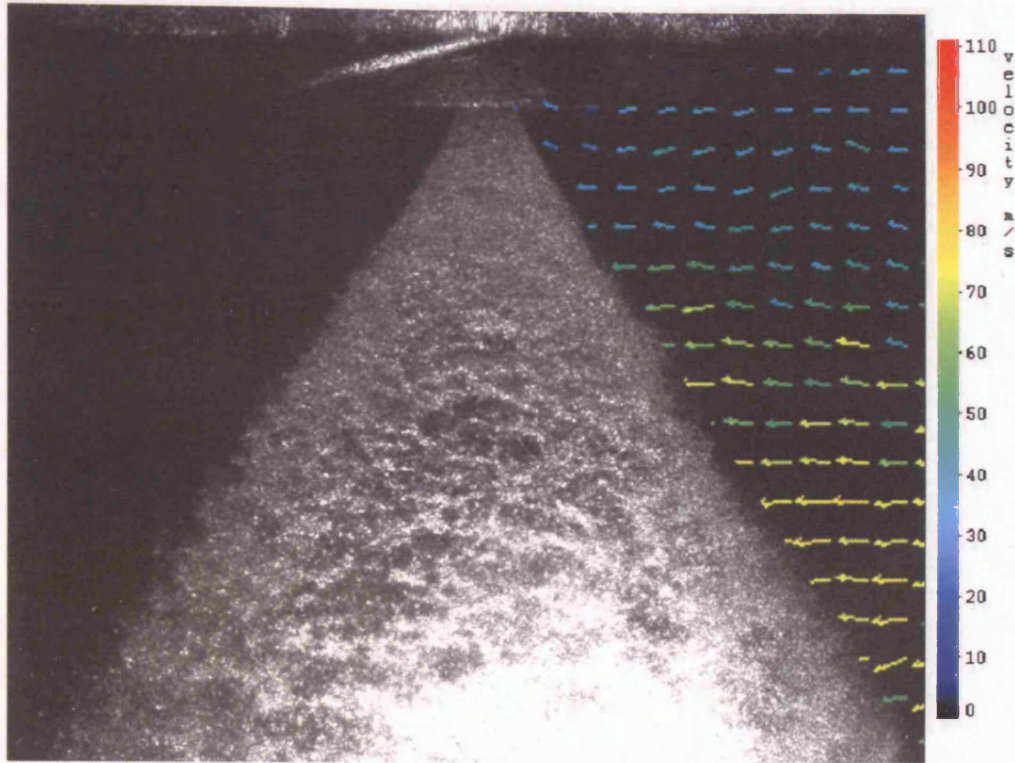
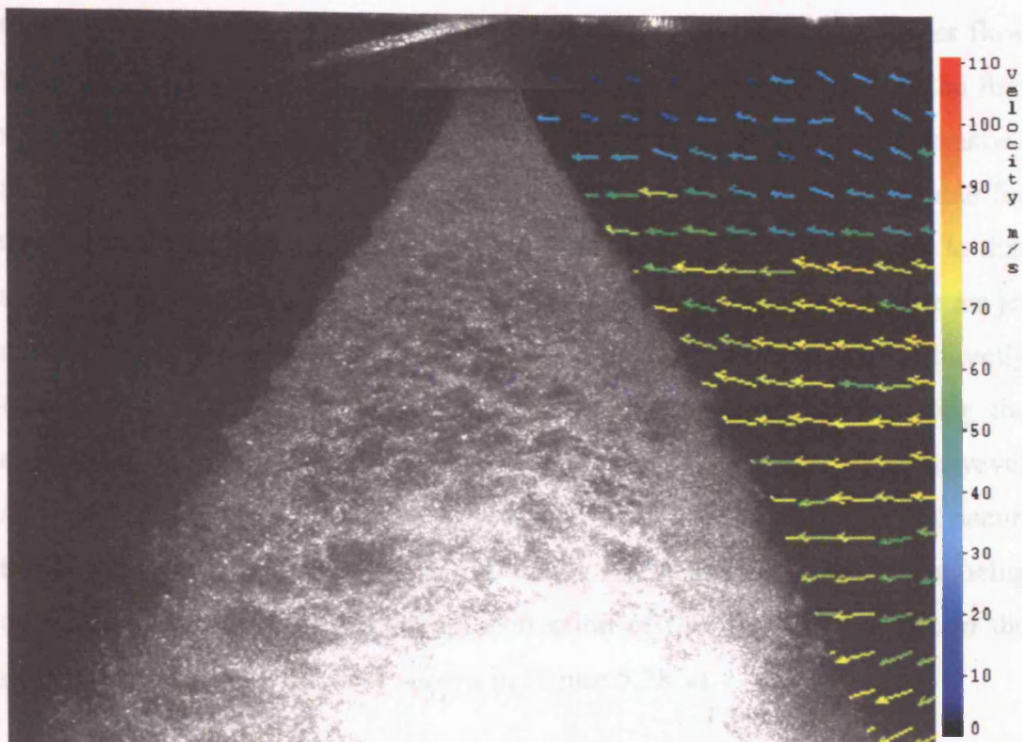


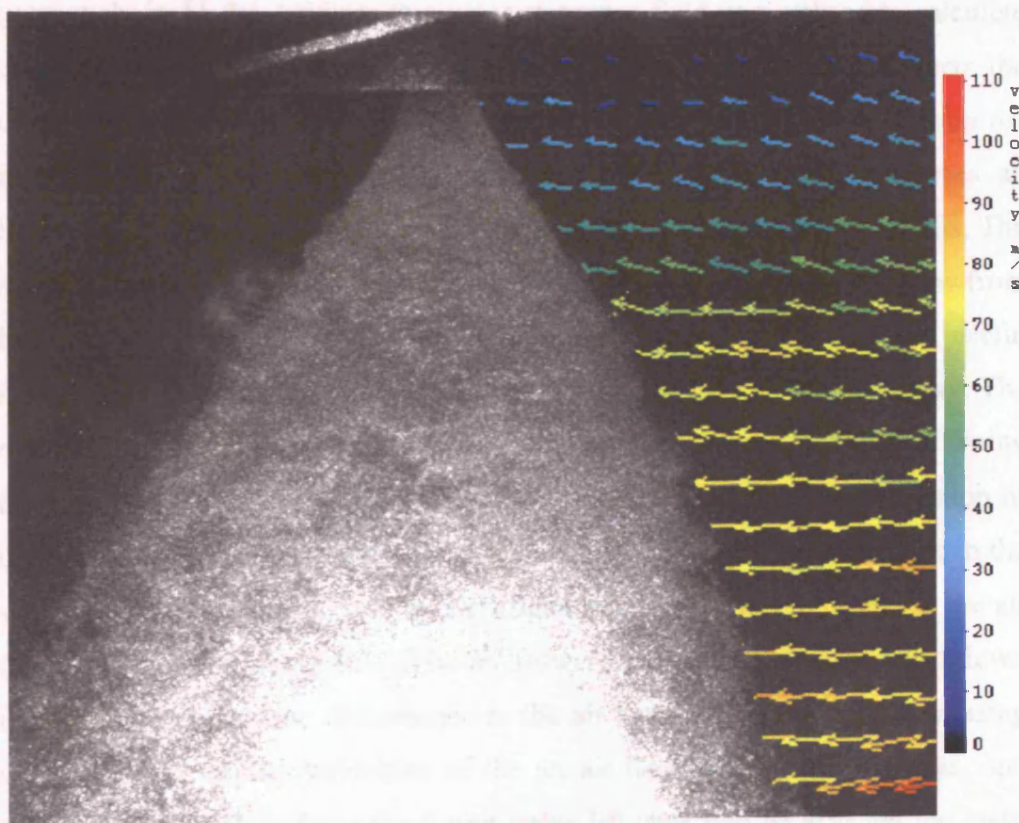
Figure 5.27 – Overlay of Valve Plane PIV Vector Field on Fuel Spray Image – 2 mm Valve Lift (Fuel Spray Image – 19.65 kPa Depression, PIV Vector Field – Scaled)

spray is due to the relatively low velocity of the air flow. Velocities of around 60 – 70 m/s are present close to the fuel spray boundary, however in the equivalent image for 5 mm valve lift, the velocities present are 80 – 90 m/s, and more importantly, due to the constant pressure difference across the valves the mass flow rate in the 5 mm valve lift case is higher, see Table 5.1. Although the effects are small it can be seen that as the flow velocity increases there is some deflection on the fuel spray, and some disruption to the fuel sheet surface. As discussed previously the air flow surrounding the fuel spray will be disturbed by the fuel spray. Therefore the overlays shown here do not show the air flow velocity vectors past the point where there is fuel. It may be expected however that the air flow a short distance from the injector tip will remain relatively unaffected by the injection event. As the air flow on the injector plane, plane B-B, interacts with the fuel spray, it will be diverted around the fuel spray, and also dragged down the fuel spray.

Figure 5.28 shows both the overlaid velocity vector fields for 3 and 5 mm valve lift. Figure 5.28(a), the 3 mm valve lift case, shows that the air velocities



(a)



(b)

Figure 5.28 – Overlay of Valve Plane PIV Vector Fields on Fuel Spray Images – (a) 3 mm and (b) 5 mm Valve Lifts, (Fuel Spray Image – 19.65 kPa Depression, PIV Vector Field – Scaled)

of 70 – 80 m/s begin to influence the bulk of the fuel spray. The higher flow velocities towards the bottom of the fuel spray as seen here, deflect the fuel spray disrupting the sheet surface, with ligaments of fuel completely detached from the bulk of the spray. Although no velocity vector field is available for the valve plane, it is expected that the flow pattern would be similar to that shown in Figure 5.26, for 5 mm valve lift, with the distance across the air jet reduced. It must therefore be considered that the jet of air approaching directly from the valves will affect the fuel spray to some degree. Observing the overlaid images of Figure 5.28(a), the influence of the jet of air does however appear to be minimal, the large effects seen for 5 mm valve lift do not occur, there is only minimal disturbance to the bulk of the fuel spray other than being displaced to the left. The apparent deflection of the fuel spray is due to the influence of the bulk air flow shown in Figure 5.28(a).

Finally, Figure 5.28(b) shows the overlay for 5 mm valve lift, and, as seen previously in §5.4.1.1 where this velocity vector field was utilised to calculate the deflection of the bulk flow, the bulk air flow considerably deflects the main fuel spray. The combination of the bulk air flow, i.e. the air flow on the injector plane, and the jet air flow, direct from the valve, produces an increasingly significant effect on the fuel spray with increasing valve lifts. The images shown here are simplifications of the complex nature of the flow from inlet valves within a DISI engine head, however they provide useful information on the flow structure and how that flow affects the fuel spray. The results from the PIV imaging tie in well with the fuel spray imaging, allowing the results from the fuel spray imaging to be explained by the observation of the surrounding air flow. However, as discussed previously the air flow in the vicinity of the fuel spray will be significantly different to that found in the air flow visualisation using PIV. The air flow will be diverted around and down the fuel spray, with the disturbance to the air flow increasing with decreasing valve lift. The higher velocities of the jet air flow will be affected less, and therefore the jet flow from the 5 mm valve lift case will be affected the least, this may be seen by observing Figure 5.26, where the jet flow significantly affects the fuel spray.

5.5.2 Void Fraction Analysis

A void fraction analysis was carried out using the same algorithm as described in §4.4.2.1, adapted for the differing light intensity levels, AOI positioning etc. The same method for determining the threshold levels was used as described in §4.4.3.1. The lighting method utilised in the single shot testing described in Chapter 4 was used again, therefore the light intensity levels were again found to vary exponentially with distance from the injector tip, this may be seen in Figure 5.29, an example of the light intensity variation for 2 mm valve lift. All three sets of images for 2, 3 and 5 mm valve lifts were found to have an exponential variation of light intensity. The threshold levels were therefore varied exponentially to produce appropriate thresholded images, before the void fraction evaluation was conducted.

The relatively large field of view, 10.75×8.125 mm, allowed for more AOI's to be used than in the previous work, therefore more data points were available to analyse the break-up process. 20 images were taken and used to calculate an average void fraction for each test case, a sample of these may be seen in Appendix V. Observing Figure 5.30 it may be seen that the classic profile of a rising void fraction, followed by a reduction as the spray begins to break-up into droplets is again present. Although images were taken further downstream from the injector tip than the results shown here, as discussed previously in Chapter 4, they were not utilised as the void fraction had clearly progressed

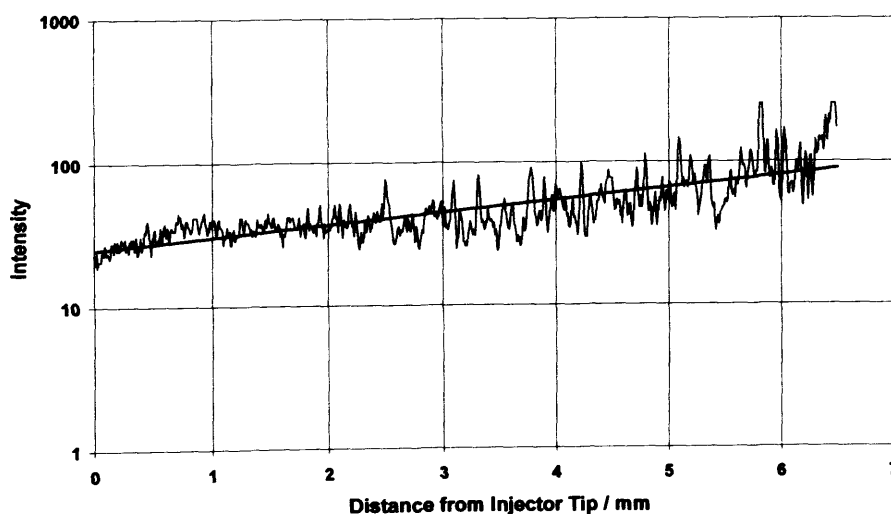


Figure 5.29 – Plot of light intensity variation with distance along injector axis

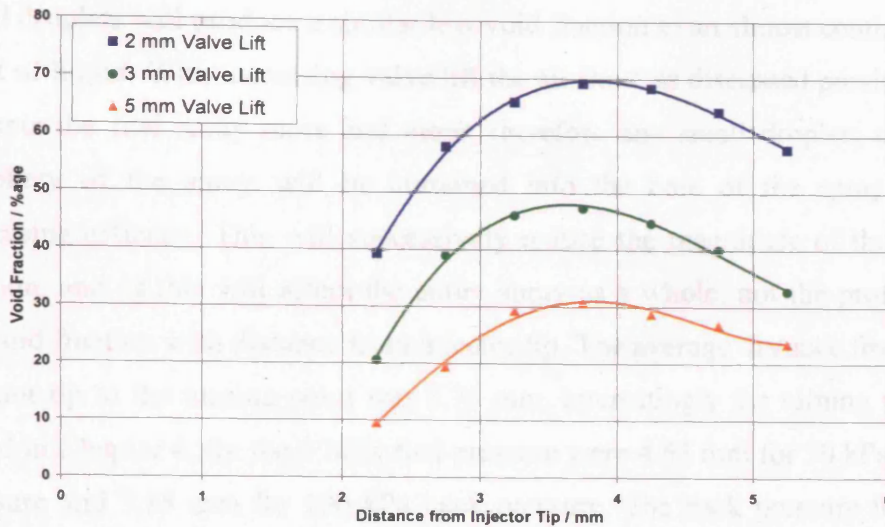


Figure 5.30 – Plot of Void Fraction Analysis for 2, 3, and 5 mm Valve Lifts – 19.65 kPa Depression

through the turning point, with a number of data points showing the decrease after the peak.

It can be seen in Figure 5.30 that the gradient of initial rise in void fraction is dependent on valve lift, with the steepest gradient occurring for the 2 mm valve lift. However it can be seen that the peak occurs at approximately the same point for all three cases, Table 5.4 shows the distance from the injector tip that the turning points occur for all three valve lift cases.

Valve Lift / mm	2	3	5	Average
Turning Point / mm	3.82	3.63	3.82	3.76

Table 5.4 – Table of Void Fraction turning points for varying Valve Lifts

This shows that the impinging air flow produces a small difference in the fundamental break-up process with the only difference in the void fractions in this region being the magnitudes at the turning points. The void fraction magnitude is highest for the 2 mm valve lift case because the air flow disrupts the fuel spray the least, therefore less small droplets will be entrained into the core of the spray. This in turn will show up in the void fraction process as larger holes, as, due to the method of thresholding the spray, dense clouds of

small droplets will produce a similar low void fraction to an almost continuous sheet of liquid. With increasing valve lift the air flow, as discussed previously, disrupts the fuel spray more and more, therefore any small droplets on the periphery of the spray will be entrained into the core of the spray with increasing efficacy. This will successively reduce the magnitude of the void fraction, and as this will affect the entire spray as a whole, not the profile of the void fraction with distance from injector tip. The average distance from the injector tip to the turning point was 3.76 mm, interestingly the turning points found in Chapter 4, for the 5 MPa fuel pressure were 4.63 mm for 50 kPa back pressure and 3.18 mm for 100 kPa back pressure. The back pressure for the series of tests discussed here was 80.35 kPa, and therefore the turning point would be expected to occur in between the two. This will be discussed further in the next chapter.

It can be seen that for 2 and 5 mm valve lifts the void fraction turning points appear to remain unaffected by the impinging air flow, however for the 3 mm case the turning point is 0.19 mm, 5 % closer to the injector tip. This is not significant, however the impinging air jet will affect the fuel spray break-up the most for 3 mm valve lift. This is because the air jet for the 2 mm valve lift case has a smaller mass flow rate, and is smaller spatially, and the 5 mm valve lift, although having a larger mass flow rate, it impinges on the fuel spray below the point of primary break-up, and does therefore not affect it. The primary break-up for the 3 mm valve lift case may therefore be affected by the impinging air jet.

The affect of the impinging air jet from the 5 mm valve lift case may be seen in the final point of the void fraction analysis in Figure 5.30. Despite care being taken to ensure that the AOI's did not include the edge of the spray boundary, the void fraction was still affected, (The AOI's utilised for the 2 and 3 mm valve lift cases would include a significant proportion of image outside of the spray boundary for the 5 mm case due to the deflection of the fuel spray). The profile 'kicks up' as the fuel spray is significantly disturbed by the air flow, this is caused by the fuel spray being 'ripped' apart by the air flow, causing relatively large voids.

5.6 Conclusion

A study of a pressure swirl atomiser commonly used in a DISI engine has been carried out to determine the effects of an impinging air flow on the liquid fuel break-up mechanisms. The study was carried out at a single fuel pressure, 5 MPa, and three different valve lifts 2, 3 and 5 mm, within a steady state flow rig, designed to model a DISI cylinder and engine head. An initial study was carried out to determine the air flow characteristics associated with the flow rig using particle image velocimetry, PIV. Two planes of interest were studied using this technique, the valve centreline, and the injector centreline. Further to this, macroscopic and microscopic images were obtained of the fuel spray using a Nikor macro lens and a K2 infinity microscope lens, respectively in conjunction with a CCD camera, utilising an Nd:YAG laser for illumination. The results of the macroscopic imaging show that the penetration rate, and fully developed cone angle are unaffected by the impinging air flow. However the early spray development is affected by the air flow, in decreasing amounts with increasing valve lift due to the location of the air jet. Although the penetration and fully developed cone angle were not affected. The entire fuel spray was found to be deflected away from the injector axis, by increasing amounts with increasing valve lift.

A presence probability imaging technique was utilised to analyse the effects of the air flow while eliminating any effects due to cycle to cycle variability. It was found that both edges of the fuel spray as viewed were affected to varying degrees by the air flow. The side closest to the valves was affected the most, with the 5 mm valve lift case affected the greatest, producing a spray with the largest amount of variability in the spray boundary, due to the break-up regime of the fuel spray.

The results of the PIV show that there was a jet of air issuing from the valve, this jet was influential in the disruption of the fuel spray. The level of disruption was found to vary with the valve lift, with the maximum disturbance occurring for the maximum valve lift of 5 mm. The velocity

vector fields were utilised to calculate the expected profile of the fuel spray, they were then compared to the actual spray profile. The results of the theoretical analysis compared favourably, especially for the 5 mm valve lift case. The velocity vector fields were also superimposed onto the fuel spray images, it was found that they align well, and explain the massive disruption to the side of the fuel spray closest to the valves. These results show that a simplistic view of the air flow may be used to estimate the fuel spray structure accurately.

Furthermore a void fraction analysis was carried out on the fuel spray images obtained with two separate fields of view. It was found that the magnitude of the void fraction varies with valve lift, however the turning point and therefore the break-up length does not change with varying valve lift. It was also shown that the break-up far downstream is affected by the air flow. This is most prominent with the 5 mm valve lift case as the cause is the air flow disrupting the fuel spray breaking up the ligaments and displacing the small droplets, causing relatively large voids in the fuel sheet. Therefore when considering the initial break-up of the fuel spray from a pressure-swirl atomiser the surrounding air flow, can be considered to have a negligible effect. However the secondary break-up, i.e. break-up of liquid ligaments, is affected by the air flow and must therefore be considered. The impinging air flow is also important when considering the spatial location of the fuel spray, as even with small air flows the entire fuel spray will be deflected from its axis.

Chapter 6
Analysis of the Near Nozzle Spray
Phenomenon of a Pressure-Swirl Atomiser –
Conclusions

Chapter 6 Analysis of the Near Nozzle Spray Phenomenon of a Pressure-Swirl Atomiser - Conclusions

6.1 Introduction

As discussed previously in Chapters 4 and 5 the literature regarding the near nozzle characteristics of a pressure-swirl atomiser is limited. Inadequate information is available due to the difficulty in obtaining high quality meaningful results in this area due to the high density of the fuel, small dimensions involved and in the case of in-cylinder imaging, restricted optical access to the area of interest. The work presented here, through the use of simplified experimental test rigs, has attempted to greatly enhance the current level of knowledge in the near nozzle region. The test rigs utilised, a static pressure chamber and a steady state flow rig, were designed to simulate the effects of increasing cylinder pressure and the impinging air flows respectively, that are associated with direct injection spark ignition engines. In this chapter the author presents the findings of these studies, how they relate to each other and their relevance to modelling of pressure-swirl atomisers. Finally an adaptation of the currently available models will be given accounting for the break-up regime found in this study.

6.2 Effects of Back Pressure on the Near-Nozzle Spray Characteristics

6.2.1 General Fuel Spray Characteristics

The general spray characteristics, the penetration rate, and cone angle were measured for increasing back pressure. In agreement with published data the penetration rate and the cone angle decreased with back pressure. It was found that the collapse of the fuel spray due to the pressure difference across the spray was both determinate on the back pressure and the fuel pressure. Both factors affect the drag on the fuel spray and therefore the low gas pressure caused in the core of the fuel spray. Increasing the fuel pressure increases the

penetration rate and therefore the drag forces, while increasing the back pressure increases the density of the ambient air, and therefore the drag force. The fuel spray collapses to a critical point, whereby increasing the back pressure no longer affects the cone angle. This is caused by the spray collapsing into the core of the spray, filling it and therefore eliminating the pressure difference across the fuel sheet. For the injector used in this study this occurs at different back pressures depending on the fuel pressure, for 5 MPa fuel pressure this occurs at a back pressure between 400 and 600 kPa, for 10 MPa fuel pressure this occurs at a back pressure between 200 and 400 kPa.

The collapsing fuel cone will also affect the near nozzle break-up of the fuel spray to some extent. The decreasing cone angle will increase the thickness of the fuel sheet at any one point along the spray axis due to conservation of mass. This factor alone would increase the break-up length as the fuel spray could remain stable for a longer distance from the injector tip. However the increasing velocity/back pressure will increase the drag forces acting on the fuel spray, therefore decreasing the break-up length. These two factors acting against each other cause the break-up length of the spray to decrease rapidly initially. With each subsequent increase in back pressure the break-up length decreases less.

6.2.2 Near Nozzle Fuel Spray Characteristics – Back Pressure

The general fuel spray characteristics provided an insight into the overall fuel spray properties, indicating the possible effects of back pressure on the break-up length. However they provided no detailed explanation of the mechanisms behind the break-up of a pressure swirl atomiser, therefore further imaging of the fuel spray very close to the injector tip was carried out. This enabled the fuel spray to be imaged in very fine detail, allowing the fuel spray break-up process to be visualised from continuous sheet to individual droplets.

The global imaging was carried out at a number of different back pressures up to 1000 kPa, unfortunately due to limitations in the imaging system it was not possible to successfully reveal the details of the fuel spray in the near field with a back pressure exceeding 200 kPa. This was due to the collapse of the

spray cone interfering with the novel method of illuminating the fuel spray by backlighting from within the core itself. However the three separate test conditions for 5 MPa fuel pressure and the two test conditions for 10 MPa fuel pressure enabled the break-up mechanisms to be discovered. It was found that the hollow cone fuel spray from the pressure-swirl atomiser utilised the break-up mechanism of perforated sheet disintegration. This mechanism operates through small disturbances on the sheet surface, which will expand if their diameter is greater than the sheet thickness, creating holes in the sheet. The holes expand due to uneven surface tension forces, eventually they interact with other holes in the sheet, producing ligaments which undergo further break-up into droplets.

Considering a single hole in a uniform continuous sheet, as the hole expands the liquid once contained in the sheet builds up around the circumference of the hole in the form of a toroid. The hole will remain regular in shape providing there are no external forces acting on the sheet and will continue to grow until the toroid of fuel itself becomes unstable. This same process occurs in the break-up of the fuel sheet issuing from a pressure-swirl atomiser, however the liquid sheet is no longer uniform and continuous, it has curvature and progressively thins as it proceeds away from the nozzle due to conservation of mass. Also other factors are acting on the fuel sheet, including possible pressure differences across the spray and non-uniformities in the sheet thickness, multiple holes present in the sheet etc. Therefore the circular hole formed in the uniform continuous sheet may no longer exist, it is stretched and compressed by the expanding and decelerating sheet respectively. This will produce an elliptical shape hole that will interact with other holes in the fuel sheet. The interactions will produce larger holes through the action of the ligaments between holes breaking up into droplets. As the fuel sheet breaks up further the ligaments will further break-up into droplets, which will fill the holes, eventually the fuel spray will be entirely made up of a distribution of droplets.

A void fraction analysis was carried out to determine the increase in size of the holes in the fuel sheet with increasing distance from the injector tip, allowing

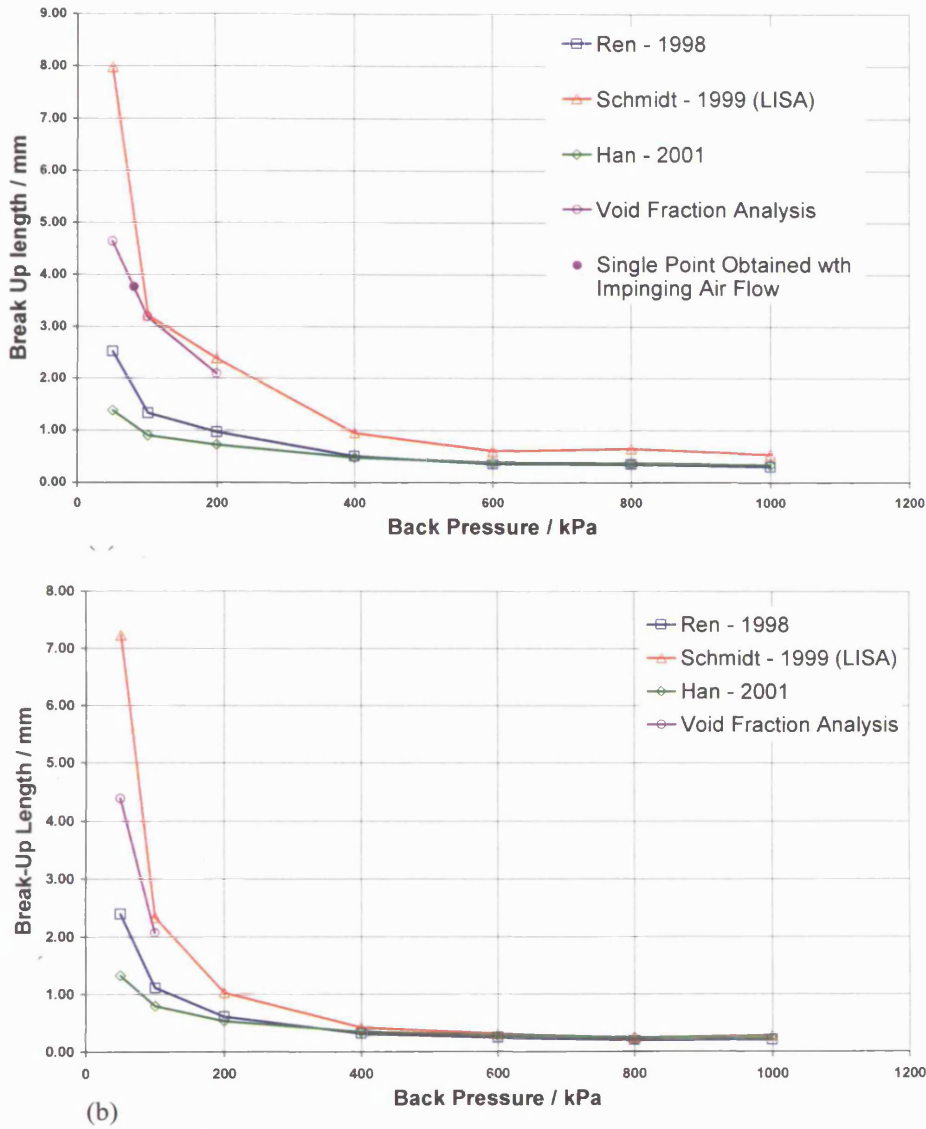


Figure 6.1 - Plot to show Break-up Length versus Back Pressure for the three models studied and the Break-up lengths obtained from the void fraction analysis. (a) for 5 MPa fuel pressure and (b) for 10 MPa fuel pressure.

the break-up point of the spray to be located. The break-up point of the fuel spray was defined as the turning point of the void fraction. It was found that the void fraction initially rises as the holes expand, however as the fuel sheet begins to break-up into ligaments and droplets it begins to fall as the fuel spray appears to be a continuous sheet once more, due to the high density of droplets within the holes. The turning points and therefore break-up lengths for both fuel pressures and all back pressures may be seen in Table 6.1 below;

Test Parameters	Turning point / mm
5 MPa – 50 kPa	4.63
5 MPa – 100 kPa	3.18
5 MPa – 200 kPa	2.09
10 MPa – 50 kPa	4.39
10 MPa – 100 kPa	2.07

Table 6.1 – Table of Turning Points / break-up lengths obtained using the Void Fraction Technique

A comparison was made between the results shown here and published mathematical models available. Three models were chosen by Ren and Nally [1998], Schmidt *et al.* [1999] and Han *et al.* [2001], the Ren and Han models were based on the conservation of mass, leading to a thinning sheet that can no longer remain stable. The Schmidt model was based on linear instabilities introduced into the spray that grew until the sheet could no longer remain stable. Figure 6.1 shows the results of the three models for Injector A used in this study, also shown are the break-up lengths found using the void fraction analysis. As it can be seen the results are in good agreement with the Schmidt linear instability model, with the greatest difference occurring at low back pressures. The other two models significantly underestimate the break-up length for all of the test cases.

The results found for the break-up length using the void fraction technique agree qualitatively with what may be seen in the images. Observing Figure 6.2, it may be seen that the break-up point obtained using the void fraction analysis has been superimposed onto the image. It may be seen that above the line the ligaments form a continuous sheet, however below the line at approximately 4.63 mm from the injector tip, the spray has broken up into individual ligaments and droplets. In terms of modelling the fuel spray, after this point secondary break-up may be allowed to occur, where the ligaments and droplets can undergo break-up into smaller droplets and fuel vapour.

The author believes that the significant underestimate of the break-up length is caused by the mechanism through which the fuel spray breaks up. The

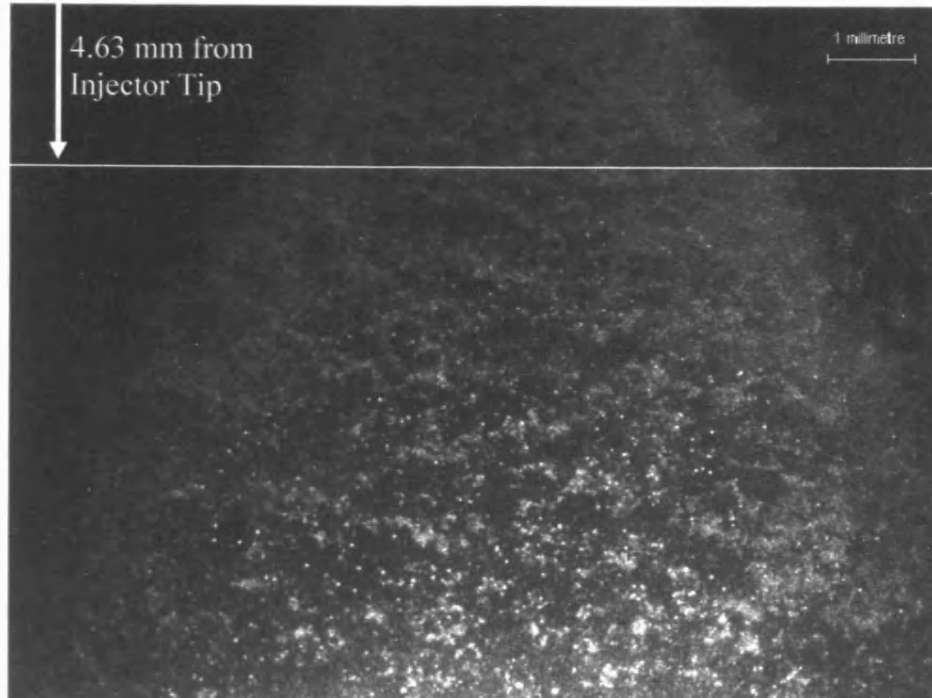


Figure 6.2 – Image of Fuel Spray for 5 MPa fuel pressure – 50 kPa back pressure, showing the break-up point found from the void fraction analysis

perforated sheet mechanism for sheet break-up as discussed previously, produces holes in the sheet with an area of toroidal fuel build up around the circumference. This effectively thickens the sheet producing a more stable structure, increasing the time required for the sheet to thin to a point where it can no longer remain stable, this is not taken into account in the currently available models. The alternative method utilised by Schmidt *et al.* [1999], of assuming small disturbances on the sheet surface that are allowed to grow, produces far more accurate results. However for sub-atmospheric ambient conditions, the Schmidt model overestimates the break-up length by approximately 72 % and 65 % for the 5 and 10 MPa fuel pressure cases respectively. In practice the inherent non-uniformity of the fuel sheet will lead to the break-up occurring in a shorter distance than suggested by Schmidt, this factor will become less important with reducing break-up length, as other factors will become dominant.

As discussed previously it was not possible to image the fuel spray at back pressures over 200 kPa for the 5 MPa fuel pressure case and 100 kPa back pressure for the 10 MPa fuel pressure case. Observing Figure 6.1 at these back

pressures, it may be seen that for both fuel pressures the break-up length, as predicted by Schmidt, approaches 1 mm. This is significant as the void fraction, even in the suitable images, could not be measured closer than approximately 1 mm from the injector tip due to a highly dense fuel spray, and the inability to illuminate the spray successfully. Therefore to obtain suitable images for higher back pressures, a significantly smaller field of view, and an altered method of illumination would be required. It could be argued that where the break-up length is very short, i.e. less than 1 mm the effect of the build up of fuel around the holes is no longer important in the break-up process. It may also be seen that all three models converge to the same values.

Periodic structures were also found on the surface of the fuel spray, in the form of large scale waves independent of the small scale waves influential in the eventual break-up of the fuel sheet. These structures are caused by the Kelvin-Helmholtz instabilities present when large slip velocities between a liquid sheet and a gas are present. The slip velocity causes aerodynamic instabilities, similar to those found by Yule *et al.* [1999], the wave instabilities cause local thinning of the sheet, aiding in the break-up process. The author found that the wavelengths reduce with both increasing fuel pressure and back pressure, these effectively increase the drag forces on the sheet, as the increasing fuel pressure increases the relative velocities and the increasing back pressure increases the density. This was a similar result to that found by Yule *et al.* [1999], where increasing the relative velocities reduced the wavelength, and also the break-up length.

6.3 Adaptation of Mathematical Model

As discussed previously the measurement of the break-up length of a pressure-swirl atomiser has shown that the current models do not produce accurate results. However the general trend of the models agrees well with the experimental results, see Figure 6.1, therefore the most appropriate model was selected and modified to take into account the break-up regime presented in this thesis. The model by Ren and Nally [1998] was found to be the most

appropriate to adaptation. Observing Figure 6.1 it can be seen that the initial gradient of the break-up length plot is the most similar to the experimental results. Although the Schmidt model produces the most accurate results with no adaptation, it is a computationally intensive model, and as such was not chosen to be an appropriate model. The profile of the break-up length versus back pressure was also slightly different to that measured experimentally, the initial reduction in break-up length was much greater.

The sheet thickness that would have existed in an ideal non-perforated fuel sheet was analysed at the break-up lengths measured experimentally, and at the break-up lengths calculated using the Ren model. It was found that the average sheet thickness at the break-up length for the Ren model was double that of the sheet thickness at the measured break-up length. The standard deviation of the ratio between the sheet thickness at the Ren break-up length and the measured break-up length was 0.22, or approximately 11 %. The difference in the sheet thicknesses may be explained by taking into account the revised break-up regime, i.e. the extra fuel available around the holes in the sheet, allowing the fuel sheet to remain stable for a longer distance from the injector tip. Therefore the sheet thickness at the point of break-up is double that of the ideal smooth fuel sheet with no perforations.

Furthermore observing the differences between the actual break-up lengths of the Ren model and those measured experimentally, again it can be seen that the average measured break-up length is double that of the Ren model. The standard deviation of the ratio between the measured break-up length and that of the Ren model was 0.23 or approximately 11 %. Therefore the constant in the Ren model was modified by a factor of 2. The results of the revised model may be seen in Figure 6.3. The new model is therefore thus;

$$L = E \left[\frac{\rho_l \sigma h \cos \theta}{\rho_g^2 V_r^2} \right]^{1/2} \quad \text{eq. 6.1.}$$

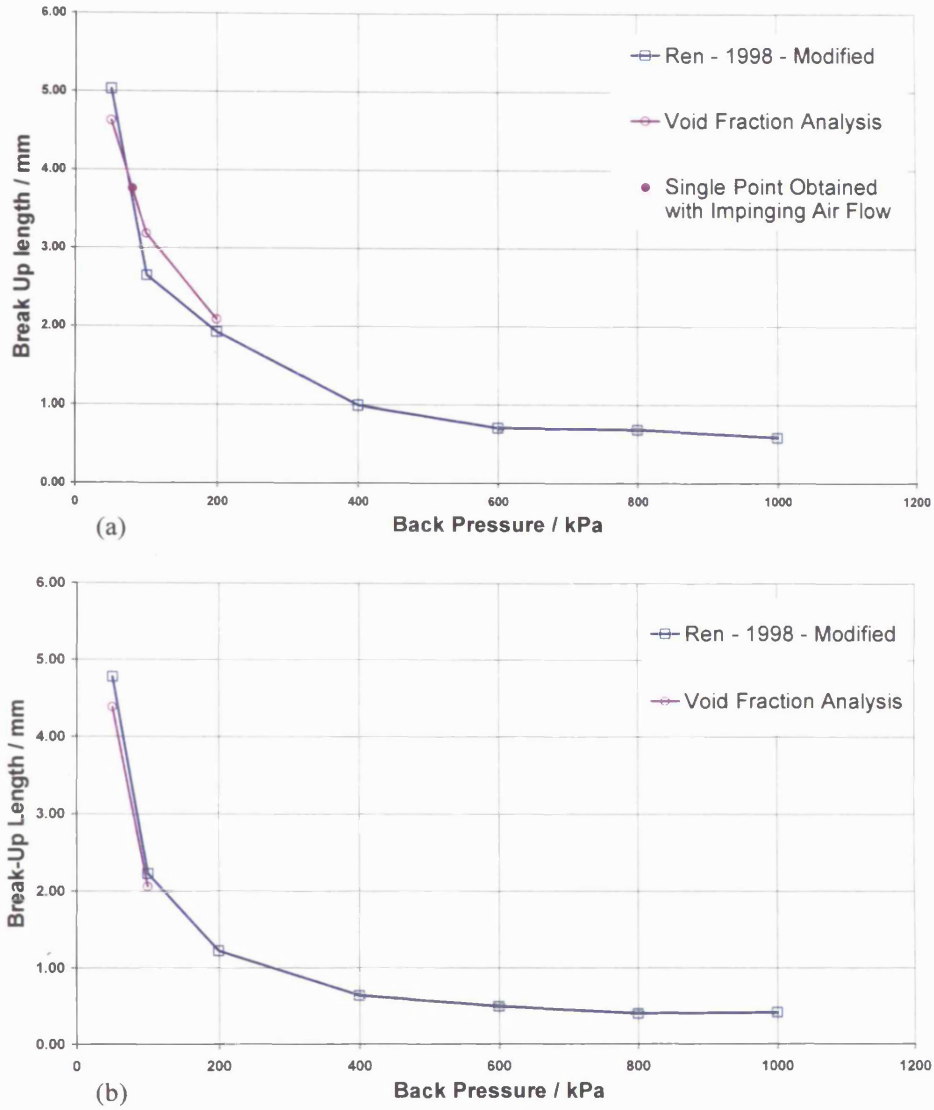


Figure 6.3 - Plot to show Break-up Length versus Back Pressure for the modified model and the Break-up lengths obtained from the void fraction analysis. (a) for 5 MPa fuel pressure and (b) for 10 MPa fuel pressure.

Where $E = 3.4$, or $2 \times C$, where C was the constant of proportionality utilised in the original Ren model. This model produces results that are within 17 % for 5 MPa fuel pressure and within 8.5 % for the 10 MPa fuel pressure case.

This is a simple mathematical model that may be utilised to calculate more accurately the break-up length of a fuel sheet from a pressure-swirl atomiser, prior to further modelling of droplet break-up. This is an extremely valuable result which can easily be integrated into the computational models used by researchers around the world.

6.4 Effects of an Impinging Air Flow on the Near-Nozzle Spray Characteristics

6.4.1 General Fuel Spray Characteristics

The general fuel spray characteristics provided an insight into the overall fuel spray properties, indicating the possible effects of an impinging air flow on the break-up length. It was found that the air flow had little effect on the penetration rate and the fully developed cone angle. However the early spray development was affected by the air flow, with decreasing effect as the valve lift was increased. The main fuel spray was also affected by the air flow, although the cone angle remained constant, the entire spray was deflected away from the injector axis, by increasing amounts with increasing valve lift.

A presence probability imaging method was utilised to analyse the affects of an impinging air flow on the general fuel spray characteristics. This procedure allowed the variability in the fuel spray to be analysed while observing the effects of an impinging air flow. It was seen that the effect on the fuel spray increased with increasing valve lift, not only due to the increasing momentum of the air flow, but also due to the position that the air jet impacted with the fuel spray. For the 2 and 3 mm valve lift cases the air jet impacted with the fuel spray at a location where the fuel spray remained continuous, therefore it was less susceptible to the air flow. However for the 5 mm valve lift case the impinging air jet coincided with the fuel spray at a point where the fuel spray had already undergone significant break-up and this had a population of droplets. This effect combined with the increased mass flow rate of air produced a much greater deflection of the fuel spray. The position of the air jet for the 5 mm valve lift case also led to a far higher degree of variability between injection events, caused by the slightly different break-up lengths for each injection event. This agrees with the findings presented in Chapter 4, where the error bars were larger around the turning point of the void fraction profile due to differences in the break-up length of separate injection events.

The PPI also enabled the effects on the fuel spray to be analysed on the opposite side to the impinging air jet. This side of the fuel spray was also deflected away from the valve, to a lesser degree. It was found that for the 5 mm valve lift case the small droplets around the periphery of the spray were deflected away from the bulk of the spray. The air flow will be highly 3-dimensional in this area with the air flow being diverted around the fuel spray, and converging again, this will cause a depression creating a force on the fuel spray, leading to the bulk deflection of the fuel spray.

An algorithm was developed to utilise the PIV vector fields obtained to calculate the expected spray boundary profile. It was found that for the low valve lift cases the error associated with scaling the vector fields led to large differences between the calculated and measured spray boundaries. The boundary calculated for the 5 mm valve lift case however produced excellent results, with a spray boundary profile very similar to the measured case. The vector field utilised for this was scaled directly from a measured vector field and therefore produced more accurate results. When calculating the effects on the spray boundary profile, a suitable vector field must therefore be utilised, either directly measured or scaled from a similar vector field, i.e. the same valve lift. This same algorithm may be utilised in conjunction with CFD of the internal flow characteristics of a DISI engine to allow the expected location of the fuel spray to be calculated based on relatively simple imaging of the fuel spray in a quiescent environment. This may prove to be a simpler method of producing these results as obtaining optical access to an engine cylinder is difficult, especially at high operating speeds.

6.4.2 Near Nozzle Fuel Spray Characteristics – Impinging Air Flow

The near nozzle characteristics were analysed using microscopic imaging for the three valve lifts of 2, 3 and 5 mm. It was found that for the 2 mm valve lift case there was negligible effect on the break-up, even at the relatively high mass flow rate utilised in the test. The same perforated sheet mode break-up was seen as discussed in §6.2.2, where small disturbances on the sheet surface produce holes, which then grow, producing a perforated sheet which then breaks up into ligaments. The high momentum of the fuel spray does not allow

the impinging air flow to disturb this break-up mechanism, however the small droplets produced appear to be deflected away from the sheet surface producing a fuel sheet, initially with empty holes. This may also be seen quantitatively by comparing the maximum void fraction for this test case and the maximum found in a comparable test in Chapter 4, (5 MPa – 100 kPa). The maximum void fraction with an impinging air flow was approximately 70 %, while with no flow the maximum was approximately 40 %. This effect reduces with increasing valve lift, despite the increased flow rates. This is caused by the ligaments breaking up into smaller droplets faster with increasing air flow, therefore the imaged fuel sheet has the appearance of a smoother sheet with less holes. However observing the void fraction analysis carried out on these images it can be seen that the turning point is not affected by the impinging air flow, only the magnitudes are affected. The break-up length from this series of testing was plotted along with the break-up lengths from the study involving back pressure, and may be seen in Figure 6.1 and Figure 6.3 in comparison to the break-up lengths obtained from the mathematical models. As it can be seen despite the air flow the break-up length fits in well with the overall trend.

It was shown that the impinging air jet was responsible for the deflection of the fuel spray. The PIV vector field for the valve plane for 5 mm valve lift was overlaid onto the equivalent fuel spray image. It could be seen that the large deflection at the bottom of the image was of a direct consequence of this air jet. Unfortunately due to difficulties in the imaging process equivalent valve plane PIV vector fields could not be obtained for the 2 and 3 mm valve lift cases. To further prove the effect of the air jet it would be necessary to utilise a PIV set-up capable of less than 20 μ s time difference between the two laser light pulses, this would enable suitable PIV vector fields to be obtained at the other two valve lifts. These vector fields would also increase the accuracy of the calculated spray boundary profiles.

6.5 Summary of the Main Findings of this Work

This section has provided a summary of the findings presented in this thesis, where two separate experimental test rigs were utilised to provide detailed information on the near-nozzle characteristics of a pressure-swirl atomiser commonly used in a direct injection spark ignition engine.

It was found that the general spray characteristics, penetration and cone angle, agreed well with published data, allowing any future findings to be applied to generic pressure-swirl atomisers. The mechanism through which the pressure swirl atomiser breaks up into droplets was found to be a perforated sheet mode of break-up, this is extremely significant as the current literature available in this area do not show in detail the break-up regime. A novel void fraction analysis was designed to discover the break-up length of the fuel spray. This was extremely successful in providing the break-up lengths for varying back pressure and varying impinging air flows. The following may be said about the break-up process:

- Fuel pressure affects the break-up length of the fuel spray. Increasing the fuel pressure decreases the break-up length, however the break-up mechanism remains unaltered.
- Back pressure affects the initial break-up length of the fuel spray. Increasing the back pressure decreases the break-up length, again the break-up mechanism remains unaltered.
- Impinging air flows do not affect the initial break-up length of the fuel spray.
- Impinging air flows do affect the secondary break-up of the fuel spray. Increasing the mass flow rate of the air flow decreases the time taken for secondary break-up.

The results obtained experimentally were compared to those calculated using currently available mathematical models. The three models utilised were by Ren and Nally [1998], Schmidt *et al.* [1999] and Han *et al.* [2001], the Ren

and Han models were based on conservation of mass, while the Schmidt model was based on linear instabilities induced on the spray. The following highly relevant points may be made about the models:

- All three models produced a similar profile, but different length for spray break-up with varying back pressure.
- It has been shown that the Ren and Han models significantly underestimate the break-up length, this is due to the difference between the break-up process assumed by these models and that seen experimentally. The actual method of break-up of the fuel spray permits the spray to remain stable for longer. This is highly significant as the models currently being utilised are inaccurate and should be revised.
- The void fraction analysis confirmed the underestimation of the fuel spray break-up lengths of the Ren and Han models, therefore for this type of model the method of break-up must be reconsidered.
- For sub-atmospheric back pressures the Schmidt model overestimates the break-up length, however for back pressures above atmospheric the model data agrees well with the findings of this author.
- The method of break-up found experimentally must therefore be considered for low back pressures, however for higher back pressures it may not be necessary as the Schmidt model copes well.
- Impinging air flows are not currently considered in any of the models. It was shown that this was not necessary for the evaluation of the initial break-up length, however for subsequent droplet break-up models it would be necessary to include this factor.
- A novel mathematical model was proposed based on the Ren model. It was shown to estimate the break-up length extremely well compared to the original model. It is recommended that this revised model is incorporated into computational codes.

Two publications have resulted from this work Loustalan *et al.* [2003(a)] and Loustalan and Davy [2003(b)], it is expected that a future publication will

present the results obtained since these publications and the mathematical model developed.

To further increase the knowledge of the near-nozzle characteristics of a pressure-swirl atomiser for varying ambient conditions a study of temperature and fuel volatility effects would be required.

References

- Alloca L, Bella G, De Vita A, Di Angelo L. [2002]** – “Experimental Validation of a GDI Spray Model”, *SAE Technical Paper No. 2002-01-1137*.
- Anderson R. W, Yang J, Brehob D, Vallence J. K, Whiteaker R. M. [1996]** – “Understanding the Thermodynamics of Direct Injection Spark Ignition (DISI) Combustion Systems: An Analytical and Experimental Investigation”, *SAE Technical Paper No. 962018*.
- Araneo L, Coghe A, Brunello G, Dondé R. [2000]** – “Effects of Fuel Temperature and Ambient Pressure on a GDI Swirled Injector Spray”, *SAE Technical Paper No. 2000-01-1901*.
- Arcoumanis C, Gavaises M, Argueyrolles B, Galzin F. [1999]** – “Modelling of Pressure-Swirl Atomizers for GDI Engines”, *SAE Technical Paper No. 1999-01-0500*.
- Befrui B, Kneer R, Breuer S, Reckers W, Robart D, Wanlin H, Weiten C. [2002]** – “Investigation of a DISI Fuel Injector for a Close-Arranged Spray-Guided Combustion System”, *SAE Technical Paper No. 2002-01-1133*.
- Cathcart G, Zavier C. [2000]** – “Fundamental Characteristics of an Air-Assisted Direct Injection Combustion System as Applied to 4-Stroke Automotive Gasoline Engines”, *SAE Technical Paper No. 2000-01-0256*.
- Choi J, Lee S, Shin H, Bae C. [2000]** – “Fuel-Spray Characteristics of High Pressure Gasoline Injection in Flowing Fields”, *JSME International Journal, Series B, Vol 43, No 4, pp 576-581*.
- Clark C. J, Dombrowski N. [1972]** – “Aerodynamic Instability and Disintegration of Inviscid Liquid Sheets”, *Proc. R. Soc. Lond. A. 329, pp467-478*.
- Connif P. J. [2001]** – “Design of an Optically-Accessed Test Chamber for Analysis of Direct Injection Sprays”, M.Sc. Thesis, Department of Mechanical Engineering University College London.
- Cousin J, Nuglisch H. J. [2001]** – “Modelling of Internal Flow in High Pressure Swirl Injectors”, *SAE Technical Paper No. 2001-01-0963*.

Davy M. H, Williams P. A, and Anderson R. W. [1998] – "Effects of Injection Timing on Liquid-Phase Fuel Distributions in a Centrally-Injected Four-Valve Direct-Injection Spark-Ignition Engine", *SAE Technical Paper No. 982699*.

Davy M. H, Williams P. A, Anderson R. W. [2000] – "Effects of Composition on Mixture Formation in a Firing Direct-Injection Spark-Ignition (DISI) Engine: An Experimental Study using Mie-Scattering and Planar Laser-Induced Fluorescence (PLIF) Techniques", *SAE Technical Paper No. 2000-01-1904*.

Davy M. H, Williams P. A. [1999] – "The Effects of Flash Boiling on Mixture Formation in a Firing Direct-Injection Spark-Ignition (DISI) Engine, *Proc. Of International Congress on Direkteinspritzung im Ottomotor II (Gasoline Direct Injection Engines)*, 16-17 Nov, Munich, Germany, pp. 154 – 170, Ed. Spicher U, Expert Verlag, ISBN 3-8169-1822-0.

Davy M. H. [2000] – "Two-Phase Fuel Visualisation in a Direct-Injection Gasoline Engine", Ph.D. Thesis, Department of Mechanical Engineering University College London.

Doumas M, Laster R. [1953] – "Liquid-Film Properties for Centrifugal Spray Nozzles", *Chem. Eng. Prog.*, Vol. 49, No. 10, pp 518 – 526.

Drain L. E. [1980] – "The Laser Doppler Technique", 1st Ed. *John Wiley & Sons Publishers*, ISBN 0 471 27627 8.

Eckbreth A. [1996] – "Laser Diagnostics For Combustion Temperature and Species", 2nd Ed. *Gordon and Breach Publishers*, ISBN 90-5699-532-4.

Ekenberg M, Johansson B. [2000] – "Fuel Distribution in an Air Assist Direct Injection Spark Ignition Engine with Central Injection and Spark Plug measured with Laser Induced Fluorescence", *SAE Technical Paper No. 2000-01-1898*.

Faure M. A, Sadler M, Oversby K. K, Stokes J, Begg S. M, Pommier L. S, Heikal M. R. [1998] – "Application of LDA and PIV Techniques to the Validation of a CFD Model of a Direct Injection Gasoline Engine", *SAE Technical Paper No. 982705*.

- Fraidl G.K, Piock W.F, Wirth M, [1996]** – “Gasoline Direct Injection: Actual Trends and Future Strategies for Injection and Combustion Systems”, *SAE Technical Paper No. 960465*.
- Fraser R. P, Eisenklam P, Dombrowski N, Hasson D. [1962]** – “Drop Formation from Rapidly Moving Liquid Sheets”, *A.I.Ch.E Journal*, Vol. 8, No. 5, pp. 672 – 680.
- Fraser R. P, Eisenklam P. [1953]** – “Research into the Performance of Atomisers for Liquids”, *Imp. Coll. Chem. Eng. Soc. J*, Vol. 7, pp. 52 – 68.
- Fry M, King J, White C. [1999]** – “A Comparison of Gasoline Direct Injection Systems and Discussion of Development Techniques”, *SAE Technical Paper No. 1999-01-0171*.
- Fry M. D. [1994]** – “Optimisation of Mixture Preparation in a SI Engine”, Ph.D. Thesis, Department of Mechanical Engineering University College London.
- Gajdeczko B. F, Bracco F. V. [1999]** – “Application of Two-Color Particle Image Velocimetry to a Firing Production Direct-Injection Stratified-Charge Engine” *SAE Technical Paper No. 1999-01-1111*.
- Gavaises M, Abo-serie E, Arcoumanis C. [2002]** – “Nozzle Hole Film Formation and its Link to Spray Characteristics in Swirl-Pressure Atomizers for Direct-injection Gasoline Engines”, *SAE Technical Paper No. 2002-01-1136*.
- Gavaises M, Arcoumanis C. [2001]** – “Modelling of Sprays from High-Pressure Swirl Atomizers”, *Int. J. Engine Research* Vol 2. No.2.
- Georjon T, Bourguignon E, Duverger T, Delhay B, Voisard P. [2000]** – “Characteristics of Mixture Formation and Combustion in a Spray-Guided Concept Gasoline Direct Injection Engine: An Experimental and Numerical Approach”, *SAE Technical Paper No. 2000-01-0534*.
- Glaspie C. R, Jaye J. R, Lawrence T. G, Lounsbury T. H, Mann L. B, Opra J. J, Roth D. B, Zhao F. Q. [1999]** – “Application of Design and Development Techniques For Direct Injection Spark Ignition Engines”, *SAE Technical Paper No. 1999-01-0506*.

- Golombok M, Morin V, Mounaim-Rouselle C. [1998]** – “Droplet Diameter and the Interference Fringes between Reflected and Refracted Light”, *J. Phys. D: Appl. Phys.* No. 31, pp 59 – 62.
- Gorokhovski M. [2001]** – “The Stochastic Lagrangian Model of Drop Breakup in the Computation of Liquid Sprays”, *Atomization and Sprays*, Vol 11, pp 505-519.
- Grimaldi C. N, Postrioti L, Stan C, Tröger R. [2000]** – “Analysis Method for the Spray Characteristics of a GDI System with High Pressure Modulation”, *SAE Technical Paper No. 2000-01-1043*.
- Guerrier M. P. [1999]** – “The Development and Evaluation of Phosphorent Particle Tracking”, Ph.D. Thesis, Department of Mechanical Engineering University College London.
- Han D, Steeper R. R. [2002]** – “Examination of Iso-Octane/Ketone Mixtures for Quantitative LIF Measurements in a DISI Engine”, *SAE Technical Paper No. 2002-01-0837*.
- Han Z, Fan L, Reitz R. D. [1997a]** – “Multidimensional Modelling of Spray Atomization and Air-Fuel Mixing in a Direct-Injection Spark-Ignition Engine”, *SAE Technical Paper No. 970884*.
- Han Z, Parrish S, Farrell P. V, Reitz R. D, [1997b]** – “Modelling Atomization Processes of Pressure-Swirl Hollow-Cone Fuel Sprays”, *Atomization and Sprays*, Vol 7, pp 663-684.
- Han Z, Xu Z, Wooldridge T, Yi J, Lavoie G. [2001]** – “Modelling of DISI Engine Sprays with Comparison to Experimental In-Cylinder Spray Images”, *SAE Technical Paper No. 2001-01-3667*.
- Harada J, Tomita T, Mizuno H, Mashiki Z, Ito Y. [1997]** – “Development of Direct Injection Gasoline Engine”, *SAE Technical Paper No. 970540*.
- Hecht E. [1998]** – “Optics”, 3rd Ed. *Reading, Mass: Addison-Wesley*, ISBN 020183887
- Hentschel W, Homburg A, Ohmstede G, Müller T, Grünefeld G. [1999]** – “Investigation of Spray Formation of DI Gasoline Hollow-Cone Injectors Inside a Pressure Chamber and a Glass Ring Engine by Multiple Optical Techniques”, *SAE Technical Paper No. 1999-01-3660*.

- Heywood J.B. [1988]** – “Internal Combustion Engine Fundamentals”, *McGraw-Hill International Edition*, ISBN 0-07-100499-8.
- Hinze J. O. [1955]** – “Fundamentals of the Hydrodynamic Mechanism of Splitting in Dispersion Processes”, *A.I.Ch.E Journal*, Vol. 1, No. 3, pp 289 – 295.
- Hochgreb S, VanDerWege Brad. [1998]** – “The Effect of Fuel Volatility on Early Spray Development from High-Pressure Swirl Injectors”, *Direkteinspritzung im Ottomotor I*, pp. 107-116. ISBN 3-8169-1685-6.
- Huang Y, Alger T, Matthews R, Ellzey J. [2001]** – “The Effects of Fuel Volatility and Structure on HC Emissions from Piston Wetting in DISI Engines”, *SAE Technical Paper No. 2001-01-1205*.
- Hung D. L. S, Chmiel D. M, Markle L. E. [2003]** – “Application of an Imaging-based Diagnostic Technique to Quantify the Fuel Spray Variations in a Direct-Injection Spark-Ignition Engine”, *SAE Technical Paper No. 2003-01-0062*.
- Ipp W, Wagner V, Krämer H, Wensing M, Leipertz A, Arndt S, Jain A. [1999]** – “Spray Formation of High Pressure Swirl Gasoline Injectors Investigated by Two-Dimensional Mie and LIEF Techniques”, *SAE Technical Paper No. 1999-01-0498*.
- Iwamoto Y, Noma K, Nakayama O, Yamauchi T, Ando H. [1997]** – “Development of Gasoline Direct Injection Engine”, *SAE Technical Paper No. 970541*.
- James G. [1999]** – “Advanced Modern Engineering Mathematics”, 2nd Ed. *Addison-Wesley Publishers*, ISBN 0201596210.
- Jermy M. [2002]** – “Advanced Measurement Techniques for Fluid Flows”, *A 3 Day Course, PERDAC/UMIST*, Jan 2002.
- Kakuhou A, Urushihara T, Itoh T, Takagi Y. [1999]** – “Characteristics of Mixture Formation in a Direct Injection SI Engine with Optimized In-Cylinder Swirl Air Motion”, *SAE Technical Paper No. 1999-01-0505*.
- Karaiskos E, Arcoumanis C, Hale T. [2002]** – “Flow and Spray Investigation in Direct Injection Gasoline Engines”, *SAE Technical Paper No. 2002-01-0832*.

- Kawahara N, Tomita E, Kasahara D, Nakayama T. [2004]** – “Fuel Breakup near Nozzle Exit of High-Pressure Swirl Injector for Gasoline Direct Injection Engine”, *SAE Technical Paper No. 2004-01-0542*.
- Kawajiri K, Yonezawa T, Ohuchi H, Sumida M, Katashiba H. [2002]** – “Study of Interaction Between Spray and Air Motion, and Spray Wall Impingement”, *SAE Technical Paper no. 2002-01-0836*.
- Kim J-I, No S-Y, Lee Y-J. [2001]** – “Experimental Analysis of Breakup Length in Pressure-Swirl Atomiser”, *6th Annual Conf. on Liquid Atomization and Sprays*.
- Kim J-S, Park J-H, Chon M-S, Yun J-E. [2000]** – “A Study on the In-Cylinder Flow Characteristics of GDI High-Pressure Fuel Injector Using a Transparent Engine System”, *Seoul 2000 FISITA World Automotive Congress*, June 12-15, Seoul, Korea.
- Kobayashi T, Kawaguchi T, Maeda M. [2000]** – “Measurement of Spray Flow by an Improved Interferometric Laser Imaging Droplet Sizing (ILIDS) System”, *10th. Int. Symp. Applications of Laser Techniques to Fluid Mechanics*, Lisbon-Portgal, 10.2.
- Koh K. U, Kim J. Y, Lee S. Y. [2001]** – “Determination of In-Focus Criteria and Depth of Field in Image Processing of Spray Particles”, *Atomization and Sprays*, Vol 11, pp 317-333.
- Kubo M, Sakakida A, Iiyama A. [2001]** – “Technique for Analyzing Swirl Injectors of Direct-Injection Gasoline Engines”, *SAE Technical Paper No. 2001-01-0964*.
- Kume T, Iwamoto Y, Iida K, Murakami M, Akishino K, Ando H. [1996]** – “Combustion Control Technologies for Direct Injection SI Engines”, *SAE Technical Paper No. 960600*.
- Ledoyen S, Dumouchel C, Preterre C. [1999]** – “Experimental Investigation on the Characteristics and on the Reproducibility of the Flow issuing from a High-Pressure Direct-Injection Nozzle”, *SAE Technical Paper No. 1999-01-3655*.
- Lee C. S, Lee K. H, Chon M. S, Kim D. S. [2001]** – “Spray Structure and Characteristics of High-Pressure Gasoline Injectors for Direct-Injection Engine Applications”, *Atomization and Sprays*, Vol 11, pp 35-48.

- Lee J, Yamakawa M, Isshiki S, Nishida K. [2002]** – “An Analysis of Droplets and Ambient Air interaction in a D.I. Gasoline Spray using LIF-PIV Technique”, *SAE Technical Paper No. 2002-01-0743*.
- Lefebvre A. H. [1989]** – “Atomization and Sprays”, 1st Ed. *Hemisphere Publishing Corporation*, ISBN 0-89116-603-3.
- Loustalan P. W, Davy M. H, Williams P. A. [2003(a)]** – “Experimental Investigation into the Liquid Sheet Break-Up of High-Pressure DISI Swirl Atomisers”, *SAE Technical Paper No. 2003-01-3102*.
- Loustalan P. W, Davy M. H. [2003(b)]** – “Preliminary Analysis of the Near Nozzle Break-Up from a Pressure-Swirl Atomiser using a Void Fraction Technique”, *Proc. of International Congress on Direkteinspritzung im Ottomotor IV (Gasoline Direct Injection Engines)*.
- Melling A. [1997]** – “Tracer Particles and Seeding for Particle Image Velocimetry”, *Meas. Sci. Technology*. Vol. 8, pp 1406-1416.
- Münch K. U, Leipertz A. [1992]** – “Investigation of Spray Penetration and Fuel Distribution Inside the Piston Bowl of a 1.9l DI Diesel Engine using Two-Dimensional Mie Scattering”, *SAE Technical Paper No. 922204*.
- Nogi T, Shiraishi T, Nakayama Y, Ohsuga M, Kurihara N. [1998]** – “Stability Improvement of Direct Injection Engine Under Lean Combustion Operation”, *SAE Technical Paper No. 982703*.
- Nouri J. M, Whitelaw J. H. [2001]** – “Spray Characteristics of a Gasoline Direct Injection Injector with Short Durations of Injection”, *Experiments in Fluids* 31, pp 377-383.
- Ohsuga M, Shiraishi T, Nogi T, Nakayama Y, Sukegawa Y. [1997]** – “Mixture Preparation for Direct-Injection SI Engines”, *SAE Technical Paper No. 970542*.
- O'Rourke, P. J, Amsden A, A. [1987]** – “The TAB Method for Numerical Calculation of Spray Droplet Breakup”, *SAE Technical Paper No. 872089*.
- Park J-H, Yoon Y, Hwang S-S. [2002]** – “Improved Tab Model for Prediction of Spray Droplet Deformation and Breakup”, *Atomization and Sprays*, Vol 12, pp 387-401.

- Preussner C, Döring C, Fehler S, Kampmann S. [1998]** – “GDI: Interaction Between Mixture Preparation, Combustion System and Injector Performance”, *SAE Technical Paper No.* 980498.
- Ren W. M, Nally, Jr. J. F. [1998]** – “Computation of Hollow-Cone Sprays from a Pressure-Swirl Injector”, *SAE Technical Paper No.* 982610.
- Robart D, Kneer R, Lai M-C. [2001]** – “Application of a High Temporal Resolution Laser Diffraction Technique to the Concentration of Gasoline Direct Injection Sprays”, *Direkteinspritzung im Ottomotor III*, pp. 169-187. ISBN 3-8169-2014-4.
- Russ J. C. [2002]** – “The Image Processing Handbook”, 4th Ed. *CRC Press*, ISBN 0-8493-1142-X.
- Salter D, Williams P, Greig A, Brehob D. [1996]** – “Fuel Spray Characterisation within an Optically Accessed Gasoline Direct Injection Engine Using a CCD Imaging System”, *SAE Technical Paper No.* 961149.
- Sandquist H, Lindgren R, Denbratt I. [2000]** – “Sources of Hydrocarbon Emissions from a Direct Injection Stratified Charge Sprak Ignition Engine”, *SAE Technical Paper No.* 2000-01-1906.
- Schmidt D. P, Nouar I, Senecal P. K, Rutland C. J, Martin J. K, Reitz R. D, Hoffman J. A. [1999]** – “Pressure-Swirl Atomization in the near Field”, *SAE Technical Paper No.* 1999-01-0496.
- Schmitz I, Ipp W, Leipertz A. [2002]** – “Flash Boiling Effects on the Development of Gasoline Direct-Injection Engine Sprays”, *SAE Technical Paper No.* 2002-01-2661.
- Senecal P. K, Schmidt D. P, Nouar I, Rutlanad C. J, Reitz R. D, Corradini M. L. [1999]** – “Modelling High-Speed Viscous Liquid Sheet Atomization”, *Intl. J. Multiphase Flow*, May 1999.
- Shayler P. J, Jones S. T, Horn G, Eade D. [2001]** – “Characterisation of DISI Emissions and Fuel Economy in Homogeneous and Stratified Charge Modes of Operation”, *SAE Technical Paper No.* 2001-01-3671.
- Shelby M. H, VanDerWege B. A, Hochgreb S. [1998]** – “Early Spray Development in Gasoline Direct-Injected Spark Ignition Engines”, *SAE Technical Paper No.* 980160.

- Sick V, Stojkovic B. [2001]** – “Attenuation Effects on Imaging Diagnostics of Hollow-Cone Sprays”, *Applied Optics* Vol.40, No. 15, pp 2435-2442.
- Simko A, Chome M. A, Repko L. L. [1972]** – “Exhaust Emission Control by the Ford Programmed Combustion Process – PROCOCO”, *SAE Technical Paper No. 720052*.
- Squire H. B. [1953]** – “Investigation of the instability of a Moving Liquid Film”, *Brit. J. Applied Physics*, Vol. 4, No. 6, pp 167-169.
- Stanglmaier R. H, Hall M. J, Matthews R. D. [1998]** – “Fuel-Spray/Charge Interaction within the Cylinder of a Direct-Injected, 4-Valve, SI Engine”, *SAE Technical Paper No. 980155*.
- Takagi Y, Itoh T, Muranaka S, Iiyama A, Iwakiri Y, Urushihara T, Naitoh K. [1998]** – “Simultaneous Attainment of Low Fuel Consumption, High Output Power and Low Exhaust Emissions in Direct Injection SI Engines”, *SAE Technical Paper No. 980149*.
- Takeda K, Sugimoto T, Tsuchiya T, Ogawa M, Ueda S, Yoneshige K. [2000]** – “Slit Nozzle Injector for a New Concept of Direct Injection SI Gasoline Engine”, *SAE Technical Paper No. 2000-01-1902*.
- Tomoda T, Sasaki S, Sawada D, Saito A, Sami H. [1997]** – “Development of Direct Injection Gasoline Engine – Study of Stratified Mixture Formation”, *SAE Technical Paper No. 970539*.
- VanDerWege B. A, Hochgreb S. [2000]** – “Experimental Study of the Effects of Fuel Volatility and Operating Conditions on Fuel Sprays in DISI Engines Part I: Planar Laser-Induced Fluorescence”, *SAE Technical Paper No. 2000-01-0535*.
- Wagner V, Ipp W, Wensing M, Leipertz A. [1999]** – “Fuel Distribution and Mixture Formation Inside a Direct Injection SI Engine investigated by 2D Mie and LIEF Techniques”, *SAE Technical Paper No. 1999-01-3659*.
- Williams P, O’Donoghue S, Anderson R. W, Richardson S. H. [2001]** – “An Experimental Study of the Spray Characteristics of Pressure-Swirl Atomizers for DISI Combustion Systems”, *SAE Technical Paper No. 2001-01-1974*.

- Williams P. A, Davy M. H, Brehob D. D. [1998]** – “Effects of Injection Timing on the Exhaust Emissions of a Centrally-Injected Four-Valve Direct-Injection Spark-Ignition Engine”, *SAE Technical Paper No. 982700*.
- Williams P. A. [1994]** – “Characterization of Fuel Sprays in Spark Ignition Engines – Volume 1” Ph.D. Thesis, Department of Mechanical Engineering University College London.
- Xu M, Markle L. E, [1998]** – “CFD-Aided Development of Spray for an Outwardly Opening Direct Injection Gasoline Injector”, *SAE Technical Paper No. 980493*.
- Yamauchi T, Wakisaka T, Kaneko T, Kaneko M, Kato S, Hosaka H. [1998]** – “Numerical Analysis of Stratified Charge Mixture Formation in Direct-Injection Gasoline Engines”, *Direkteinspritzung im Ottomotor I*, pp. 166-185.
- Yamauchi T, Wakisaka T. [1996]** – “Computation of the Hollow-Cone Sprays from a High-Pressure Swirl Injector for a Gasoline Direct-injection SI Engine”, *SAE Technical Paper No. 962016*.
- Young W. C. [1989]** – “Roark’s Formulas for Stress and Strain”, 6th Ed. *New York: McGraw Publishers*, ISBN 0071003738.
- Yule A. J, Vamvakoglou K, Shrimpton J. S. [1998]** – “Break-Up of a Thin Flat Sheet Adjacent to a Wide, High Velocity Air Stream”, *Proc. ILASS-Europe '98*.
- Yule A. J, Vamvakoglou K. [1999]** – “Break-Up of a Liquid Sheet Adjacent to a Single Air Stream”, *Proc. ILASS-Europe '99*.
- Zeng Y, Lee C-F. [2000]** – “Modelling of Spray Vaporization and Air-Fuel Mixing in Gasoline Direct-Injection Engines”, *SAE Technical Paper No. 2000-01-0537*.
- Zhao F, Harrington D. L, Lai M-C. [2002]** – “Automotive Gasoline Direct – Injection Engines”, 1st Ed. *SAE Int. Inc*, ISBN 0-7680-0882-4.
- Zhao F, Lai M-C, Harrington D. L. [1999]** – “Automotive Spark-Ignited Direct-Injection Gasoline Engines”, *Prog. In Energy and Combustion Science*, 25. Pp 437-562.

Zhao F-Q, Lai M-C, Harrington D.L. [1997] – “A Review of Mixture Preparation and Combustion Control Strategies for Spark-Ignited Direct-Injection Gasoline Engines”, *SAE Technical Paper No. 970627*.

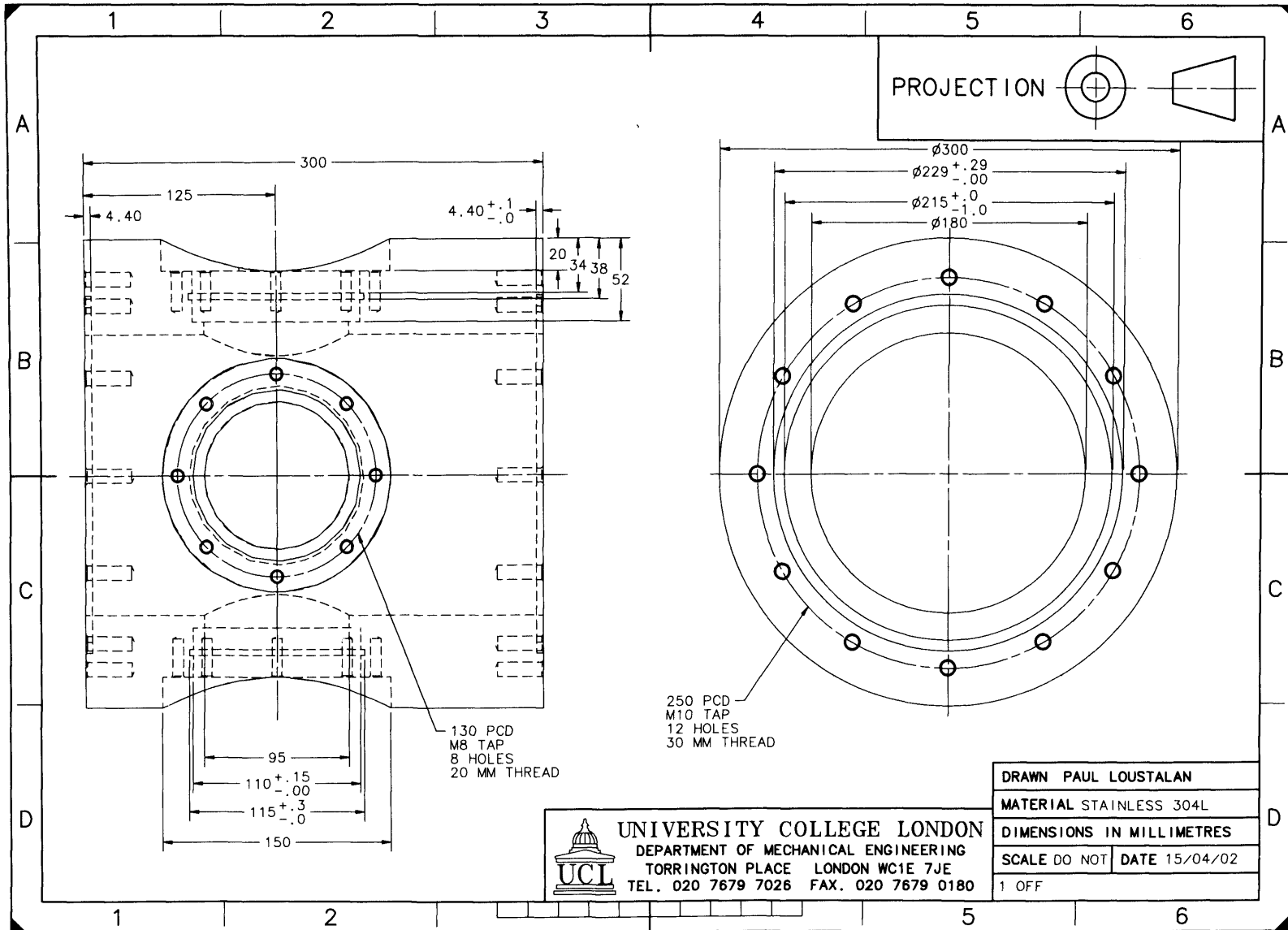
Zhao F-Q, Yoo J-H, Lai M-C. [1996] – “Spray Dynamics of High Pressure Fuel Injectors for DI Gasoline Engines”, *SAE Technical Paper No. 961925*.

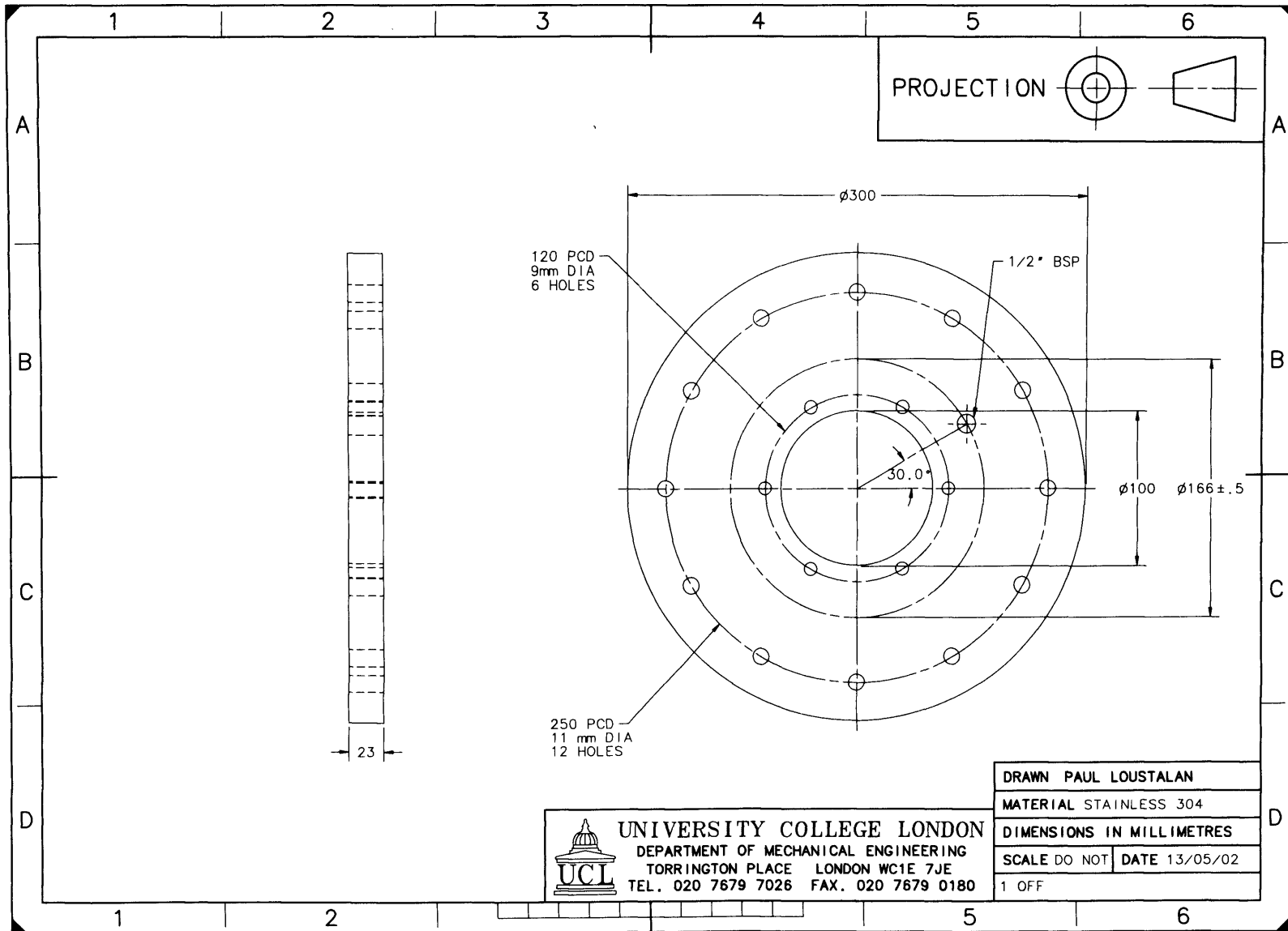
“*DaVis FlowMaster Manual*” – [2002], PIV Hardware manual for DaVis 6.2, La Vision GmbH.

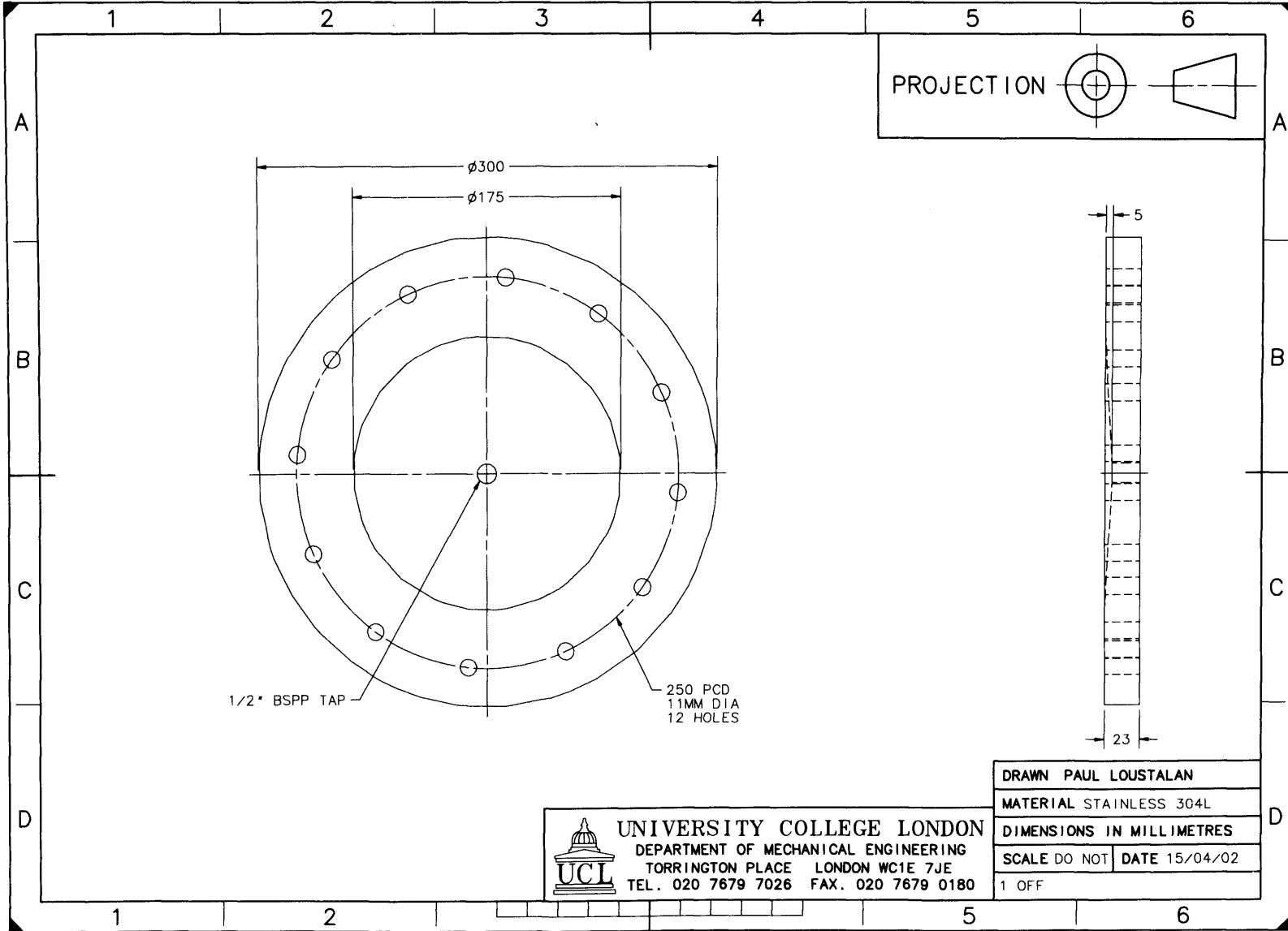
Appendix I

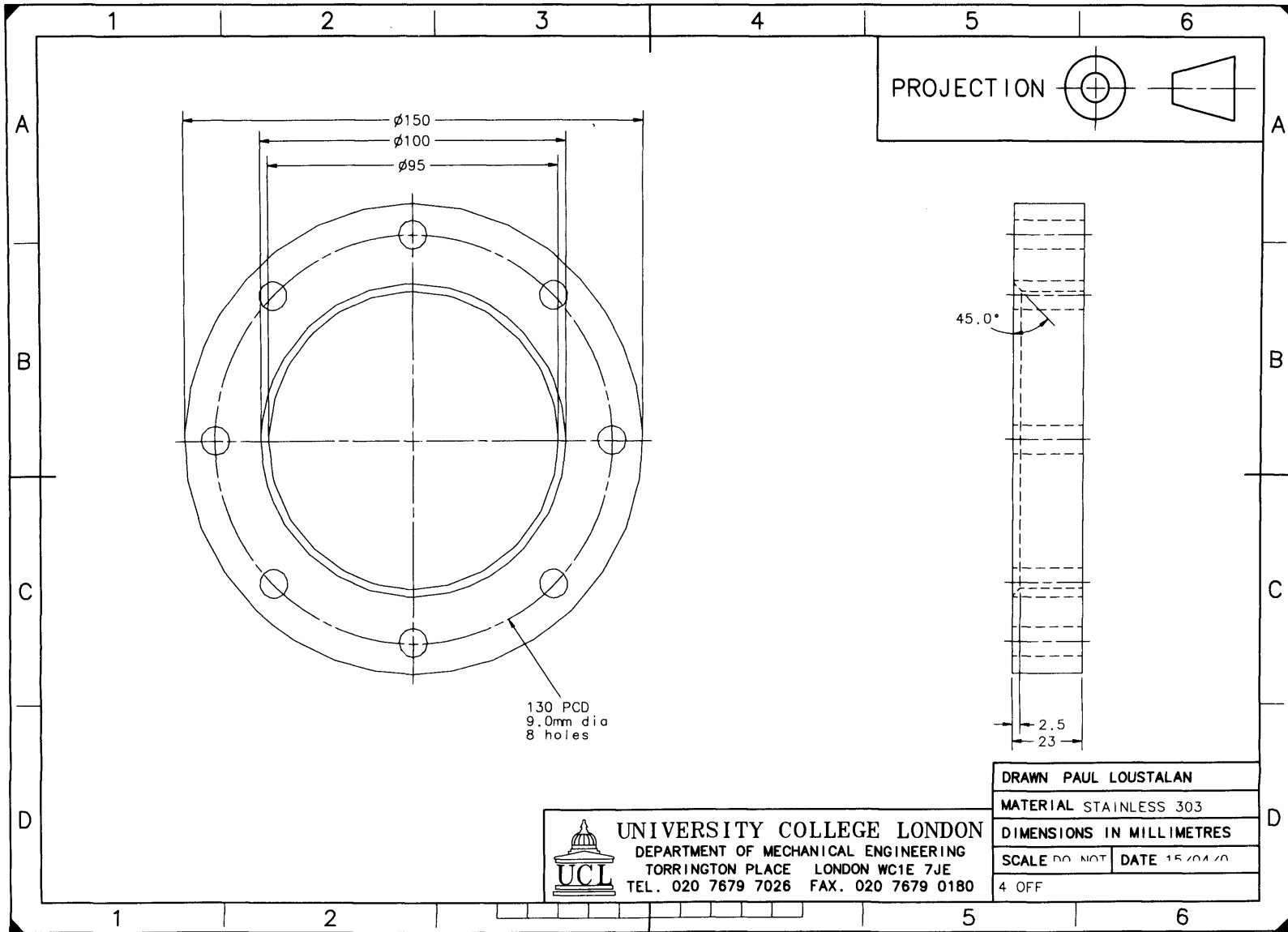
Technical Drawings

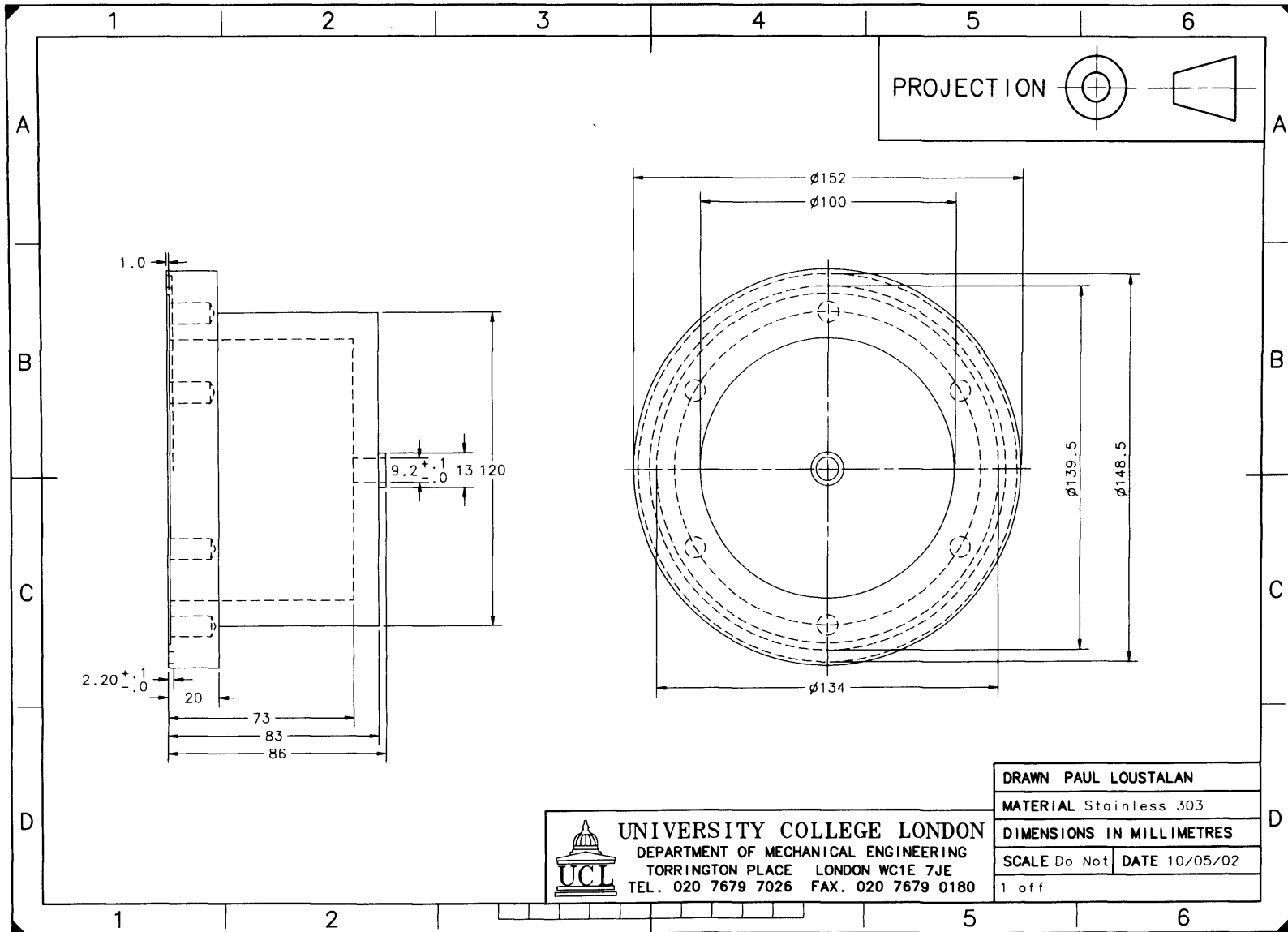
Static Pressure Chamber Drawings:







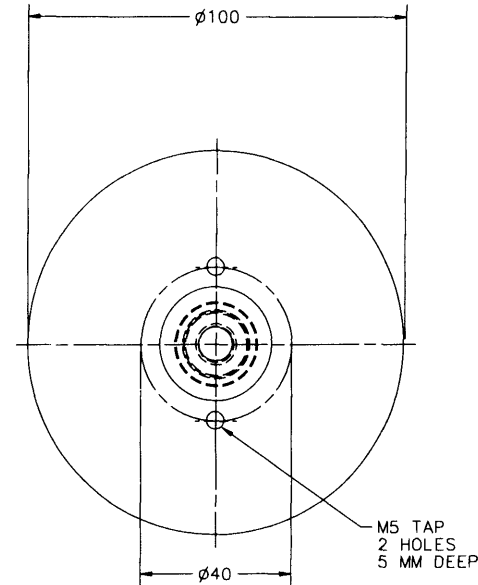
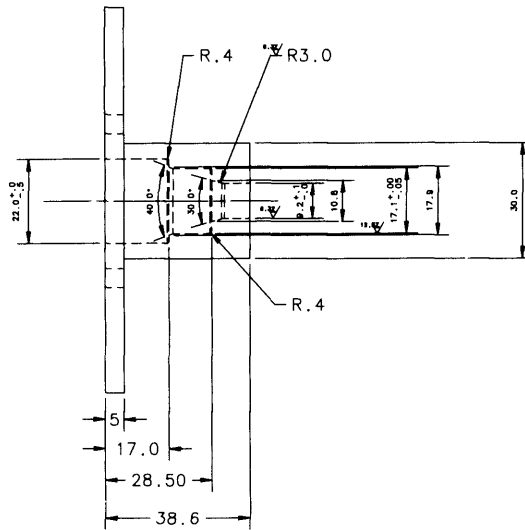
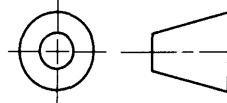




NB: TO FIT ID OF PART NAME: HOLDER

Critical to align Hole in HOLDER and Hole in INSERT

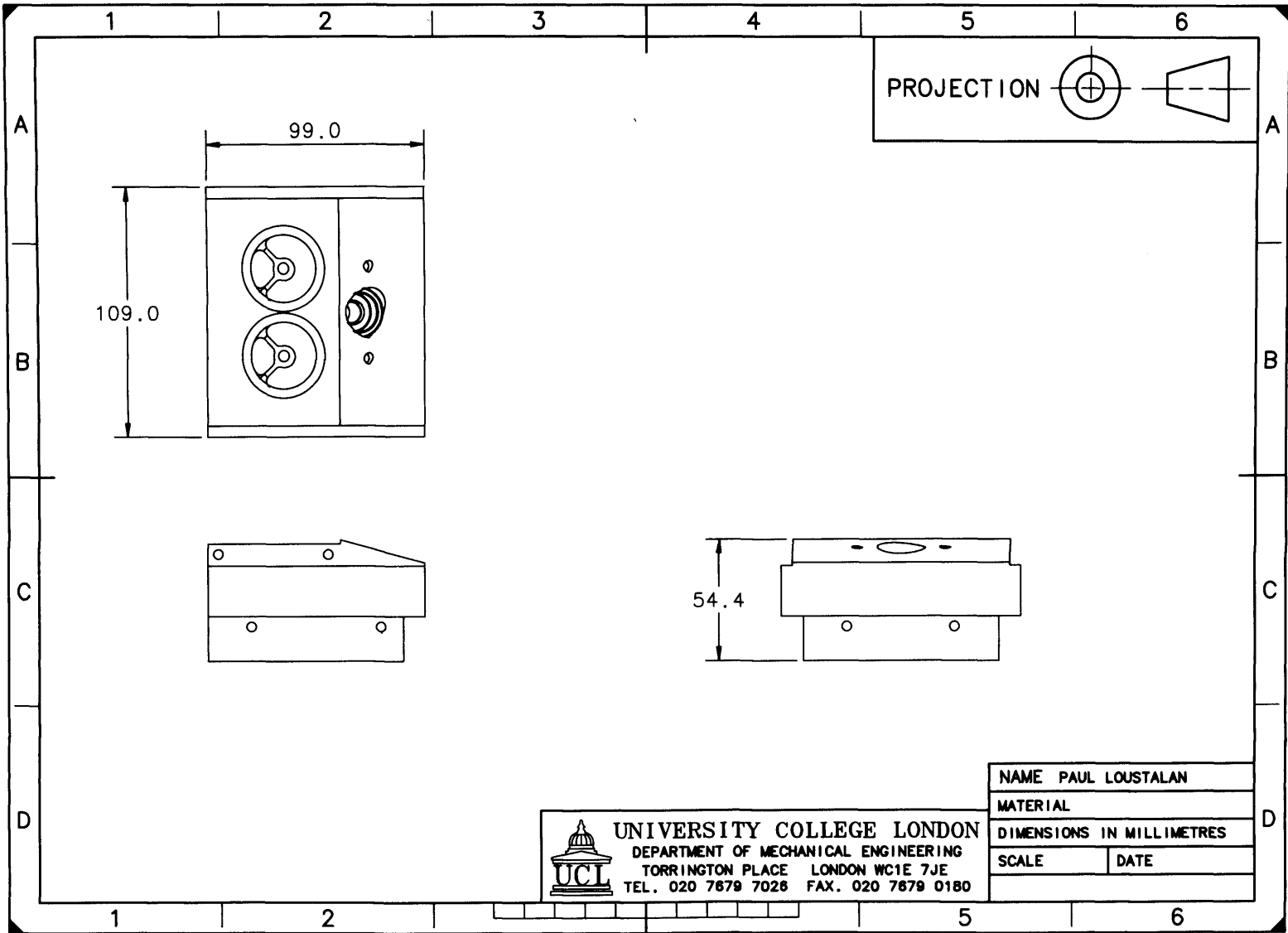
PROJECTION

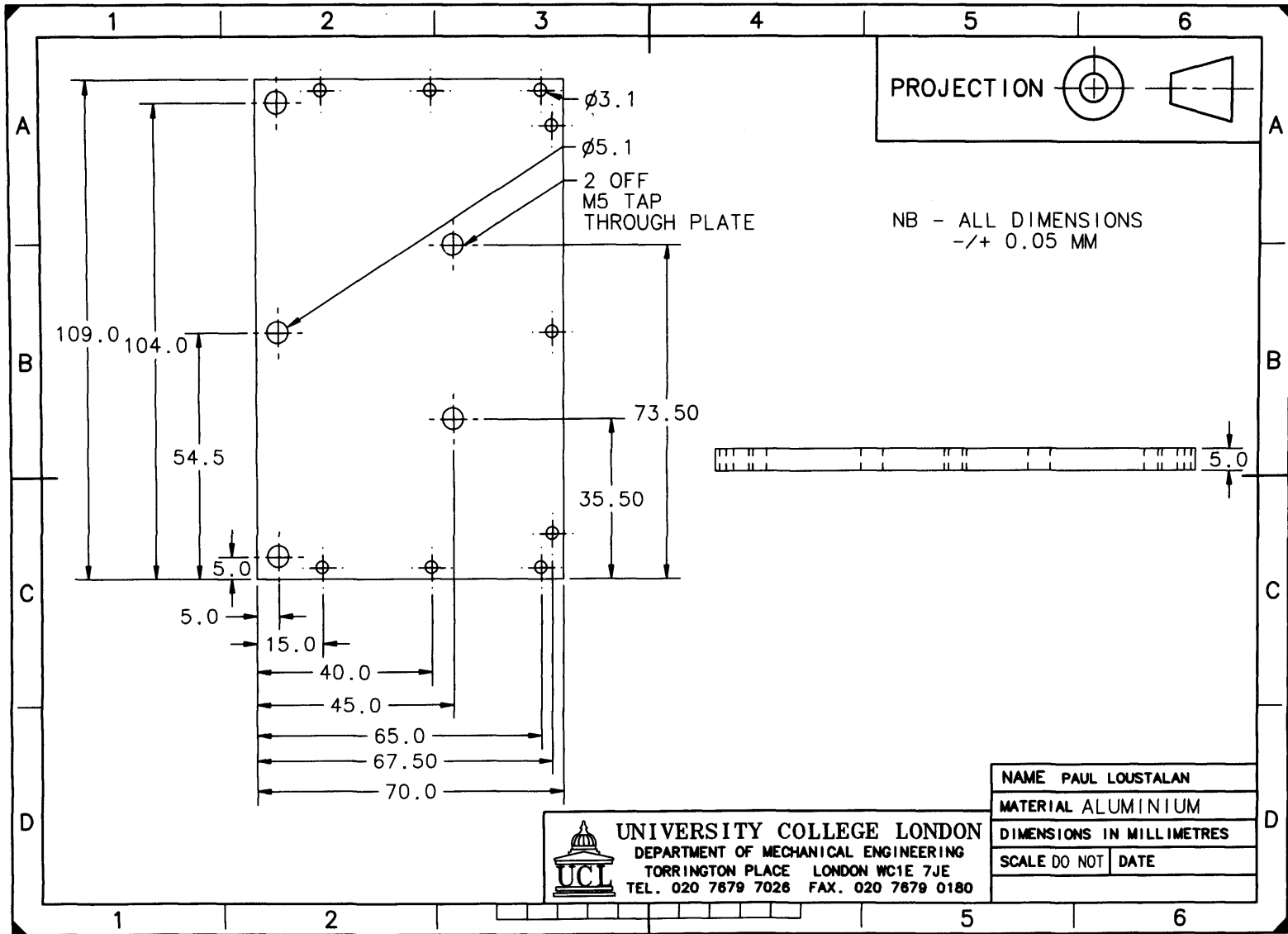


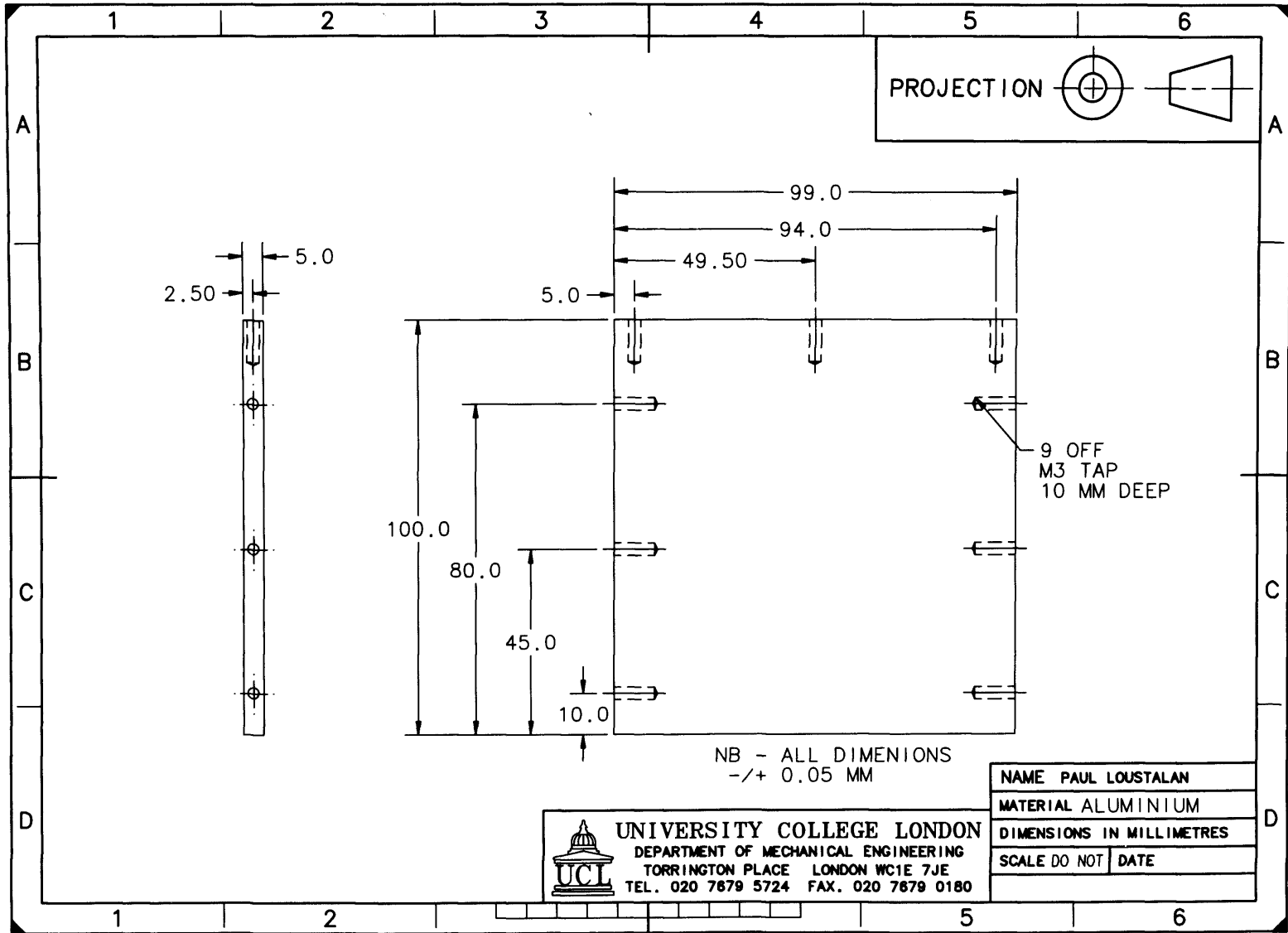
DRAWN PAUL LOUSTALAN	
MATERIAL ALUMINIUM	
DIMENSIONS IN MILLIMETRES	
SCALE DO NOT	DATE 28/05/02
1 OFF	

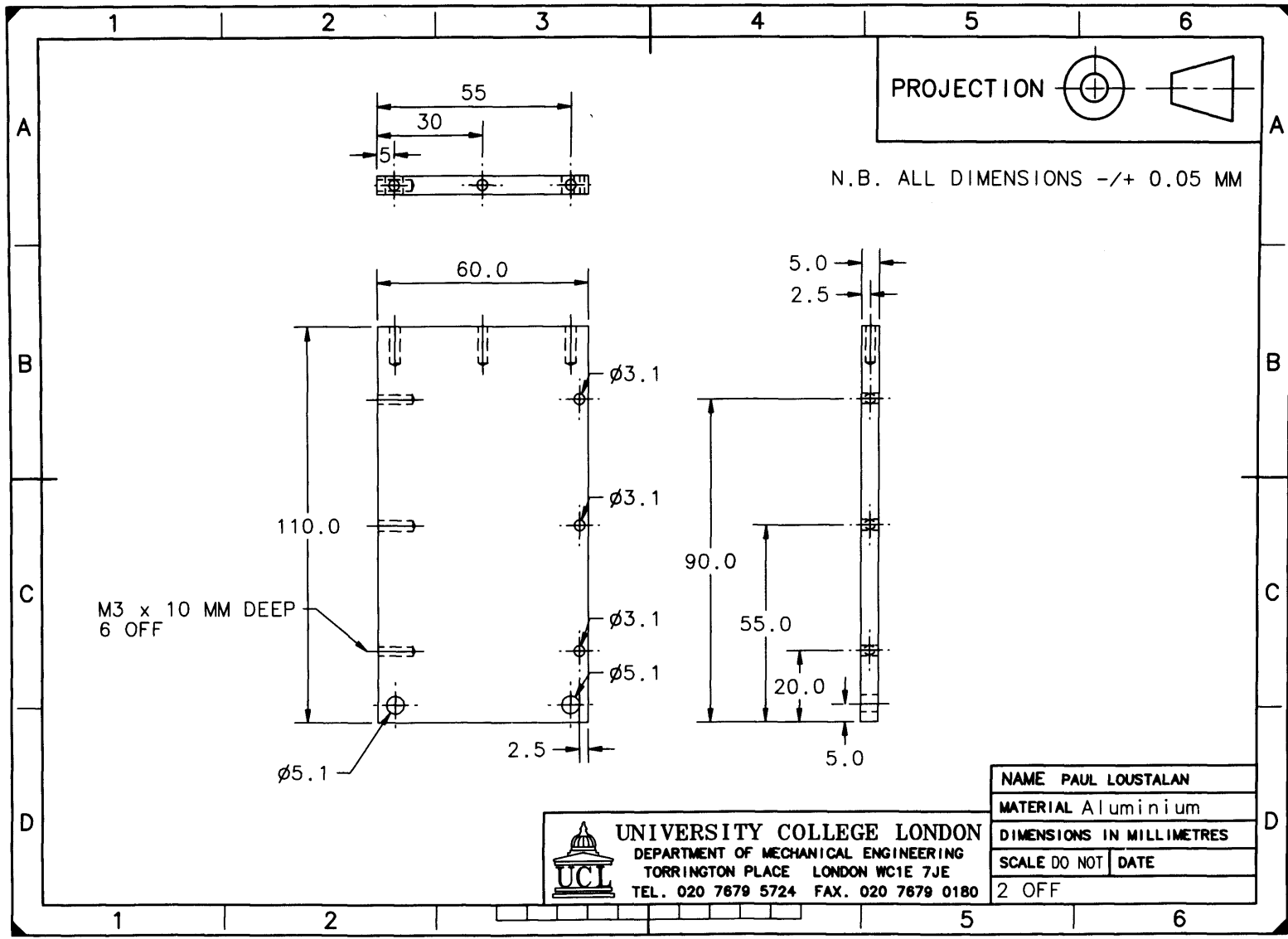


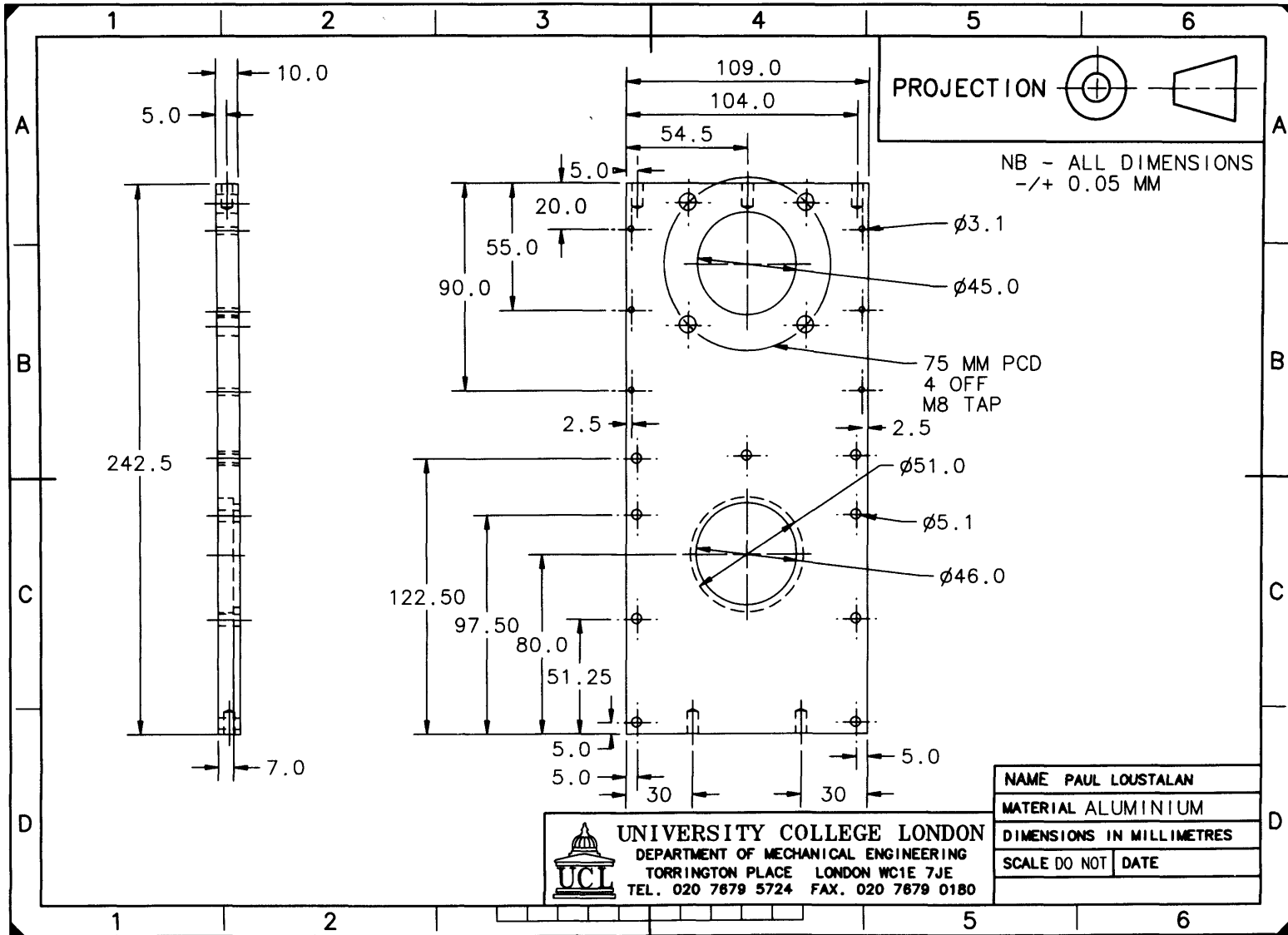
UNIVERSITY COLLEGE LONDON
DEPARTMENT OF MECHANICAL ENGINEERING
TORRINGTON PLACE LONDON WC1E 7JE
TEL. 020 7679 7026 FAX. 020 7679 0180

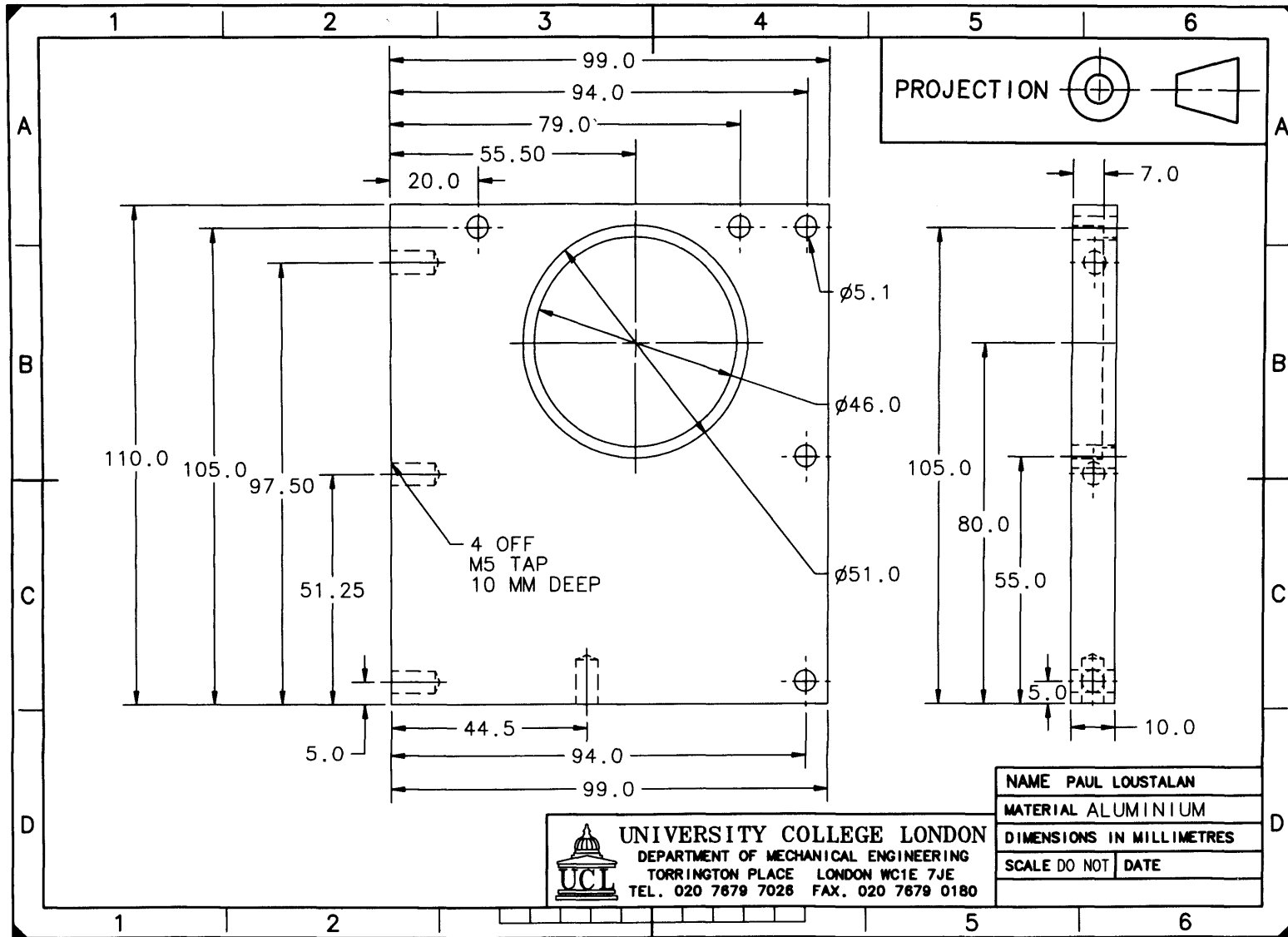


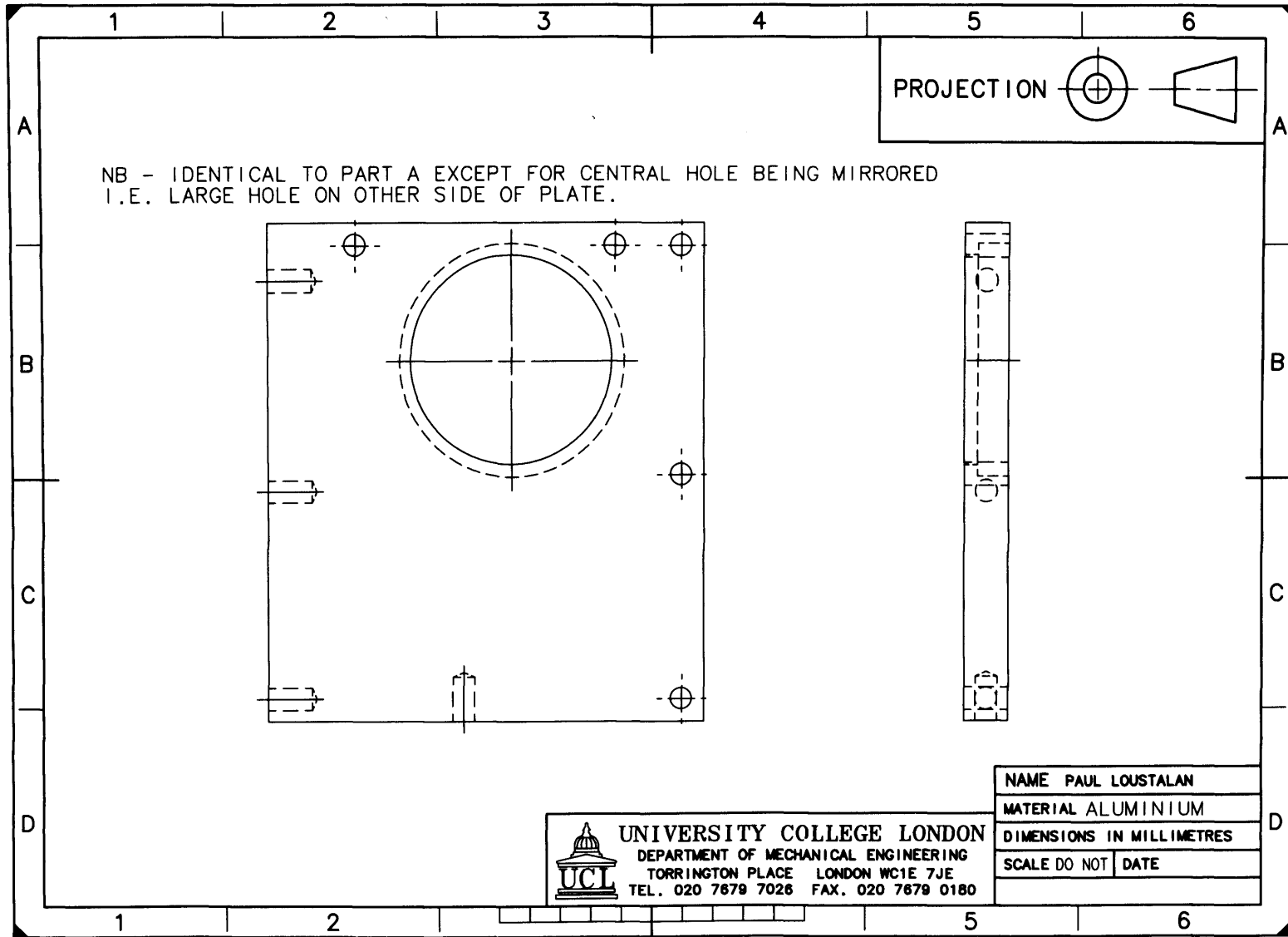


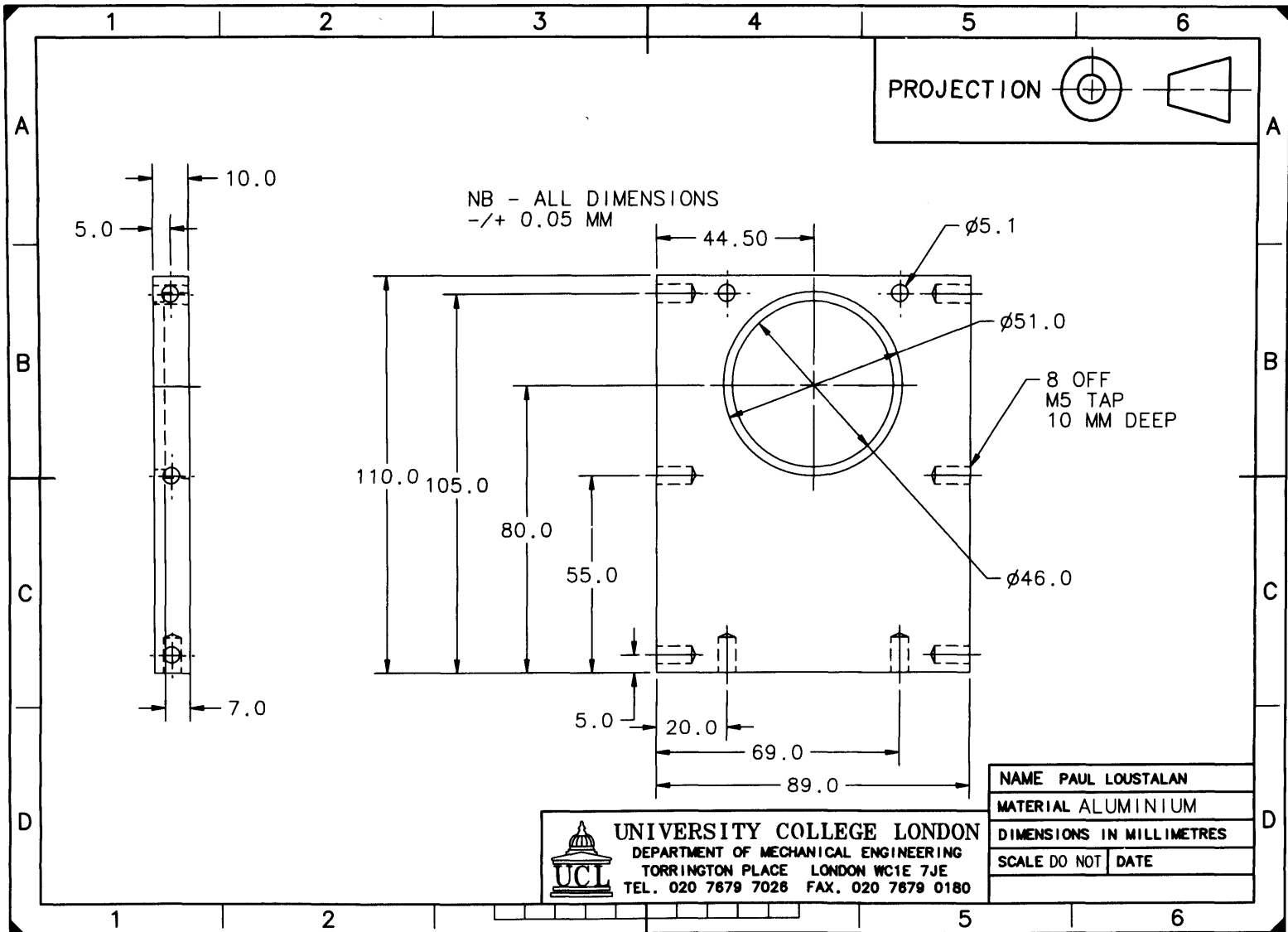


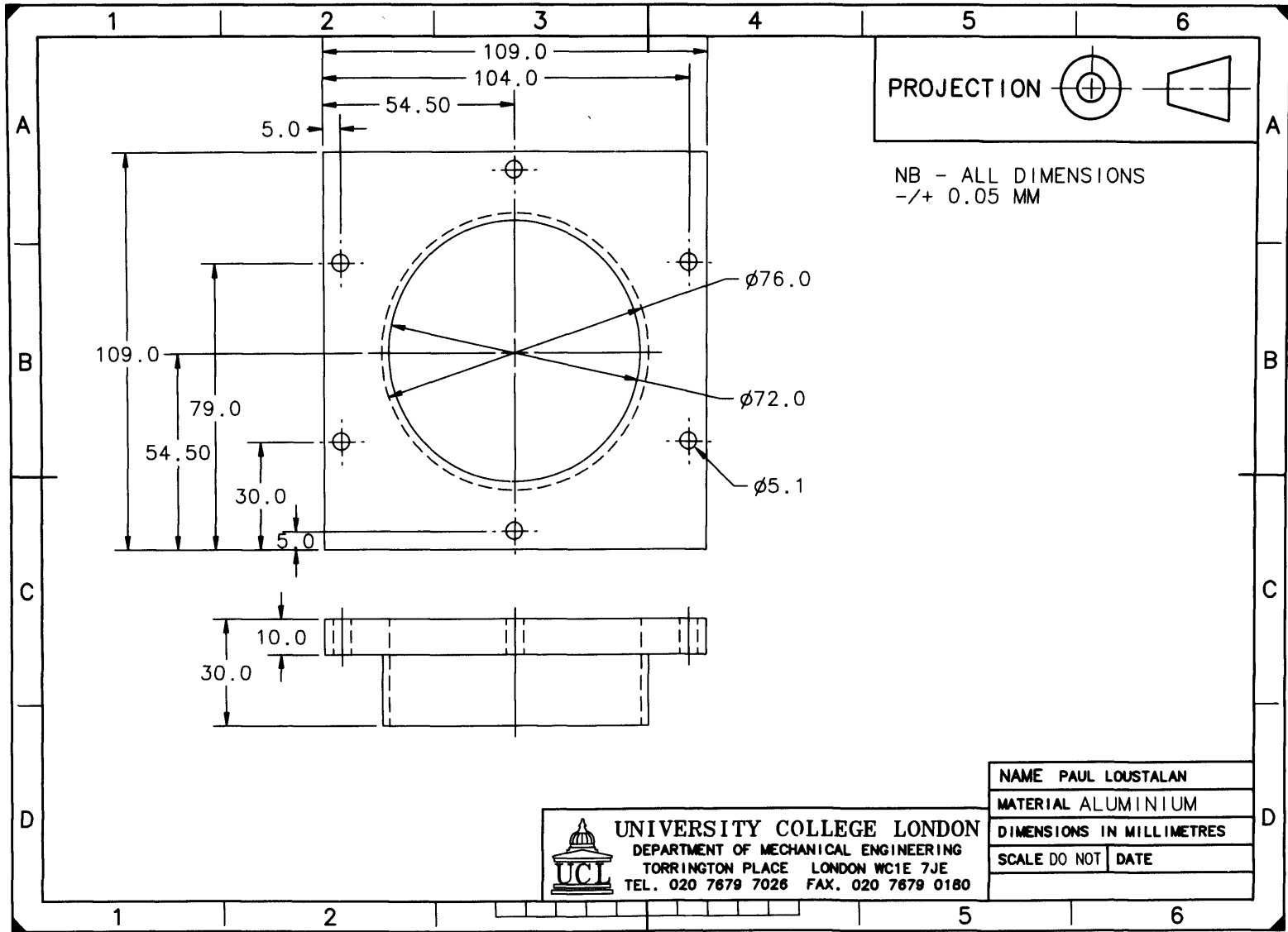












Appendix II
Macro Programs – Image Pro Plus™

Void Recognition Program – Offset Injector

(“&” signifies continuation of program code over more than one line, this does not appear in the macro code)

Option Explicit

'Declare Global Variables

```
Dim number As Integer           'How many AOI's
Dim calib As Single             'Variable to set AOI height
Dim perholes(49) As Single      'Percentage holes array
Dim AOIname As String
Dim pressure As Single
```

```
Dim cpressure As Single
Dim saveit As Integer
Dim spressure As String
Dim scpressure As String
```

```
Dim xlapp As Object
Dim xlbook As Object
Dim xlsheet As Object
```

```
'InitExcel() initializes the OLE link to Excel and returns the Object
'in the xlApplication parameter. Return value: 0 = success; -1 =
'failure
```

```
Function InitExcel(ByRef xlApplication As Object) As Integer
```

```
InitExcel = 0      ' Make sure the function is initialized
```

```
'On Error Resume Next continue if an error is generated
Err.Clear          ' clear the error flag
```

```
Set xlApplication = GetObject(,"Excel.Application")
```

```
' GetObject will return an error if Excel isn't open
If Err.Number <> 0 Then
    ' Start Excel with CreateObject. If this fails, we
    'exit the macro.
```

```
Err.Clear
```

```
Set xlApplication = CreateObject ("Excel.Application")
```

Appendix II – Macro Programs – Image Pro Plus™

```
If Err.Number <> 0 Then

MsgBox "Can't find Excel.", vbOkOnly+vbCritical, "OLE Error"

InitExcel = -1
Exit Function
End If
End If

'show Excel (don't run in background)
xlApplication.Visible = True

If Err.Number <> 0 Then
MsgBox "Error showing Excel!", vbOkOnly+vbCritical, "OLE Error"
InitExcel = -2
End If
End Function
```

```
Sub Hole_Count

Dim Terminate As Integer      'Variable to terminate macro
Dim height As Single          'AOI Height
Dim point1 As pointapi, point2 As pointapi    'AOI user input size
Dim check1 As Integer
Dim check2 As Integer        'Check for valid AOI user input points

Dim aoi As Integer            'Check to see if another AOI is required
Dim pixheight As Integer     'Height of AOI in pixels
Dim tipcentre As pointapi    'Coordinates of Injector tip centre
Dim distance As Single       'Dist from Inj tip to centre of 1st AOI

Dim temp As String * 10      'Temp string to store pos of Excel data
Dim j As Integer             'Counter
Dim disarray(49) As Single   'Array of distances of all AOI's from
                              'injector tip

Dim docname As String * 255
Dim docnames As String
Dim spraytime As Single

number = 0                    'Set initial number of AOI's to zero
aoi = 1                       'Initially an AOI is required so set to 1
terminate = 1                 'Set initially to 1 to start do loop
```

Appendix II – Macro Programs – Image Pro Plus™

```
Do While terminate = 1                                'Main do loop

    terminate = ipmacrostop("Do you wish to open an image for &
    processing?" , ms_modal + ms_yesno + ms_quest)
    'Determine whether or not more processing is required
If terminate = 1 Then

    'Start up excel and create a new worksheet

If InitExcel(xlapp) < 0 Then
Exit Sub
End If

'create a new workbook for the data
Set xlbook = xlapp.Workbooks.Add
xlbook.Activate
Set xlsheet = xlbook.ActiveSheet
xlsheet.Activate
xlapp.Visible = True
xlapp.WindowState = xlMinimized

ret = iptemplatemode(1)
    'Request image to be processed is opened by user
ret = ipwsload("", "TIF")
ret = iptemplatemode(0)

ret = ipdocgetstr(inf_name, docsel_active, docname)
docnames = Left(docname, InStr(docname, ".")-1)
docnames = Right(docnames, 3)

If Mid$(docnames,3,1)= "0" Then

docnames = Right(docnames, 2)

Else

docnames = LTrim(Replace$(docnames,"0",""))

End If

spraytime = (CSng(docnames) - 1) / 20
AOIname = LTrim(Str$(spraytime))

If Mid$(AOIname,1,1) = "." Then
```

Appendix II – Macro Programs – Image Pro Plus™

```
AOIname = "0" + AOIname

End If

If Mid$(AOIname,1,1) = "1" And Len(AOIname) = 1 Then

AOIname = AOIname + "."

End If

If Len(AOIname) <> 4 Then

AOIname = AOIname + "0"

If Len(AOIname) <> 4 Then

AOIname = AOIname + "0"

End If

End If

ret = ipstgetfloat("Enter the fuel pressure", pressure,& 50, 50, 100,
50)

ret = ipstgetfloat("Enter the chamber pressure",& cpressure, 0.5, 0.5,
2.0, 0.5)

saveit = ipmacrostop("Save these files?", ms_modal + & ms_yesno)

ret = ipstgetfloat("Enter the required height of the & AOI", height,
0.5, 0.0, 1.0, 0.05)
'Dialog box to ask user for required AOI height

If ret = 0 Then GoTo ending
'Exit out of macro upon cancel being pressed

ret = ipdocclick("Please click on the centre of the & Injector Tip",
tipcentre)

calib = 452.94117650

pixheight = Int(calib * height)
'calculate AOI height in pixels
```

Appendix II – Macro Programs – Image Pro Plus™

```
iprect.Top = tipcentre.x + calib*(0.9 - (height/2))
    'Initially set AOI pixel coordinates

iprect.bottom = iprect.Top + pixheight
Do While aoi = 1
    'Repeat process for multiple AOI's within a single image

If aoi = 1 Then

check1 = ipdocclick("Select left point of AOI", point1)

    If check1 >=0 Then

check2 = ipdocclick("Select right point of AOI", point2)

If check1 = check2 Then

If number = 0 Then

number = number + 1

iprect.Left = point1.x
    'Set coordinates of AOI from user inputs
iprect.Right = point2.x
ret = ipaoicreatebox(iprect)

ret = ipwsduplicate()
ret = iphstequalize(eq_bestfit)

Call process

        aoi = ipmacrostop("Do you require another &
        AOI?", ms_modal + ms_yesno + ms_quest)

ElseIf number >= 1 Then

'All remaining AOI's to be positioned automatically

number = number + 1
ret = ipaoiget(getbounds, 0, iprect)
iprect.Left = point1.x
    'Set coordinates
of AOI from user inputs
iprect.Right = point2.x
iprect.top = iprect.bottom
```

Appendix II – Macro Programs – Image Pro Plus™

```
iprect.bottom = iprect.bottom + pixheight           'Progress AOI
sequentially down the image
ret = ipaoicreatebox(iprect)

ret = ipwsduplicate()
ret = iphstequalize(eq_bestfit)

Call process

aoi = ipmacrostop("Do you require another & AOI?", ms_modal + ms_yesno
+ ms_quest)

End If

End If

End If

End If

Loop

'Find starting point and calculate distance from tip to first AOI

'Ask for user input of centre of injector tip

distance = 0.9                                     'Calculate
the distance in mm

        xlsheet.Range(xlapp.Cells(99,1), xlapp.Cells(99,1)).value = &
"Distance from Tip"

        xlsheet.Range(xlapp.Cells(99,2), xlapp.Cells(99,2)).value = &
"%age Holes"

For j = 0 To number-1

disarray(j) = distance + height*j

xlsheet.Range(xlapp.Cells(100+j,1),xlapp.Cells(100+j,1)). & Value =
disarray(j)
xlsheet.Range(xlapp.Cells(100+j,2), xlapp.Cells(100+j,2)). & Value =
perholes(j)

Next
```

Appendix II – Macro Programs – Image Pro Plus™

```
xlsheet.Range(xlapp.Cells(1,1), xlapp.Cells(1,1)).value = spressure
xlsheet.Range(xlapp.Cells(1,2), xlapp.Cells(1,2)).value = scpressure
xlsheet.Range(xlapp.Cells(1,3), xlapp.Cells(1,3)).value = AOIname

End If

Loop                                'End of main do loop, and end of macro

ending:                              'Exit linelabel

ret = ipappcloseall()

xlsheet.Rows("2:2").Font.Bold = True

xlsheet.Range(xlapp.Cells(100,1), xlapp.Cells(104,1)).NumberFormat = &
"0.0"

xlsheet.Columns("A:x").AutoFit
xlsheet.Columns("A:x").HorizontalAlignment = xlCenter

xlsheet.Range(xlapp.Cells(1,1), xlapp.Cells(1,1)).Select

xlapp.WindowState = xlMaximized

Set xlsheet = Nothing
Set xlbook = Nothing
Set xlapp = Nothing

End Sub
```

```
Sub process

'A subroutine to process the aoi's created by hole_count

Dim docid As Integer
ReDim stats(10) As Single           'Define variable with 10 elements
                                   'for stats from histogram

Dim hstcor As Single               'Variable for thresholding
Dim outlinef As String * 100       'Name of file for Hole Outlines
Dim i As Integer                   'Counter
Dim dinfo As ipdocinfo             'Variable for information about
                                   'image

Dim areaaoi As Single              'Area of the active AOI
```

Appendix II – Macro Programs – Image Pro Plus™

```
Dim a As Single           'Holding variable
Dim b As Single           'Holding variable
Dim objstats(9) As Single 'Variable with 10 elements for the
                          'stats of the count
Dim percentageholes As Single 'Percentage holes of the AOI
Dim temp As String * 100  'Temporary variable to hold info
                          'about the Excel cell reference
Dim Imagename As String * 500 'Variable for the name of the AOI to
                              'be saved

Dim Areastats(200) As Single
Dim boxwstats(200) As Single
Dim boxhstats(200) As Single

If calib = 0 Then

ret = ipstgetfloat("Enter Calibration value", calib, & 452.94117650,
0.1, 1000, 0.01) 'Dialog box to ask for Calibration
                  'if the main macro has not been run
                  number = 1

End If

'Background Correction
'First perform rank levelling to allow for uneven lighting, use this
'background image to correct
'original image

ret = ipwsduplicate()
ret = iphstequalize(eq_bestfit)

ret = iphstget(getstats, 0 , stats(0))

hstcor = Int(stats(0) - (0.12*stats(0))) 'Use mean minus 12%
                                          '(decided empirically) to threshold
ret = iplutbinarize(0,hstcor,1)

'Erosion and Dilation to eliminate rogue pixels and smooth edges

ret = ipfilterode(morpho_2x2square,4) 'Erosion

ret = ipfltdilate(morpho_2x2square,4) 'Dilation

'Perform count and measurement operations
```

Appendix II – Macro Programs – Image Pro Plus™

```
ret = ipblbloadsetting("C:\Documents and Settings\Paul Loustalan\My &
Documents\TestingJul-Oct2002\holes.env")

ret = ipblbsetattr(blob_labelmode,0)

ret = ipblbcount()

ret = ipblbget(getrangestats, 0, blbm_area, objstats(0))

ret = ipdocget(getdocinfo, docsel_active, dinfo)

a = dinfo.height / calib
b = dinfo.width / calib

areaaai = a * b

percentageholes = objstats(5)*100/areaaai

ret = IpBlbData(blbm_area, 0, objstats(8), areastats(0))
ret = IpBlbData(BLBM_BOXX, 0, objstats(8), boxwstats(0))
ret = IpBlbData(BLBM_BOXY, 0, objstats(8), boxhstats(0))

'Output data to Excel

For i = 3 To objstats(8)+2

xlsheet.Range(xlapp.Cells(i, (5*number-4)), xlapp.Cells(i, (5*number- &
4))).Value = i-2
xlsheet.Range(xlapp.Cells(i, (5*number-3)), xlapp.Cells(i, (5*number- &
3))).Value = areastats(i-3)
xlsheet.Range(xlapp.Cells(i, (5*number-2)), xlapp.Cells(i, (5*number- &
2))).Value = boxwstats(i-3)
xlsheet.Range(xlapp.Cells(i, (5*number-1)), xlapp.Cells(i, (5*number- &
1))).Value = boxhstats(i-3)

Next

xlsheet.Range(xlapp.Cells(2, (5*number-4)), xlapp.Cells(2, (5*number- &
4))).Value = "Object"
xlsheet.Range(xlapp.Cells(2, (5*number-3)), xlapp.Cells(2, (5*number- &
3))).Value = "Area"
xlsheet.Range(xlapp.Cells(2, (5*number-2)), xlapp.Cells(2, (5*number- &
2))).Value = "Width"
xlsheet.Range(xlapp.Cells(2, (5*number-1)), xlapp.Cells(2, (5*number- &
1))).Value = "Height"
```

Appendix II – Macro Programs – Image Pro Plus™

```
xlsheet.Range(xlapp.Cells(objstats(8)+3,(5*number-4)), &
xlapp.Cells(objstats(8)+3,(5*number-4))).Value = "Total"
xlsheet.Range(xlapp.Cells(objstats(8)+4,(5*number-4)), &
xlapp.Cells(objstats(8)+4,(5*number-4))).Value = "Total Area"
xlsheet.Range(xlapp.Cells(objstats(8)+5,(5*number-4)), &
xlapp.Cells(objstats(8)+5,(5*number-4))).Value = "%age Holes"

xlsheet.Range(xlapp.Cells(objstats(8)+3,(5*number-3)), &
xlapp.Cells(objstats(8)+3,(5*number-3))).Value = objstats(5)
xlsheet.Range(xlapp.Cells(objstats(8)+4,(5*number-3)), &
xlapp.Cells(objstats(8)+4,(5*number-3))).Value = areaaoi
xlsheet.Range(xlapp.Cells(objstats(8)+5,(5*number-3)), &
xlapp.Cells(objstats(8)+5,(5*number-3))).Value = percentageholes

ret = ipblbget(getrangestats, 0, blbm_boxx, objstats(0))
xlsheet.Range(xlapp.Cells(objstats(8)+3,(5*number-2)), &
xlapp.Cells(objstats(8)+3,(5*number-2))).Value = objstats(0)

ret = ipblbget(getrangestats, 0, blbm_boxy, objstats(0))
xlsheet.Range(xlapp.Cells(objstats(8)+3,(5*number-1)), &
xlapp.Cells(objstats(8)+3,(5*number-1))).Value = objstats(0)

xlsheet.Range(xlapp.Cells(objstats(8)+3,(5*number)), &
xlapp.Cells(objstats(8)+3,(5*number))).FormulaR1C1 = "=RC[-2]/RC[-1]"

ret = ipstautoname("C:\Documents and Settings\Paul Loustalan\My &
Documents\TestingJul-Oct2002\Outline###.scl",number,outlinef)

ret = ipblbsaveoutline(outlineF)

ret = ipdocclose() 'Close thresholded image

ret = ipblbloadoutline(outlinef) 'Load outlines onto bestfit
' image AOI

'Save image to holding folder, then move to correct folder afterwards

spressure = LTrim(Str$(pressure))

scpressure = LTrim(Str$(cpresure))

If Mid$(scpressure,1,1) = "." Then

scpressure = "0" + scpressure
```

Appendix II – Macro Programs – Image Pro Plus™

Else

scpressure = scpressure + ".0"

End If

If saveit = 1 Then

ret = ipstautoname("TEST" + scpressure + "bar" + spressure + "bar" + &
"-###.TIF", number, Imagename)

ret = ipwssaveas("C:\Documents And Settings\Paul Loustalan\My &
Documents\TestingJul-Oct2002\Near Field\Analysis Images\"+spressure &
+ "Bar-" + scpressure + "Bar\" + spressure +"bar" + AOIname + "ms\"+ &
Imagename, "TIF")

End If

perholes(number-1) = percentageholes

End Sub

Void Recognition Program –Straight Injector

(“&” signifies continuation of program code over more than one line, this does not appear in the macro code)

Option Explicit

'Declare Global Variables

```
Dim number As Integer           'How many AOI's
Dim calib As Single             'Variable to set AOI height
Dim perholes(49) As Single      'Percentage holes array
Dim AOIname As String
Dim pressure As Single
```

```
Dim cpressure As Single
Dim saveit As Integer
Dim spressure As String
Dim scpressure As String
```

```
Dim hstcor(7) As Single         'Variable for thresholding
Dim xlapp As Object
Dim xlbook As Object
Dim xlsheet As Object
```

```
'InitExcel() initializes the OLE link to Excel and returns the Object
'in the xlApplication parameter. Return value: 0 = success; -1 =
'failure
```

```
Function InitExcel(ByRef xlApplication As Object) As Integer
```

```
InitExcel = 0      ' Make sure the function is initialized
```

```
'On Error Resume Next continue if an error is generated
Err.Clear          ' clear the error flag
```

```
Set xlApplication = GetObject(,"Excel.Application")
```

```
' GetObject will return an error if Excel isn't open
If Err.Number <> 0 Then
    ' Start Excel with CreateObject. If this fails, we
    'exit the macro.
```

Appendix II – Macro Programs – Image Pro Plus™

```
Err.Clear
Set xlApplication = CreateObject ("Excel.Application")
If Err.Number <> 0 Then

MsgBox "Can't find Excel.", vbOkOnly+vbCritical, "OLE Error"

InitExcel = -1
Exit Function
End If
End If

'show Excel (don't run in background)
xlApplication.Visible = True

If Err.Number <> 0 Then
MsgBox "Error showing Excel!", vbOkOnly+vbCritical, "OLE Error"
InitExcel = -2
End If
End Function
```

```
Sub Hole_Count_SS

Dim Terminate As Integer          'Variable to terminate macro
Dim height As Single              'AOI Height
Dim point1 As pointapi, point2 As pointapi  'AOI user input size
Dim check1 As Integer
Dim check2 As Integer            'Check for valid AOI user input point

Dim aoileft(7) As Integer         'AOI coordinates left
Dim aoiright(7) As Integer       'AOI coordinates right
Dim pixheight As Integer         'Height of AOI in pixels
Dim tipcentre As pointapi        'Coordinates of Injector tip centre

Dim distance As Single           'Dist from Inj tip to centre of 1st AOI
Dim temp As String * 10         'Temporary string to store position of
                                'Excel data
Dim j As Integer                'Counter
Dim disarray(49) As Single       'Array of distances of all AOI's
                                'from injector tip

Dim docname As String * 255
Dim docnames As String
Dim spraytime As Single
Dim docid As Integer
Dim i As Integer
```

Appendix II – Macro Programs – Image Pro Plus™

```
terminate = 1          'Set initially to 1 to start do loop

'Fixed Coordinates of AOI's
aoileft(1) = 376
aoileft(2) = 326
aoileft(3) = 270
aoileft(4) = 202
aoileft(5) = 176
aoileft(6) = 148
aoileft(7) = 102

aoiright(1) = 870
aoiright(2) = 910
aoiright(3) = 1000
aoiright(4) = 1038
aoiright(5) = 1108
aoiright(6) = 1182
aoiright(7) = 1218

Do While terminate = 1          'Main do loop

terminate = ipmacrostop("Do you wish to open an image for &
processing?" , ms_modal + ms_yesno + ms_quest)
    'Determine whether or not more processing is required

number = 0

If terminate = 1 Then

'Start up excel and create a new worksheet

If InitExcel(xlapp) < 0 Then
Exit Sub
End If

'Create a new workbook for your data
Set xlbook = xlapp.Workbooks.Add
xlbook.Activate
Set xlsheet = xlbook.ActiveSheet
xlsheet.Activate
xlapp.Visible = True
xlapp.WindowState = xlMinimized
```

Appendix II – Macro Programs – Image Pro Plus™

```
ret = iptemplatemode(1)    'Request image to be processed
                           'is opened by user

ret = ipwsload("", "TIF")
ret = iptemplatemode(0)

ret = ipdocgetstr(inf_name, docsel_active, docname)

docnames = Left(docname, InStr(docname, ".")-1)

AOIname = RTrim(docnames) + "-0" + Trim(Str$(number))

ret = ipdocget(getactdoc, 0, docid)

ret = ipwsconvertimage(imc_gray, conv_scale, 0, 0, 0, 0)
    'Convert To 8 bit For thresholding

ret = ipdoccloseex(docid)

ret = ipdocget(getactdoc, 0, docid)

ret = ipstgetfloat("Enter the fuel pressure", pressure, & 50, 50, 100,
50)

ret = ipstgetfloat("Enter the chamber pressure", & cpressure, 0.5, 0.5,
2.0, 0.5)

'Open thresholding data files

If pressure = 50 And cpressure = 0.5 Then

Open "5050" For Input As #1

ElseIf pressure = 50 And cpressure = 1.0 Then

Open "50100" For Input As #1

ElseIf pressure = 100 And cpressure = 0.5 Then

Open "10050" For Input As #1

Else

Open "100100" For Input As #1

End If
```

Appendix II – Macro Programs – Image Pro Plus™

```
Input #1,hstcor(1),hstcor(2),hstcor(3),hstcor(4), &
hstcor(5),hstcor(6),hstcor(7)

Close #1

saveit = ipmacrostop("Save these files?", ms_modal + & ms_yesno)
If ret = 0 Then GoTo ending
    'Exit out of macro upon cancel being pressed

calib = 234.6751892

height = 0.5

pixheight = Int(calib * height)
    'calculate AOI height in pixels
iprect.Top = 0.40 * calib
    'Initially set AOI pixel coordinates

iprect.bottom = iprect.Top + pixheight

For i = 1 To 7

ipappselectdoc(docid)

number = number + 1

iprect.Left = aoileft(i)
    'Set coordinates of AOI from user inputs
iprect.Right = aoiright(i)

If i > 1 Then

iprect.Top = iprect.bottom
iprect.bottom = iprect.bottom + pixheight

End If

ret = ipaoicreatebox(iprect)

ret = ipwsduplicate()
ret = iphstequalize(eq_bestfit)

Call process
Next
'Find starting point and calculate distance from tip to first AOI
```

Appendix II – Macro Programs – Image Pro Plus™

```
distance = 1.9                                'Calculate
the distance in mm

xlsheet.Range(xlapp.Cells(149,1), xlapp.Cells(149,1)).Value = &
"Distance from Tip"

xlsheet.Range(xlapp.Cells(149,2), xlapp.Cells(149,2)).Value = "%age &
Holes"

For j = 0 To number-1

disarray(j) = distance + height*j

xlsheet.Range(xlapp.Cells(150+j,1), xlapp.Cells(150+j,1)).Value = &
disarray(j)
xlsheet.Range(xlapp.Cells(150+j,2), xlapp.Cells(150+j,2)).Value = &
perholes(j)

Next

xlsheet.Range(xlapp.Cells(1,1), xlapp.Cells(1,1)).value = spressure
xlsheet.Range(xlapp.Cells(1,2), xlapp.Cells(1,2)).value = scpressure
xlsheet.Range(xlapp.Cells(1,3), xlapp.Cells(1,3)).Value = AOIname

End If

ret = ipappcloseall()

xlsheet.Rows("2:2").Font.Bold = True

xlsheet.Range(xlapp.Cells(150,1), xlapp.Cells(160,1)).NumberFormat = &
"0.0"

xlsheet.Columns("A:x").AutoFit
xlsheet.Columns("A:x").HorizontalAlignment = xlCenter

Loop                                          'End of main do loop, and end of macro

ending:                                     'Exit linelabel

xlsheet.Range(xlapp.Cells(1,1), xlapp.Cells(1,1)).Select

xlapp.WindowState = xlMaximized
```

Appendix II – Macro Programs – Image Pro Plus™

```
Set xlsheet = Nothing
Set xlbook = Nothing
Set xlapp = Nothing
```

```
End Sub
```

```
Sub process
```

```
'A subroutine to process the aoi's created by hole_count
```

```
Dim docid As Integer
```

```
ReDim stats(10) As Single      'Define variable with 10 elements
                              'for stats from histogram
```

```
Dim outlinef As String * 100  'Name of file for Hole Outlines
```

```
Dim i As Integer              'Counter
```

```
Dim dinfo As ipdocinfo        'Variable for information about image
```

```
Dim areaaoi As Single         'Area of the active AOI
```

```
Dim a As Single               'Holding variable
```

```
Dim b As Single               'Holding variable
```

```
Dim objstats(9) As Single     'Variable with 10 elements for the
                              'stats of the count
```

```
Dim percentageholes As Single 'Percentage holes of the AOI
```

```
Dim temp As String * 100      'Temporary variable to hold info
                              'about the Excel cell reference
```

```
Dim Imagename As String * 500 'Variable for the name of the AOI to
                              'be saved
```

```
Dim Areastats(500) As Single
```

```
Dim boxwstats(500) As Single
```

```
Dim boxhstats(500) As Single
```

```
Dim numbin As Integer
```

```
Dim holder As Integer
```

```
Dim Mode
```

```
ret = ipwsduplicate()         'Duplicate and perform best fit
                              'operation on AOI
```

```
ret = iphstequalize(eq_bestfit)
```

```
ret = iplutbinarize(0,hstcor(number),1)
```

```
'Erosion and Dilation to eliminate rogue pixels and smooth edges
```

```
ret = ipfilterode(morpho_2x2square,3)
```

Appendix II – Macro Programs – Image Pro Plus™

```
ret = ipfltdilate(morpho_2x2square,3)

ret = ipblbloadsetting("C:\Documents and Settings\Paul Loustalan\My &
Documents\PhdtestingJune03\holes-SS.env")

ret = ipblbsetattr(blob_labelmode,0)

ret = ipblbcount()

ret = ipblbget(getrangestats, 0, blbm_area, objstats(0))

ret = ipdocget(getdocinfo, docsel_active, dinfo)

a = dinfo.height / calib
b = dinfo.width / calib

areaaoi = a * b

percentageholes = objstats(5)*100/areaaoi

ret = IpBlbData(blbm_area, 0, objstats(8), areastats(0))
ret = IpBlbData(BLBM_BOXX, 0, objstats(8), boxwstats(0))
ret = IpBlbData(BLBM_BOXY, 0, objstats(8), boxhstats(0))

For i = 3 To objstats(8)+2

xlsheet.Range(xlapp.Cells(i, (5*number-4)), xlapp.Cells(i, (5*number- &
4))).Value = i-2
xlsheet.Range(xlapp.Cells(i, (5*number-3)), xlapp.Cells(i, (5*number- &
3))).Value = areastats(i-3)
xlsheet.Range(xlapp.Cells(i, (5*number-2)), xlapp.Cells(i, (5*number- &
2))).Value = boxwstats(i-3)
xlsheet.Range(xlapp.Cells(i, (5*number-1)), xlapp.Cells(i, (5*number- &
1))).Value = boxhstats(i-3)

Next

xlsheet.Range(xlapp.Cells(2, (5*number-4)), xlapp.Cells(2, (5*number- &
4))).Value = "Object"
xlsheet.Range(xlapp.Cells(2, (5*number-3)), xlapp.Cells(2, (5*number- &
3))).Value = "Area"
xlsheet.Range(xlapp.Cells(2, (5*number-2)), xlapp.Cells(2, (5*number- &
2))).Value = "Width"
xlsheet.Range(xlapp.Cells(2, (5*number-1)), xlapp.Cells(2, (5*number- &
1))).Value = "Height"
```

Appendix II – Macro Programs – Image Pro Plus™

```
xlsheet.Range(xlapp.Cells(objstats(8)+3,(5*number-4)), &
xlapp.Cells(objstats(8)+3,(5*number-4))).Value = "Total"
xlsheet.Range(xlapp.Cells(objstats(8)+4,(5*number-4)), &
xlapp.Cells(objstats(8)+4,(5*number-4))).Value = "Total Area"
xlsheet.Range(xlapp.Cells(objstats(8)+5,(5*number-4)), &
xlapp.Cells(objstats(8)+5,(5*number-4))).Value = "%age Holes"

xlsheet.Range(xlapp.Cells(objstats(8)+3,(5*number-3)), &
xlapp.Cells(objstats(8)+3,(5*number-3))).Value = objstats(5)
xlsheet.Range(xlapp.Cells(objstats(8)+4,(5*number-3)), &
xlapp.Cells(objstats(8)+4,(5*number-3))).Value = areaaoi
xlsheet.Range(xlapp.Cells(objstats(8)+5,(5*number-3)), &
xlapp.Cells(objstats(8)+5,(5*number-3))).Value = percentageholes

ret = ipblbget(getrangestats, 0, blbm_boxx, objstats(0))
xlsheet.Range(xlapp.Cells(objstats(8)+3,(5*number-2)), &
xlapp.Cells(objstats(8)+3,(5*number-2))).Value = objstats(0)

ret = ipblbget(getrangestats, 0, blbm_boxy, objstats(0))
xlsheet.Range(xlapp.Cells(objstats(8)+3,(5*number-1)), &
xlapp.Cells(objstats(8)+3,(5*number-1))).Value = objstats(0)

xlsheet.Range(xlapp.Cells(objstats(8)+3,(5*number)), &
xlapp.Cells(objstats(8)+3,(5*number))).FormulaR1C1 = "=RC[-2]/RC[-1]"

ret = ipstautoname("C:\Documents and Settings\Paul Loustalan\My &
Documents\PHDTESTINGJUNE03\Outline###.scl",number,outlinef)

ret = ipblbsaveoutline(outlinef)

ret = ipdocclose()           'Close thresholded image

ret = ipblbloadoutline(outlinef)   'Load outlines onto bestfit
                                   'image AOI

'Save image

spressure = LTrim(Str$(pressure))

scpressure = LTrim(Str$(cpressure))

If Mid$(scpressure,1,1) = "." Then

scpressure = "0" + scpressure
```

Else

scpressure = scpressure + ".0"

End If

If saveit = 1 Then

ret = ipstautoname(AOIname + ".TIF",number,Imagename)

ret = ipwssaveas("C:\Documents and Settings\Paul Loustalan\My &
Documents\PHDTESTINGJUNE03\Analysis Images\" + scpressure + "Bar-" + &
scpressure + "Bar\" + Imagename, "TIF")

End If

perholes(number-1) = percentageholes

End Sub

Appendix III
Time offsets for Global Imaging

Appendix III – Time Offsets for Global Imaging

Back Pressure / kPa	Time Offset / μs
50	-45.0
100	-50.0
200	14.0
400	-20.0
600	-47.0
800	-9.0
1000	10.0

Table AIII.1 – Table of time offset data for 5 MPa fuel pressure.

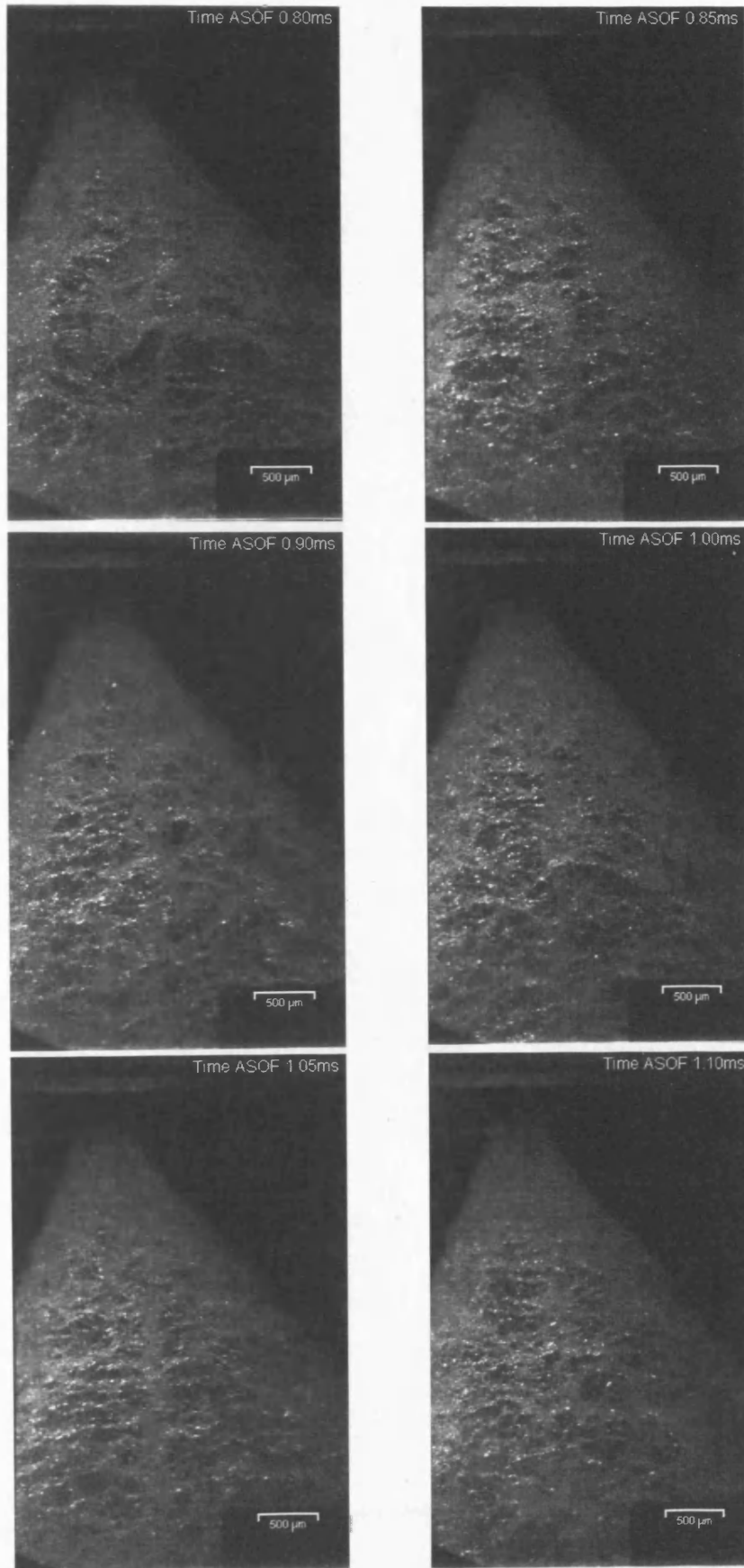
Back Pressure / kPa	Time Offset / μs
50	-88.6
100	-71.8
200	-87.1
400	-45.6
600	-23.6
800	-23.0
1000	-9.2

Table AIII.2 – Table of time offset data for 10 MPa fuel pressure.

Appendix IV
Images – Varying Back Pressure

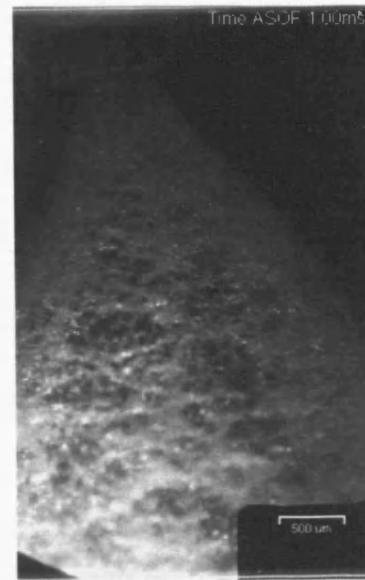
Near-Field Imaging – Injector A

5 MPa Fuel Pressure – 50 kPa Back Pressure



Near Field Imaging – Injector A

5 MPa Fuel Pressure – 100 kPa Back Pressure



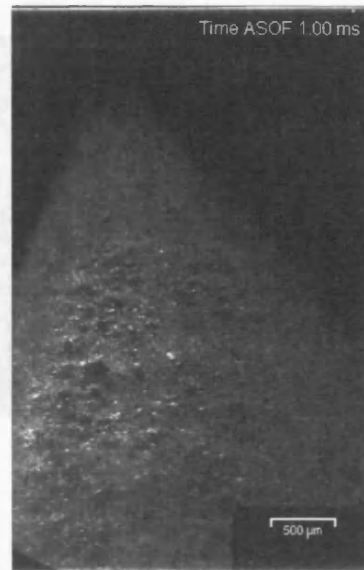
Near Field Imaging – Injector A

10 MPa Fuel Pressure – 50 kPa Back Pressure



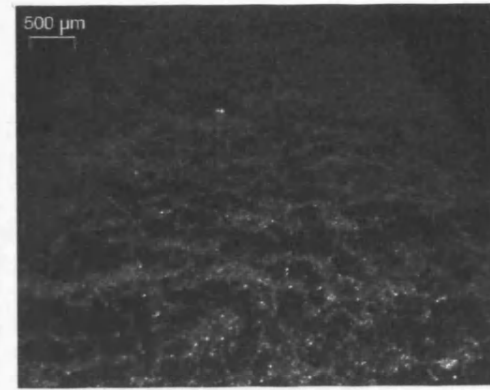
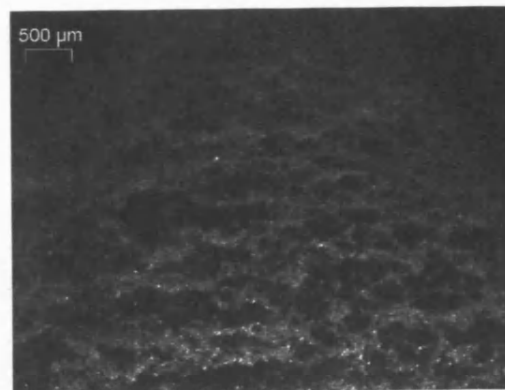
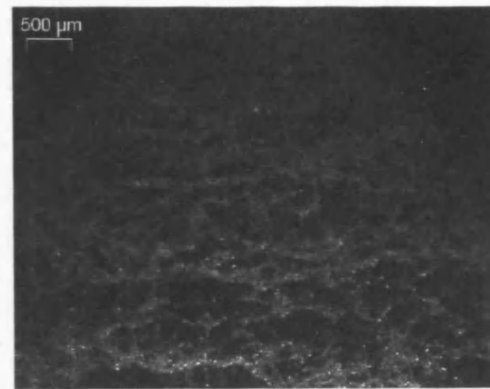
Near Field Imaging – Injector A

10 MPa Fuel Pressure – 100 kPa Back Pressure



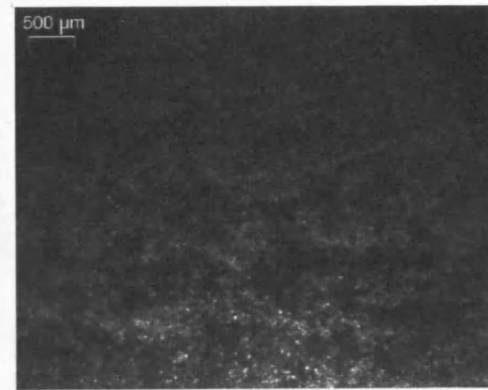
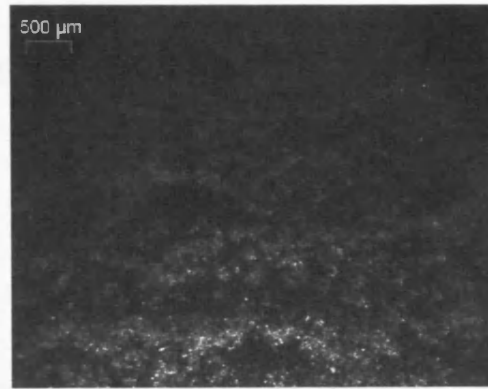
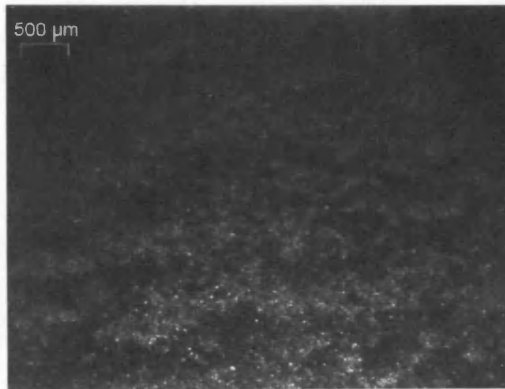
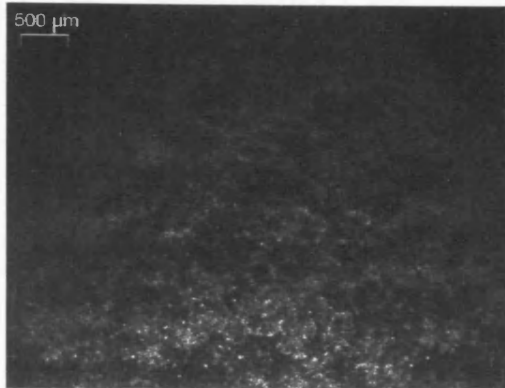
Near Field Imaging – Single Shot Testing – Injector B

5 MPa Fuel Pressure – 50 kPa Back Pressure – 1.5 ms ASOI



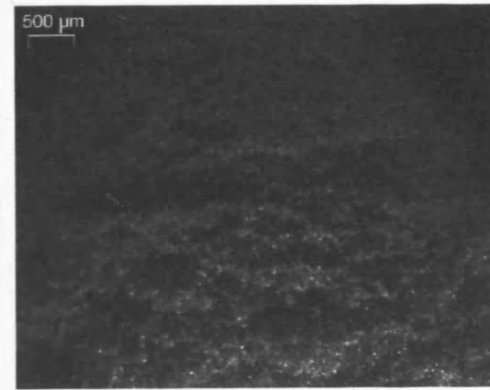
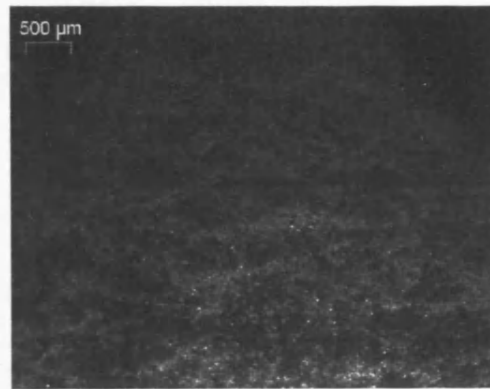
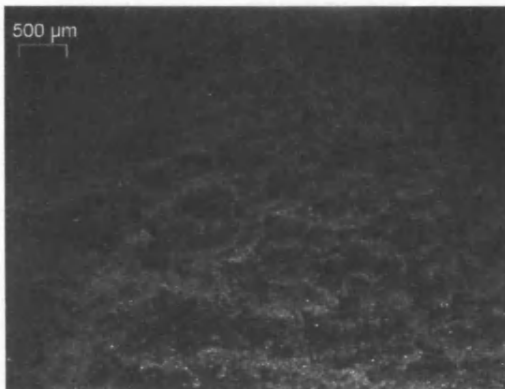
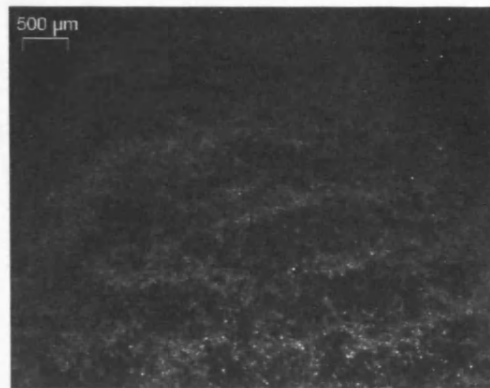
Near Field Imaging – Single Shot Testing – Injector B

5 MPa Fuel Pressure – 100 kPa Back Pressure – 1.5 ms ASOI



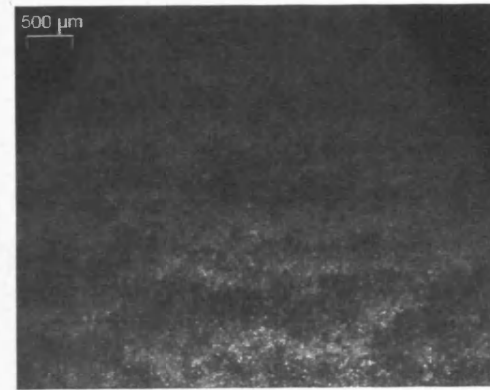
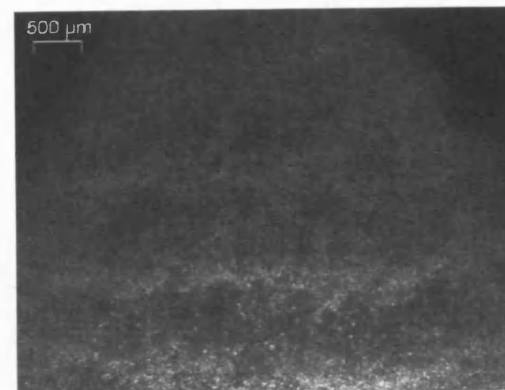
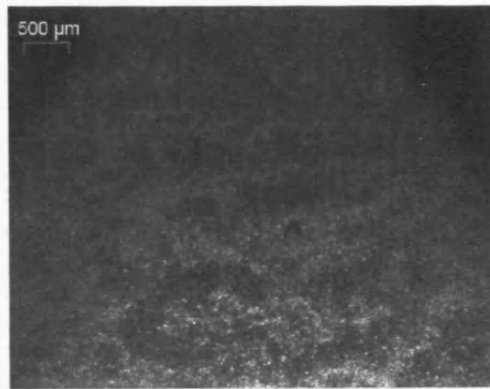
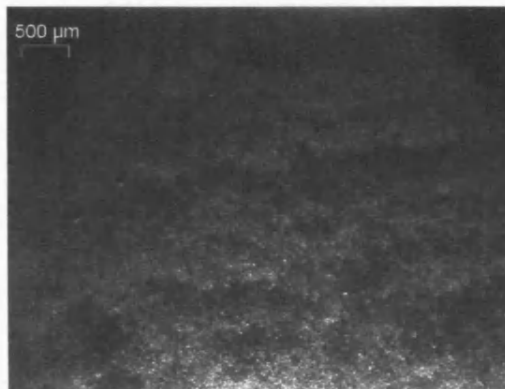
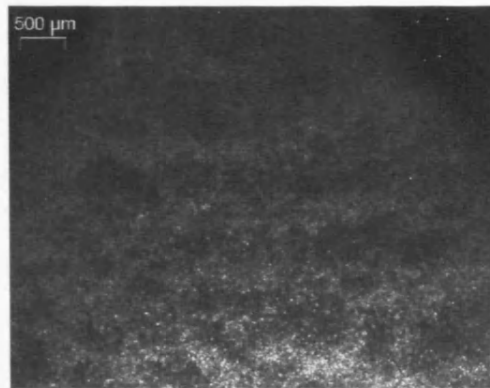
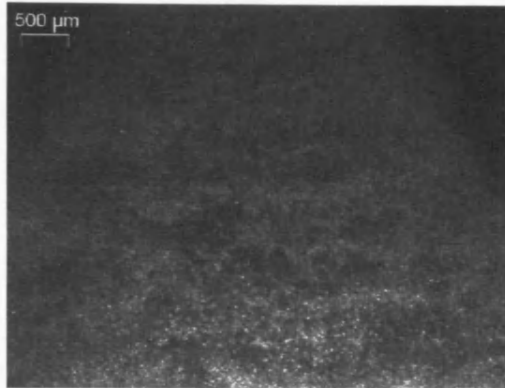
Near Field Imaging – Single Shot Testing – Injector B

10 MPa Fuel Pressure – 50 kPa Back Pressure – 1.5 ms ASOI

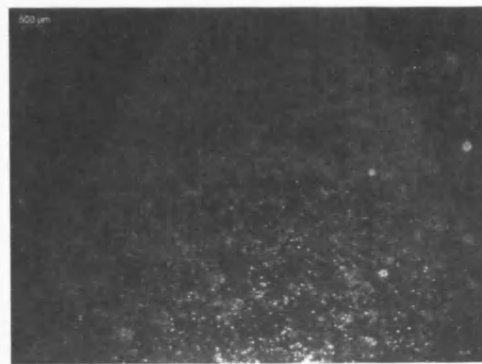
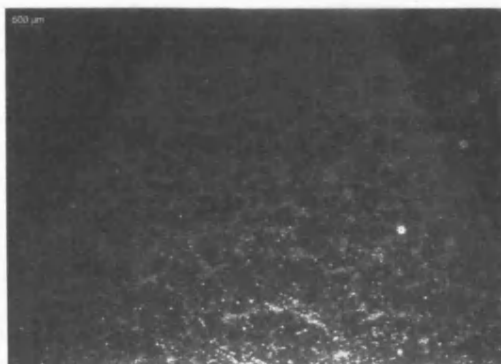
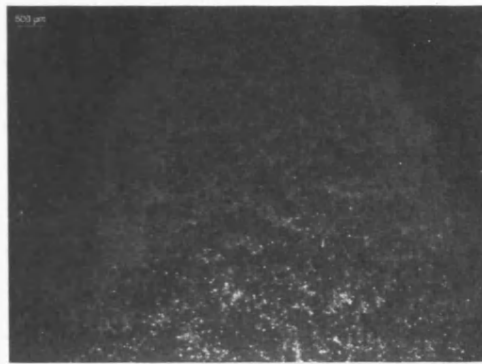


Near Field Imaging – Single Shot Testing – Injector B

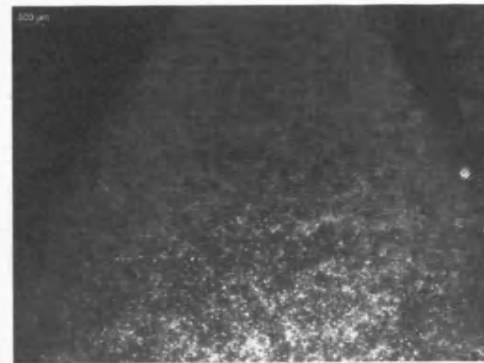
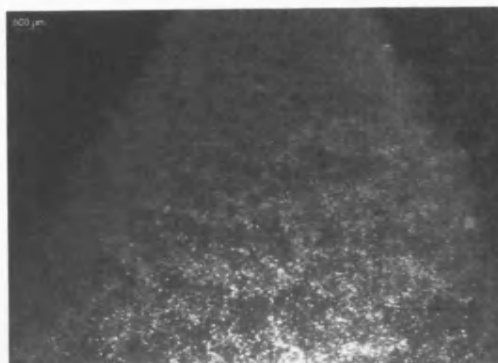
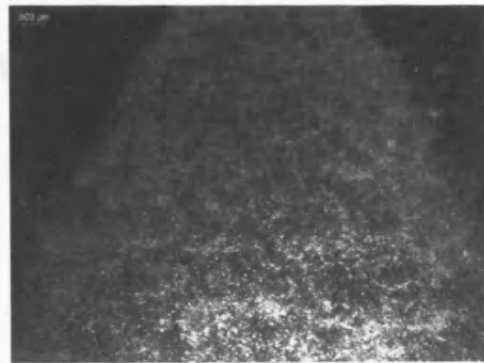
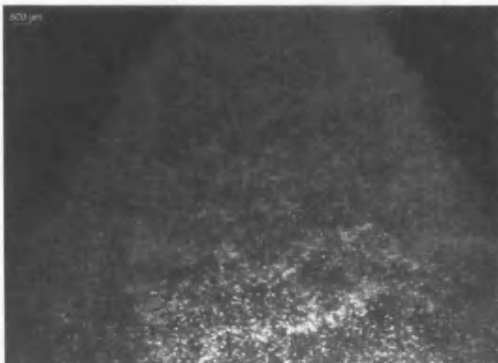
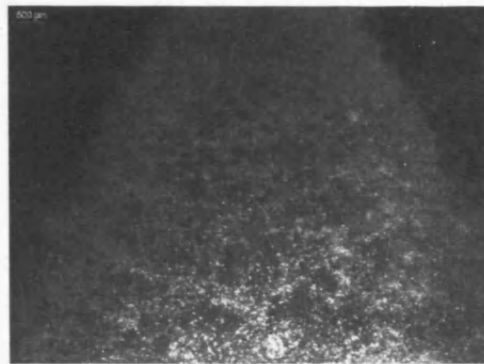
10 MPa Fuel Pressure – 100 kPa Back Pressure – 1.5 ms ASOI



Further Downstream Imaging – Single Shot Testing – Injector A
5 MPa Fuel Pressure – 50 kPa Back Pressure – 1.0 ms ASOI



Further Downstream Imaging – Single Shot Testing – Injector A
10 MPa Fuel Pressure – 50 kPa Back Pressure – 1.0 ms ASOI



Appendix V
Images – Impinging Air Flow

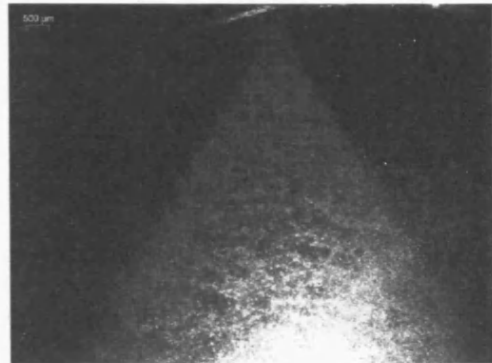
Near Field Imaging – Injector A

2 mm Valve Lift – 5 MPa Fuel Pressure – 19.35 kPa Pressure Drop



Near Field Imaging – Injector A

3 mm Valve Lift – 5 MPa Fuel Pressure – 19.35 kPa Pressure Drop



Near Field Imaging – Injector A

5 mm Valve Lift – 5 MPa Fuel Pressure – 19.35 kPa Pressure Drop

